PHYSIK-DEPARTMENT

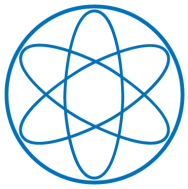

Extraction of Resonance Parameters of Light Meson Resonances in the Charged Three-Pion Final State at the COMPASS Experiment (CERN)

Masterarbeit von Stefan Wallner

TECHNISCHE UNIVERSITÄT MÜNCHEN

Technische Universität München
Physik-Department E18

Extraction of Resonance Parameters of Light Meson Resonances in the Charged Three-Pion Final State at the COMPASS Experiment (CERN)

Stefan Wallner

Erstgutachter (Themensteller): Prof. Dr. Stephan Paul
Zweitgutachter: Prof. Dr. Laura Fabbietti

Die Masterarbeit wurde am 07.10.2015 eingereicht.

Abstract

Light unflavored mesons are a laboratory to investigate low-energy QCD. A good channel to study them is the $\pi^-\pi^-\pi^+$ final state, produced in high-energy diffractive pion-proton scattering, $\pi^- + p \to \pi^-\pi^-\pi^+ + p_{\text{recoil}}$. The COMPASS collaboration has measured this final state in the mass range of $0.5 < m_{3\pi} < 2.5\,\text{GeV}/c^2$ and squared four-momentum transfer range of $0.1 < t' < 1.0\,(\text{GeV}/c)^2$ with an unprecedented statistical precision. A partial-wave analysis (PWA) was performed using 88 partial waves, which is the largest wave sets ever used in this channel. The PWA was performed in bins of the squared four-momentum transfer t', which allows to investigate the t' dependence of the partial waves and their various structures. The result of this decomposition forms the basis of this analysis. The characteristics of the mesons, namely their masses and widths, are extracted performing a so-called resonance-model fit, in which resonant and non-resonant contributions of the extracted partial-wave amplitudes are parameterized. This parameterization goes hand in hand with systematic uncertainties, which are in the focus of this thesis. In total, 14 partial waves from six J^{PC} sectors (0^{-+}, 1^{++}, 1^{-+}, 2^{++}, 2^{-+} and 4^{++}) are fitted with a resonance model including 11 meson resonances and one non-resonant term for each wave, which accounts for other production mechanisms. This is the largest resonance model ever used in this channel.

The well-known resonances like the $a_2(1320)$, $a_4(2040)$, $\pi(1800)$ and the $\pi_2(1670)$, which are included in the fit, are extracted with a small systematic uncertainty. In contrast, the resonance parameters of the $a_1(1260)$, which is the ground state in the $J^{PC} = 1^{++}$ sector, reveal larger systematic instabilities, which presumably arise from the larger non-resonant contributions in the 1^{++} waves. A bimodal behavior between solutions with a wider and a narrower $a_1(1260)$ is observed in some of the systematic studies. This goes together with a change in the t' slope parameter from $12.7\,(\text{GeV}/c)^{-2}$ in the solution with the wide $a_1(1260)$ to a smaller slope parameter of around $8\,(\text{GeV}/c)^{-2}$ for the narrow $a_1(1260)$. The 2^{-+} partial waves exhibit spectra with interesting structures. Within the analyzed resonance model, a consistent description of all these features is only possible by including three π_2 resonances, the $\pi_2(1670)$, the $\pi_2(1880)$ and the $\pi_2'(2005)$. A novel narrow signal slightly above $1.4\,\text{GeV}/c^2$ in the $1^{++}\,0^+\,f_0(980)\,\pi\,P$ wave, observed for the first time by the COMPASS experiment and named $a_1(1420)$, shows clear resonance-like behavior. Its Breit-Wigner parameters and t' dependence are very robust against systematic effects with a mass of $1411.8\,^{+1.0}_{-4}\,\text{MeV}/c^2$ and a width of $158\,^{+8}_{-8}\,\text{MeV}/c^2$. Furthermore, a possible $\pi_1(1600)$ resonance interpretation of the broad intensity enhancement, observed in the $1^{-+}\,1^+\,\rho(770)\,\pi\,P$ wave with spin-exotic quantum numbers, is investigated in this thesis. The results show a dramatic change of the relative intensity of the $\pi_1(1600)$ with respect to the non-resonant contribution in this wave with t'. The extracted $\pi_1(1600)$ mass of $1600\,^{+100}_{-50}\,\text{MeV}/c^2$ and width of $600\,^{+60}_{-240}\,\text{MeV}/c^2$ have large systematic uncertainties. The shape of the $\pi_1(1600)$ t' dependence does not follow the expected single-exponential function. However, the extracted average t' slope parameter of $7.2\,^{+1.0}_{-3.1}\,(\text{GeV}/c)^{-2}$ and the slow production-phase motion with t' are consistent with a resonance structure. For a conclusive statement on the $\pi_1(1600)$, an improvement of the fit model and especially a more realistic non-resonant parameterization, is mandatory.

Zusammenfassung

Leichte flavourlose Mesonen bieten die Möglichkeit, QCD bei niedrigen Energien zu untersuchen. Ein gut geeigneter Kanal hierfür ist der $\pi^-\pi^-\pi^+$ Endzustand, welcher in diffraktiver Pion-Proton Streuung erzeugt werden kann, $\pi^- + p \rightarrow \pi^-\pi^-\pi^+ + p_{\text{recoil}}$. Das COMPASS Experiment hat diese Reaktion im Massenbereich von $0.5 < m_{3\pi} < 2.5\,\text{GeV}/c^2$ und im Bereich des quadrierten Viererimpulsübertrages von $0.1 < t' < 1.0\,(\text{GeV}/c)^2$ mit einer noch nie dagewesenen statistischen Präzision gemessen. Eine Partialwellenanalyse (PWA), mit einem aus 88 Wellen bestehendem Modell, das größte bis dato verwendet, wurde in t'-Bins durchgeführt. Dies ermöglicht die Untersuchung der t'-Abhängigkeit der unterschiedlichen Partialwellen und ihrer Strukturen. Mit Hilfe des sogenannten Resonanzmodellfits werden die Eigenschaften der Mesonen, nämlich ihre Massen und Breiten bestimmt. Im Resonanzmodell wird die Massenabhängigkeit der resonanten und nicht-resonanten Komponenten der Partialwellen parameterisiert, was zu systematischen Unsicherheiten führt. Diese systematischen Unsicherheiten werden in dieser Arbeit untersucht. Insgesamt werden 14 Partialwellen aus sechs J^{PC} Quantenzahlen (0^{-+}, 1^{++}, 1^{-+}, 2^{++}, 2^{-+} and 4^{++}) im Resonanzmodell mit 11 Resonanzen und einem nicht-resonanten Term für jede Welle beschrieben. Dies ist das größte Resonanzmodell das jemals in diesem Kanal verwendet wurde.

Die gut bekannten Resonanzen wie das $a_2(1320)$, $a_4(2040)$, $\pi(1800)$ und das $\pi_2(1670)$, können mit kleinener Unsicherheit bestimmt werden. Im Gegensatz dazu zeigt die $a_1(1260)$ Resonanz, der 1^{++} Grundzustand, größere systematische Unsicherheiten, welche vermutlich durch den großen nicht-resonanten Anteil in der 1^{++} Welle hervorgerufen werden. Zwei Arten von Lösungen für das $a_1(1260)$, eine mit einem breiten und eine mit einem schmalen $a_1(1260)$, werden in den systematischen Studien beobachtet. Dies führt unter anderem zu einer größeren Steilheit der t'-Abhängigkeit von $12.7\,(\text{GeV}/c)^{-2}$ in der breiten $a_1(1260)$ Lösung, im Vergleich zu ca. $8\,(\text{GeV}/c)^{-2}$ in der schmalen $a_1(1260)$ Lösung. Die 2^{-+} Partialwellen zeigen ein vielfältiges Spektrum interessanter Strukturen. Im verwendeten Modell mit drei π_2 Resonanzen, nämlich dem $\pi_2(1670)$, sowie dem $\pi_2(1880)$ und dem $\pi_2'(2005)$, können alle diese Details beschrieben werden. Ein bisher unbekanntes Signal wurde in der $1^{++}\,0^+\,f_0(980)\,\pi\,P$ Welle knapp oberhalb von $1.4\,\text{GeV}/c^2$ das erste Mal von COMPASS beobachtet und $a_1(1420)$ benannt. Dieses Signal zeigt einen klaren Resonanzcharakter. Seine Breit-Wigner Parameter und der t'-Steilheitsparameter sind in den systematischen Studien sehr stabil. Eine Masse von $1411.8\,^{+1.0}_{-4}\,\text{MeV}/c^2$ und eine Breite von $158\,^{+8}_{-8}\,\text{MeV}/c^2$ werden gemessen. Desweiteren wird in dieser Arbeit eine mögliche Resonanz, das $\pi_1(1600)$, in der $1^{-+}\,1^+\,\rho(770)\,\pi\,P$ Welle mit spin-exotischen Quantenzahlen untersucht. Es wird eine deutliche t'-Abhängigkeit der Intensität des $\pi_1(1600)$ relativ zu dem nicht-resonanten Anteil beobachtet. Die extrahierte $\pi_1(1600)$ Masse von $1600\,^{+100}_{-50}\,\text{MeV}/c^2$, sowie die Breite von $600\,^{+60}_{-240}\,\text{MeV}/c^2$ haben große systematische Unsicherheiten. Auch die t'-Abhängigkeit entspricht nicht der erwarteten exponentiellen Form. Andererseits ist der extrahierte t'-Steilheitsparameter von $7.2\,^{+1.0}_{-3.1}\,(\text{GeV}/c)^{-2}$ und die von t' unabhängige Produktionsphase konsistent mit einer Resonanzinterpretation. Um endgültige Aussagen zum $\pi_1(1600)$ treffen zu können, muss das Fitmodell und speziell die Parametrisierung der nicht-resonanten Beiträge verbessert werden.

Contents

CHAPTER 1

Introduction

The strong interaction is one of the four fundamental interactions that are responsible for all physics processes. It appears in a broad range of physics processes from high-energy particle collisions, like in the LHC, down to the very low energies, like e.g. in the binding of neutrons and protons in nuclei. Quantum Chromodynamics (QCD) is believed to be the fundamental theory of strong interaction. QCD describes the interaction of quarks via gluon exchange. However, as gluons carry color charge, they interact also with themselves.

In contrast to the high-energy region of QCD, where the coupling constant of the strong interaction becomes small, the self interaction of the gluons leads to an increasing coupling when going to lower energies such that perturbative methods are no longer applicable to solve QCD from first principles. The increasing coupling results in the so-called confinement of quarks and gluons into bound states called hadrons. This means, that no free quarks or gluons can be directly observed in the experiments, but only their bound states can be investigated. A quantitative understanding of the confinement is one of the last open questions of the Standard Model. Similar to QED where the energy spectra of the atoms, which are the QED bound states, give information about the electromagnetic interaction, the hadron masses and widths reflect the inner workings of QCD.

1.1 Constituent Quark Model and the Light Meson Sector

Hadrons are differentiated by their spin. Half-integer spin hadrons are called baryons while those with integer spin are called mesons. Similar to atoms where their valence electrons determine their quantum numbers, the constituent quark model describes the quantum numbers of the hadrons by the contribution of valence quarks. In this non-relativistic model, mesons are quark-antiquark systems ($q\bar{q}'$) and baryons consist of three quarks ($qq'q''$).

In the constituent-quark picture, so-called light mesons are build from up-, down- or strange-quarks. Light unflavored mesons are those without strangeness, which means that they have either no strangeness content or hidden strangeness like the $\phi(1020) = s\bar{s}$. The similar mass of

the up and down quarks, manifests itself as isospin symmetry. The up and down quarks form an isospin duplet ($I = {}^1\!/_2$, $I_3 = \pm{}^1\!/_2$), while the strange quark is an isospin singlet state ($I = I_3 = 0$). This means that unflavored mesons can be isoscalar $I = 0$ or isovector $I = 1$ states[1].

As quarks have spin ½, $q\bar{q}'$ pairs can only have integer total intrinsic spin of

$$S = 0 \quad \text{or} \quad S = 1. \tag{1.1}$$

Furthermore, the $q\bar{q}'$ system has an orbital angular momentum L, which couples with the spin S to the total spin J of the meson:

$$|L - S| \leq J \leq L + S. \tag{1.2}$$

The parity P of the meson is given by the parity of the valence quarks and the parity of the spatial wave function of the $q\bar{q}'$ system as

$$P = (+1)(-1)(-1)^L = (-1)^{L+1}. \tag{1.3}$$

For neutral mesons, the C-parity is defined in the following way

$$C = (-1)^{L+S}. \tag{1.4}$$

However, as charged mesons are not eigenstates of charge conjugation, their C-parity is not defined. Therefore, the so-called G-parity was introduced. By an additional rotation of 180° around the I_2-axis in the isospin space, which corresponds to a charge flip, charged mesons become eigenstates of the G-parity with eigenvalue

$$G = C \cdot e^{i\pi I_2} = (-1)^{L+S+I}. \tag{1.5}$$

Here, I is the isospin of the meson. It is conventional to assign to the charged mesons the C quantum number of their neutral isospin partner[2]. The mesons are named according to their quantum numbers:

$$I^G J^{PC}. \tag{1.6}$$

For example, isovector states ($I = 1$) with positive parity and negative G-parity ($1^- J^{++}$) are called a_J, while those with negative parity and G-parity ($1^- J^{-+}$) are called π_J[3]. However, in the constituent quark model, not all possible combinations of these quantum numbers are allowed. The following combinations cannot be constructed from a $q\bar{q}'$ system in the non-relativistic limit [1]

$$J^{PC} = 0^{--}, \quad \text{odd}^{-+} \text{ and } \text{even}^{+-}. \tag{1.7}$$

Mesons with such quantum numbers are called exotic states and are of special interest. As a

[1] A system of only up or down quarks can be $I = 0$ or $I = 1$ while strange quarks do not contribute to the isospin.
[2] The π^- and π^+ for example get the same C-parity as the π^0 of $C = +1$.
[3] The C-parity is fixed by the G-parity and the isospin.

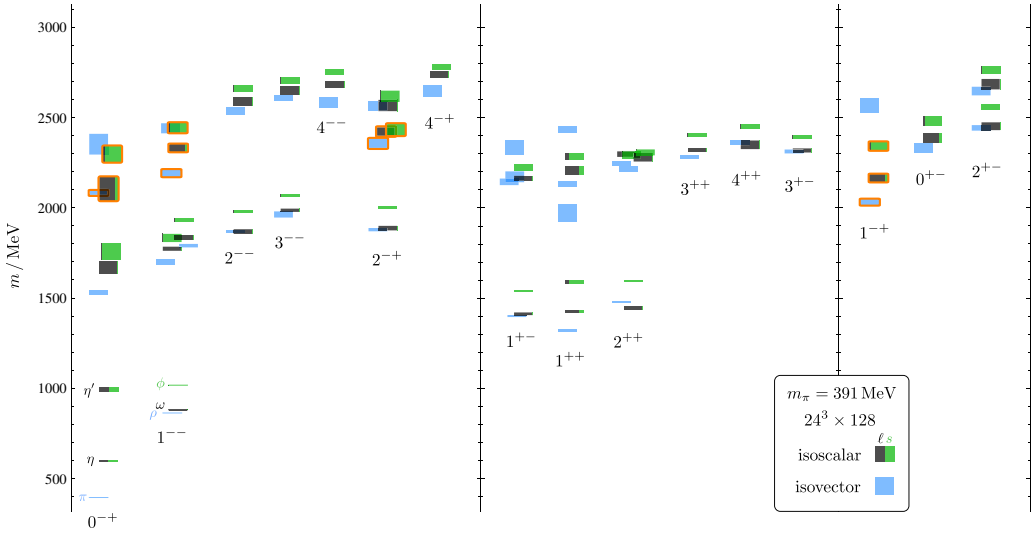

Figure 1.1: Isoscalar (black/green) and isovector (blue) meson spectrum from lattice QCD calculations [3]. The height of the box represents the statistical uncertainty of the mass determination. Orange outlined states are candidates for a hybrid meson interpretation.

simple $q\bar{q}'$ content is excluded, they could either be identified as hybrids with a gluonic excitation, which contributes to the quantum numbers of the state, or they are purely gluonic states like gluballs. Furthermore, states with more than two valence quarks like tetraquarks or mesonic molecules are discussed [2]. An experimental confirmation of such states would give valuable insight into the low-energy region of QCD. One should notice, that there are no exotic states in the baryon sector as all possible J^{PC} combinations are accessible. This is one of the reason that make the investigation of the meson sector so interesting.

The growth of available computing power has opened up a further possibility to investigate the low-energy regime of QCD. In lattice QCD, which is currently the only approach to solve low-energy QCD from first principles, the quark and gluon fields are simulated on a discrete space-time lattice. As the computational costs are directly related to the quark masses, the calculations still have to be performed at unphysically light quark masses, which leads to pion masses as large as $391\,\mathrm{MeV}/c^2$ [3]. Figure 1.1 shows the results of a state-of-the-art lattice calculation of masses of isoscalar ($I = 0$) and isovector ($I = 1$) light unflavored mesons. Not only one state is predicted for each $I^G\,J^{PC}$ sector, but a whole spectrum of excited states is predicted by lattice QCD. Furthermore, lattice QCD allows for a direct identification of hybrid states with gluonic content (framed in orange in figure 1.1). The lightest state with exotic quantum numbers is predicted to be in the $J^{PC} = 1^{-+}$ sector roughly $1.3\,\mathrm{GeV}/c^2$ heavier than the $\rho(770)$ meson [4].

On the experimental side, since the discovery of the pion in 1947 by Powell et. al. [5], a zoo of hadrons was discovered by various experiments. Figure 1.2 shows the current state of established light isovector mesons, as listed by the Particle Data Group (PDG) [6]. The different boxes

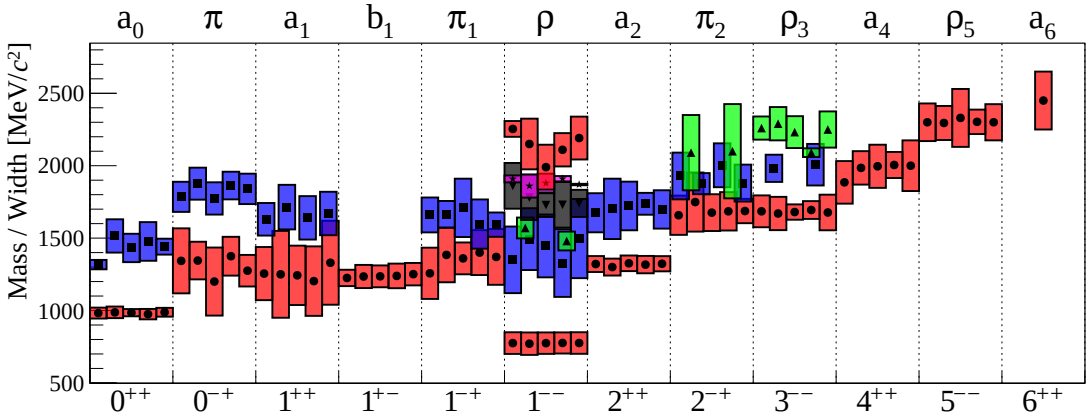

Figure 1.2: Experimental data on light isovector meson resonances ($1^G\,J^{PC}$) above 500 MeV/c^2. Each box correspond to one experimental measurement. The different colors correspond to different resonances. The center of the box indicates the mass of the resonance, while the box height shows its width. For each resonance, the latest five measurements are taken from the PDG [6].

show the five latest measurements for each state. The height of the boxes represents the width of the state. In addition to the ground states, also excited states have been observed. While some ground states are very well known, like the $a_2(1320)$, the 2^{++} ground state, other regions still rise question marks.

For the excitations of the pion ($J^{PC} = 0^{-+}$), two resonances, the $\pi(1300)$ and the $\pi(1800)$, have been experimentally observed. However, there are tensions between the measurements. For example, for the $\pi(1800)$, two clusters of observations for its mass, one slightly below 1800 MeV/c^2 and one around 1860 MeV/c^2, are listed by the PDG [6]. Lattice calculations predict, that the $\pi(1800)$ is a hybrid with a considerable gluonic content which makes a detailed investigation if this state interesting.

Another much debated sector is the 1^{++} sector with the $a_1(1260)$ ground state. This resonance has a large width, which varies strongly among the different measurements. Furthermore, other non-resonant reactions have been discussed to be partly responsible for the $a_1(1260)$ signal [7, 8] in diffractive reactions. A clarification of the details of this structure is still needed.

Also the 2^{-+} sector gives rise to questions. The ground state, the $\pi_2(1670)$, is well-known. However, the proximity of the observed first excitation, the $\pi_2(1880)$, to the ground state leads to speculations about its nature. Furthermore, a variety of different π_2 resonances around 2 GeV/c^2 with different widths have been observed by different experiments [9, 10]. A verification of these claims is needed.

One of the most disputed sectors of light mesons is the spin-exotic 1^{-+} sector. The experimentally best investigated spin-exotic candidate is the $\pi_1(1600)$ [1]. In the COMPASS data, a broad bump from 0.9 to 1.8 GeV/c^2 is found, which may contain a possible $\pi_1(1600)$ signal. A similar structure was found by the VES experiment [11], while two different analyses ([12] and [13]) of

data from the BNL E852 experiment revealed different structures, also in disagreement with the COMPASS findings. In [1] it is demonstrated, that the different structures in the BNL analyses arise from a too limited analysis models. Still, the resonance interpretation of this structures is an open question.

To investigate these open questions, the COMPASS experiment has collected the so far largest data set of a_J and π_J like resonances. The analysis of these data requires sophisticated methods. Decomposing the data into their J^{PC} contributions, the so-called partial-wave analysis (PWA), allows to extract the resonance content from the data. Based on the achievements and developments of previous works [1, 14], the main goal of this thesis is to extract the masses and widths of the a_J and π_J like resonances. However, the PWA introduces systematic dependencies on the employed model, which become increasingly important for data sets with high statistical precision like it is the case for the analysis performed here. Therefore, a honest estimate of the systematic uncertainties of the extracted resonance parameters will be given in this work.

1.2 The Three-Pion Final State

1.2.1 Diffractive Dissociation

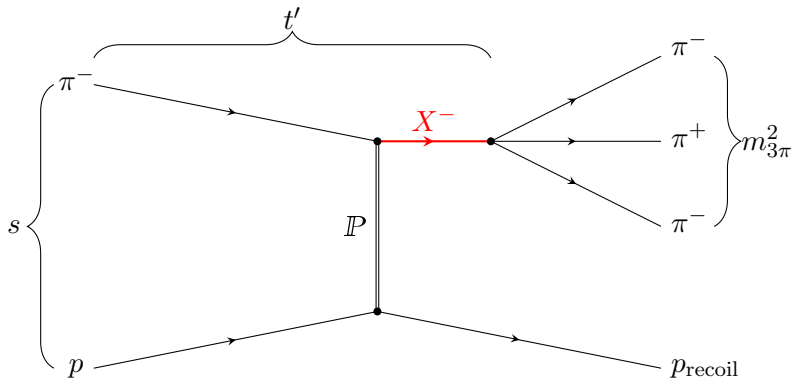

Figure 1.3: Meson production in diffractive $\pi^- + p \to \pi^-\pi^-\pi^+ + p_{\text{recoil}}$ scattering.

Almost all unflavored isovector meson resonances with negative G-parity (1^- J^{P+}) can decay into three charged pions ($\pi^-\pi^-\pi^+$), which brought this final state into the focus of many analyses (see [12, 15–17]). Furthermore, the $\pi^-\pi^-\pi^+$ final state is claimed to be one of the golden channels for the observation of exotic states [4]. The COMPASS collaboration has collected the so far largest data set of this final state in high-energy pion-proton scattering, $\pi^- + p \to \pi^-\pi^-\pi^+ + p_{\text{recoil}}$ [1], which is the basis of this analysis. The reaction is depicted in figure 1.3. The very short-lived intermediate 3π meson resonances X^- are produced via an excitation of the beam pion by strong interaction with the target proton and subsequently decay into three charged pions. The strong interaction in the pion-proton scattering can be described in the framework of Regge theory via

so-called Pomeron exchange $\mathbb{P}$. The interested reader may find further information in [18]. The invariant mass of the three-pion system

$$m_{3\pi}^2 = \left(\sum_{i=1}^{3} p_i \right)^2 / c^2, \tag{1.8}$$

where the p_i are the four-momenta of the final-state pions, is the mass of the intermediate state X^-. To avoid excitations of the target, only soft scattering is considered, where the target proton stays intact. This limits the range of the squared four-momentum transfer

$$t = \left(\left[\sum_{i=1}^{3} p_i \right] - p_{\pi,\text{beam}} \right)^2 \leq 0 \tag{1.9}$$

from the beam pion to the target proton. Due to kinematic restrictions, a minimum squared four-momentum of [2]

$$|t|_{\text{min}} \approx \left(\frac{(m_{3\pi}c)^2 - (m_\pi c)^2}{2|\vec{p}_{\text{beam}}|} \right)^2 \tag{1.10}$$

has to be transfered to generate a state with a certain mass $m_{3\pi}$. Hence, the so-called reduced four-momentum transfer squared

$$t' = |t| - |t|_{\text{min}} \geq 0 \tag{1.11}$$

is defined. For simplicity, t' is called squared four-momentum transfer in the further text. In addition to t' and the invariant three-pion mass $m_{3\pi}$, the kinematics of the 3π decay is described by a set of five phase-space variables denoted by τ. As the beam energy is fixed, also the center-of-mass energy s is fixed.

According to the current state of knowledge, the strong interaction conserves isospin and G-parity. Taking into account, that the pion is an isovector meson with $G = -1$, and that the Pomeron carries the vacuum quantum numbers ($I^G = 0^+$) [19], only a_J or π_J like states X^- with

$$I^G J^{PC} = 1^- J^{P+} \tag{1.12}$$

can be produced in the reaction $\pi^- + p \to \pi^-\pi^-\pi^+ + p_{\text{recoil}}$. Therefore, for the rest of the text and especially in the partial-wave names, the I^G quantum numbers are omitted.

1.2.2 Further Reactions

Diffractive dissociation is not the only process, contributing to the three-pion final state when scattering high-energy pions at protons. Due to the very short lifetime of the intermediate

states in the range of 10^{-24} s[4], only the decay fragments, in this case $\pi^-\pi^-\pi^+$, can be detected in the experiment, which makes the separation between the different production mechanisms complicated. At least two other reaction mechanisms contribute to the $\pi^-\pi^-\pi^+$ spectrum.

Central Production

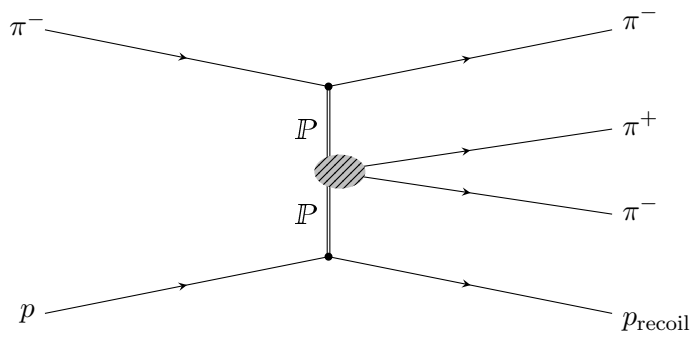

Figure 1.4: Central production reaction leading to the $\pi^-\pi^-\pi^+$ final state.

Two Pomerons fuse and decay into two charged pions (see figure 1.4). Together with the scattered beam pion, this also yields three pions in the final-state. However, in this so-called central production, the different reaction kinematics allows at least for a partial separation between diffractive and central production reaction, which is used in the event selection (see section 2.2).

Deck-like Reactions

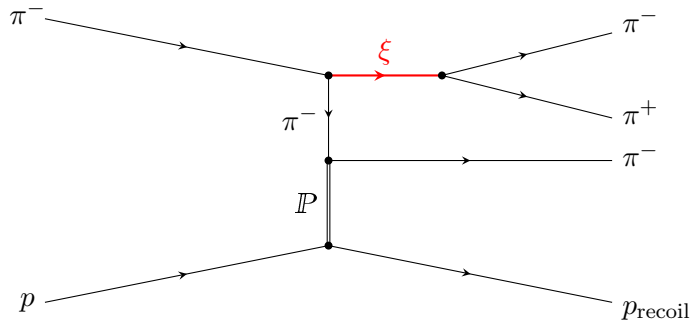

Figure 1.5: Deck-like process.

Another possible reaction path was originally proposed by R. Deck [7] to explain the $a_1(1260)$ peak in the $1^{++}\,0^+\,\rho(770)\,\pi\,S$ wave (see section 5.4). It is shown in figure 1.5. In this reaction, the

[4] $\Delta T \approx \frac{\hbar}{\Gamma_0} = 6.6 \times 10^{-24}$ s with a typical meson-resonace width of $\Gamma_0 = 100$ MeV

beam pion dissociates into a two-pion resonance ξ and a virtual pion. The virtual pion rescatters from the proton via Pomeron exchange and forms with the two pions from the ξ decay the three-pion final state. In contrast to central production, Deck-like reactions cannot be separated from diffractive dissociation on the level of event selection. Thus, they have to be treated at the level of the-resonance model fit (see section 4.1).

CHAPTER 2

Data Set

In this chapter, a basic introduction into the setup of the COMPASS experiment and the event selection for the charged three-pion final state is given. This is followed by a discussion of the obtained kinematic distributions. The occurrence of well-known resonance patterns in the three-pion invariant mass spectrum are presented alongside with the correlation of the mass spectrum with the reduced four-momentum transfer squared t'.

2.1 The COMPASS Experiment at CERN

2.1.1 Physics Program

The main goal of the COMPASS[1] experiment is to deepen the understanding of QCD in the low-energy regime by the investigation of the structure and dynamics of hadrons [20]. One approach is to explore the spectrum of light meson resonances, produced either in diffractive pion-proton scattering (see section 1.2.1), which will be the topic of this thesis, or in central production reactions (see section 1.2.2 or [21]). Further insight into the internal dynamics of hadrons can be obtained by measuring of the polarisability of pions [22] and kaons. In addition to this physics program with hadrons, measurements with a high energy muon beam focus on the internal structure of nucleons, like, for example, the measurement of the gluon polarization within the nucleon [23].

[1] Common Muon and Proton Apparatus for Structure and Spectroscopy

2.1.2 Experimental Setup

The COMPASS experiment is operated since 2002 at the Super Proton Synchrotron (SPS) accelerator at CERN[2]. It is a fixed-target experiment where various kinds of highly energetic hadron or lepton beams, interact with different targets. The scattered and produced particles are highly boosted in forward direction and are detected by a two-stage magnetic spectrometer. The experimental setup used for the hadron data-taking campaign in 2008 and 2009, during which the data of this analysis were recorded, is explained in detail in [20]. A short overview will be given in this section.

Beam Line

The COMPASS experiment is located at the M2 beam line. A 400 GeV proton beam from the SPS accelerator hits a beryllium production target, where showers of various secondary hadrons, mainly pions, kaons and antiprotons, are produced. The beam type and energy is selected by a series of dipole and quadrupole magnets and collimators, which focus the beam onto the COMPASS target. Different beam configurations are possible. High-energy positive or negative hadron beams, as well as muon or electron beams can be used. The data for this analysis were recorded with a 190 GeV negative hadron beam, which mainly consists of negative pions, but also contains small kaon and antiproton components (see table 2.1). Two Cherenkov counters (CEDARs) were placed upstream of the COMPASS target which identify the beam particles by exploiting the different angles under which the Cherenkov photons are emitted by particles with different mass, but the same momentum.

Table 2.1: Composition of the negative 190 GeV hadron beam at the COMPASS target [20].

	π^-	K^-	$\bar{p}$
Relative beam content	96.8 %	2.4 %	0.8 %

Spectrometer Layout

The large variety in the COMPASS physics program requires a multi-purpose experimental setup, which manifests itself in the layout of the spectrometer. Figure 2.1 shows the schematic layout used during the 2008 and 2009 data taking. The setup can be subdivided roughly into three parts. The target region, including the target and a set of detectors placed around it. The Large-Angle Spectrometer (LAS), which is placed directly after the target region, measures outgoing particles produced under polar angles of up to 180 mrad. The LAS is followed by the Small-Angle Spectrometer (SAS) which extends the acceptance down to the very forward

[2] "Conseil Européen pour la Recherche Nucléaire" or "European Council for Nuclear Resarch".

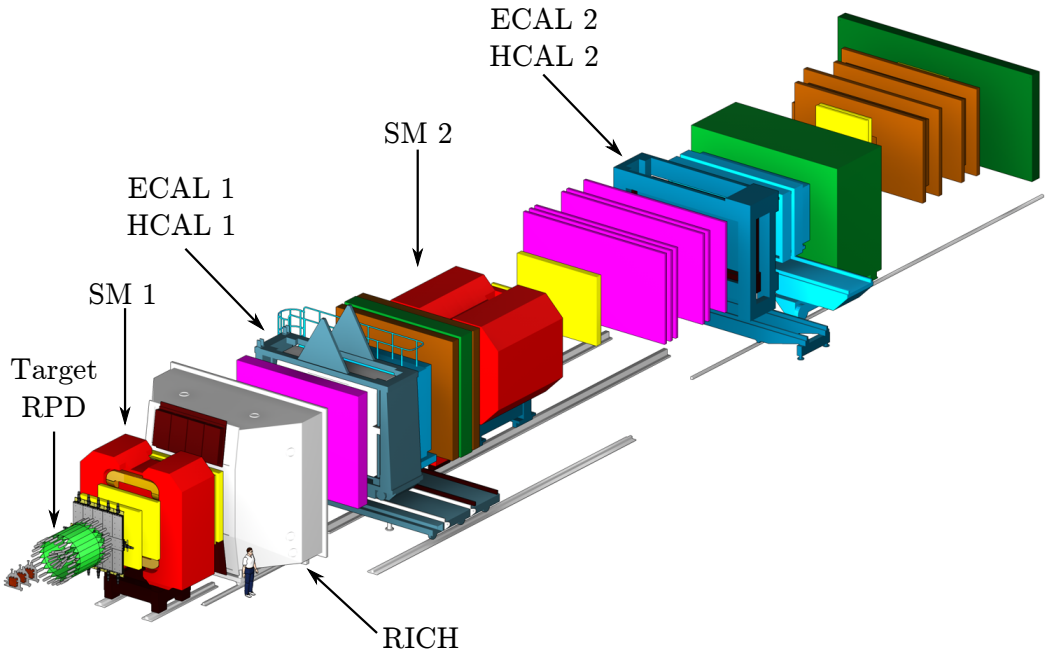

Figure 2.1: Layout of the COMPASS spectrometer for measurements with hadron beams [20].

direction. By this spectrometer layout, a uniform acceptance over a broad kinematic range is achieved, which is mandatory to investigate the data using partial-wave analysis methods [20].

The experimental setup allows to use different targets. To measure diffractive pion scattering from protons, a 400 mm long liquid hydrogen target is used. High-resolution tracking stations immediately up- and downstream of the target measure the trajectories of the beam and that of the outgoing particles for a precise vertex reconstruction. The so-called Recoil Proton Detector (RPD) measures the recoiling target protons and helps to ensure exclusivity of the measurement. A squared minimum momentum transfer of $|t| = 0.07\,(\mathrm{GeV}/c)^2$ from the beam pion to the proton is needed for the proton to be detected by the RPD.

Both, the small- and the large-angle spectrometer stages have a similar layout. The core element in both is a strong bending magnet (SM1 or SM2), which is surrounded by tracking stations to measure the momenta of charged particles. The tracking stations are composed of planar tracking detectors of different types to meet the variable resolution and rate requirements in different parts of the spectrometer. Each stage is equipped with an electromagnetic calorimeter (ECAL1/2) to measure the energy of electromagnetically interacting particles like electrons or photons and a hadronic calorimeter (HCAL1/2) to trigger on hadronic particles like pions, kaons or protons. Additionally, the LAS is equipped with the ring-imaging Cherenkov (RICH) counter. Similar to the CEDARs, this detector uses the Cherenkov photons radiated by the particles to identify pions, kaons and protons with momenta up to $50\,\mathrm{GeV}/c$.

2.2 Event Selection

With the experimental setup described in the previous section, an almost seven week long period was dedicated to the measurement of diffractive dissociation reactions using a 190 GeV negatively charged secondary hadron beam mostly containing π^-. The main aim of this analysis is to study meson resonances that are produced in these reactions and that decay into $\pi^-\pi^-\pi^+$ (see section 1.2). To obtain a clean data sample of exclusive $\pi^- + p \to \pi^-\pi^-\pi^+ + p_{\text{recoil}}$ events, an event selection was performed in [1]. Its major aspects are summarized in the following.

Even before the actual event selection, a first pre-selection of diffractive-event candidates is performed by the trigger system. The so-called diffractive trigger (DT0) is a combination of three independent trigger signals. The beam trigger selects single incoming beam particles. To observe diffractive meson production, the low to intermediate t' range is of interest. In this range the recoiling target proton should mostly stay intact. Therefore, the recoil-proton trigger selects events with a slow proton, which leaves the target and is measured in the RPD. The third DT0 condition requires no signal from the veto system, which rejects incoming beam particles with trajectories far from the nominal one, events with particles leaving the target outside of the geometrical acceptance of the COMPASS spectrometer as well as events with non-interacting beam particles.

In total more than 6×10^9 events have been measured by COMPASS during the hadron campaign. The first group of cuts in the event selection require, that exactly one vertex, which is associated with the beam particle, is reconstructed within the volume of the liquid-hydrogen target. As the goal is to analyze the $\pi^-\pi^-\pi^+$ final state, only events with three charged particles leaving the primary vertex with a total charge of $Q_{3\pi} = -1$ are considered.

The energy of the incident beam particle is not measured, but the average beam energy of 190 GeV and its energy spread of 1 % are known [1]. Under the assumption that all reaction products are detected, one can calculate the energy of the incoming beam pion from the momenta of the three charged tracks and the inclination of the beam particle, measured by the tracking stations upstream of the target (see appendix A for details). This reconstructed beam energy E_{Beam} is shown in figure 2.2a. The open histogram shows the distribution without RPD information, the full histogram illustrates the beam energy after all selection cuts. One finds a clear peak around the nominal beam energy with a tail reaching down to low energies. This tail originates from non-exclusive events, where for example not all particles of the final state are detected. The additional information from the measured track of the recoiling proton in the RPD is used to suppress non-exclusive events. Momentum conservations requires, that the transverse momenta of the recoiling proton and the three-pion system have opposite directions. Events which do not fulfill this requirement are rejected. This clearly removes most of the non-exclusive background in the beam-energy spectrum (compare filled vs. open histogram in figure 2.2a). Finally, a cut on the reconstructed beam energy of ±3.78 GeV around the average beam energy is applied to further remove non-exclusive events (see figure 2.2b).

The largest contamination of the pion data sample is due to kaons in the initial or final state [1].

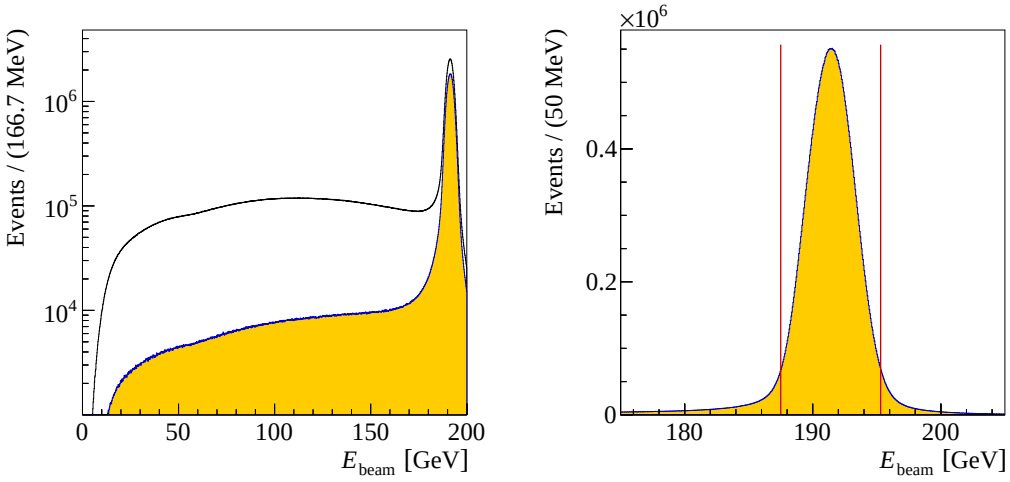

(a) Reconstructed beam energy (b) Zoom in the range of the nominal beam energy

Figure 2.2: Reconstructed beam energy without the RPD information (open histogram) and after all selection cuts (filled histogram). The vertical red lines in (b) indicate the selected energy range [2].

As the beam consists of 2.4 % kaons [2], events are rejected when the beam particle is identified as a kaon by one of the two CEDAR detectors. Furthermore, kaons may also appear in the final state. Many $\pi^-\pi^+$ resonances, like the $f_2(1270)$ or the $f_0(980)$, also have a considerable branching fraction into $K\overline{K}$. To suppress reactions like $\pi^- + p \to \pi^- K\overline{K} + p_{\text{recoil}}$, events where one of the forward-going particles is identified by the RICH detector as a kaon, proton, electron, muon or noise are rejected.

Using the discussed cuts, a clean data sample for the three-pion final state is selected from the data. However, as discussed in section 1.2.2, there are various reactions, contributing to the three-pion spectrum. The goal of this analysis is to investigate three-pion resonances. Therefore, only diffractive dissociation reactions are of interest. Deck-like processes are hard to separate from diffractive dissociation. Hence, these contributions have to be treated at the level of the resonance-model fit, as it will be described in chapter 4. In contrast, central production reactions show a different kinematic characteristic, compared to diffractive dissociation, which is exploited to suppress these contributions in the data sample. For central production, a fast π^- is expected together with a slower $\pi^-\pi^+$ system, which leads to a large difference between the rapidity

$$y = \frac{1}{2} \ln \frac{E + p_z}{E - p_z} \tag{2.1}$$

of the fast negative pion and that of the $\pi^-\pi^+$ system. Furthermore, Feynman's

$$x_{\text{F}} \approx \frac{2p_{z,\text{CM}}}{\sqrt{s}} \tag{2.2}$$

variable, where $p_{z,\text{CM}}$ is the momentum component of the fast pion along the beam axis in the overall center-of-mass frame of beam and target, is expected to be close to one for centrally

produced events. Therefore, events are selected, if their rapidity gap is within 2.7 to 4.5 and if Feynman's x_F is smaller than 0.9.

After all cuts, a data-sample of 46×10^6 exclusive events in the analyzed kinematic region of $0.5 < m_{3\pi} < 2.5\,\mathrm{GeV}/c^2$ and $0.1 < t' < 1.0\,(\mathrm{GeV}/c)^2$ is obtained. At the moment, this is the world's largest three-pion dataset [12, 15].

2.3 Kinematic Distributions

Three-pion resonances are expected to show up as enhancements in the three-pion invariant mass spectrum, which is therefore the first interesting kinematic distribution to look at (see figure 2.3a). A clear peak at a mass of $1.3\,\mathrm{GeV}/c^2$ is observed with a broad shoulder in its low-mass tail. The narrow peak can be associated with the well-known $a_2(1320)$ resonance [6] while the broad shoulder presumably arises from the $a_1(1260)$. The second peak around $1.7\,\mathrm{GeV}/c^2$ can be identified with the $\pi_2(1670)$ resonance, observed by many other experiments [10–12]. Furthermore, the $m_{3\pi}$ spectrum shows a broad high-mass tail without further dedicated peaks.

In figure 2.3b, the invariant-mass spectrum of the $\pi^-\pi^+$ subsystem is shown. The spectrum shows a rich peak structure with a clear dominant peak from the $\rho(770)$ resonance. In the high-mass tail of the $\rho(770)$, a shoulder from the $f_0(980)$ resonance is observed. A second distinct peak from the $f_2(1270)$ resonance is visible at around $1.3\,\mathrm{GeV}/c^2$ and the $\rho_3(1690)$ resonance appears as a slight enhancement at around $1.7\,\mathrm{GeV}/c^2$. The rich resonance structure in the $\pi^-\pi^+$ subsystem is exploited in the partial-wave decomposition (see chapter 3).

Figure 2.3a shows the $m_{3\pi}$ spectrum over the full analyzed t' range from 0.1 to $1.0\,(\mathrm{GeV}/c)^2$. However, in the different t' regions, the $m_{3\pi}$ distribution exhibits a different shape. In the low-t' region (see figure 2.4a) the narrow $a_2(1320)$ peak and its broad low-mass shoulder merge to one broad bump, while in the high-t' region (see figure 2.4b) the narrow $a_2(1320)$ peak sticks out more prominently and the broad shoulder is suppressed. As figure 2.5 illustrates, also the t' spectrum depends on $m_{3\pi}$ and shows a different shape in the low- and high-$m_{3\pi}$ region. To tread these strong correlations of $m_{3\pi}$ spectra on t' and vice versa, a two-dimensional analysis in bins of $m_{3\pi}$ and t' is necessary, as presented in the following chapter.

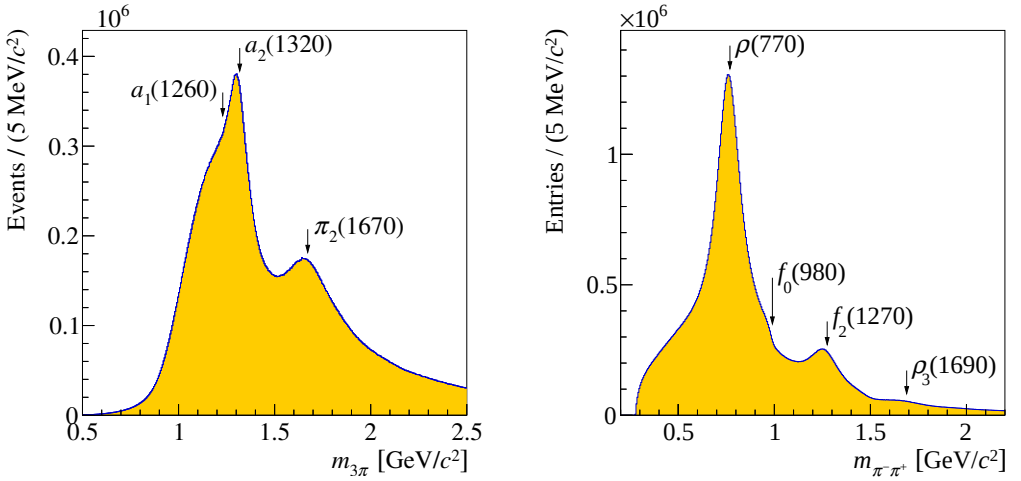

(a) Three-pion invariant mass spectrum (b) Invariant-mass spectrum of the $\pi^-\pi^+$ subsystem

Figure 2.3: Three-pion invariant mass spectrum (a) and the invariant-mass spectrum of the $\pi^-\pi^+$ subsystem (b). Histogram (b) has two entries per event for the two possible $\pi^-\pi^+$ combinations [2]. The position of known resonances, as listed in the PDG [6], is indicated in the figures.

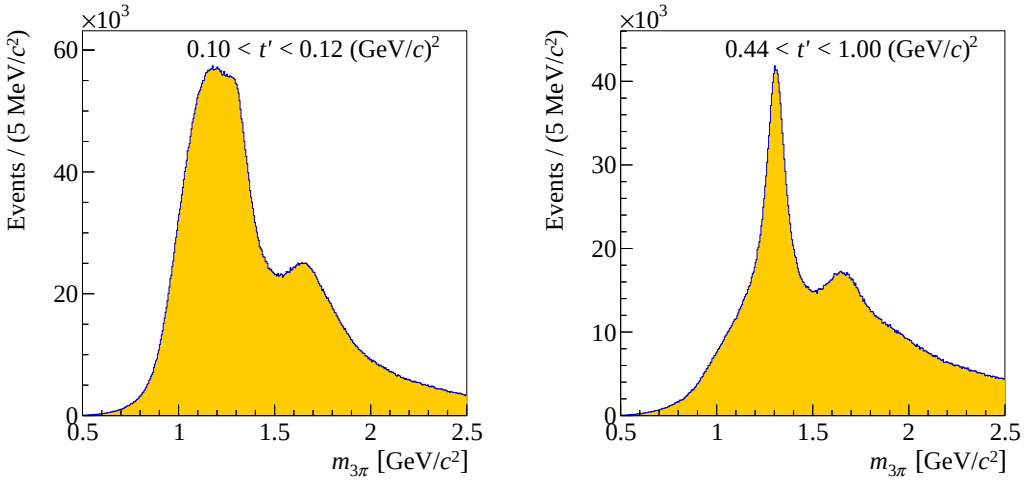

(a) Low-t' region (b) High-t' region

Figure 2.4: Three-pion invariant mass spectrum in the low- (a) and high-t' region (b) [2].

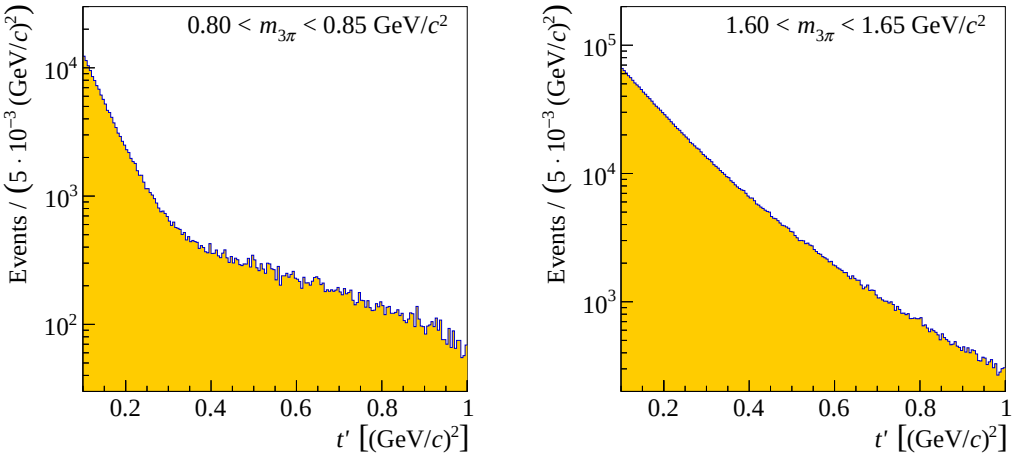

(a) Low-$m_{3\pi}$ region (b) High-$m_{3\pi}$ region

Figure 2.5: t' spectrum for low (a) and high (b) three-pion invariant masses [2].

CHAPTER 3

Partial-Wave Analysis

The basic approach of the partial-wave analysis is discussed in this chapter. First, an overview over the various analysis steps from the data towards the extraction of resonances and their parameters is given. In section 3.2, the partial-wave formalism is introduced, which is the basic language of this analysis. Finally, the main results of the partial-wave decomposition are discussed in section 3.3.

3.1 Analysis Chain

The three-pion invariant mass spectrum has not enough information to directly extract the meson resonances. As figure 1.2 in section 1.1 shows, most of the three-pion resonances are in similar overlapping mass regions and have large widths, which makes their separation difficult. Even if this would be possible, still their quantum numbers $J^{PC}\, M^{\varepsilon}$ cannot be determined. However, the fact, that the meson resonances can be distinguished by their quantum numbers is a possible solution to this problem. As it will be discussed in the following section, each J^{PC} sector has its own characteristic in the phase-space distribution of the decay products ($\pi^-\pi^-\pi^+$), which is the momentum distribution of the final-state particles. Since the phase-space distribution of the $\pi^-\pi^-\pi^+$ systems is measured by the experiment, both information can be combined to disentangle the contributions of the different J^{PC}, called partial waves, to the data. Afterwards, the resonance content in each partial wave is then investigated.

The partial-wave analysis is divided into two steps, as illustrated in figure 3.1. In a first step, the data is divided into narrow bins in $m_{3\pi}$ of $20\,\mathrm{MeV}/c^2$ width. Within the mass bin the $m_{3\pi}$ dependence can be safely neglected. As discussed in section 2.3, a strong correlation between the shape of the $m_{3\pi}$ and the t' spectra is observed. One common approach is to model this t' dependence. This, however, introduces a model bias, due to the lack of an unique theory model. The large data set measured by the COMPASS experiment allows for a different approach, where the data are subdivided further into narrow t' bins. Again, the t' dependence within each t' is assumed to be constant. The data are divided into 11 t' bins (see table 3.1) such that the

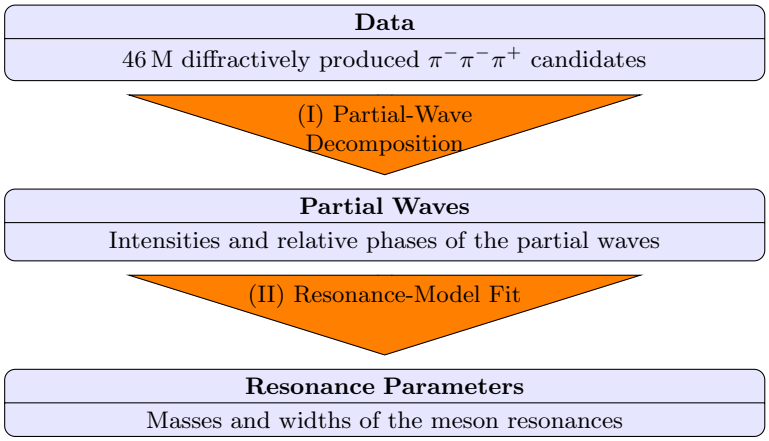

Figure 3.1: Illustration of the steps in the analysis chain to extract resonance parameters.

number of events in each bin is approximately the same. Only the last t' range is divided further into two bins, to guarantee narrow enough bins. After this two-dimensional binning, the data is decomposed in its partial-wave contributions, independently in each $m_{3\pi}$ and t' bin, in the so-called mass-independent fit.

In the second step of the partial-wave analysis, called resonance-model fit, the resonances and their parameters, namely the masses and widths, are extracted from the partial waves by modeling their $m_{3\pi}$ dependence. The resonance-model fit will be discussed in detail in chapter 4.

The division of the analysis into two steps has an important advantage. In the partial-wave decomposition, where the full data set has to be described by the partial-wave model, no assumptions about the three-pion resonances are necessary. This reduces the model bias in the first stage of the analysis. In the second analysis stage, the resonance-model fit, only a subset of partial waves can be selected for the analysis. In addition to the required computational resources, this reduces the demands on the resonance model, which has a larger model bias, as will be discussed in chapters 5 to 7.

Table 3.1: Borders of the t' binning. Taken from [2].

Bin	1	2	3	4	5	6
t' **[(GeV/c)^2]**	0.100	0.113	0.127	0.144	0.164	0.189

Bin	6	7	8	9	10	11
t' **[(GeV/c)^2]**	0.220	0.262	0.326	0.449	0.724	1.000

3.2 Partial-Wave Decomposition

In the following the basic aspects of the partial-wave decomposition are introduced. For a complete discussion the reader is referred to [2].

3.2.1 Formalism

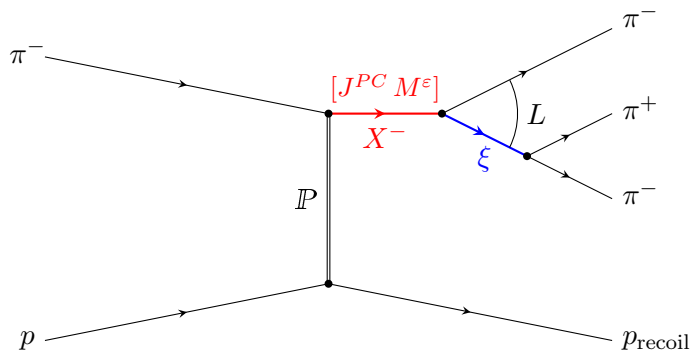

Figure 3.2: Diffractive production of a state X^- with quantum numbers $J^{PC}\ M^{\varepsilon}$ and its dissociation into three charged pions via an intermediate two-pion resonance ξ in the isobar model.

In the partial-wave decomposition it is assumed, that the diffractive $\pi^-\pi^-\pi^+$ production is dominated by intermediate resonances. Production and decay of these states X^- can be factorized. The production is characterized by the transition amplitudes $\mathcal{T}(m_{3\pi}, t')$, which depend on the mass $m_{3\pi}$ of the intermediate state and the squared four-momentum t' transfered in the pion-proton scattering. The decay of X^- is described by the decay amplitudes $\psi(\tau; m_{3\pi})$, which depend on $m_{3\pi}$ and five decay phase-space variables denoted by τ.

Furthermore, it is assumed, that the intermediate state X^- does not decay directly into three pions, but via a two-pion resonance ξ, called isobar (see figure 3.2), where L is the orbital angular momentum between the isobar and the so-called bachelor pion. The invariant mass spectrum of the $\pi^-\pi^+$ subsystem shows dominant resonance contributions (see figure 2.3b) which supports this assumption of the so-called isobar model. The decay amplitudes $\psi(\tau; m_{3\pi})$ are calculated in the so-called reflectivity basis, where positive and negative spin projections M are combined to $M \geq 0$ and an additional quantum number $\varepsilon = \pm 1$. As states with different reflectivities are produced by Regge-trajectories with different naturalities, they are not interfering and thus have to be treated separately from the other quantum numbers[1].

The couplings of certain decay modes (ξ, L) to certain states $J^{PC}\ M$ are generally not known but can be pulled out of the decay amplitudes and absorbed by the transition amplitudes. Therefore,

[1] As only waves with positive reflectivity are discussed in this thesis, a discussion of the reflectivity is omitted. Details can be found in [1, 2].

the transition amplitudes $\mathcal{T}_\alpha^\varepsilon(m_{3\pi}, t')$ are not independent of the decay, but there is one specific transition amplitude for each decay mode. Accordingly, the index $\alpha = (J^{PC}\ M, \xi\, L)$ describes a certain state and its decay. Together with the reflectivity ε, this is, what is defined as a partial wave in the notation

$$J^{PC}\, M^\varepsilon\, \xi\, \pi\, L. \tag{3.1}$$

For a given $m_{3\pi}$ and t' bin, the factorization of production and decay of X^- allows to write the intensity distribution as a function of the phase-space variables τ in the form of a coherent sum over the possible partial waves:

$$\mathcal{I}(\tau; m_{3\pi}, t') = \sum_{\varepsilon=\pm1} \left| \sum_\alpha \mathcal{T}_\alpha^\varepsilon(m_{3\pi}, t')\, \psi_\alpha^\varepsilon(\tau; m_{3\pi}) \right|^2 + \mathcal{I}_{\text{Flat}}(m_{3\pi}, t'). \tag{3.2}$$

$\mathcal{I}_{\text{Flat}}$ is an additional contribution, isotropic in τ, which absorbs intensity from uncorrelated three pions in the final state. After expanding the $|\ldots|^2$

$$\begin{aligned}\mathcal{I}(\tau; m_{3\pi}, t') = \sum_{\varepsilon=\pm1} \sum_{\alpha,\beta} \mathcal{T}_\alpha^\varepsilon(m_{3\pi}, t') \mathcal{T}_\beta^{\varepsilon*}(m_{3\pi}, t')\, \psi_\alpha^\varepsilon(\tau; m_{3\pi}) \psi_\beta^{\varepsilon*}(\tau; m_{3\pi}) \\ + \mathcal{I}_{\text{Flat}}(m_{3\pi}, t'),\end{aligned} \tag{3.3}$$

one finds that products of two transition amplitudes appear, which can be summarized in a complex-valued matrix, called spin-density matrix

$$\rho_{\alpha\beta}^\varepsilon(m_{3\pi}, t') = \mathcal{T}_\alpha^\varepsilon(m_{3\pi}, t') \mathcal{T}_\beta^{\varepsilon*}(m_{3\pi}, t'). \tag{3.4}$$

The diagonal elements of this matrix $\rho_{\alpha\,\alpha}^\varepsilon = \left|\mathcal{T}_\alpha^\varepsilon\right|^2$ represent the intensities of the corresponding partial wave α[2], while the off-diagonal elements $\rho_{\alpha\beta}^\varepsilon$ express the interference between wave α and β. Since the decomposition of $\rho_{\alpha\beta}^\varepsilon$ into the transition amplitudes $\mathcal{T}_\alpha^\varepsilon$ is not unique, the full obtainable information about the intermediate states X^- is contained in the spin-density matrix.

3.2.2 Calculation of Decay Amplitudes

In the isobar model, the decay amplitude factorizes further into two two-body decay amplitudes. Using the helicity formalism (see section 3.1 in [2] for details), the two-body decay amplitude can be factorized into a dynamic part, describing the mass dependence and an angular part, describing the angular distribution of the daughter particles.

The spherical angles of the $X^- \to \xi\,\pi^-$ decay $(\vartheta_X^{\text{GJ}}, \phi_X^{\text{TJ}})$ are defined in the so-called Gottfried-Jackson system, which is the rest frame of the X^- state with the z^{GJ}-axis in the direction of

[2] The intensity is the expected number of events for a perfect detector with unit acceptance.

the beam particle. y^{GJ} is orientated perpendicular to the production plane. The isobar decay $\xi \to \pi^+\pi^-$ is described by the spherical angles $(\vartheta_\xi^{\mathrm{HF}}, \phi_\xi^{\mathrm{HF}})$ in the helicity frame, which is the rest system of the isobar with the z^{HF}-axis along the direction of the isobar in the Gottfried-Jackson frame. For details the reader is referred to [2].

The amplitude for the decay of the X^- state with spin-projection M into the bachelor pion and the isobar ξ with helicity λ and angular momentum L between bachelor pion and isobar (see figure 3.2) can be written in the following form:

$$\tilde{\mathcal{A}}^{(X)}_{M\,\lambda}(\vartheta_X^{\mathrm{GJ}}, \phi_X^{\mathrm{TJ}}, m_\xi; m_X) = D^{J*}_{M\,\lambda}(\vartheta_X^{\mathrm{GJ}}, \phi_X^{\mathrm{TJ}}, 0)\, f^J_\lambda(m_\xi; m_X). \tag{3.5}$$

The angular distribution is described by Wigner D-functions. The dynamic term

$$f^J_\lambda(m_\xi; m_X) = \sqrt{2L+1}\,(L0\,J_\xi\lambda|J\lambda)\,F_L(q_X) \tag{3.6}$$

includes the Clebsch-Gordan coefficients $(L0\,J_\xi\lambda|J\lambda)$ of the L-S coupling in the $\xi\,\pi^-$ system and the angular-momentum barrier factors $F_L(q_X)$ [24], which account for the suppression of decay modes with large angular momentum L between the two decay products. The barrier factor $F_L(q_X)$ depend on the two-body break-up momentum q_X in the X^- decay [see equation (D.8)]. A discussion of these factors can be found in section 6.1.7.

The amplitude

$$\tilde{\mathcal{A}}^{(\xi)}_\lambda(\vartheta_\xi^{\mathrm{HF}}, \phi_\xi^{\mathrm{HF}}, m_\xi) = D^{J_\xi *}_{\lambda\,0}(\vartheta_\xi^{\mathrm{HF}}, \phi_\xi^{\mathrm{HF}}, 0)\, f^{J_\xi}(m_\xi) \tag{3.7}$$

of the $\xi \to \pi^+\pi^-$ decay has the same form as the one of the X^- decay. The dynamic function $f^{J_\xi}(m_\xi)$ has basically the same structure as that for the X^- decay, but it contains the isobar line shape (see [2] for details).

Using $m_X = m_{3\pi}$ and $m_\xi = m_{\pi^-\pi^+}$, the complete decay amplitude

$$\tilde{\psi}_\alpha(\underbrace{\vartheta_X^{\mathrm{GJ}}, \phi_X^{\mathrm{TJ}}, m_{\pi^-\pi^+}, \vartheta_\xi^{\mathrm{HF}}, \phi_\xi^{\mathrm{HF}}}_{\tau}; m_{3\pi}) = \sum_\lambda \tilde{\mathcal{A}}^{(X)}_{M\,\lambda}(\vartheta_X^{\mathrm{GJ}}, \phi_X^{\mathrm{TJ}}, m_{\pi^-\pi^+}; m_{3\pi})\, \tilde{\mathcal{A}}^{(\xi)}_\lambda(\vartheta_\xi^{\mathrm{HF}}, \phi_\xi^{\mathrm{HF}}, m_{\pi^-\pi^+}) \tag{3.8}$$

for a certain state X^- is given by summing over the helicity λ of the intermediate state ξ[3]. For a given three-pion mass $m_{3\pi}$, the two decay angles in the two sub-decays, together with the invariant mass of the $\pi^-\pi^+$ subsystem, span the five dimensional three-pion phase space $\varphi(\tau; m_{3\pi})$. Finally, to interpret the decay amplitudes as probability amplitudes, they have to be normalized:

$$\psi^\varepsilon_\alpha(\tau; m_{3\pi}) = \frac{\tilde{\psi}^\varepsilon_\alpha(\tau; m_{3\pi})}{\sqrt{\varphi^\varepsilon_\alpha(m_{3\pi})}}. \tag{3.9}$$

[3] As both π^- are indistinguishable, the decay amplitude is in addition Bose symmetrized as discussed in [2].

Here $\varphi_\alpha^\varepsilon(m_{3\pi})$ is the integrated phase-space volume of the corresponding partial wave (α, ε)

$$\varphi_\alpha^\varepsilon(m_{3\pi}) = \int \mathrm{d}\varphi(\tau; m_{3\pi}) \left|\tilde{\psi}_\alpha^\varepsilon(\tau; m_{3\pi})\right|^2 . \tag{3.10}$$

For a given partial wave $J^{PC}\, M^\varepsilon\, \xi\, \pi\, L$, the decay amplitude $\psi_\alpha^\varepsilon(\tau; m_{3\pi})$ can now be calculated. Since $\mathcal{I}(\tau; m_{3\pi}, t')$ was measured in the experiment, this allows to determine the transition amplitudes from the data. As no states with negative reflectivity are considered for this analysis the reflectivity index is omitted for the rest of the text.

3.2.3 Fit of Transition Amplitudes

To extract the transition amplitudes $\mathcal{T}_\alpha$ [4] for each mass and t' bin, an unbined extended maximum-likelihood fit is performed. This fit maximizes the likelihood of the data for the given partial-wave model by optimizing the transition amplitudes, which are the fit parameters. The likelihood in each mass and t' bin is written as a product of the Poisson probability for observing N events in the experiment when $\bar{N}$ are expected by the model and the product of the probabilities of each event:

$$\mathcal{L} = \mathrm{P}_{\mathrm{Poisson}}(N, \overline{N}) \cdot \prod_{i=1}^{N} \mathrm{P}_{\mathrm{event}}(\tau_i) \tag{3.11}$$

$$= \frac{\overline{N}^N}{N!} e^{-\overline{N}} \cdot \prod_{i=1}^{N} \frac{\mathcal{I}(\tau_i)}{\int \mathrm{d}\varphi(\tau)\, \eta(\tau) \mathcal{I}(\tau)} . \tag{3.12}$$

The probability of one event is the expected intensity for its kinematic variables $\mathcal{I}(\tau_i)$, divided by the normalization integral[5]. The normalization has been chosen to be equal to the expected number of events

$$\overline{N} = \int \mathrm{d}\varphi(\tau)\, \eta(\tau) \mathcal{I}(\tau), \tag{3.13}$$

such that the absolute squared transition amplitudes can be interpreted as the expected number of events in the corresponding partial wave. The calculation of the expected number of events takes the acceptance of the experimental setup $\eta(\tau)$ into account. Using the definition of the intensity in equation (3.3) the transition amplitudes can be fitted to the data by maximizing $\mathcal{L}$.

[4] As fits are done in bins with fixed $m_{3\pi}$ and t', for simplicity, in this section the $m_{3\pi}$ and t' dependence is omitted.

[5] As $\prod_{i=1}^{N}$ includes only the experimentally observed events, the acceptance is already respected [25].

3.2.4 Partial-Wave Model

For a mathematically complete description, in principle an infinite number of partial waves has to be considered in the the sum over the partial waves in equation (3.3). In practice, only a finite number of data and computational time is available. Therefore, the wave set has to be truncated. The maximal spin of the intermediate state X^- was chosen to be $J \leq 6$, with a maximal angular momentum of $L \leq 6$ in the decay. The spin projections $M = 0, 1$ and 2 have been considered. According to the $\pi^-\pi^+$ invariant mass spectrum, shown in figure 2.3b, six isobars $[\pi\pi]_S$, $\rho(770)$, $f_0(980)$, $f_2(1270)$, $f_0(1500)$ and $\rho_3(1690)$ are included. A careful selection from all possible waves has been performed to minimize the bias and leakage[6] and to maximize the stability of the fit. The details of the wave-set selection can be found in [1]. In total, the partial-wave decomposition is performed using 88 partial waves, listed in table B.1.

3.3 Results of the Partial-Wave Decomposition

In this section, a first look into the main results of the partial-wave decomposition will be given. An extended discussion of selected results can be found in [1, 2]. Figure 3.3 shows the intensities for four partial waves summed over all 11 t' bins, which in the rest of the text will be referred to as t'-summed intensities. As expected, the narrow $a_2(1320)$ peak in the total $m_{3\pi}$ spectrum (see figure 2.3a in section 2.3) is found in one of the 2^{++} waves. Figure 3.3b shows the intensity spectrum of the $2^{++}\,1^+\,\rho(770)\,\pi\,D$ wave, which is the dominant 2^{++} wave. In contrast to the total $m_{3\pi}$ spectrum, the peak appears here nearly background free without interfering with other non-2^{++} resonances, which demonstrates the advantage of the partial-wave decomposition. The broad shoulder at about $1.1\,\mathrm{GeV}/c^2$ in figure 2.3 corresponds to the broad peak in the $1^{++}\,0^+$ $\rho(770)\,\pi\,S$ wave shown in figure 3.3a, which presumably arises from the $a_1(1260)$. The $1^{++}\,0^+$ $\rho(770)\,\pi\,S$ wave is the largest wave with 32.7 % of the total intensity[7]. The second peak in the total $m_{3\pi}$ spectrum shows up as a clear signal for the $\pi_2(1670)$ in the $2^{-+}\,0^+\,f_2(1270)\,\pi\,S$ wave (see figure 3.3c), which is the dominant 2^{-+} wave. In addition to these structures that are directly observable in the total $m_{3\pi}$ spectrum, the partial-wave decomposition reveals weaker signals like in the $4^{++}\,1^+\,\rho(770)\,\pi\,G$ wave, which contributes only 0.8 % to the total intensity and is shown in figure 3.3d. The peak in this wave is the known $a_4(2040)$ resonance. However, the shoulder in the high-mass tail of the peak already suggests, that not all of the intensity arises from the resonance, but that some additional, so-called non-resonant contribution is visible. Therefore, a careful separation between resonances and non-resonant contributions is necessary to interpret such signals in terms of resonances and extract their parameters. This is done in the resonance-model fit, introduced in the following chapter.

[6] Intensity, which is assigned to the wrong partial wave.
[7] Neglecting interference between the waves.

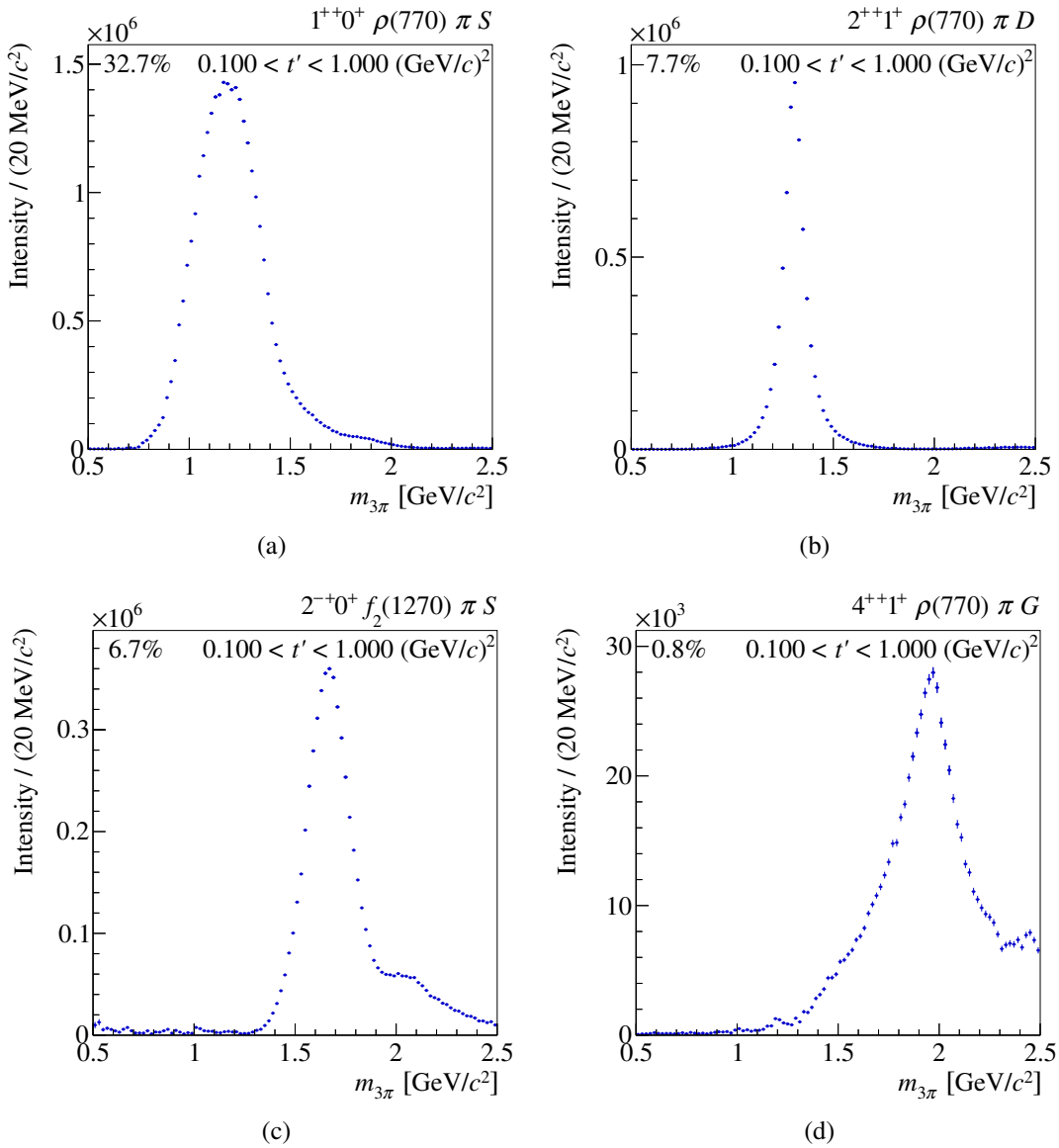

Figure 3.3: t'-summed intensity spectra of three dominant waves [(a), (b), (c)] and the smaller 4^{++} wave (d). Plots are taken from [2].

CHAPTER 4

Resonance-Model Fit

One of the major aims of this analysis is the extraction of resonance parameters and their systematic uncertainties. The first step towards this goal is the decomposition of the data into partial waves, as described in the previous chapter. In general more than one resonance may appear in the same wave. In addition, the partial waves contain not only pure resonance signals. Also non-resonant components may contribute to the spectra, as will be discussed below. All these different components of a partial wave are interfering with each other. In this chapter, the ansatz of the resonance-model fit is introduced, followed by the definition of the Main fit model. Finally, the used fit method is explained.

4.1 Ansatz

The approach of the resonance-model fit is to separate the various contributions to the partial waves by parameterizing their three-pion-mass dependence. Therefore, each transition amplitude is parameterized by the resonance model (RM) as a coherent sum over the various components $k \in \mathrm{Comp}_\alpha$, assumed to contribute to the corresponding wave α:

$$^{\mathrm{RM}}\mathcal{T}_\alpha(m_{3\pi}, t') = \left[\sum_{k \in \mathrm{Comp}_\alpha} C_\alpha^k(t')\, \mathcal{D}^k(m_{3\pi}, t'; \zeta_k) \right] \sqrt{\varphi_\alpha(m_{3\pi})}\, \sqrt{\Psi(m_{3\pi})}. \tag{4.1}$$

Each component is described by a complex-valued coupling parameter $C_\alpha^k(t')$ and a dynamic function $\mathcal{D}^k(m_{3\pi}, t'; \zeta_k)$, that parameterizes the $m_{3\pi}$ dependence and depends on so-called "shape parameters" ζ_k. The coupling parameter represents the t' dependence of the strength and phase of the corresponding component in the partial wave and is only $C_\alpha^k(t') \neq 0$ if the component k is in wave α. The integrated phase-space volume $\varphi_\alpha(m_{3\pi})$ for wave α has been pulled out of the dynamic functions and appears as a factor, such that the dynamic functions are not specific to a certain wave α. To account for the decreasing probability of producing a state X^- with growing $m_{3\pi}$, a "production" phase-space factor $\Psi(m_{3\pi})$ is introduced (see appendix D for details).

Typically, a resonance can decay via several decay modes, i.e. isobars, but the resonance parameters should be the same for all of them. Therefore, a resonance component $\mathcal{D}^k(m_{3\pi}, t'; \zeta_k)$, is not specific to a wave, but can contribute to more than one partial wave with the same shape, but different couplings $C^k_\alpha(t')$. The non-resonant terms are different for each partial wave. The couplings and the shape parameters ζ_k (e.g. masses and widths of resonances) are the free parameters, to be determined by the resonance-model fit.

In addition to resonances, non-resonant terms contribute to the transition amplitudes. It is supposed, that their main source are Deck-like reactions, introduced in section 1.2.2. As there is no unique model for them, a phenomenological parameterization for the non-resonant term was developed (for details see appendix D):

$$^{\mathrm{NR}}\mathcal{D}^k(m_{3\pi}, t'; b, c_0, c_1, c_2) = (m_{3\pi} - m_{\mathrm{thr}})^b e^{(c_0 + c_1 t' + c_2 t'^2)\cdot \widetilde{q}^{\,2}(m_{3\pi})}. \tag{4.2}$$

It parameterizes, the non-resonant contributions using a real-valued amplitude, which is exponentially suppressed with increasing two-body break-up momentum $\widetilde{q}(m)$ [see equation (D.7)]. The b parameter allows the resonance-model fit to adjust the rising low-mass intensity of the phase-space opening. The parameter m_{thr} is empirically fixed to $0.5\,\mathrm{GeV}/c^2$.

Resonances, are parameterized using relativistic Breit-Wigner amplitudes [26]:

$$^{\mathrm{R}}\mathcal{D}^k(m_{3\pi}; m_0, \Gamma_0) = \frac{\sqrt{m_0\,\Gamma_0}}{m_0^2 - m_{3\pi}^2 - i\,m_0\,\Gamma(m_{3\pi})}. \tag{4.3}$$

The total width $\Gamma(m_{3\pi})$ encodes the increase of the decay-width with increasing $m_{3\pi}$ due to the expanding phase space in all possible decays of the resonance. Figure 4.1 illustrates intensity and phase of a Breit-Wigner amplitude in the simplest case of a so-called fixed-width Breit-Wigner with $\Gamma(m_{3\pi}) = \Gamma_0$. In addition to the peak in the intensity spectrum, a resonance is characterized by a distinct phase motion of 180° across the peak position (see figure 4.1b).

The complicated interplay of the contributions to the partial waves and their interferences make a simple “bump-hunting” approach, that only takes the intensity spectra into account, unfeasible. The characteristic phase motions of resonances have been included in order to separate the different components. However, no absolute phases can be measured but only the relative phases between the different partial waves. Therefore, many partial waves have to be described simultaneously, in order to take advantage of their interferences. This is realized by

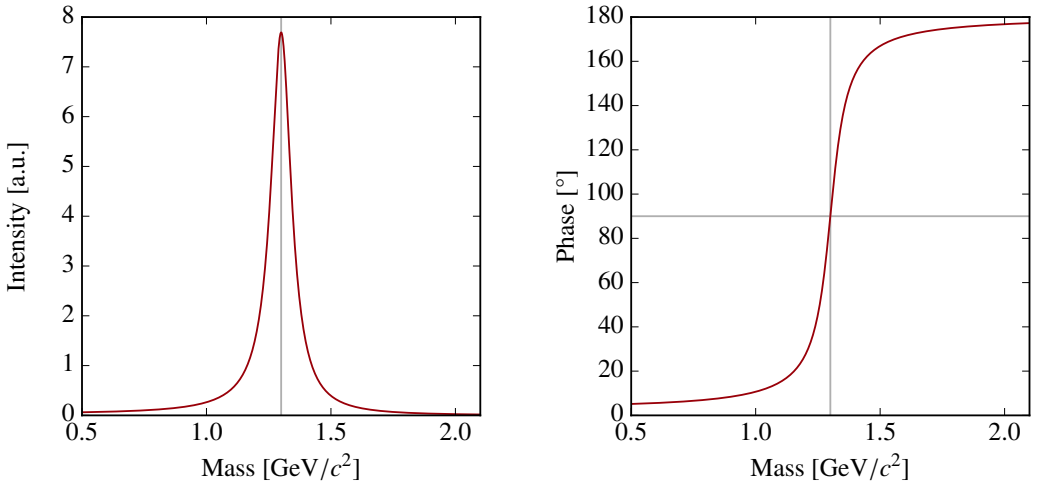

(a) Intensity (b) Phase

Figure 4.1: Intensity (a) and phase (b) of a fixed-width Breit-Wigner with $\Gamma(m_{3\pi}) = \Gamma_0$ at a mass of $m_0 = 1.3\,\mathrm{GeV}/c^2$ and a width of $\Gamma_0 = 0.1\,\mathrm{GeV}/c^2$ [25].

parameterizing the data in terms of the spin-density matrix

$$
\begin{aligned}
{}^{\mathrm{RM}}\rho_{\alpha\beta}(m_{3\pi}, t') &= {}^{\mathrm{RM}}\mathcal{T}_{\alpha}(m_{3\pi}, t') \cdot {}^{\mathrm{RM}}\mathcal{T}^{*}_{\beta}(m_{3\pi}, t') && (4.4)\\
&= \left[\sum_{k \in \mathrm{Comp}_{\alpha}} C^{k}_{\alpha}(t')\, \mathcal{D}^{k}(m_{3\pi}, t'; \zeta_k) \right] \sqrt{\varphi_{\alpha}(m_{3\pi})\varphi_{\beta}(m_{3\pi})}\, \Psi(m_{3\pi}) && (4.5)\\
&\quad \left[\sum_{m \in \mathrm{Comp}_{\beta}} C^{m}_{\beta}(t')\, \mathcal{D}^{m}(m_{3\pi}, t'; \zeta_m) \right]^{*} .
\end{aligned}
$$

In addition to the phase information, the t'-resolved partial-wave analysis allows to exploit the different t' dependencies of the various components (see chapter 7). The resonance parameterizations are chosen to be independent of t'. The t' dependence is completely encoded in the couplings. This is not true for some of the non-resonant terms, which may include an explicit t' dependence [see equation (4.2)]. By fitting not only one t' bin, but simultaneously all 11 t' bins, while keeping the shape parameters the same in all t' bins, the separation between the various components, especially that between the resonant and non-resonant contributions, is greatly improved. This also allows to extract the t' dependences of the model components, instead of introducing model bias by parameterizing them.

Using the approach described above, the shape parameters ζ_k, e.g. the masses and widths of the resonances, are extracted by fitting the resonance model to the spin-density matrix $\rho_{\alpha\beta}(m_{3\pi}, t')$ that is obtained from the mass-independent fit.

4.2 Fit Model

The fit model, used for this analysis, is summarized in table 4.1. It is based on a selected subset of 14 partial waves, containing well-known resonances, like the $a_2(1320)$, the $a_4(2040)$, the $\pi(1800)$ and the $\pi_2(1670)$ plus potential excitations of these states. This basic wave set acts as an interferometer to determine the content of more interesting waves, like the $1^{++}\,0^+\,f_0(980)\,\pi\,P$ wave, in which a new narrow signal is observed. Additionally, the $1^{-+}\,1^+\,\rho(770)\,\pi\,P$ wave with spin-exotic quantum numbers was included to investigate its possible resonance content. The fitted wave set consists of 14 partial waves in six different J^{PC} sectors. This subset incorporates 56.9 % of the total intensity. The basic structure of the fit model was developed in [14] and has been further refined in this work to increase the stability of the fit and reduce systematic effects. For each partial wave, an individual $m_{3\pi}$ fit-range is chosen (see table 4.1), according to its mass range in the mass-independent fit (see table B.1) and the features of the intensity and phase spectra of that wave.

Each partial wave is described by one or more resonances and a single non-resonant term. While the same resonance may appear in more than one wave, each partial wave has an individual non-resonant term, which is parameterized according to equation (4.2). To reduce the number of free parameters and thus increase the fit stability, for some partial waves, where the non-resonant term is small, it is parameterized with a simplified version of equation (4.2):

$$^{\mathrm{NR}}\mathcal{D}^k(m_{3\pi}; b = 0, c_0, c_1 = 0, c_2 = 0) = e^{c_0 \cdot \widetilde{q}^{\,2}(m_{3\pi})}. \tag{4.6}$$

The resonant components are parameterized using relativistic Breit-Wigner amplitudes [see equation (4.3)]. Because of a lack of detailed knowledge about the decay modes of most of the resonances, for them the dynamic width is approximated by a constant

$$\Gamma(m_{3\pi}) \approx \Gamma_0. \tag{4.7}$$

Due to the large width of the $a_1(1260)$ resonance, the variation of the decay phase-space over the resonance width has to be taken into account. This is done by using the so-called Bowler parameterization [27]

$$\Gamma_{a_1}(m_{3\pi}) = \Gamma_0 \frac{\varphi_{\rho\pi}^{1^+S}(m_{3\pi})}{\varphi_{\rho\pi}^{1^+S}(m_{a_1})} \frac{m_{a_1}}{m_{3\pi}} \tag{4.8}$$

where $\varphi_{\rho\pi}^{1^+S}(m_{3\pi})$ is the phase-space of the $\rho(770)\,\pi\,S$ decay of the $a_1(1260)$, taking into account the finite width of the $\rho(770)$. For the $a_2(1320)$, the two dominant decay modes, $\rho(770)\,\pi$ and

$\eta\,\pi$ D-wave, are used to calculate the total width:

$$\Gamma_{a_2}(m_{3\pi}) = \Gamma_0 \frac{m_{a_2}}{m_{3\pi}} \left[(1-x) \frac{q_{\rho\pi}(m_{3\pi}) F_D^2\left(q_{\rho\pi}(m_{3\pi})\right)}{q_{\rho\pi}(m_{a_2}) F_D^2\left(q_{\rho\pi}(m_{a_2})\right)} + x \frac{q_{\eta\pi}(m_{3\pi}) F_D^2\left(q_{\eta\pi}(m_{3\pi})\right)}{q_{\eta\pi}(m_{a_2}) F_D^2\left(q_{\eta\pi}(m_{a_2})\right)} \right] \tag{4.9}$$

where $q(m)$ is the two-body break-up momentum [see equation (D.8)] and $F_D(q)$ are the angular-momentum barrier factors (see section 3.2). In this approximation, $\rho(770)$ and η are treated as quasi-stable particles. Based on other measurements [6], a relative branching fraction $x = 20\,\%$ between both decay modes is used.

Since we assume a factorization between production and decay of the resonance (see section 3.2), states in waves with the same quantum numbers ($J^{PC}\,M^{\varepsilon}$) are expected to show the same t' dependence even in different decay modes. An example is the $a_1(1260)$ resonance that appears in the $1^{++}\,0^+\,\rho(770)\,\pi\,S$ and $1^{++}\,0^+\,f_2(1270)\,\pi\,P$ partial waves. To stabilize the fit and reduce the number of free parameters the relative branching of resonances k appearing in waves α and β with the same $J^{PC}\,M^{\varepsilon}$ quantum numbers is fixed by

$$C_\alpha^k(t') = {}_\alpha B_\beta^k \cdot C_\beta^k(t'). \tag{4.10}$$

Therefore the 11 independent couplings $C_\alpha^k(t')$, one for each t' bin, are replace by one fixed branching ${}_\alpha B_\beta^k$. This means, that the t' dependence of the resonance is forced to be the same with a constant complex-valued branching factor ${}_\alpha B_\beta^k$ between them [14]. For the example of the $a_1(1260)$ this reads as follows:

$$C^{a_1(1260)}_{1^{++}\,0^+\,f_2(1270)\,\pi\,P}(t') = {}_{1^{++}\,0^+\,f_2(1270)\,\pi\,P}B^{a_1(1260)}_{1^{++}\,0^+\,\rho(770)\,\pi\,S} \cdot C^{a_1(1260)}_{1^{++}\,0^+\,\rho(770)\,\pi\,S}(t'). \tag{4.11}$$

The brackets in the rightmost column of table 4.1 group the waves whose resonance components have fixed relative branchings. A discussion about the influences of this assumption can be found in section 6.1.3 and in chapter 7.

To fix the unmeasurable global phase in each t' bin, the couplings of the $a_1(1260)$ component in the $1^{++}\,0^+\,\rho(770)\,\pi\,S$ wave are chosen to be real-valued.

The 14-wave fit model leads to a spin-density matrix with 196 elements for each of the 11 t' bins, yielding a total amount 76 505 data points. To describe the 11 resonances, 22 shape parameters (masses and widths) are needed. Additional 29 shape parameters are used for the non-resonant terms. Together with 649 coupling parameters and 22 branching parameters, the resonance model consists in total of 722 free real parameters, to be determined by the fit. To illustrate the huge amount of informations that needs to be described consistently by the resonance-model fit, the full spin-density matrix for the lowest of the 11 t' bins is shown in figure 4.2. The spin-density matrix in all t' bins is shown in detail in appendix F.

Table 4.1: Main fit model with 11 resonances in 14 partial waves from six J^{PC} sectors. The equation numbers of the used parameterizations are given in square brackets. The brackets in the rightmost column group waves whose resonance components have fixed relative branchings (see text).

Partial wave	Resonances	Non-resonant term eq.	Fit range [GeV/c^2]	
$0^{-+}\,0^{+}\,f_0(980)\,\pi\,S$	$\pi(1800)$ [(4.7)]	(4.6)	1.20 to 2.30	
$1^{++}\,0^{+}\,\rho(770)\,\pi\,S$	$a_1(1260)$ [(4.8)], a_1' [(4.7)]	(4.2)	0.90 to 2.30	]
$1^{++}\,0^{+}\,f_2(1270)\,\pi\,P$		(4.6)	1.40 to 2.10	]
$2^{++}\,1^{+}\,\rho(770)\,\pi\,D$	$a_2(1320)$ [(4.9)], a_2' [(4.7)]	(4.2)	0.90 to 2.00	]
$2^{++}\,1^{+}\,f_2(1270)\,\pi\,P$		(4.6)	1.00 to 2.00	]
$2^{++}\,2^{+}\,\rho(770)\,\pi\,D$		(4.6)	1.00 to 2.00	
$2^{-+}\,0^{+}\,f_2(1270)\,\pi\,S$	$\pi_2(1670)$ [(4.7)], $\pi_2(1880)$ [(4.7)], $\pi_2'(2005)$ [(4.7)]	(4.2)	1.40 to 2.30	]
$2^{-+}\,0^{+}\,f_2(1270)\,\pi\,D$		(4.6)	1.60 to 2.30	]
$2^{-+}\,0^{+}\,\rho(770)\,\pi\,F$		(4.2)	1.40 to 2.10	]
$2^{-+}\,1^{+}\,f_2(1270)\,\pi\,S$		(4.6)	1.40 to 2.30	
$4^{++}\,1^{+}\,\rho(770)\,\pi\,G$	$a_4(2040)$ [(4.7)]	(4.6)	1.25 to 2.30	]
$4^{++}\,1^{+}\,f_2(1270)\,\pi\,F$		(4.6)	1.40 to 2.30	]
$1^{++}\,0^{+}\,f_0(980)\,\pi\,P$	$a_1(1420)$ [(4.7)]	(4.6)	1.30 to 1.60	
$1^{-+}\,1^{+}\,\rho(770)\,\pi\,P$	$\pi_1(1600)$ [(4.7)]	(4.2)	0.90 to 2.00	

Based on the model described above, a resonance-model fit, the so-called "Main" fit, was performed. The results of this fit will be discussed in chapter 5. The systematics of this model have been investigated in extensive studies. A detailed discussion of the systematic effects on the resonance parameters can be found in chapter 6. Finally, the extracted t' dependences of the model components will be discussed in chapter 7.

4.3 Fit Method

Using the resonance model, described in the previous section, the masses and widths of the included resonances were determined by a χ^2 fit. However, previous analyses [14] showed, that the outcome of the fit depends on the values of the starting parameters and their release order in the fit. To overcome this problem, a large number of randomly chosen sets of start-parameter values is generated and for each set different release orders of the parameters are used. This section gives a brief description of this method. A more detailed discussion can be found in [14].

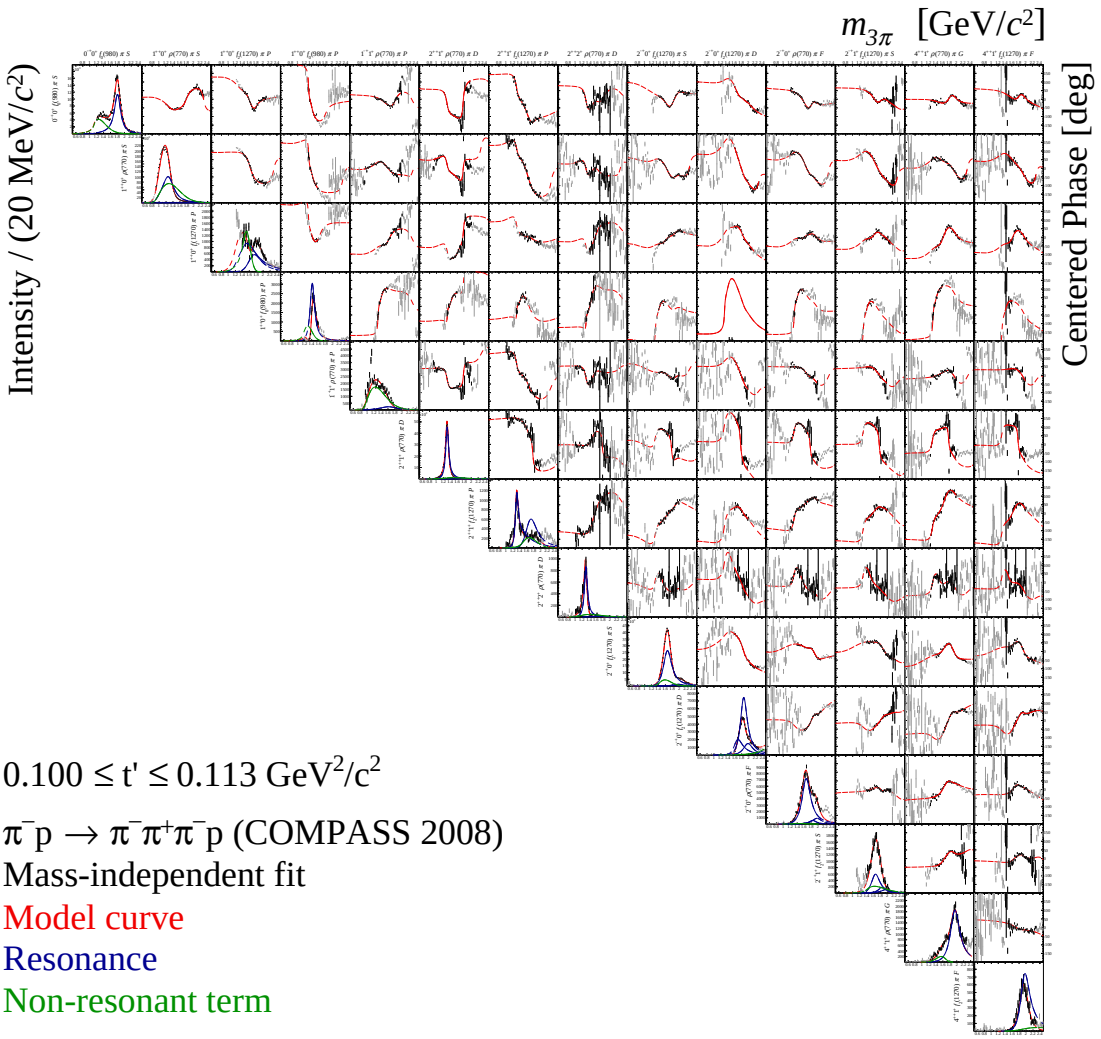

Figure 4.2: For illustration, the full spin-density matrix of the lowest t' bin entering the resonance-model fit is shown. The diagonal elements are the partial-wave intensities, the interference terms of the waves are represented by the relative phases between the partial waves in the off-diagonal plots. The fit result will be discussed in chapter 5. A complete collection of result figures can be found in appendix F.

4.3.1 χ^2 Formulation

The spin-density matrix $\rho_{\alpha\beta}$ as determined by the mass-independent fit is a complex-valued hermitian matrix. It can be transfered into an $N_{\text{waves}} \times N_{\text{waves}}$ real matrix

$$\Lambda_{\alpha\beta}(m_{3\pi}, t') = \begin{cases} \Re\left[\rho_{\alpha\beta}(m_{3\pi}, t')\right] & \alpha < \beta \\ \Im\left[\rho_{\beta\alpha}(m_{3\pi}, t')\right] & \alpha > \beta \\ \rho_{\alpha\alpha}(m_{3\pi}, t') = |\mathcal{T}_\alpha(m_{3\pi}, t')|^2 & \alpha = \beta \end{cases}, \tag{4.12}$$

where the partial-wave intensities are on the diagonal and the real parts of the interference terms of $\rho_{\alpha\beta}$ are the upper right off-diagonal elements. The corresponding imaginary parts are the lower left off-diagonal elements. The deviation between the resonance model, parameterized by ${}^{\text{RM}}\Lambda_{\alpha\beta}$, and the spin-density matrix $\Lambda_{\alpha\beta}$ from the partial-wave decomposition is measured with a χ^2 formulation defined as

$$\chi^2 = \sum_{t'} \sum_{\alpha\beta} \sum_{m_{3\pi} \in \text{Range}_{\alpha\beta}} \left[\frac{(\Lambda_{\alpha\beta} - {}^{\text{RM}}\Lambda_{\alpha\beta})^2}{\sigma^2_{\alpha\beta}} \right]_{(m_{3\pi}, t')} \tag{4.13}$$

with $\sigma_{\alpha\beta}$ being the statistical error of $\Lambda_{\alpha\beta}$ as obtained from the mass-independent fit. The residuals are summed over the 11 t' bins and the $m_{3\pi}$ bins within the fit range of the waves α and β. The fitted mass-ranges of the interference terms of the spin-density matrix are defined by the overlap of the fit ranges of both waves α and β.

The χ^2 value is minimized using the MIGRAD minimization algorithm from the MINUIT package, which uses the covariance matrix to determine the search direction with a variable metric and checks for positive-definiteness [28].

4.3.2 Fitting Scheme

To generate different sets of start-parameter values, the resonance masses and widths were picked randomly from uniform distributions. The range of these distributions were chosen based on previous measurements, large enough to avoid biasing the results. The start-parameter ranges are visualized in figure 4.3 and listed in table C.1. Due to a lack of prior knowledge, the start parameters for the non-resonant terms were randomly picked from rather wide uniform distributions. Details can be found in table C.2 in appendix C. For the Main fit, 250 sets of start-parameter values were generated. For the performed systematic studies, typically 50 start-parameter sets were sufficient to find the best solution. For each set of start-parameter values for the shape parameters, the start-parameter values of the branching and coupling parameters were generated according to a uniform distribution (see appendix C).

To increase the stability of the fit, it is necessary to limit the values of the parameters in the

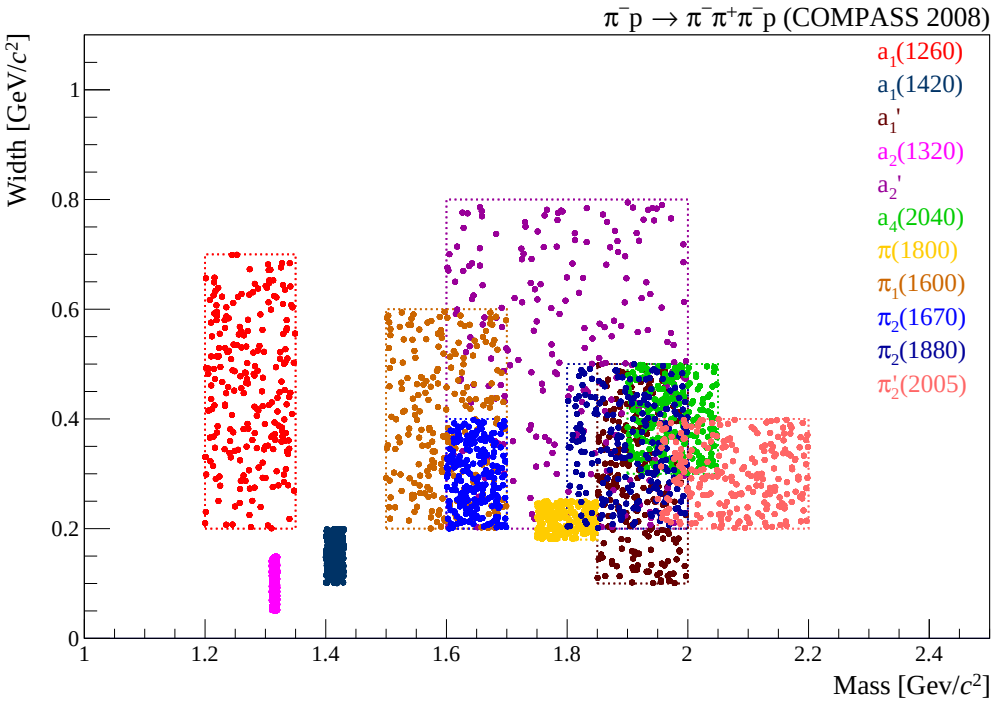

Figure 4.3: Distribution of the randomly generated start-parameter values (masses and widths) for all resonances. The different colors encode the different resonances. The boxes represent the regions over which the start parameters are distributed uniformly. The corresponding numbers for the ranges can be found in table C.1.

fit [29]. However, wide parameter ranges were chosen in order to avoid bias on the fit results. The mass parameters are limited to a range from 1.0 to 3.0 GeV/c^2, the width parameters have to be within 0.04 to 1.0 GeV/c^2. For all non-resonant shape parameters, a limit of −100 to 100 a.u. is enforced.

Also the order in which the parameters are released during the fit turned out to influence the fit outcome [14]. Therefore, for each start-parameter set, different release orders are applied. The release of the fit parameters is performed in the following three steps, illustrated in figure 4.4. As the coupling C_α^k and branching ${}_\alpha B_\beta^k$ parameters enter at most quadratically in the χ^2 formulation, in contrast to the shape parameters which enter in a complicated way, it is simpler for the fitter to optimize the coupling and branching parameters than to optimize the shape parameters. Therefore, first the coupling parameters are fitted in two different ways, keeping all other parameters fixed. Using the best solution of these fits as start values for the couplings, the branchings are fitted. With optimized couplings and branchings for each start-parameter set, the shape parameters are fitted in four different release orders. Details can be found in appendix C. Using this scheme we obtain 1000 fit attempts for the Main fit from 250 independent start-parameter sets. Performing this fits is related to large computational costs. The average time for each fit attempt to converge is around 30 h, which leads to a total amount of 30 000 CPUh for the Main fit.

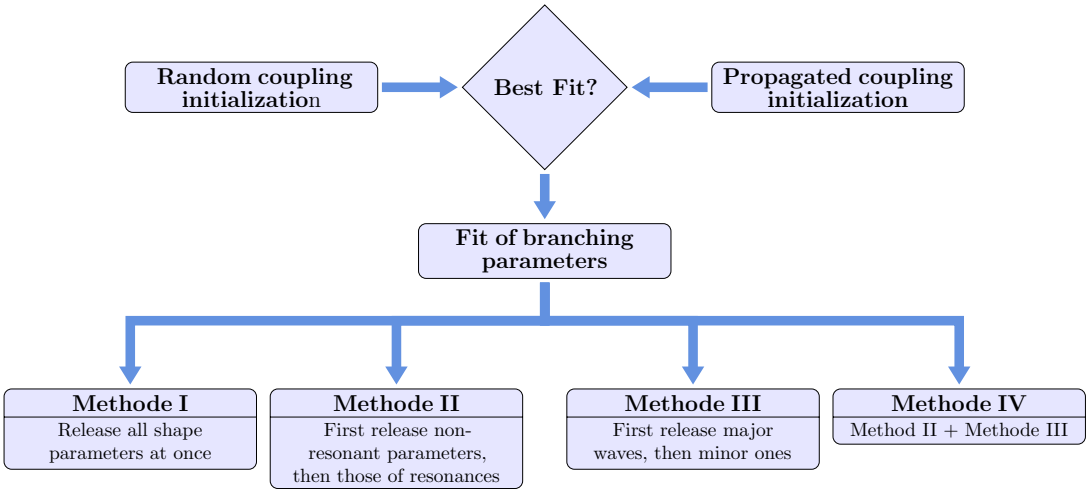

Figure 4.4: Flow diagram of the three steps in the resonance-model fit procedure applied to each set of start-parameter values. A detailed explanation of the steps can be found in appendix C.

Figure 4.5a shows the frequency distribution of the χ^2 values from the 1000 fit attempts, binned in narrow χ^2 bins of 0.1 units. Within this resolution, two fits within the same bin are assumed to have identical solutions. The χ^2 distribution of the performed fit attempts extends over a broad range from 288 618 to 2.2×10^{18} units. At lower χ^2 values, it shows a few clear peaks that correspond to solutions that are found more often by the fit. The most dominant peak with 167 fit attempts is at a χ^2 of 289 356 units. Most other solutions are found only once or twice.

This large number of different fit outcomes, and especially the large number of rare solutions, indicates that the χ^2 surface in the parameter space is very rough with many local minima. It is easy for the minimizer to get trapped in these local minima.

Figure 4.6 shows the parameters of the 1^{++} resonances [$a_1(1260)$, a_1'] for all converged fit attempts. The lines connect parameters of the same solution. The majority of the solutions scatter within a cluster at a mass around 1.3 GeV/c^2 for the $a_1(1260)$ and 1.75 GeV/c^2 for the a_1'. Many unphysical solutions can be identified. For some of them, the resonances are at the mass limits of 1.0 to 3.0 GeV/c^2. Another cluster is found where the $a_1(1260)$ and a_1' resonances are roughly at the same position ($m_0 \approx 1.35\,\mathrm{GeV}/c^2$, $\Gamma_0 \approx 0.7\,\mathrm{GeV}/c^2$). In these fits, the second resonance is misused to compensate for imperfections in the description of the peak shape by the $a_1(1260)$ component. This example shows, that many of the found solutions have an unphysical characteristic. To clean the set of solutions, a series of selection cuts is applied, which can be found in table 4.2. In the following, these cuts are introduced. A more detailed discussion can be found in [14].

From 1000 fit attempts, 88 have not been finished as either one of the intermediate steps failed or the final fit step took more than 120 h. From all 912 finished fits, 12 % did not converge and additionally 17 % are dropped, because at least one of the shape parameters is at its limit. In a third step so-called spurious solutions, which are rarely found, are removed from the results. To

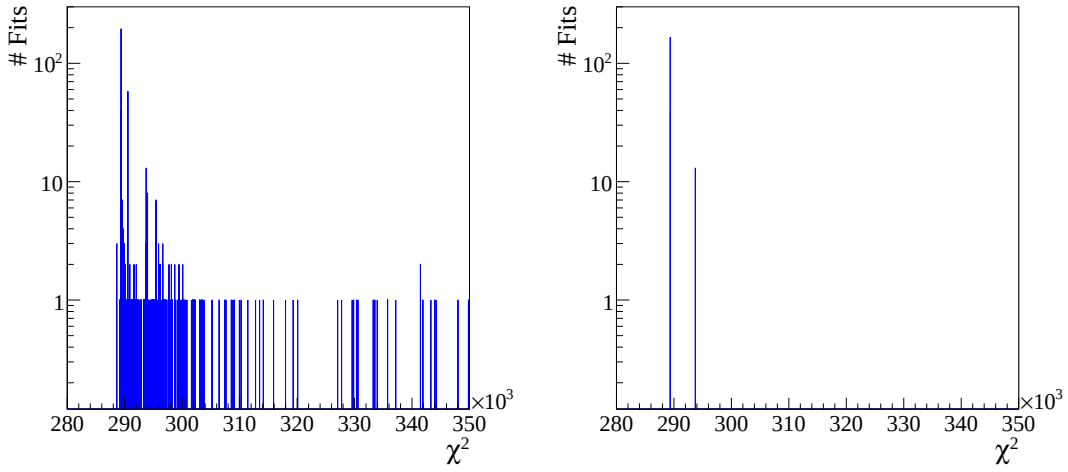

(a) χ^2 distribution before cuts

(b) χ^2 distribution after all cuts

Figure 4.5: χ^2 distributions of all converged solutions before (a) and after (b) selection criteria are applied to the solutions.

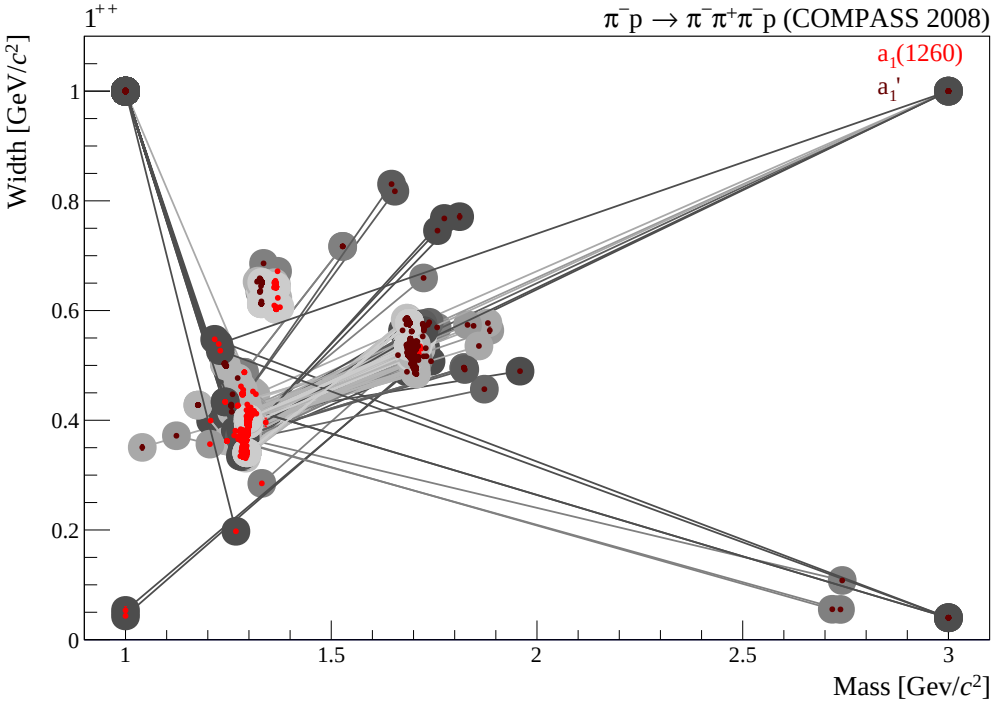

Figure 4.6: Resonance parameters of $a_1(1260)$ and a_1' of all converged fit attempts of the Main resonance model. The lines connect parameters, belonging to the same solution. The color of the lines and cycles indicates the χ^2 value of the solution (darker means lower χ^2).

determine the threshold of this cut, the probability, that $N_{\text{same }\chi^2}$ fits are in the same χ^2 interval is calculated. Figure 4.7b shows the corresponding non-normalized distribution[1]. For spurious solutions, a fast drop with $N_{\text{same }\chi^2}$ is expected, as it can be observed. Frequent solutions have a linear behavior, because there should be exactly one cluster with the same χ^2 for a given $N_{\text{same }\chi^2}$, which is found exactly $N_{\text{same }\chi^2}$ times. Therefore, the threshold is chosen in the minimum of the distribution, where the falling spurious-solution distribution goes over to the linearly increasing frequent-solution distribution. The spurious-solution cut rejects around half of the fit attempts, accepted so far. An additional cut filters solutions where the positions in mass of two resonances in the same partial wave [e.g. $a_1(1260)$, a_1'] are interchanged. To avoid solutions, where a second resonance is misused to improve the description of the shape of the dominant one, as seen for example for the $a_1(1260)$ and a_1' resonances, solutions with overlapping resonances are rejected[2]. The final cut rejects solutions, where the resonance position of at least one resonance is outside of the $m_{3\pi}$ fit range of the corresponding partial wave.

After applying the selection cutes to the 1000 fit attempts, 219 fits with physical solutions are found. Figure 4.7a compares the χ^2 distributions of the physical (blue) and unphysical (green) solutions. One can see, that in addition to the rare solutions, there are also frequent unphysical solutions. Especially the solution with the lowest χ^2 has been rejected by the interchange-of-resonances cut. Furthermore, it should be stressed, that the spurious-solution cut does not reject solutions, which are better than the best physical one, but only cleans up the sample of solution. The final χ^2 distribution is shown in figure 4.5b. The solution with the lowest χ^2 of 289 356 units, called the Main solution in the rest of the text, which describes the data best, is also the most frequent one with 167 fit attempts. More than 75 % of all fits with physical solutions and around 17 % of all fit attempts converged to this best solution. A second solution, Main.2, with a only 37 units higher χ^2 is found in 39 fit attempts. It is not visible in figure 4.5b because of its proximity to the Main solution. The third solution with a significantly worse χ^2 of 293 723 units is found 13 times. Because this third solution describes the data clearly worse compared to the best solution, it is not of further interest. In the following chapter, the description of the partial waves by the fit is discussed.

[1] It is determined by projecting the χ^2 distribution (see figure 4.5a) on the vertical axis and multiplying the obtained distribution with the corresponding $N_{\text{same }\chi^2}$ value.

[2] Two resonances overlap, if the $m_{3\pi}$ regions around their resonance masses over which their phase changes by 45° do overlap [14].

Table 4.2: Number of solutions after each cut and total number of solutions rejected by the cuts.

Cut	# solutions	total # rejected solutions
Total	1000	
Finished	912	88
Convergence	800	112
At Limits	641	230
Spurious Solutions	329	581
Interchange of Resonances	287	307
Proximity of Resonances	234	418
Resonances outside fit range	219	213

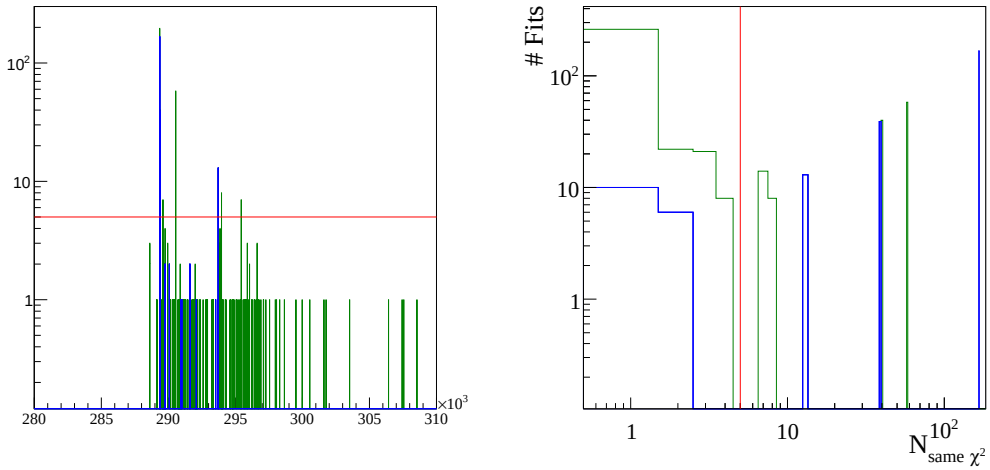

(a) χ^2 distribution

(b) #Fits($N_{same\chi^2}$)

Figure 4.7: Comparison between the χ^2 distribution of physical (blue) and unphysical (green) solutions. The left plot shows the χ^2 distribution, the right figure presents the number of fit attempts which are in the same χ^2 bin with N_{same,χ^2} other fit attempts. The spurious solution threshold is illustrated by the red line.

CHAPTER 5

Fit Results

In the resonance-model fit, the transition amplitudes of the partial waves are parameterized by a coherent sum of resonant and non-resonant contributions. In the following, the results of the Main fit are presented. A complete set of figures can be found in appendix F. As the fit results depend on the employed parameterizations as well as on other aspects of the resonance model, extensive studies have been performed to investigate the influence of these systematics. In this chapter, the central values of the resonance parameters obtained from the Main fit will be discussed. A detailed discussion of their systematic uncertainties can be found in chapter 6.

After a short review of the two solutions, found in the Main fit, and of the definition of the χ^2 matrix, the observation of established resonances, like the $a_2(1320)$, $a_4(2040)$ or the $\pi(1800)$, are discussed first. It will be shown, that the corresponding intensity spectra of the partial waves and their relative phases are well reproduced by the resonance model. In addition to these known resonances, weaker signals like the a_2' could be extracted from the data by exploiting the different t' dependences of the resonant and non-resonant components. This clearly shows the strength of the t'-resolved partial-wave analysis.

After the presentation of these familiar findings, more interesting domains are discussed. Four of the total 17 partial-waves with $J^{PC} = 2^{-+}$ and different decay modes as well as spin projections are included in the resonance-model fit, each of them showing different structures. However, all of the various observed structures are consistently described by the employed model. The necessity of a possible third π_2 resonance, the $\pi_2'(2005)$, to consistently describe the data will be discussed.

The large intensity of the $1^{++}\,0^+\,\rho(770)\,\pi\,S$ wave, which leads to small statistical uncertainties, requires a high precision in the description of this wave by the resonance model. The significant contribution of the non-resonant term further complicates the situation, as the parameterization of this component is not known with the required level of detail. Nevertheless the major features,

of the 1^{++} sector are reproduced by the resonance model. This includes, for example, the shift of the peak position with t'. This underlines again the importance of the t' binning. As it will be shown in section 5.4, it is possible to extract the $a_1(1260)$ resonance and, using the $1^{++}\,0^+$ $f_2(1270)\,\pi\,P$ wave, also the first excited a_1 state, the a_1'. However, significant systematic effects are observed.

In addition to these dominant partial waves, also weak signals are analyzed in this work. The narrow novel signal observed in the $1^{++}\,0^+$ $f_0(980)\,\pi\,P$ wave, shows clear resonant characteristics. Within the model assumptions, the peak and the corresponding phase motions can be consistently described only by including an independent resonance structure, named $a_1(1420)$. The interpretation of the nature of this structure is so far unclear and will be shortly discussed in section 8.1 of the conclusions.

In the last section, a possible resonance interpretation of the broad enhancement, observed in the intensity spectrum of the spin-exotic $1^{-+}\,1^+$ $\rho(770)\,\pi\,P$ wave will be discussed. Using a resonance and a non-resonant component, the data is described by the resonance-model fit and a systematic study clearly shows the need for a term with phase motion in this partial wave. However, no conclusive statement on a possible resonance interpretation can be made due to the observed systematic uncertainties and model deficits.

5.0.3 Comparison between the Two Solutions of the Main Fit

In addition to the best solution with the lowest χ^2, some fit attempts find a second solution with a χ^2 that is only 37 units larger. The obtained resonance parameters of both solutions are compared in figure 5.1. The plot shows the resonance widths (vertical axis) and masses (horizontal axis) for all resonances (different colors) of the resonance model. The full circles represent the parameters of the best solutions, the open circles illustrate the second solution. Both solutions lead to essentially the same resonance parameters, except for the widths of the $a_1(1260)$, a_1' and $\pi_1(1600)$ resonant components, which tend to be slightly narrower. However, compared to the systematic uncertainties discussed in section 6.2, these deviations are negligible. Therefore, the second solution can be interpreted as a local minimum, very close to the best solution in the parameter space. It leads basically to the same resonance parameters and is thus of no further interest. The interpretation of the obtained resonance parameters are discussed in chapter 6 after a detailed discussion of the systematics of this fit.

5.0.4 χ^2 Matrix

The χ^2 value, defined in equation (4.13), measures the agreement between the spin-density matrix elements and their description by the resonance model. To gain a more detailed insight, the total χ^2 value can be spitted into the contributions from the intensity and interference terms of the partial waves. The $\chi^2_{\alpha\beta}$ matrix in figure 5.2 represents the χ^2 contribution, coming from the

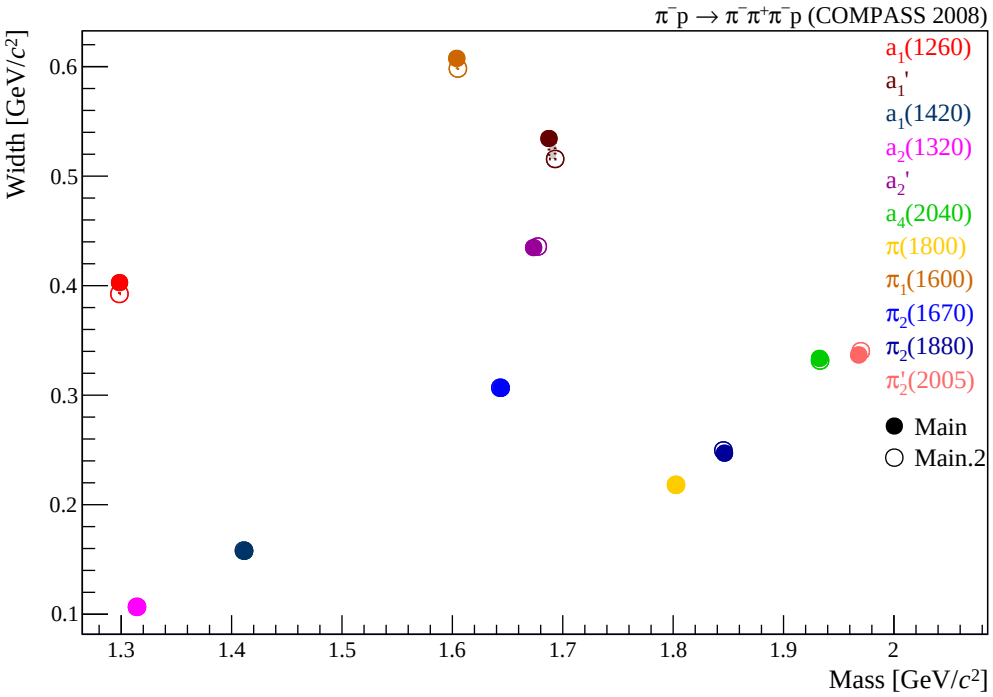

Figure 5.1: Resonance parameters of the Main fit. The full circles show the best solution, "Main.2" (open circle) is a second solution with slightly larger χ^2.

corresponding elements in the spin-density matrix

$$\chi^2_{\alpha\beta} = \sum_{t'} \sum_{m_{3\pi} \in \text{Range}_{\alpha\beta}} \left[\frac{(\Lambda_{\alpha\beta} - \Lambda^{\text{RM}}_{\alpha\beta})^2}{\sigma^2_{\alpha\beta}} \right]_{(m_{3\pi}, t')} \tag{5.1}$$

where $\Lambda_{\alpha\beta}$ [see equation (4.12)] are the intensities and real and imaginary parts of the spin-density matrix, respectively. The diagonal elements $\chi^2_{\alpha\,\alpha}$ represent the χ^2 of the corresponding intensity terms, the χ^2 contributions of the real parts are shown in the upper-right triangle sub-matrix, while the χ^2 coming from the imaginary parts are displayed in the lower-left part. The reason for the two empty elements in figure 5.2 is, that the $1^{++}\,0^+\,f_0(980)\,\pi\,P$ and $2^{-+}\,0^+\,f_2(1270)\,\pi\,D$ waves have non-overlapping mass regions in the fit (see table 4.1). One can clearly observe, that the intensity of the $1^{++}\,0^+\,\rho(770)\,\pi\,S$ wave has the largest contribution of more than 4 % of the total χ^2. This wave is the largest with 33 % of the total intensity and has thus the smallest statistical uncertainties. Therefore, even small imperfections in the description of the intensity spectrum lead to a large increase in χ^2. Further, this 1^{++} wave has the widest fit range so that more data points contribute to the χ^2. In agreement with this observation, the wave with the smallest fit range and a small intensity, the $1^{++}\,0^+\,f_0(980)\,\pi\,P$ wave, has the lowest contribution to the total χ^2. Except for the elements with the spin-exotic $1^{-+}\,1^+\,\rho(770)\,\pi\,P$ wave, which show a slightly larger χ^2, the χ^2 is more or less uniformly distributed among the other partial waves. The goodness of the fit in terms of χ^2 is reviewed in section 6.1.6. With this overall impression

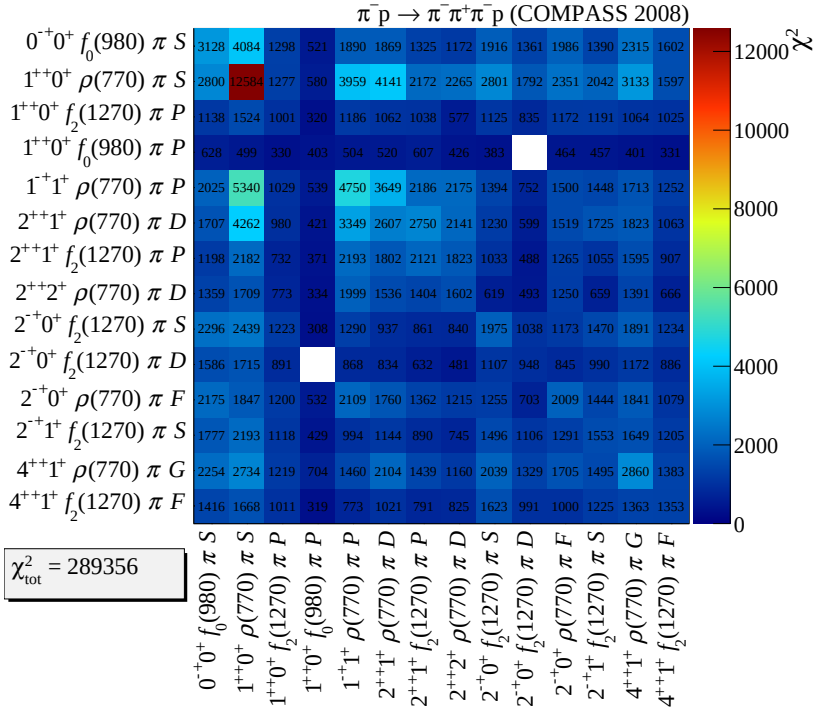

Figure 5.2: χ^2 contribution of intensity and interference terms of the partial waves to the total χ^2. The diagonal elements correspond to the χ^2 of the intensities. The off-diagonal elements represent the χ^2 of the real (upper-right) and imaginary (lower-left) parts of the interference terms [see equation (5.1)].

one can start to investigate the different J^{PC} sectors in detail, as discussed in the following sections.

5.1 The 0^{-+} and 4^{++} Partial Waves

Two well-known resonances, included in the resonance-model fit as interferometers for other partial waves, are the $a_4(2040)$ and $\pi(1800)$ resonances, observable in the $4^{++}\ 1^+\ \rho(770)\,\pi\,G$ and $4^{++}\ 1^+\ f_2(1270)\,\pi\,F$ waves and the $0^{-+}\ 0^+\ f_0(980)\,\pi\,S$ partial wave. The fit result for these waves with their relative phase is shown in figure 5.3 for the lowest t' bin. The model curve (red) is able to describe the shape of the $0^{-+}\ 0^+\ f_0(980)\,\pi\,S$ wave well. The peak structure at $1.8\,\mathrm{GeV}/c^2$ is interpreted as a dominant contribution of the $\pi(1800)$ resonance (blue). The fit finds this resonances at a mass of $m_{\pi(1800)} = 1803\,\mathrm{MeV}/c^2$ with a width of $\Gamma_{\pi(1800)} = 218\,\mathrm{MeV}/c^2$. Also the low-mass shoulder can be reproduced as a constructive interference between the low-mass tail of the $\pi(1800)$ and the non-resonant term (green). When excluding this shoulder from the fit by increasing the lower fit-range limit to $1.6\,\mathrm{GeV}/c^2$, as done in study (AB), the $\pi(1800)$ becomes $11\,\mathrm{MeV}/c^2$ broader, which is the largest width for all studies. Figure 5.4 shows the incoherent sum in t' over the intensities of the $0^{-+}\ 0^+\ f_0(980)\,\pi\,S$ wave, referenced here and in the

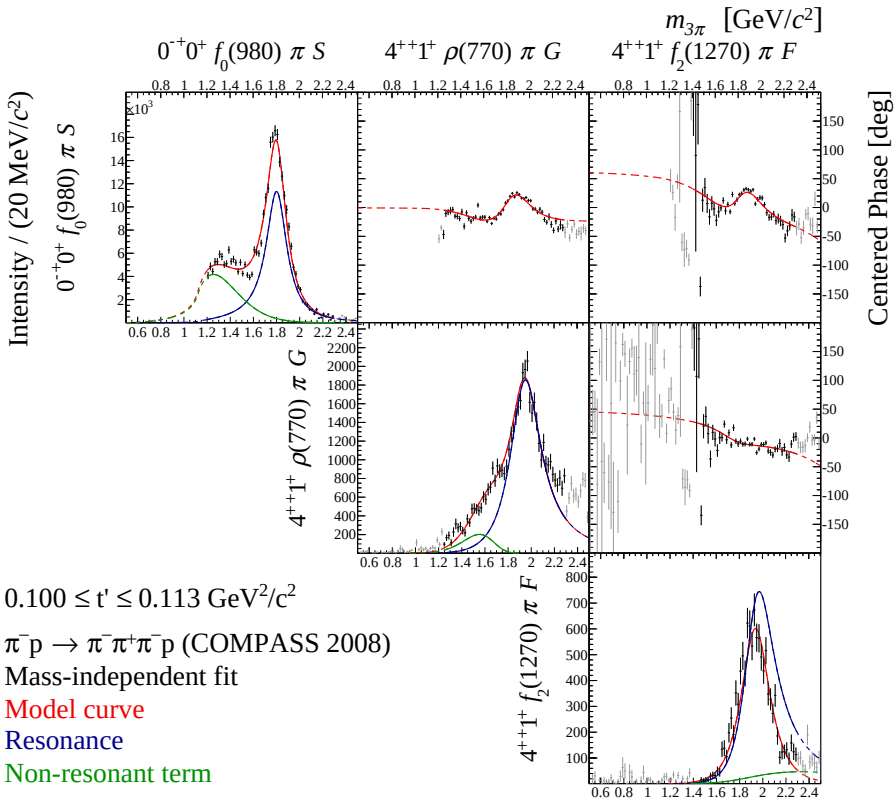

Figure 5.3: $0^{-+}\ 0^+\ f_0(980)\,\pi\,S$ vs. $4^{++}\ 1^+\ \rho(770)\,\pi\,G$ and $4^{++}\ 1^+\ f_2(1270)\,\pi\,F$ spin-density submatrix in the lowest t' bin. The relative phases are shifted so that they are centered around 0° for a better visualization. The phases are calculated by the phase of the row partial-wave minus that of the column. Thus the first row shows the phases of the $0^{-+}\ 0^+\ f_0(980)\,\pi\,S$ wave minus the phase of the corresponding 4^{++} wave.

following sections as t'-summed intensity, together with the result of study (AB). Additionally, the change of the 0^{-+} fit range affects the width of the $\pi_2'(2005)$ resonance, which becomes 80 MeV/c^2 narrower. Since the fit ignores the shoulder at the low-mass tail, the non-resonant term is vanishing. It is not misused to describe the intensity in the peak region, which clearly supports the interpretation of the Main fit, that most of the peak structure indeed arises from the $\pi(1800)$ resonance. However, it also shows how sensitive resonance yields are.

Similar to the 0^{-+} wave, the $4^{++}\ 1^+\ \rho(770)\,\pi\,G$ wave shows a clear peak at a mass of 2 GeV/c^2. In this mass region, the main contribution to the partial-wave intensity is coming from the $a_4(2040)$ resonances with a mass of $m_{a_4(2040)} = 1933\,\text{MeV}/c^2$ and a width of $\Gamma_{a_4(2040)} = 334\,\text{MeV}/c^2$. The broad shoulder in the low-mass tail of the intensity spectrum is reproduced by the fit as a constructive interference of the $a_4(2040)$ with the non-resonant term. The $a_4(2040)$ peak can also be observed in the $f_2(1270)\,\pi\,F$ decay mode of the 4^{++} states. Therefore, this wave is included in the resonance-model.

The relative phases between the 0^{-+} and 4^{++} waves exhibit a rapid phase motion of about 60° in the mass region around 1.8 GeV/c^2, followed by a slow downward motion starting at 1.9 GeV/c^2

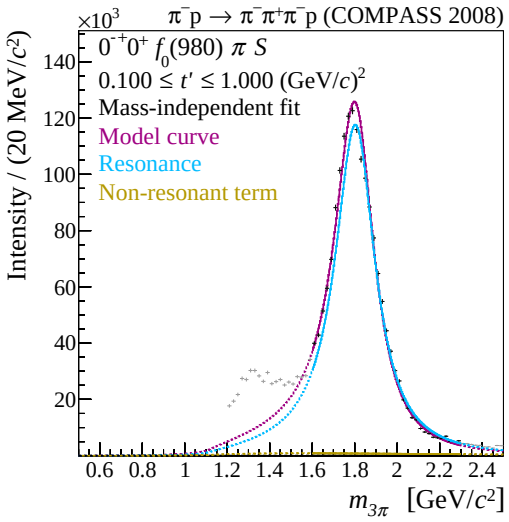

Figure 5.4: t'-summed intensity of the $0^{-+}\,0^{+}\,f_0(980)\,\pi\,S$ wave with the model curves for the study with tighter fit ranges in this wave [study (AB)].

(see figure 5.3). The rising phase can be explained by the occurrence of the $\pi(1800)$ resonance, while the falling phase motion arises from the $a_4(2040)$, due to the minus sign of the 4^{++} waves in the relative phase. Additionally, the different speeds of the phase motions are in agreement with the difference of the extracted resonance widths. This proves the importance of the phase information for the extraction of resonance parameters. The relative phase between both 4^{++} waves shows a flat phase motion within the fitted mass-region. This phase lock is in agreement with the interpretation of the resonance-model fit, that most of the intensity is coming from the $a_4(2040)$ resonance in both waves. As the $a_4(2040)$ has to have the same $m_{3\pi}$-dependent phase in both 4^{++} waves, their relative phase is flat.

5.2 The 2^{++} Partial Waves

One of the best established three-pion meson resonances is the $a_2(1320)$. The resonance model includes three 2^{++} waves, containing the $a_2(1320)$, with the $2^{++}\,1^{+}\,\rho(770)\,\pi\,D$ wave being the dominant one. The $a_2(1320)$ peak can even be directly observed in the total invariant mass spectrum before the partial-wave decomposition (see figure 2.3). But the 2^{++} waves have more interesting structures, especially when searching for weaker signals. Figure 5.5 compares the intensity spectrum of the major 2^{++} wave in the low- and high-t' region. Both regions show a clear $a_2(1320)$ peak at a mass of $1.3\,\mathrm{GeV}/c^2$. The fit result describes this signal with an almost pure contribution of the $a_2(1320)$ resonances at a mass of $m_{a_2(1320)} = 1314\,\mathrm{MeV}/c^2$ with a width of $\Gamma_{a_2(1320)} = 107\,\mathrm{MeV}/c^2$. Its narrow shape and low interference with other contributions allows for a precise extraction of the parameters of the $a_2(1320)$. Even minor influences, like integrating the theory curve of the resonance model over the mass-bin width instead of taking the theory value at the bin center, done in study (Q), affect the obtained parameters. Using integration

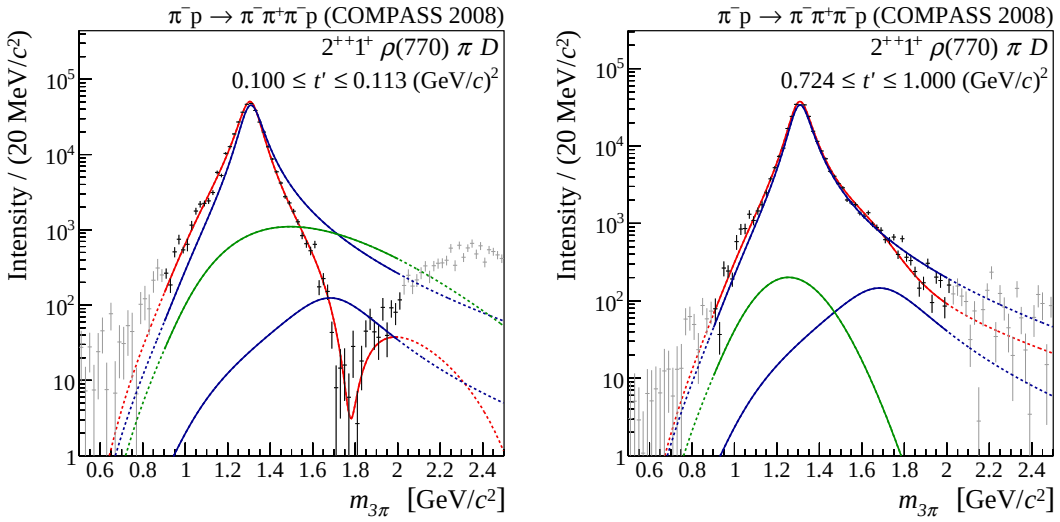

(a) Low-t' region

(b) High-t' region

Figure 5.5: Intensity of the 2^{++} 1^+ $\rho(770)\,\pi\,D$ wave in the low- and high-t' region.

over the bin width leads to a 1.4 MeV/c^2 narrower with for the $a_2(1320)$. Due to computational reasons, integration over the bin-width can neither be performed for all studies nor for the huge set of fit attempts in the Main fit.

At low t', the 2^{++} 1^+ $\rho(770)\,\pi\,D$ partial wave shows a dip in the intensity at a mass of 1.8 GeV/c^2, which moves towards higher $m_{3\pi}$ with increasing t' and vanishes in the high-t' region. The fit is able to reproduce the dip as a destructive interference of a possible a_2' resonance ($m_{a_2'}$ = 1674 MeV/c^2, $\Gamma_{a_2'}$ = 435 MeV/c^2) with the $a_2(1320)$ and the non-resonant term. The changing in the relative composition of the wave with t' leads to large destructive interference in the low-t' region, while this effect is less prominent for high t'. This clearly shows the different t' characteristics of the various components. The necessity for a second resonance in the 2^{++} waves has been tested by removing the a_2' from the resonance model and performing a fit using this reduced model [study (Z)]. The fit result has a 140 % larger χ^2. Figure 5.6 presents the difference in χ^2

$$\Delta\chi^2 = \chi^2_{\text{Main}} - \chi^2_{\text{(Z)}} \tag{5.2}$$

for the intensities (diagonal elements) of the partial waves and real (upper-right triangle) and imaginary (lower-left triangle) parts of the interference terms between the waves. A negative value means a worse description of the data by the model without the a_2'. One can clearly observe, that the intensities of the 2^{++} waves and their interference terms are described worse without a_2'. Furthermore, the interference effect in the 1.8 GeV/c^2 mass region can no longer be described without a_2'. This demonstrates the necessity of a second resonance in the 2^{++} waves.

The extrapolation of the fit beyond 2.0 GeV/c^2 underestimates the observed intensity. This may be due to a missing further excitation in the a_2 sector beyond 2.0 GeV/c^2 or because of

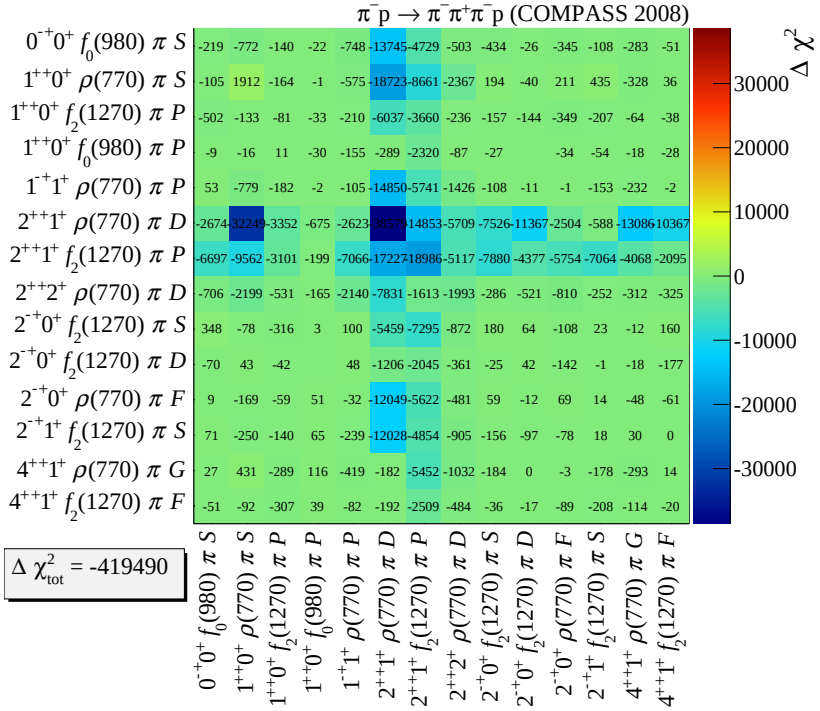

Figure 5.6: Difference in χ^2 ($\Delta\chi^2 = \chi^2_{\text{Main}} - \chi^2_{(Z)}$) between the Main solution and the fit without the a_2'. The diagonal elements show the difference in χ^2 of the partial-wave intensities. The off-diagonal elements represent the χ^2 difference of the real (upper-right) and imaginary (lower-left) parts of the interference terms between the partial waves. Negative values mean a worse description of the data by the model without the a_2'.

an inadequate parameterization of the non-resonant contribution in the high-mass region. The ability of extracting the parameters of weak signals like the a_2' by using their different t' behavior, clearly shows the strength of performing the partial-wave decomposition in bins of t' and the benefit of combining this information in the resonance-model fit.

To further stabilize the fit result, especially the a_2' resonance, the $2^{++}\,1^+\,f_2(1270)\,\pi\,P$ wave was included in the resonance-model fit. The t'-summed intensity of this wave is shown in figure 5.7a. The narrow peak at $1.3\,\text{GeV}/c^2$ is described almost completely by the $a_2(1320)$ while the fit reproduces the shape of the high-mass tail with a destructive interference between the a_2' and the high-mass tail of the $a_2(1320)$ and the non-resonant term. Figure 5.7b shows the t'-summed intensity spectrum of the $2^{++}\,2^+\,\rho(770)\,\pi\,D$ wave, which is included in the fit as third 2^{++} wave. Similar to the $2^{++}\,1^+\,\rho(770)\,\pi\,D$ wave it shows a narrow peak. However, the peak is slightly shifted to lower masses w.r.t. the $a_2(1320)$ position, but this shift can be reproduced by the fit as an interference effect of the $a_2(1320)$ with the non-resonant term.

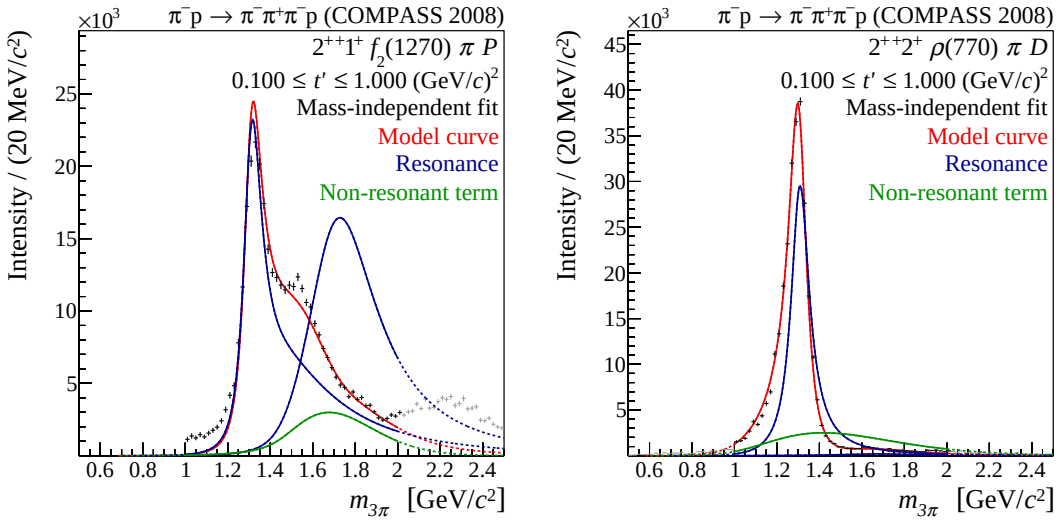

(a) $2^{++}\,1^+\,f_2(1270)\,\pi\,P$ wave

(b) $2^{++}\,2^+\,\rho(770)\,\pi\,D$ wave

Figure 5.7: t'-summed intensities of the $2^{++}\,1^+\,f_2(1270)\,\pi\,P$ and the $2^{++}\,2^+\,\rho(770)\,\pi\,D$ wave.

5.3 The 2^{-+} Partial Waves

In addition to the $a_2(1320)$ peak, the total invariant-mass spectrum shows a further peak at a mass of 1.7 GeV/c^2 (see figure 2.3). After the partial-wave decomposition, this peak appears in the 2^{-+} waves. Figure 5.8 presents the 2^{-+} waves in the $f_2(1270)\,\pi\,S$ decay with spin-projections $M = 0$ and $M = 1$. Both partial waves show a prominent peak, described by the $\pi_2(1670)$ resonance at a mass of $m_{\pi_2(1670)} = 1646\,\text{MeV}/c^2$ with a width of $\Gamma_{\pi_2(1670)} = 306\,\text{MeV}/c^2$. There are only small contributions of the other resonant components and the non-resonant term in these waves. Furthermore, the $2^{-+}\,0^+\,f_2(1270)\,\pi\,S$-wave shows a shoulder at 2.0 GeV/c^2, which is also reproduced by the model.

Considering the partial wave with $f_2(1270)\,\pi$ in a relative D instead of a S wave, shown in figure 5.9, a peak is found at a higher mass of 1.8 GeV/c^2. The fit describes this peak with a dominant contribution of the $\pi_2(1880)$ resonance ($m_{\pi_2(1880)} = 1847\,\text{MeV}/c^2$, $\Gamma_{\pi_2(1880)} = 247\,\text{MeV}/c^2$), which is the first excitation in the 2^{-+} sector and interferes destructively with the other resonant components. Almost no intensity is assigned to the non-resonant term in this wave.

The fourth 2^{-+} partial wave included into the fit describes a $\rho(770)\,\pi\,F$ decay. Figure 5.10 presents this wave in the low- and high-t' region. In the lowest t' bin, the wave features a dominant peak at 1.6 GeV/c^2 with a shoulder at 1.9 GeV/c^2 in the high-mass tail. Going to the high-t' region, the peak at 1.6 GeV/c^2 vanishes and a peak at around 2.0 GeV/c^2 appears with a significant contribution of the $\pi_2'(2005)$ resonance structure. The fit is able reproduce this change of the shape of the intensity distribution within the fitted mass region and finds the $\pi_2'(2005)$ at a mass of $m_{\pi_2'(2005)} = 1968\,\text{MeV}/c^2$ and a width of $\Gamma_{\pi_2'(2005)} = 330\,\text{MeV}/c^2$. Beyond 2.1 GeV/$c^2$, a further peak-like structure occurs at 2.3 GeV/c^2 in the low-t' region, which is less prominent at

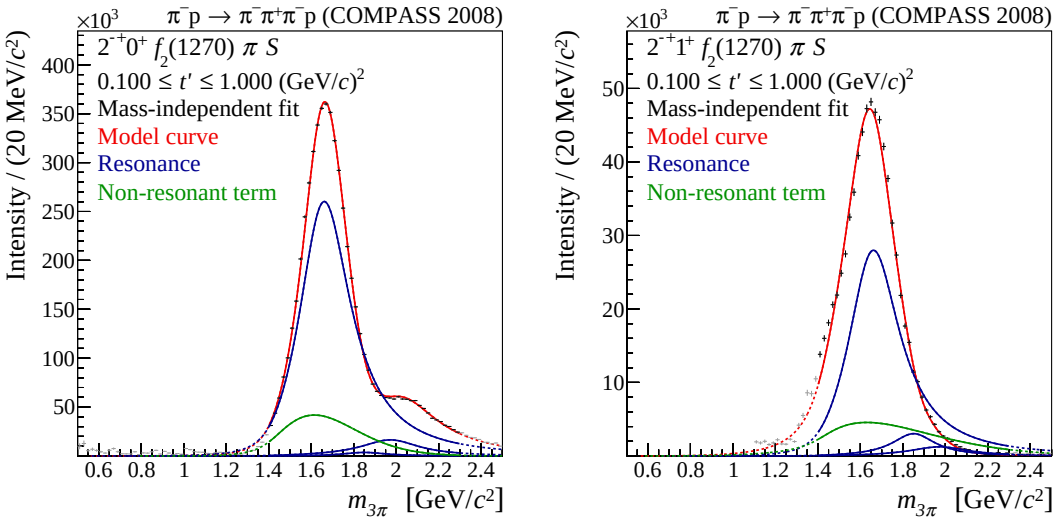

(a) $M = 0$ partial wave (b) $M = 1$ partial wave

Figure 5.8: t'-summed intensities of the 2^{-+} $f_2(1270)\,\pi\,S$ waves with spin projections $M = 0$ and $M = 1$.

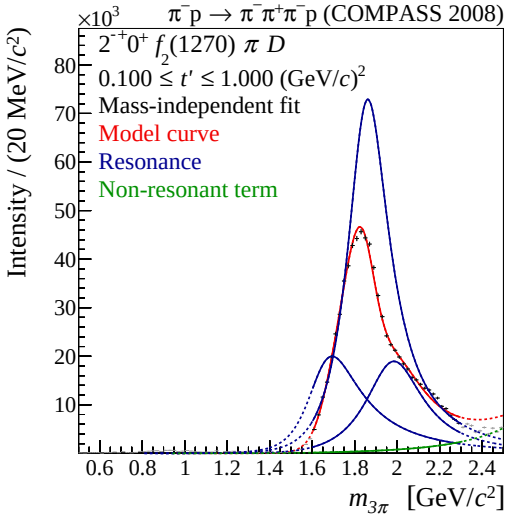

Figure 5.9: t'-summed intensities of the $2^{-+}\,0^+$ $f_2(1270)\,\pi\,D$ wave.

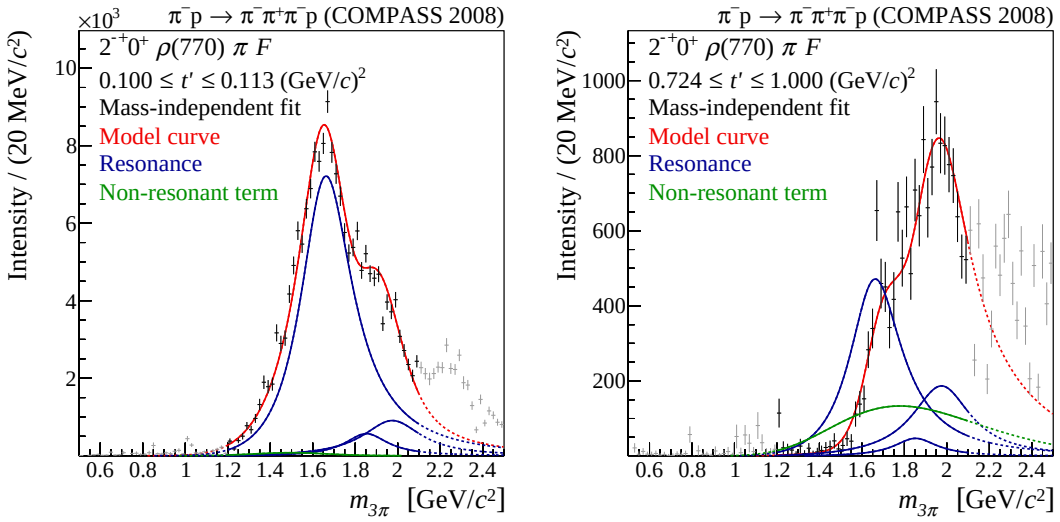

(a) Low-t' region

(b) High-t' region

Figure 5.10: Intensity of the $2^{-+}\,0^+\,\rho(770)\,\pi\,F$ wave in the low- and high-t' region.

high t'. As this analysis is focused on the low to intermediate $m_{3\pi}$ mass-region, the peak beyond 2.1 GeV/c^2 is excluded from the fit. However this illustrates that the analyzed data features more interesting structures, beyond the scope if this work.

To demonstrate that a third π_2 resonance is needed to describe the data, a fit [study (U)] has been performed, without the $\pi_2'(2005)$ resonance. Figure 5.11 compares the resonance parameters from the Main fit (full circles) with the result of this study (open circles). The obtained non-π_2 parameters are stable under omitting the $\pi_2'(2005)$ resonance, except for the $a_4(2040)$ resonance, which becomes slightly broader. However, this deviation is within the observed systematics of the $a_4(2040)$ parameters (see section 6.2). Removing the $\pi_2'(2005)$ also shows only a minor effect on the parameters of the $\pi_2(1670)$, which become 14 MeV heavier. The largest impact is observed on the $\pi_2(1880)$, which becomes almost 100 MeV broader. This can be explained by considering the intensity spectra of the 2^{-+} waves, shown in figures 5.12a and 5.12b. To gain enough intensity in the high-mass tails, the fit has to broaden the $\pi_2(1880)$ component. Still, the shape of the shoulder in the $2^{-+}\,0^+\,f_2(1270)\,\pi\,S$ wave and the second peak in the $2^{-+}\,0^+\,\rho(770)\,\pi\,F$ wave cannot be described by the fit without a third π_2 resonance. It becomes even more obvious when considering the high-t' region of the $2^{-+}\,0^+\,\rho(770)\,\pi\,F$ wave, shown in figure 5.12c. The fit uses an exponentially rising non-resonant term in trying to describe the peak around 2 GeV/c^2. The possibility of such a non-resonant term is a model artifact of the non-resonant parameterization and clearly unphysical. Another hint for the existence of a third π_2 in the data can be found in the phases, as shown for the $f_2(1270)\,\pi\,D$ and $\rho(770)\,\pi\,F$ decay modes in figure 5.12d. It shows a smoothly rising phase from 1.7 to 2.0 GeV/c^2. This phase motion can be associated with the $\pi_2(1880)$ resonance, which is dominant in the $f_2(1270)\,\pi\,D$ partial wave. At a mass of around 2.0 GeV/c^2 there is a small kink, followed by a further increase of the phase. This second phase motion is completely ignored by the fit without the $\pi_2'(2005)$, but can be reproduced using a third π_2 resonance in the model. Also the worsening in χ^2 of almost 18 900 units reflects the

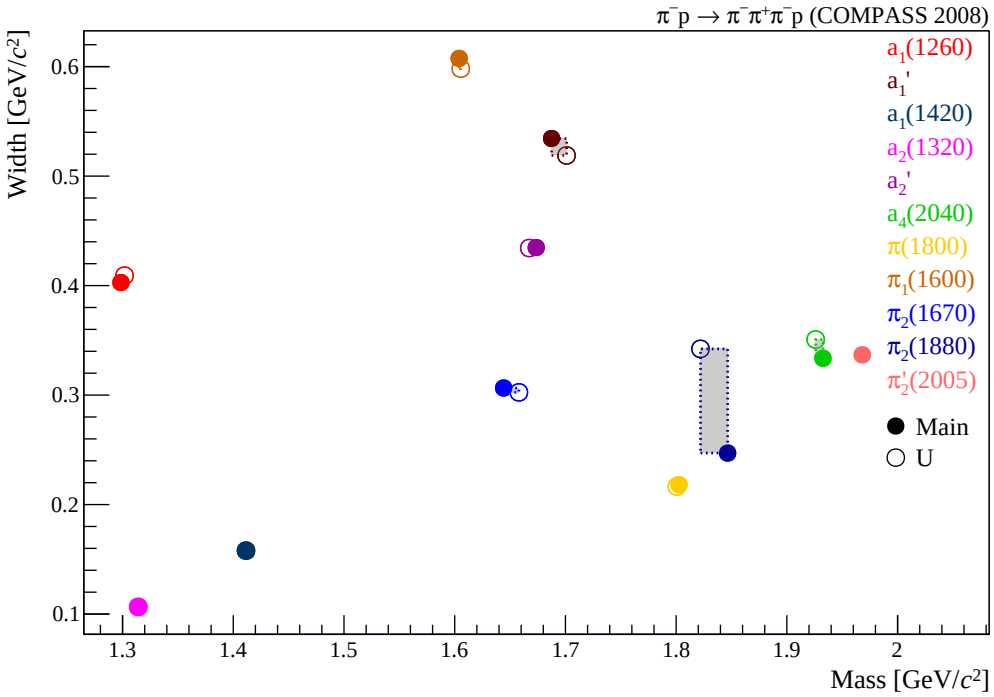

Figure 5.11: Resonance parameters from the Main fit (full circle) compared to study (U) without the $\pi_2'(2005)$ resonance (open circle). The difference of the solutions is visualized by the gray boxes.

insufficient description of the partial-wave amplitudes without the $\pi_2'(2005)$ component.

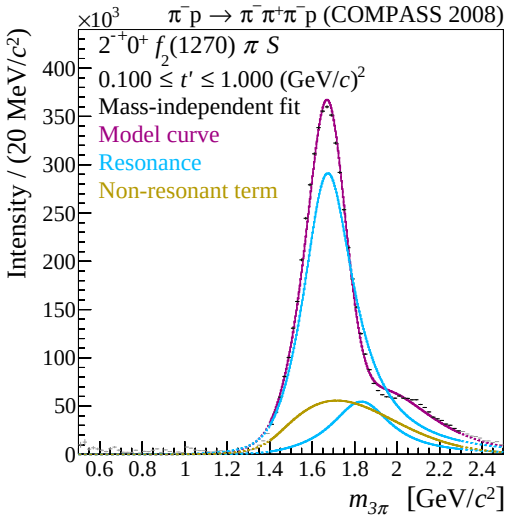

(a) $2^{-+}\,0^{+}\,f_2(1270)\,\pi\,S$ wave

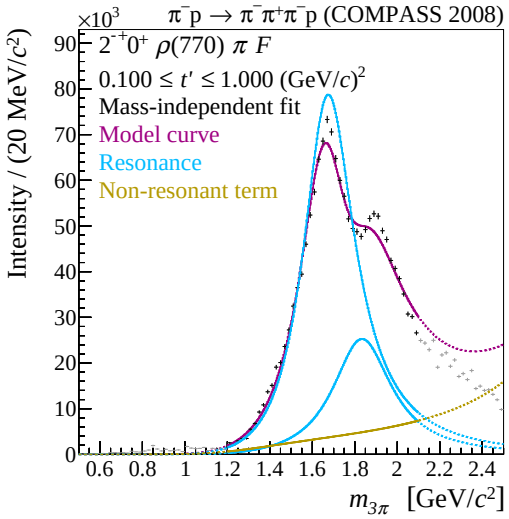

(b) $2^{-+}\,0^{+}\,\rho(770)\,\pi\,F$ wave

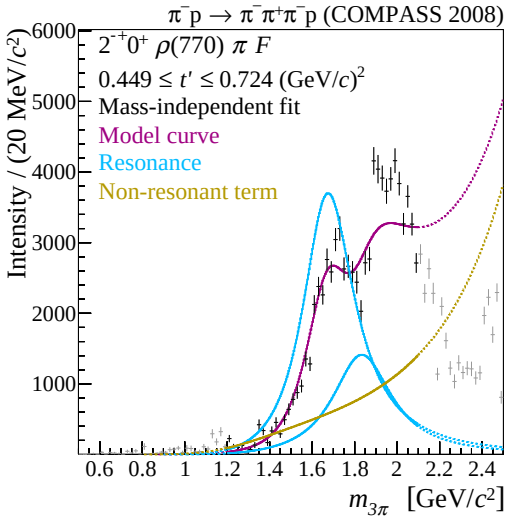

(c) $2^{-+}\,0^{+}\,\rho(770)\,\pi\,F$ wave at high t'

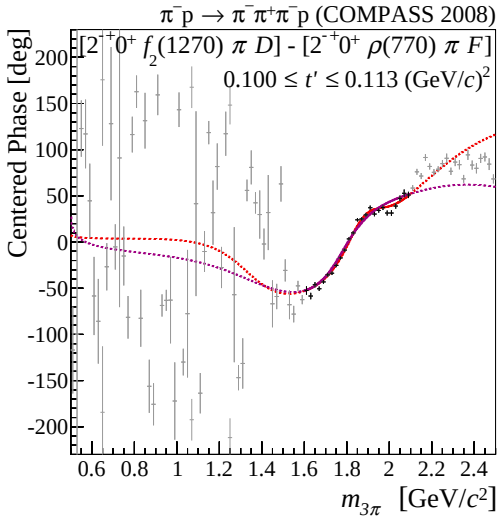

(d) Phase motion at low t' [compare study (U) (violet) to the Main fit (red)]

Figure 5.12: Fit results for study (U) without $\pi_2'(2005)$ resonance. Plots (a) and (b) show the t'-summed intensity of the $2^{-+}\,0^{+}\,f_2(1270)\,\pi\,S$ and $2^{-+}\,0^{+}\,\rho(770)\,\pi\,F$ waves. Plot (c) presents the intensity of the $2^{-+}\,0^{+}\,\rho(770)\,\pi\,F$ wave in the high-t' region and plot (c) the relative phase between the $2^{-+}\,f_2(1270)\,\pi$ D and $\rho(770)\,\pi\,F$ decay mode in the lowest t' bin.

5.4 The 1^{++} Partial Waves

The most dominant partial wave found in soft $\pi^- + p \to \pi^-\pi^-\pi^+ + p_{\text{recoil}}$ diffractive scattering is the $1^{++}\,0^+\,\rho(770)\,\pi\,S$ wave. Figure 5.13 shows the intensities of this wave in the 11 t' bins and the t'-summed intensity. A broad peak structure is observed around 1.2 GeV, which changes its shape and position with t'. The fit can reproduce the basic features of the shape of the intensity spectra in the low-t' region with an interference between the $a_1(1260)$ resonance ($m_{a_1(1260)} = 1298\,\text{MeV}/c^2$, $\Gamma_{a_1(1260)} = 400\,\text{MeV}/c^2$) and the non-resonant term. In contrast to the previously discussed waves, here, the resonant and non-resonant components are of the same order of magnitude. In the low-t' region, the low-mass tail of the $a_1(1260)$ and the non-resonant term are constructively interfering and, due to the 180° phase shift of the resonance amplitude, destructively interfering at the high-mass tail of the $a_1(1260)$. Going to higher t', this behavior changes. In the highest t' bin, the resonant and non-resonant components destructively interfere below and constructively interfere above the resonance position. This means, that the relative production phase between the $a_1(1260)$ and the non-resonant term, which is encoded in the coupling constants $C_\alpha^k(t')$, changes by approximately 180° over the analyzed t' range. This variation leads to a shift of the peak position towards higher masses when increasing t', as observed in the data. In the three highest t' bins, the shoulder at $1.9\,\text{GeV}/c^2$ in the high-mass tail becomes more distinct. The fit is not able to describe both, the narrow peak and the broad shoulder. This imperfection in the description of the peak at high t' is a hint for a still imperfect separation between resonant and non-resonant contributions, especially in situations where the non-resonant term is of the same order of magnitude as the resonance and a precise knowledge of the non-resonant shape is important. Due to the high statistical precision of the data in this wave, even small imperfections in the parameterization lead to a significant deviation between model and data. Such imperfections are observed in the description of the peak shape, illustrated in figure 5.14b. The low-mass tail of the peak is not perfectly described by the model within the small statistical errors. Furthermore, the dip around $1.2\,\text{GeV}/c^2$ is not reproduced by the fit. This illustrates the source of the large χ^2 contribution of the $1^{++}\,0^+\,\rho(770)\,\pi\,S$ partial wave and the need for a further improvement of the resonance model and especially the non-resonant parameterization.

An interesting effect occurs when omitting all three 2^{++} waves from the resonance-model fit, as done in study (D). The resonance parameters, obtained from this fit with only 11 waves, are shown in figure 5.16 (open circles). One finds a significant decrease of the $a_1(1260)$ width by $100\,\text{MeV}/c^2$. This goes together with a change in the description of the major 1^{++} wave, presented in figure 5.17. The fit assigns much more intensity to the non-resonant component (orange), which allows for a narrower $a_1(1260)$ (cyan). Study (D) further shows a second solution [(D.2), rectangles] with a worse χ^2, which is in good agreement with the Main solution. This means, that the Main solution occurs in this study as a possible description of the data. The reason for the occurrence of the narrow $a_1(1260)$ solution can be seen in the intensity spectrum of the $1^{++}\,0^+\,\rho(770)\,\pi\,S$ wave in the highest t' bin (figure 5.17b). With this more narrow $a_1(1260)$, the peak is better described by the fit (violet) and therefore leads to a significant improvement in χ^2 as seen in the χ^2 difference-matrix in figure 5.18. However, the solution with the narrow $a_1(1260)$ only improves the description of the intensity shape of the $1^{++}\,0^+\,\rho(770)\,\pi\,S$ wave.

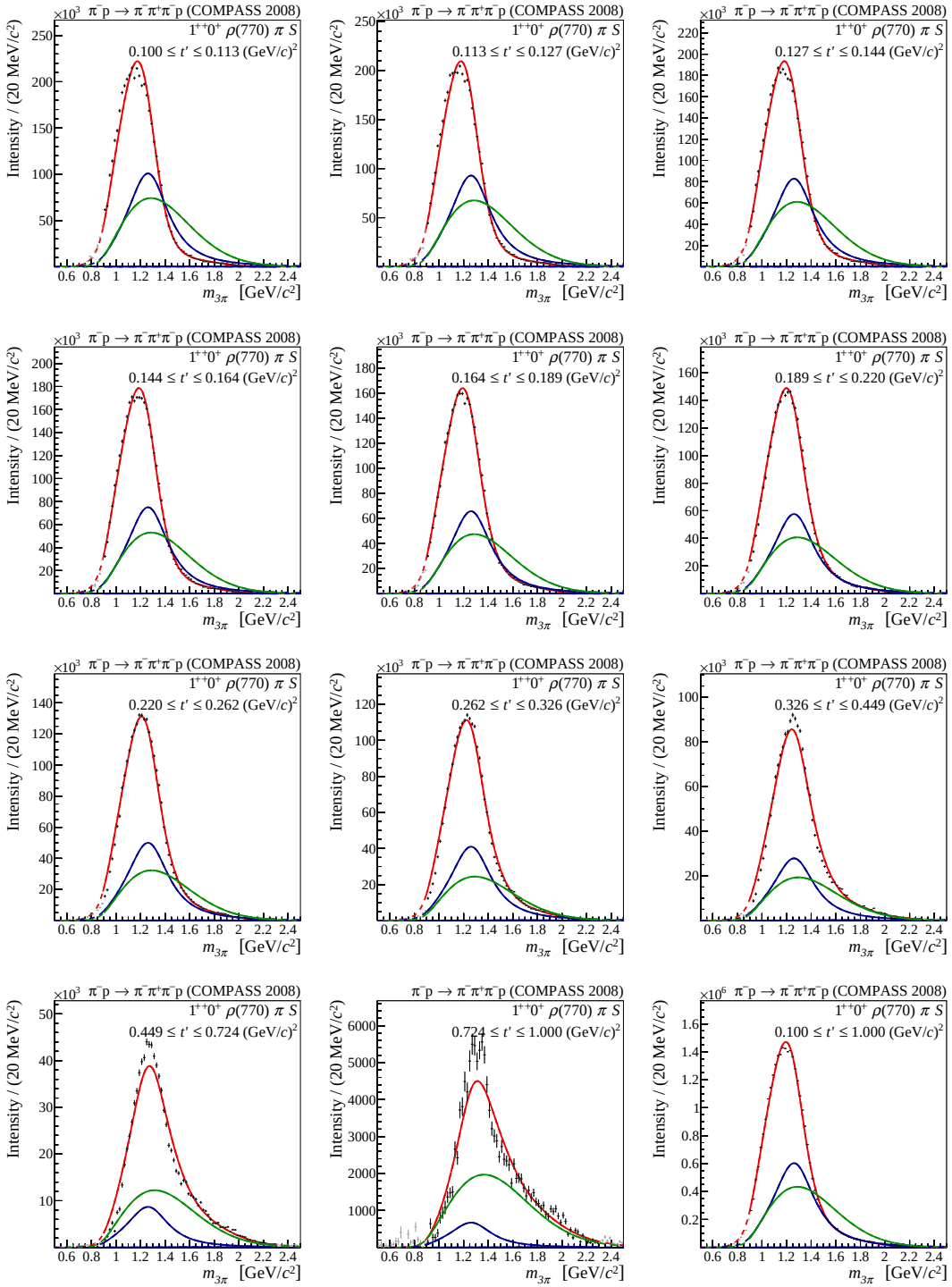

Figure 5.13: Intensity spectra of the $1^{++}\,0^{+}\,\rho(770)\,\pi\,S$ wave in the 11 t' bins, with t' increasing from upper-left to lower-right. The plot in the bottom-right corner is the t'-summed intensity.

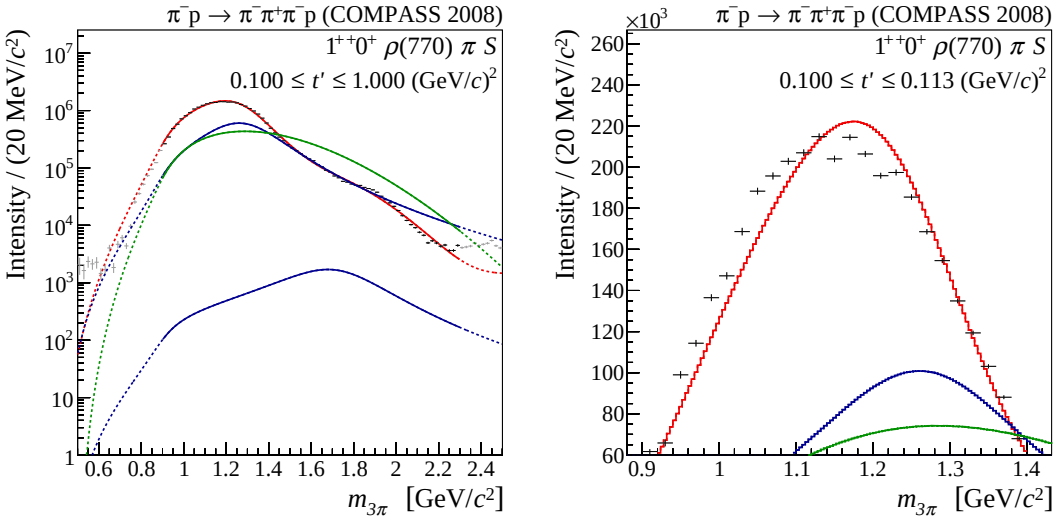

(a) Log-scale Plot (b) Enlargement of the peak region

Figure 5.14: t'-summed intensity of the $1^{++}\,0^{+}\,\rho(770)\,\pi\,S$ wave (a) and enlargement of the peak region in the lowest t'-bin (b).

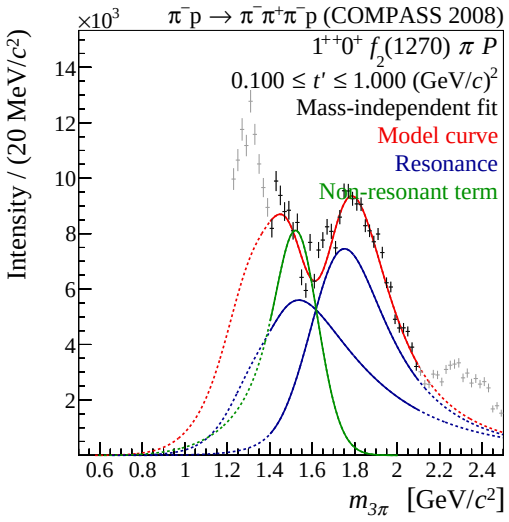

Figure 5.15: t'-summed intensity of the $1^{++}\,0^{+}\,f_2(1270)\,\pi\,P$ wave.

The interference terms with other partial waves and the description of the $1^{++}\,0^{+}\,f_2(1270)\,\pi\,F$ wave is actually worse. In the Main fit, the best solution of study (D) seems to be suppressed by the 2^{++} waves. To investigate this further, two studies have been performed where only one of the three 2^{++} waves is removed from the wave set. Without the $2^{++}\,1^{+}\,\rho(770)\,\pi\,D$ wave [study (H)], the solution found by the fit is in agreement with the Main solution. But also this study shows a second solution with the narrow $a_1(1260)$ interpretation as in study (D). However this solution has a worse χ^2. Omitting the $2^{++}\,2^{+}\,\rho(770)\,\pi\,D$ in study (I), a fit result with a narrow $a_1(1260)$, similar so study (D), is found as the best solution. This and further studies omitting various combinations of 2^{++} waves lead to the conclusion that it is mostly the information from the $2^{++}\,2^{+}\,\rho(770)\,\pi\,D$ that suppresses the solution with the narrow $a_1(1260)$. In addition to the influence on the a_1 parameters, omitting the 2^{++} waves has a dramatic impact on the width of the $\pi_1(1600)$ which becomes more than $200\,\mathrm{eV}/c^2$ narrower. All other resonance parameters remain essentially unchanged.

The signal for a potential excited state, a_1', seems to be small in the $1^{++}\,0^{+}\,\rho(770)\,\pi\,S$ wave, as it can be seen in the log-scale plot of the t'-summed intensity spectrum in figure 5.14a. The a_1' shows up more prominent in the $1^{++}\,0^{+}\,f_2(1270)\,\pi\,P$ wave (figure 5.15), which is the reason for including this wave. The resonance parameters of the first excited a_1 state are found to be $m_{a_1'} = 1680\,\mathrm{MeV}/c^2$ and $\Gamma_{a_1'} = 534\,\mathrm{MeV}/c^2$. To illustrate that this resonance is required to describe the data, study (Y) has been performed where the a_1' was excluded from the model. This study shows a significant worsening in χ^2 by approximately 42 300 units. As expected, especially the description of the $1^{++}\,0^{+}\,f_2(1270)\,\pi\,P$ wave suffers from omitting this resonance. Neither the intensity spectra nor the relative phases are described sufficiently.

The influence of the phase space on the resonance shape is clearly seen in the $1^{++}\,0^{+}\,f_2(1270)\,\pi\,P$ wave. The peak of the $a_1(1260)$ is shifted upwards to a mass of $1.5\,\mathrm{GeV}/c^2$, while the resonance mass is the same as in the $\rho(770)\,\pi\,S$ wave. The reason is, that the rising edge of the peak is dominated not by the resonance, but by the opening of the three-pion phase space in the $f_2(1270)\,\pi\,P$ decay. The opening of the phase space at around $1.4\,\mathrm{GeV}/c^2$ is blurred by the finite with of the $f_2(1270)$ isobar.

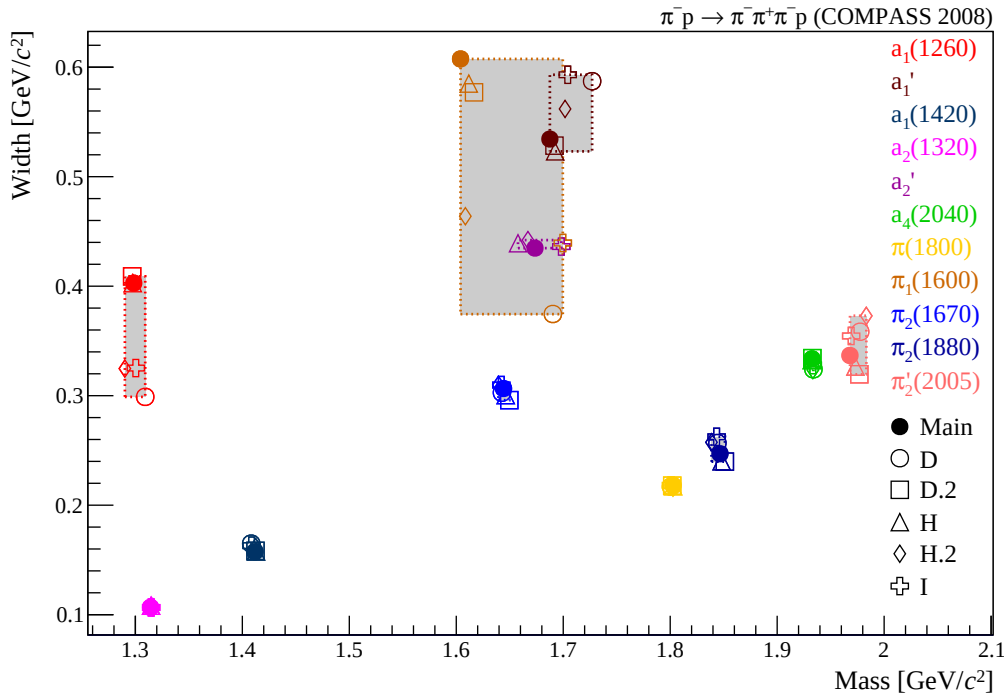

Figure 5.16: Resonance parameters obtained from the studies without the 2^{++} waves. The full circles represent the Main-solution. Study (D) (open circles) is without all three 2^{++} waves. The rectangles are the second solution of study (D). Study (H) (triangles, diamonds) is a fit without the $2^{++}\,1^{+}\,\rho(770)\,\pi\,D$ wave and in study (I) (crosses) the $2^{++}\,2^{+}\,\rho(770)\,\pi\,D$ wave has been omitted from the fit-model.

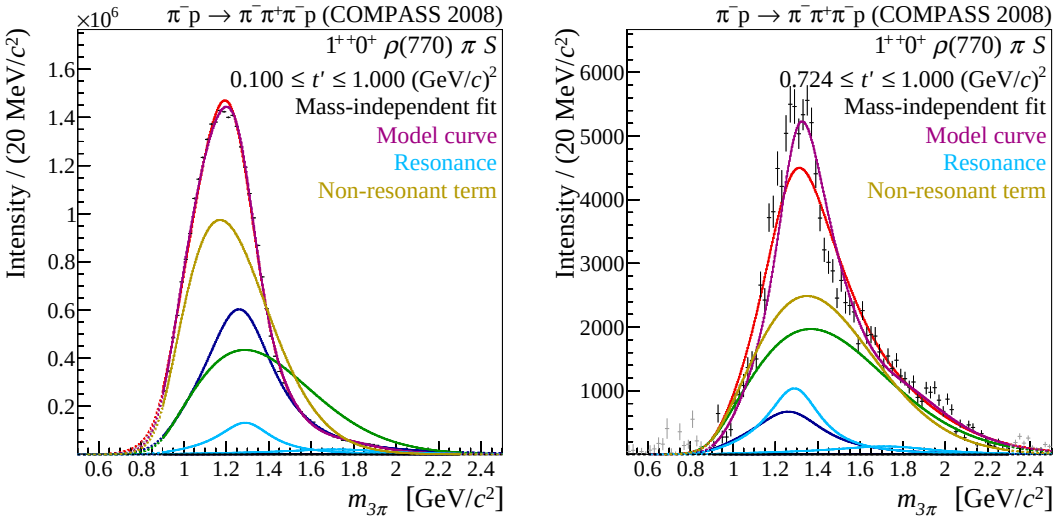

(a) t'-summed (b) Highest t' bin

Figure 5.17: Intensity spectra of the $1^{++}\,0^{+}\,\rho(770)\,\pi\,S$ wave of the study (D) without 2^{++} waves (violet/-cyan/orange) compared to the Main results (red/blue/green). The left plot shows the t'-summed intensity, the right plot the highest t' bin.

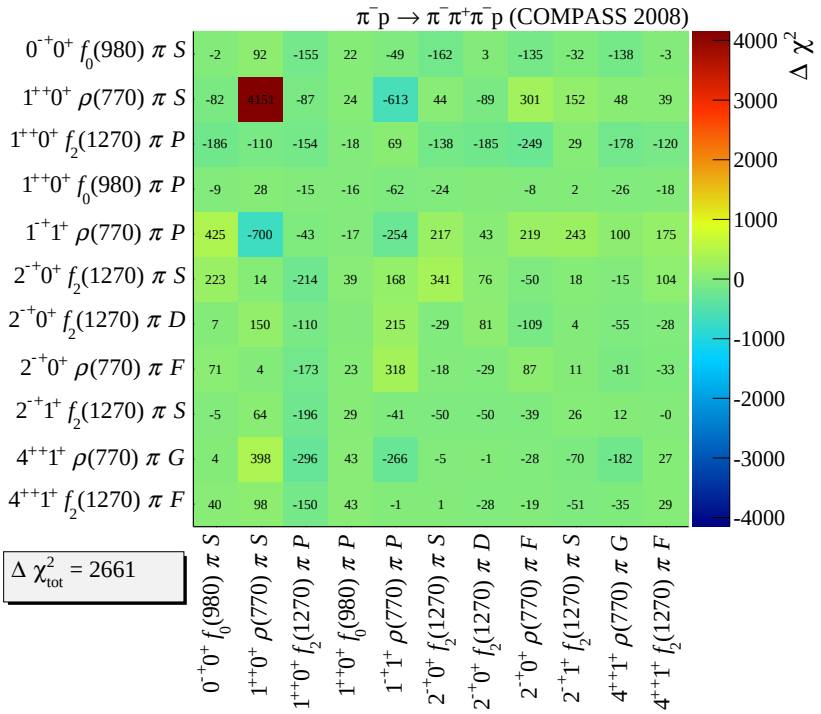

Figure 5.18: χ^2 difference between the two solutions (D) and (D.2) of the study without 2^{++} waves. A positive value means a better description in the solution (D), which has an overall lower χ^2.

5.5 The $1^{++}\,0^{+}\,f_0(980)\,\pi\,P$ Wave

One of the most interesting findings in the COMPASS data, is the clear signal slightly above $1.4\,\mathrm{GeV}/c^2$ in the $f_0(980)\,\pi\,P$ decay of the 1^{++} states (see figure 5.19). There is at the moment no known or expected 1^{++} meson resonance in this mass region. The ground state in the 1^{++} sector, the $a_1(1260)$, has a mass of about $1.2\,\mathrm{GeV}/c^2$ and the first excitation, the $a_1(1640)$, is observed at a mass of $\approx 1.65\,\mathrm{GeV}/c^2$ [6]. An additional state at $1.4\,\mathrm{GeV}/c^2$ would be difficult to explain in the quark model. In addition, the rapid 180° phase motion w.r.t. the dominant 1^{++} $0^{+}\,\rho(770)\,\pi\,S$ wave, suggests that the $f_0(980)\,\pi\,P$ and $\rho(770)\,\pi$ S decay modes have different resonance contributions within the $1.4\,\mathrm{GeV}/c^2$ region. Figure 5.19b shows this phase in different t' bins.

This $1^{++}\,0^{+}\,f_0(980)\,\pi\,P$ wave is parameterized in the resonance model using one resonant component, named $a_1(1420)$ and one non-resonant component. The fit is able to reproduce the narrow signal with a dominant contribution of the resonance term ($m_{a_1(1420)} = 1412\,\mathrm{MeV}/c^2$, $\Gamma_{a_1(1420)} = 158\,\mathrm{MeV}/c^2$), which is destructively interfering with the non-resonant component in the low-mass tail of the peak, as shown in figure 5.19a. Also the rapid phase motion in the different t' bins are reproduced by the fit with the $a_1(1420)$ resonance.

Similar to the studies performed for the a_1' and a_2', the simplest test for the existents of the

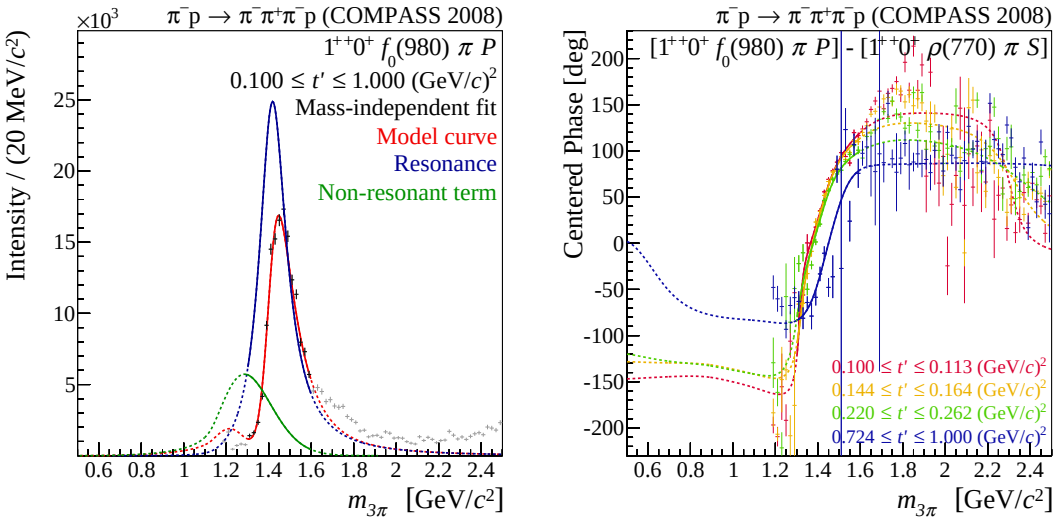

(a) Intensity (b) Phases

Figure 5.19: t'-summed intensity of the $1^{++}\,0^+\,f_0(980)\,\pi\,P$ wave (a) and its phase motion w.r.t. the $1^{++}\,0^+\,\rho(770)\,\pi\,S$ wave in four t' bins (b). The phase in the lowest t' bin has been shifted such that it is centered around 0°, the other phases are shifted accordingly.

$a_1(1420)$ resonance is to remove it from the resonance model and perform a fit. The resulting description of the $1^{++}\,0^+\,f_0(980)\,\pi\,P$ intensity and phase are shown in figure 5.20. The non-resonant contribution (orange) alone clearly does not describe the intensity distribution of the wave. Also the rapid phase motion is not reproduced without a resonant component. Without a $a_1(1420)$ term the χ^2 increases by 43 %, mainly coming from a worse description of the $1^{++}\,0^+\,f_0(980)\,\pi\,P$ wave, as shown in figure 5.21. This vast increase in χ^2 additionally proves the necessity for a resonant component to describe the narrow signal.

The $a_1(1420)$ is only observed in the $f_0(980)\,\pi\,P$ decay mode. This raises the question whether this signal is an independent resonance structure or whether it could be explained, using the $a_1(1260)$ resonance. To investigate this, study (V) has been performed without the $a_1(1420)$ resonance, but with the $a_1(1260)$ component also contributing to the $1^{++}\,0^+\,f_0(980)\,\pi\,P$ wave. The resonance parameters, obtained from this study are compared with the Main fit in figure 5.22. The best solution (open circles) shows a totally different result for the $a_1(1260)$. Its mass and width parameters are very close to those of the $a_1(1420)$ from the Main fit. This is best seen in the description of the $1^{++}\,0^+\,f_0(980)\,\pi\,P$ intensity (figure 5.23a). The result for the $a_1(1260)$ (cyan) is almost the same as the shape of the $a_1(1420)$ from the Main fit (blue). However, the peak in the $1^{++}\,0^+\,f_0(980)\,\pi\,P$ intensity is not described well by this model. This means, that even if the shape of the $a_1(1260)$ in this study is similar to that of the $a_1(1420)$, the interference with the non-resonant component is different due to the additional constrains from the phase information. The result for the dominant 1^{++} wave, shown in figure 5.23b, is similar to the solution found in the study without the 2^{++} waves (see section 5.4). The dominant part of the intensity is assigned to the non-resonant term, interfering with a small contribution from the $a_1(1260)$. The χ^2 of this study is worse by 24 000 units w.r.t. the Main solution. As the fit clearly

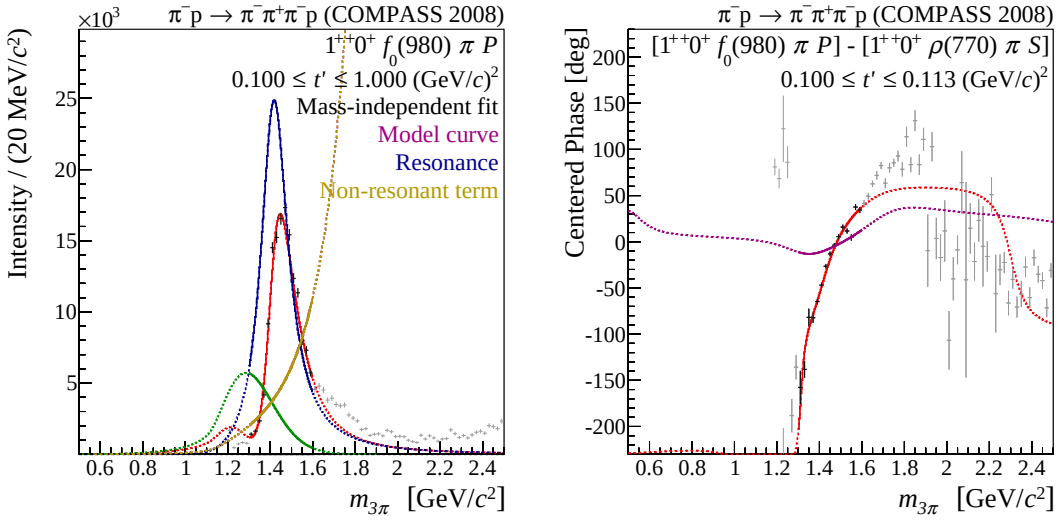

(a) Intensity (b) Phase

Figure 5.20: t'-summed intensity of the $1^{++}\,0^{+}\,f_0(980)\,\pi\,P$ wave (a) and its phase motion w.r.t. the $1^{++}\,0^{+}\,\rho(770)\,\pi\,S$ wave in the lowest t' bin (b). The solution of the study without the $a_1(1420)$ is colored in violet/cyan/orange, the Main solution in red/blue/green.

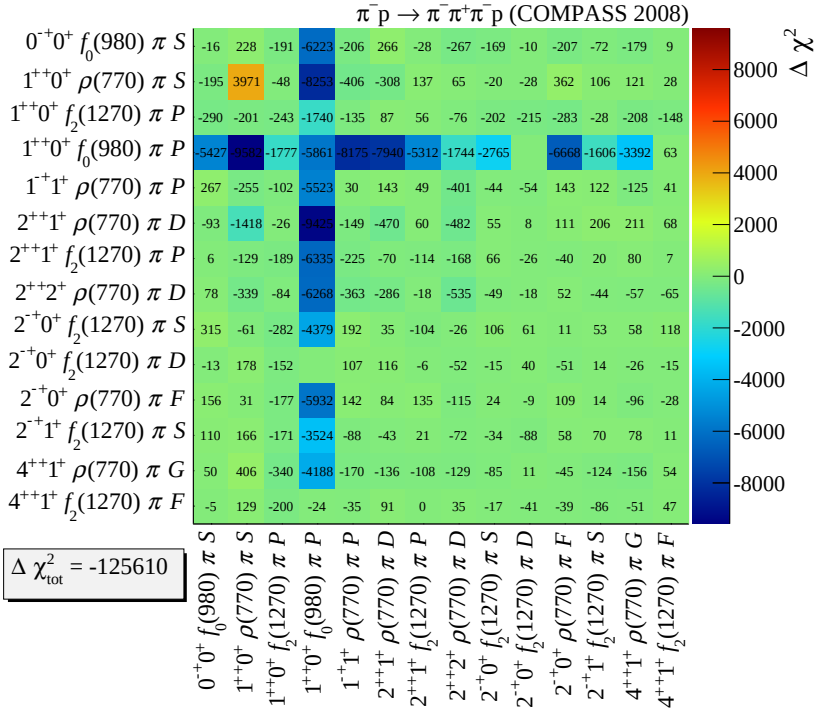

Figure 5.21: χ^2 difference beween the Main solution and the study without the $a_1(1420)$ resonance. Negative values mean worse description without $a_1(1420)$.

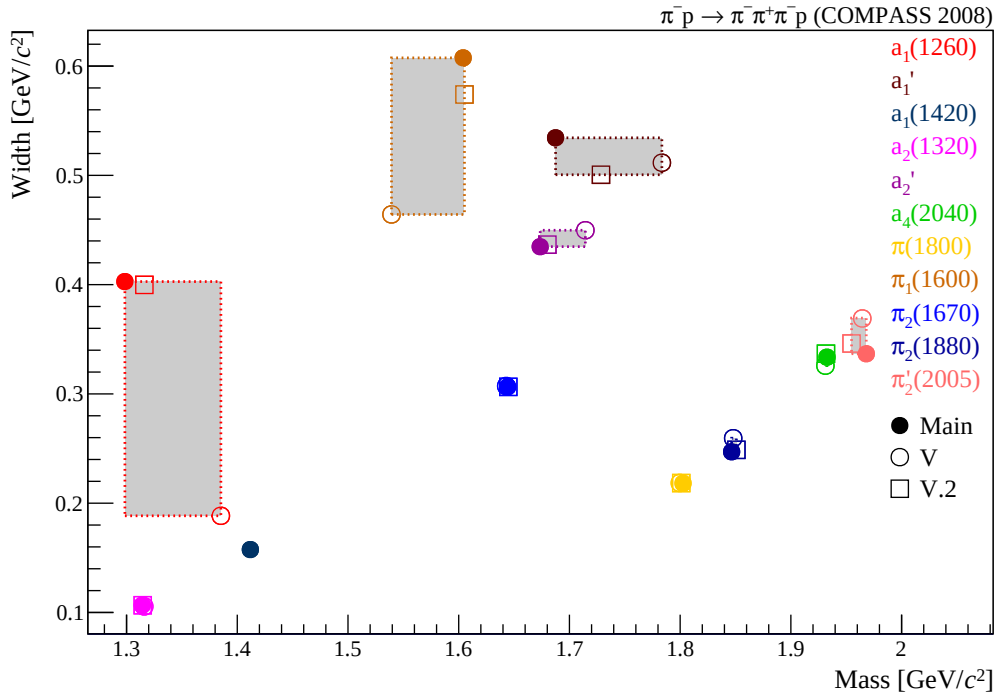

Figure 5.22: Resonance parameters obtained from study (V) with $a_1(1260)$ in $1^{++}\,0^+\,f_0(980)\,\pi\,P$ wave (open circles). The open rectangles show a second solution of this study with worse χ^2.

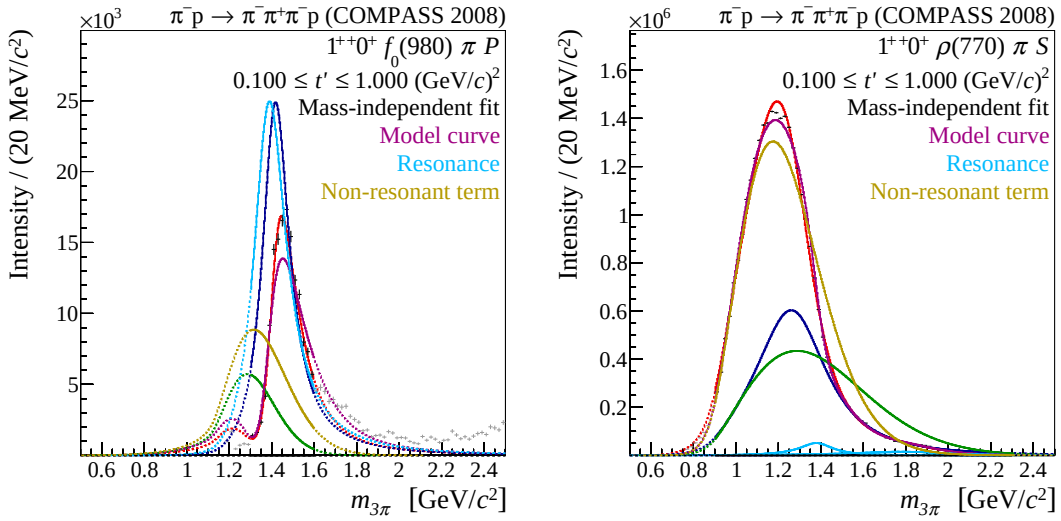

(a) $1^{++}\,0^+\,f_0(980)\,\pi\,P$ (b) $1^{++}\,0^+\,\rho(770)\,\pi\,S$

Figure 5.23: t'-summed intensities for the 1^{++} $f_0(980)\,\pi\,P$ and $\rho(770)\,\pi\,S$ decay modes with the $a_1(1260)$ in the $1^{++}\,0^+\,f_0(980)\,\pi\,P$ wave (violet/cyan/orange) compared to the Main fit result (red/blue/green).

misuses the $a_1(1260)$ component, this study is not included in the definition of the systematic uncertainties of the resonance parameters. One should also notice, that there is a second solution (V.2) of this study with a worse χ^2, which shows the same interpretation of the partial waves as the Main solution and which does not describe the $1^{++}\,0^+\,f_0(980)\,\pi\,P$ wave.

5.6 The $J^{PC} = 1^{-+}$ Spin-Exotic Wave

Signals of a spin-one state with exotic quantum numbers $J^{PC} = 1^{-+}$ have been claimed by various experiments, but there is no common agreement in the community on the resonance interpretation of these signals. Therefore, one aim of this analysis is to investigate this J^{PC} sector in the COMPASS data. The partial-wave decomposition yields a broad bump in the intensity spectrum of the $1^{-+}\,1^+\,\rho(770)\,\pi\,P$ wave, as shown in figure 5.24d. The nature of the spike at around $1.1\,\mathrm{GeV}/c^2$ is unclear. It is not related to any phase motion and its shape and strength shows a clear dependence on the used PWA model [30]. This structure has also been observed by other experiments in $\pi^- + p \to \pi^-\pi^-\pi^+ + p_{\mathrm{recoil}}$ scattering [11]. Therefore it is believed to be a model artifact. Looking into the different t' regions, the shape of the spectrum changes completely. In the low-t' region (see figure 5.24a) the intensity reveals a broad enhancement from 1.0 to $1.8\,\mathrm{GeV}/c^2$. Whereas, going to higher t', as shown in figure 5.24b, the low-mass part vanishes and a more peak-like structure occurs at around $1.6\,\mathrm{GeV}/c^2$. In the highest t' bin, the low-mass intensity has completely vanished except a little bump around $1.1\,\mathrm{GeV}/c^2$ (see figure 5.24c).

The resonance-model fit describes the intensity spectra and its variations with t', using a possible resonant component, the $\pi_1(1600)$ at a mass of $m_{\pi_1(1600)} = 1600\,\mathrm{MeV}/c^2$ and a width of $\Gamma_{\pi_1(1600)} = 600\,\mathrm{MeV}/c^2$, plus a non-resonant term. Only the spike around $1.1\,\mathrm{GeV}/c^2$ is ignored by the fit, which supports the assumption of a model artifact. In the low-t' region, almost all of the broad structure is described by the non-resonant term (green). The picture changes going to higher t', where the main contribution to the intensity is assigned to the $\pi_1(1600)$. For the t'-summed intensity, resonant and non-resonant contributions are of the same order of magnitude, like in the $1^{++}\,0^+\,\rho(770)\,\pi\,S$ wave. However, in contrast to the 1^{++} wave, the relative contributions of the different components vary strongly with t' in the spin-exotic $1^{-+}\,1^+\,\rho(770)\,\pi\,P$ wave. The relative phases of the 1^{-+} wave w.r.t. the $1^{++}\,0^+\,\rho(770)\,\pi\,S$ and $0^{-+}\,0^+\,f_0(980)\,\pi\,S$ waves are shown in figures 5.25a and 5.25b. Both phases are slowly rising with $m_{3\pi}$ around $1.6\,\mathrm{GeV}/c^2$. The phase w.r.t. the 1^{++} wave increases by approximately 90°, while the phase relative to the 0^{-+} wave shows a less rapid phase motion of only 60°. This could be explained by the overlap with the low-mass tail of the $\pi(1800)$ resonance in the 0^{-+} wave, which enters with a negative sign. The phase motions in the different t' bins are described with the used resonance model.

To investigate whether the observed spectra are in agreement with a pure non-resonant contribution or whether the $\pi_1(1600)$ component is needed to describe them, study (W) without the resonant component in the spin-exotic wave has been performed. The result has a χ^2 worse by 50 000 units, mainly from increased deviations in the $1^{-+}\,1^+\,\rho(770)\,\pi\,P$ terms. The shape of the

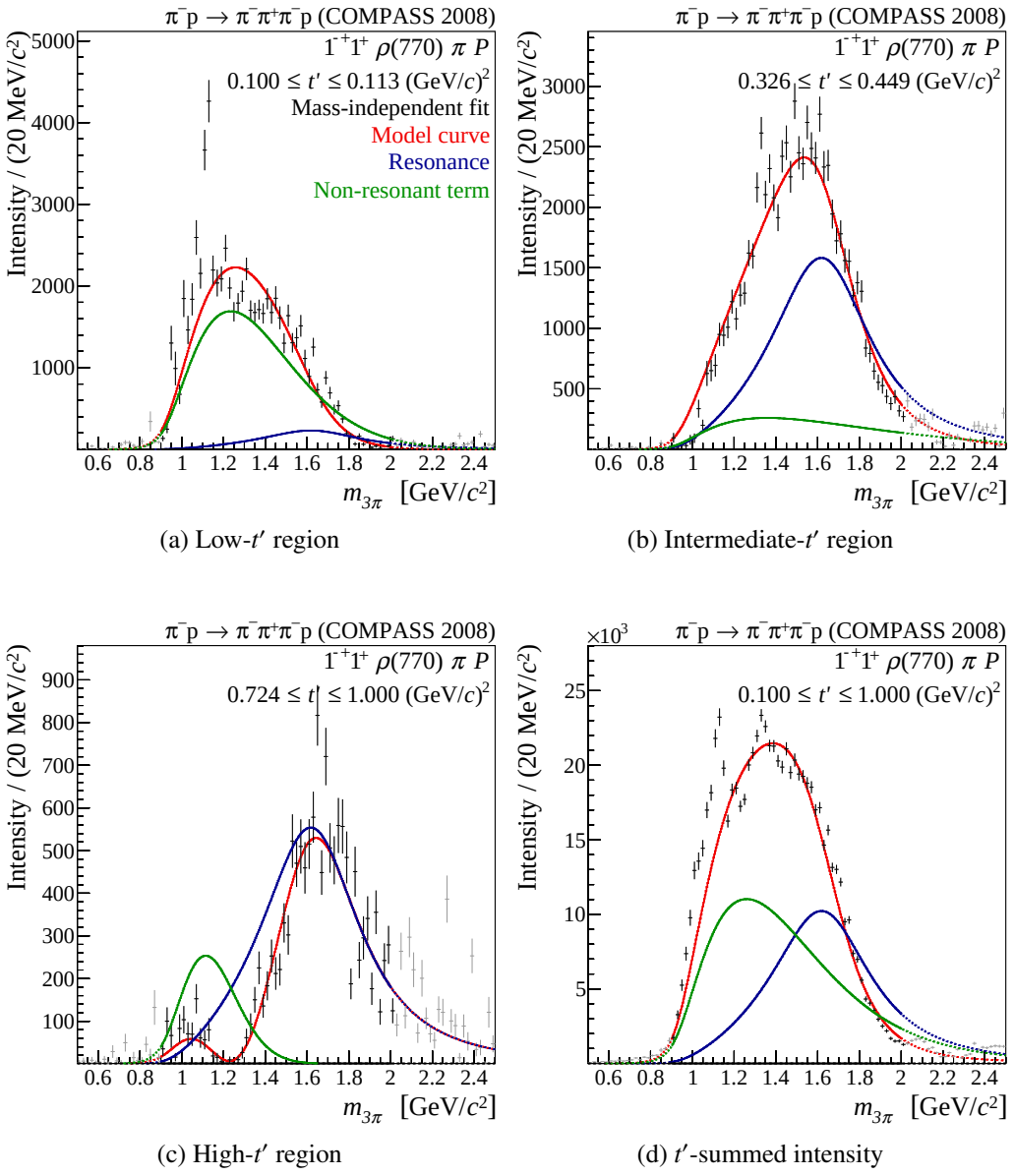

(a) Low-t' region

(b) Intermediate-t' region

(c) High-t' region

(d) t'-summed intensity

Figure 5.24: Intensities of the $1^{-+}\,1^{+}\,\rho(770)\,\pi\,P$ wave in three t' bins and the t'-summed intensity.

intensity spectrum (see figure 5.26a) is roughly reproduced by the pure non-resonant contribution (orange). The same holds for the phase motion in the low-t' region. However, in the high-t' region (see figure 5.26b), omitting the $\pi_1(1600)$ resonance leads to a lack of phase-motion and the fit (violet) is not able to describe the data. This study illustrates, that the $1^{-+}\,1^{+}\,\rho(770)\,\pi\,P$ amplitude can only be described with some additional phase motion, as the parameterization for the non-resonant contributions in the resonance model has a phase that is independent of $m_{3\pi}$. Whether this phase motion arises from a resonant contribution, or if the non-resonant term has to include an intrinsic phase motion cannot be judged from this study. Especially the peaky shape of the non-resonant term has to be related with some phase motion, if one requires analyticity for the partial-wave amplitude [31].

As the nature of the spike around $1.1\,\mathrm{GeV}/c^2$ is unclear, study (Y) has been performed where the lower limit of the 1^{-+} fit range was increased from 0.9 to $1.4\,\mathrm{GeV}/c^2$. The obtained resonance parameters are summarized in figure 5.27. Reducing the fit range slightly shifts the $\pi_1(1600)$ parameters and makes it $80\,\mathrm{MeV}/c^2$ heavier and $20\,\mathrm{MeV}/c^2$ narrower. All other resonance parameters are stable, except those of a_1 resonances. The 1^{++} waves show a similar behavior as in study (D) without 2^{++} wave (see section 5.4), where most of the intensity in the $1^{++}\,0^{+}$ $\rho(770)\,\pi\,S$ wave is assigned to the non-resonant term and the $a_1(1260)$ becomes narrower. In agreement with the previous observations, this study shows a second solution, similar to the Main solution, but with the same width of the $\pi_1(1600)$ resonance as in study (Y). It can be concluded, that the spike at $1.1\,\mathrm{GeV}/c^2$ has no major impact on the $\pi_1(1600)$ parameters.

Due to the lack of detailed knowledge about the different decay modes of a possible $\pi_1(1600)$ resonance and their branchings, a relativistic Breit-Wigner with a fixed width is used to parameterize the $\pi_1(1600)$ component (see section 4.2). However, as the extracted $\pi_1(1600)$ resonance is broad, the change of the decay width over the width of the resonance may not be negligible. Therefore, in study (AC), the $\rho(770)\,\pi\,P$ decay phase-space has been considered in the dynamic width of the resonance, according to equation (5.3).

$$\Gamma_{\pi_1(1600)}(m_{3\pi}) = \Gamma_0 \frac{m_{\pi_1}}{m_{3\pi}} \frac{q_{\rho\pi}(m_{3\pi}) F_P^2\left(q_{\rho\pi}(m_{3\pi})\right)}{q_{\rho\pi}(m_{\pi_1}) F_P^2\left(q_{\rho\pi}(m_{\pi_1})\right)} \tag{5.3}$$

The result of this study shows a slightly heavier $\pi_1(1600)$ with $m_{\pi_1(1600)} = 1.65\,\mathrm{GeV}/c^2$ and a width of $\Gamma_{\pi_1(1600)} = 0.58\,\mathrm{GeV}/c^2$. Considering the $\rho(770)\,\pi\,P$ decay mode in the dynamic width does not change the interpretation of the $1^{-+}\,1^{+}\,\rho(770)\,\pi\,P$ wave in the resonance-model fit. As the dynamic-width parameters are not directly comparable with the fixed-width parameters, this study is not considered for the systematic uncertainty of the parameters.

The resonance model consistently describes the data. To conclude on the obtained resonance parameters, a detailed review of the systematic effects will be given in the following chapter.

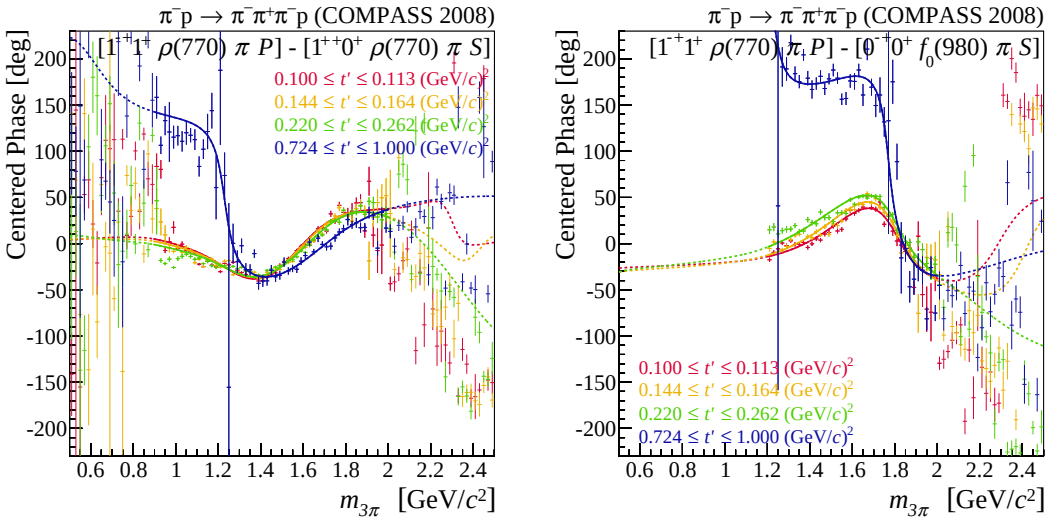

(a) Phases w.r.t. $1^{++}\,0^{+}\,\rho(770)\,\pi\,S$ wave (b) Phases w.r.t. $0^{-+}\,0^{+}\,f_0(980)\,\pi\,S$ wave

Figure 5.25: Phase motion of the $1^{-+}\,1^{+}\,\rho(770)\,\pi\,P$ wave w.r.t. the $1^{++}\,0^{+}\,\rho(770)\,\pi\,S$ and $0^{-+}\,0^{+}\,f_0(980)\,\pi\,S$ wave in four t' bins.

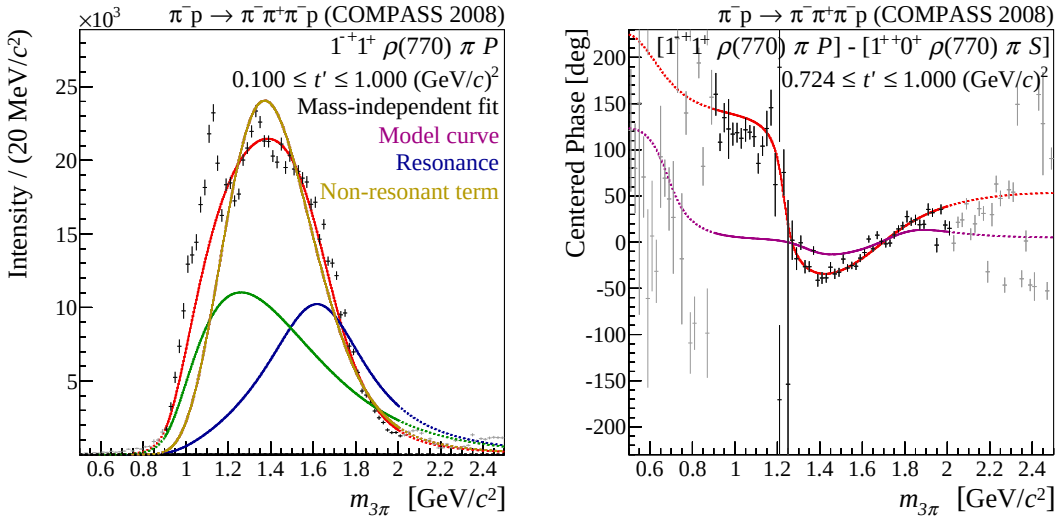

(a) Intensity (b) Phase

Figure 5.26: Intensity and phase of the spin-exotic $1^{-+}\,1^{+}\,\rho(770)\,\pi\,P$ wave w.r.t. the $1^{++}\,0^{+}\,\rho(770)\,\pi\,S$ wave obtained from study (W) without the $\pi_1(1600)$ resonance (violet/cyan/orange) compared to the Main fit (red/blue/green).

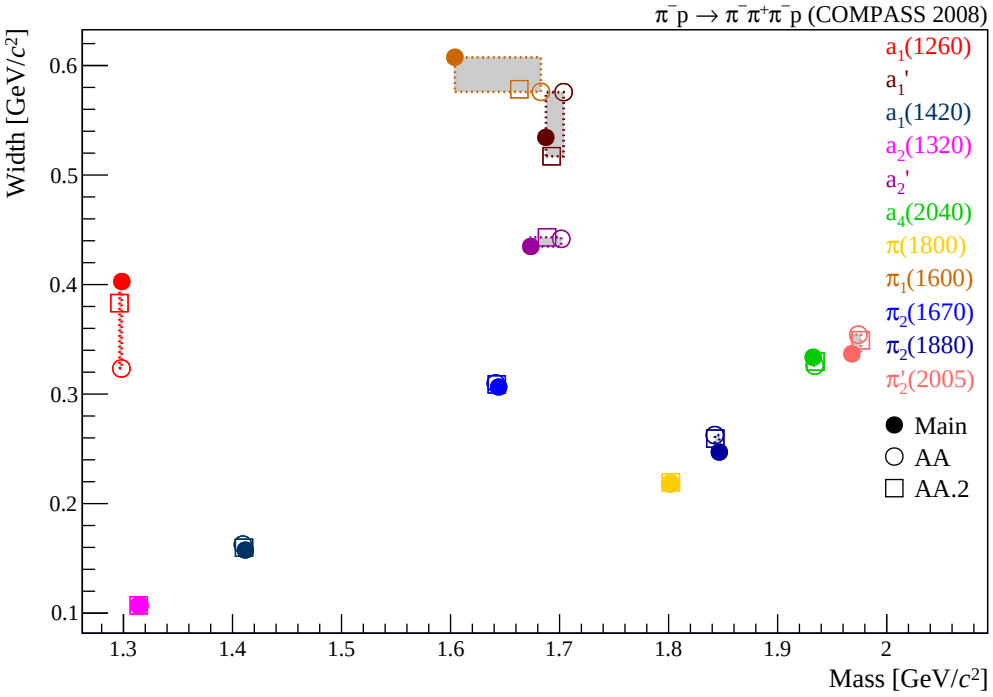

Figure 5.27: Resonance parameters obtained from the study with reduced $1^{-+}\,1^+\,\rho(770)\,\pi\,P$ fit-range (open circles). The full circles are the Main solution, the rectangles show the results of a further solution of this study with worse χ^2.

CHAPTER 6

Resonance Parameters

The main goal of the resonance-model fit is to extract the masses and widths of the resonances, included in the fit model. The previous chapter discussed the description of the partial-wave amplitudes by the resonance model, which was introduced in section 4.2. Thereby some systematic effects, influencing the different waves, were already discussed. In this chapter, this discussion will be extended by considering more general studies that address certain aspects of fit model and method. This is followed by a summary of the systematic uncertainties of the various resonance parameters. Finally, a comparison with previous measurements will be given.

The parameters of the various resonance components of the fit model show different systematic uncertainties. While some are very robust against systematic effects, like e.g. the $a_2(1320)$, the $a_4(2040)$, the $\pi(1800)$ or the $\pi_2(1670)$, the systematic error of others shows significant variation across the systematic studies. The spin exotic $\pi_1(1600)$ resonance shows large systematic uncertainties in its parameters, especially in its width. A strong correlation with the $a_1(1260)$ resonance parameters is observed. Except for the π_2 and $a_1(1420)$ resonances, using an established Deck model as parameterization for the non-resonant terms instead of the phenomenological parameterization in equation (4.2) yields results, consistent with the Main fit. Especially in the $1^{++}\,0^+\,\rho(770)\,\pi\,S$ and $1^{-+}\,1^+\,\rho(770)\,\pi\,P$ wave, in which a large non-resonant contribution is observed, the Deck MC describes the spectra remarkably well. A further systematic study reveals, that the choice of the χ^2 definition has an impact on the fit result, which is an indication for tensions within the resonance model.

6.1 Systematic Studies

In addition to the extraction of resonance parameter values, a proper determination of their uncertainties is very important. Due to the very large size of the used data set, the statistical uncertainties of the resonance parameters are more than one order of magnitude smaller than the systematic ones. Furthermore, the systemic studies, already discussed in chapter 5 show, that the obtained results are model dependent. A fair estimate of the systematic uncertainties is one of

the main goals of this analysis. To this end, in total more than 200 studies have been performed. Some of them have been introduced during the development of the resonance model, others to investigate certain systematic effects in detail. Finally, a set of 29 studies which cover all observed systematic effects, has been selected to be discussed here. Studies which do not describe the data or with clearly unphysical fit results are not included into the definition of the systematic uncertainties. Before defining the systematic uncertainties of the resonance parameters, a number of further systematic effects will be discussed.

6.1.1 Looser Cuts in the Event Selection

The first step towards a partial-wave analysis is the event selection. Various cuts are applied to select the process of interest, in this case the diffractive production of a charged three-pion final state (see section 2.2). To investigate the influence of these cuts on the extracted resonance parameters, study (K) has been performed where the following cuts are omitted. No cuts on the particle identification in the initial (CEDAR) and final (RICH) state are applied and the cuts to veto central production are omitted. This increases the contaminations, from central production, kaon diffraction or reactions with two kaons in the final state. Furthermore, the coplanarity cut and the requirement of exactly one reconstructed track in the RPD are taken out of the event selection, which increases the number of non-exclusive events (compare open and filled histogram in figure 2.2a). Based on this looser event selection, a partial-wave decomposition is performed, whose outcome is fitted with the Main resonance model. The results are shown in figure 6.2. Except for the a_1' and $\pi_1(1600)$, the extracted resonance parameters are in good agreement with the more restrictive event selection of the Main fit. The partial-wave intensities typically increase proportional to the total number of events. However, the description of this increase by the resonance-model fit differs from wave to wave. For example, in the 4^{++} waves (see figure 6.1c), the intensity of the resonant $a_4(2040)$ component scales with the total intensity. The same is observed for the intensity of the $a_2(1320)$ resonance. This is in contrast to the spin-exotic $1^{-+}\,1^{+}\,\rho(770)\,\pi\,P$ wave, which shows an increase only in the non-resonant contribution. Also the $\pi_1(1600)$ parameters shift. It becomes $0.12\,\mathrm{GeV}/c^2$ narrower and slightly heavier. In the lowest t' bin of the $1^{++}\,0^{+}\,\rho(770)\,\pi\,S$ wave, shown in figure 6.1a, the contribution of the $a_1(1260)$ resonance does not significantly increase (compare blue vs. cyan curve), while the non-resonant term (green vs. orange curve) gains in intensity. In contrast, at higher t', also the resonant contributions gain in intensity as shown in figure 6.1b.

The different effects in the partial waves when relaxing the event-selection cuts, are a hint for an imperfect separation between resonant and non-resonant components. Except for the a_1 parameters, the deviations from the Main solution are smaller than that of other systematic effects.

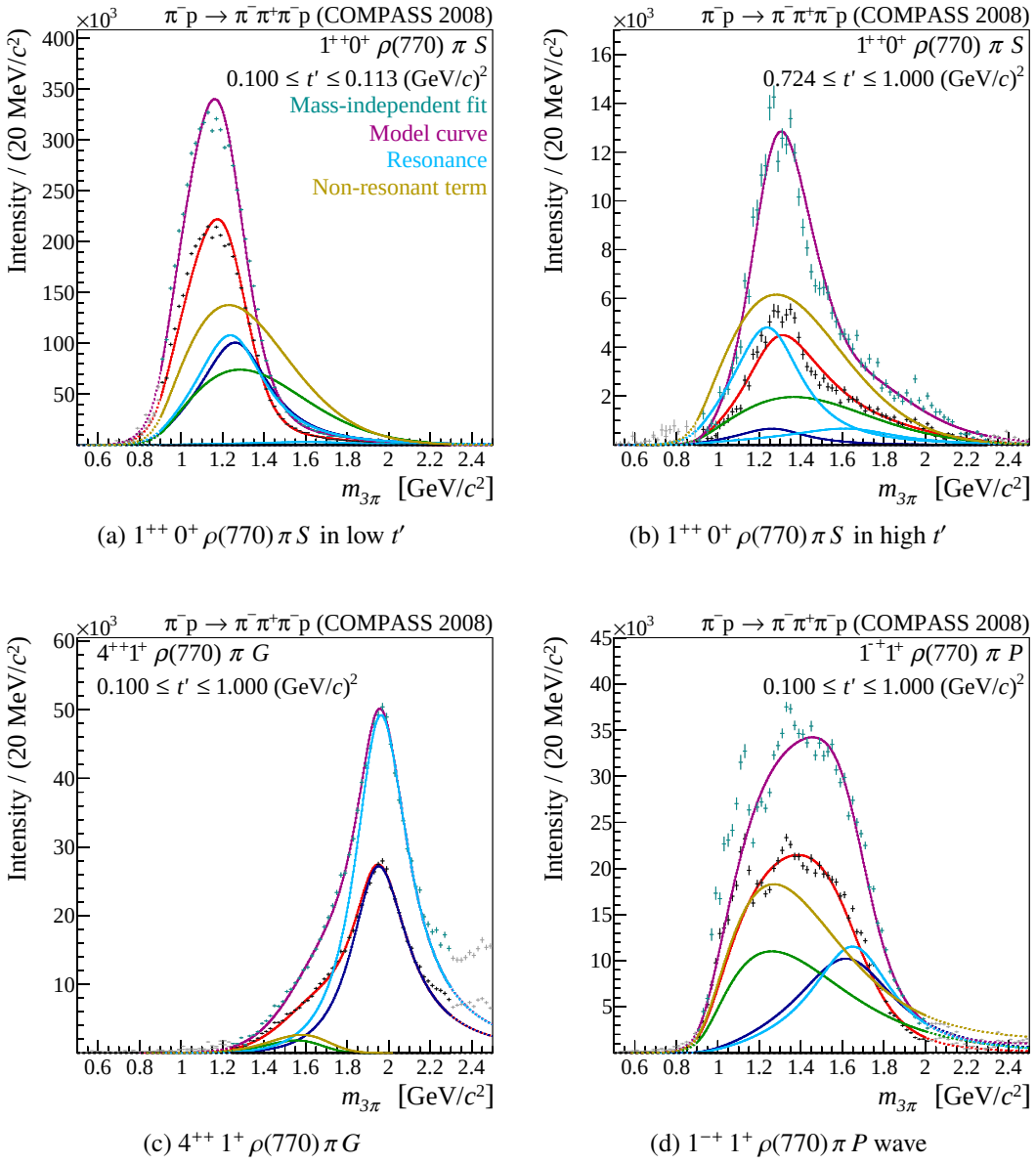

(a) $1^{++}\ 0^+\ \rho(770)\,\pi\,S$ in low t'

(b) $1^{++}\ 0^+\ \rho(770)\,\pi\,S$ in high t'

(c) $4^{++}\ 1^+\ \rho(770)\,\pi\,G$

(d) $1^{-+}\ 1^+\ \rho(770)\,\pi\,P$ wave

Figure 6.1: Fit results of study (K) using a looser event selection (teal data points and violet/cyan/orange curves) compared to the Main solution (black data points and red/blue/green curves) for the low and high t' region of the $1^{++}\ 0^+\ \rho(770)\,\pi\,S$ wave (top) and the t'-summed intensities of the $4^{++}\ 1^+\ \rho(770)\,\pi\,G$ and $1^{-+}\ 1^+\ \rho(770)\,\pi\,P$ wave.

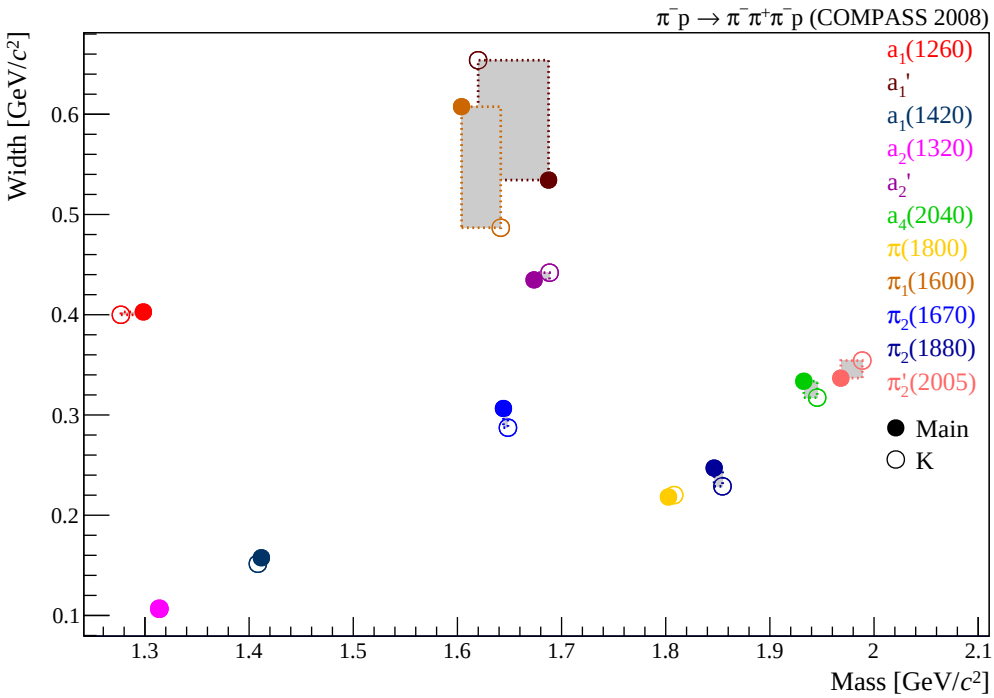

Figure 6.2: Resonance parameters obtained from study (K) with looser cuts in the event selection (open circles), compared to the Main solution (full circles).

6.1.2 Coarser t' Binning

The next step after the event selection and before performing the partial-wave decomposition, is the binning of the data. Especially the binning in t' yields important information for the resonance-model fit. To investigate the influence of the t' binning, in study (L) the data were subdivided in to 8 instead of 11 t' bins. The binning has been chosen to be the same as used for the analysis of the neutral three-pion final state $\pi^-\pi^0\pi^0$ (see section 8.2 or [32]). The obtained resonance parameters of this coarser t' binning (open circles) are compared with the Main solution (full circles) in figure 6.3. The only significant deviation is observed for the $\pi_1(1600)$, which becomes 70 MeV/c^2 heavier and 40 MeV/c^2 narrower. This illustrates again the strong t' dependence of the $1^{-+}\,1^+\,\rho(770)\,\pi\,P$ wave (see section 5.6) and the necessity of performing this analysis in narrow t' bins. The stability of the results indicates, that 11 t' bins are sufficient to account for the various t' dependences.

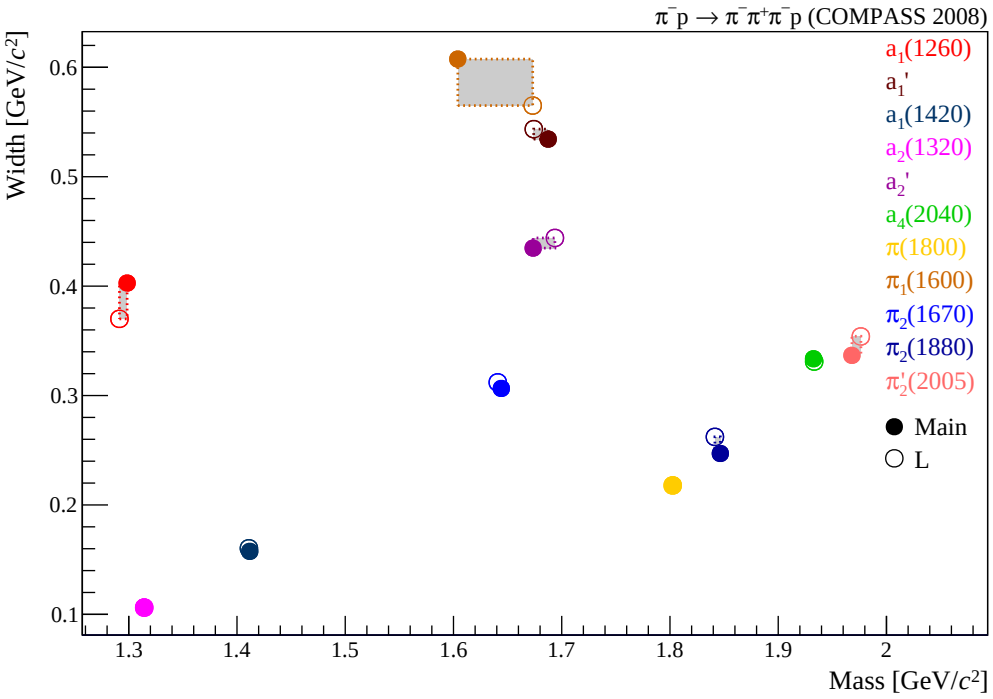

Figure 6.3: Resonance parameters obtained from study (L) with coarser t' binning (open circles), compared to the Main solution (full circles).

6.1.3 Effect of t'-independent relative Branchings

One negative side effect of the t' binning is the large number of coupling parameters in the fit, as each t' bin is described with an independent set of coupling parameters. Under the assumption that only the production process depends on t', different decay modes of the same produced state ($J^{PC}\ M^{\varepsilon}$) should have the same t' dependence. This can be exploited to reduce the number of coupling parameters by replacing the different t'-dependent couplings of different decay modes by one fixed complex-valued branching between them (see section 4.2). To study the influences of this assumption on the resonance parameters and t' distributions, study (T) is performed, where all components have independent couplings for all 11 t' bins. Figure 6.4 shows the results of this study. A clear shift of the $a_1(1260)$ width to a $60\,\mathrm{MeV}/c^2$ smaller value is observed. Also some of the π_2 parameters are affected. The $\pi_2'(2005)$ becomes $60\,\mathrm{MeV}/c^2$ narrower and the $\pi_2(1880)$ broader, which shows that the parameters of both resonances are correlated. The $\pi_2(1670)$, however, remains approximately the same. Even if the $\pi_1(1600)$ component has no relative branchings, its width is lowered by $85\,\mathrm{MeV}/c^2$ due to the interference with other waves. The variations of the other resonance parameters are small compared to their total systematic uncertainty and reflect the imperfection of the resonance model. Therefore, the physics condition of branchings is needed, not only to reduce the number of parameters, but also to stabilize the fit, as it is observed in the t' spectra which are discussed in chapter 7.

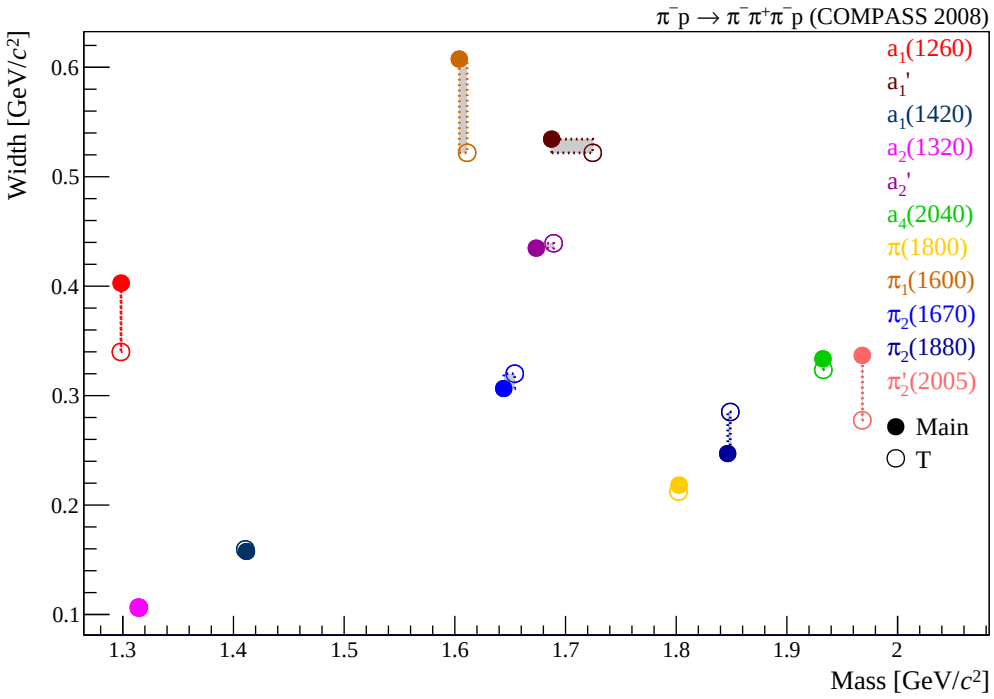

Figure 6.4: Resonance parameters obtained from study (T) without fixed branchings (open circles), compared to the Main solution (full circles).

6.1.4 Influence of the chosen Wave Sub-Set

In section 5.4, the influence of removing the 2^{++} waves in study (D) from the fitted subset of waves has already been discussed. To study the influence of the other partial waves and to reveal possible tensions between them, further fits without the 2^{-+} [study (A)] and 4^{++} [study (C)] waves have been performed. In addition, in study (B) the $1^{++}\,0^{+}\,\rho(770)\,\pi\,S$ and $1^{++}\,0^{+}$ $f_0(980)\,\pi\,P$ waves have been omitted. The results of all these wave set studies are shown in figure 6.5 in comparison to the Main fit. For most of the resonances, no big effects are observed. Apart from the already discussed effects on the $a_1(1260)$ parameters of removing the 2^{++} waves, this studies reveal a tension between the 2^{++} waves and the $\pi_1(1600)$ parameters, because the fit without the 2^{++} waves prefers a much narrower $\pi_1(1600)$. While omitting the 1^{++}, 4^{++} or 2^{++} waves shows a narrowing, removing the 2^{-+} waves leads to a slightly broader and lighter $\pi_1(1600)$. This means that the 1^{++}, 4^{++} and 2^{++} sector prefer a broader $\pi_1(1600)$ shape while the 2^{-+} waves tend to a more narrower structure. This tension within the model results probably from imperfections of the employed parameterizations and confirms the urgency for a proper determination of the systematic uncertainties.

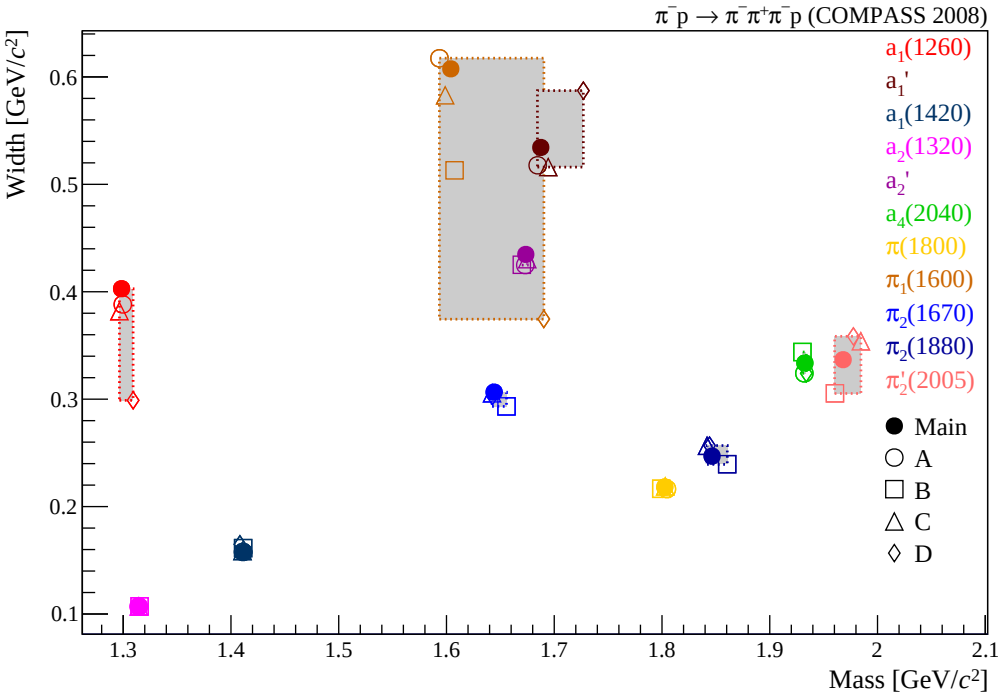

Figure 6.5: Resonance parameters obtained from the studies with different wave sets. Study (A) is a fit without the 2^{-+} waves. A fit without the $1^{++}\,0^{+}\,\rho(770)\,\pi\,S$ and $1^{++}\,0^{+}\,f_2(1270)\,\pi\,P$ waves has been performed in study (B). In study (C) the 4^{++} waves have been omitted and study (D) is the fit without the 2^{++} waves.

6.1.5 Non-Resonant Term from Deck Monte Carlo

In addition to the wave set, the parameterization of the various components is a crucial part of the resonance model. Especially the model used for the non-resonant contributions (see section 4.1) may introduce systematic uncertainties in waves where this contribution becomes significant, like the $1^{++}\,0^{+}\,\rho(770)\,\pi\,S$ or the $1^{-+}\,1^{+}\,\rho(770)\,\pi\,P$ wave. It is not fully clear, which processes are responsible for the non-resonant component in the three-pion spectra. However, the main contribution is believed to originate from Deck-like processes, introduced in section 1.2.2. An alternative description for the non-resonant terms was developed by using a model for the Deck amplitude. However, there is no unique parameterization of the Deck process. Following [33], the Deck process can be modeled as the dissociation of the incoming pion into a two-pion resonance, e.g. $\rho(770)$, and a virtual pion, where the virtual pion scatters from the target proton.

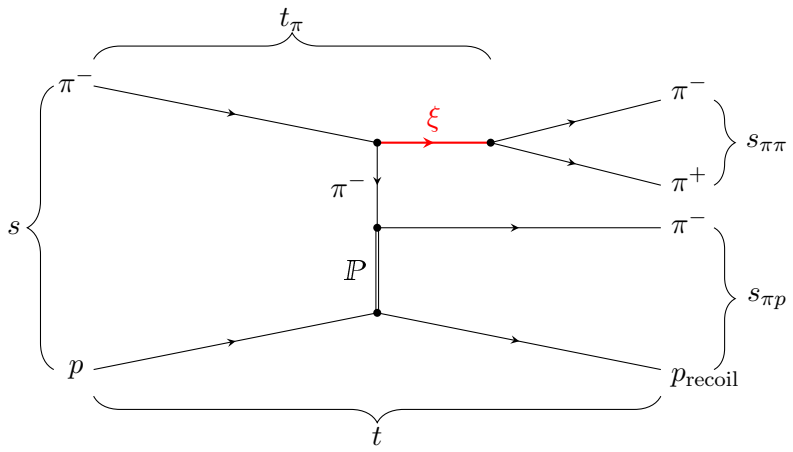

Figure 6.6: Deck-like process.

In this picture, the amplitude can be parameterized as

$$\mathcal{A}(s_{\pi\pi}, t_\pi, t) = \frac{\mathcal{A}_{\pi\pi}(s_{\pi\pi}, t_\pi) \cdot \mathcal{A}_{\pi p}(s_{\pi p}, t)}{m_\pi^2 - t_\pi} \tag{6.1}$$

using the $\pi\pi$ scattering amplitude $\mathcal{A}_{\pi\pi}$ to describe the dissociation $\xi \to \pi^+\pi^-$ and the elastic πp scattering amplitude

$$\mathcal{A}_{\pi p}(s_{\pi p}, t) = i s_{\pi p} \sigma_t e^{at} \tag{6.2}$$

together with the pion propagator. In order to account for more recent findings, other parameters than in [33] have been used, as described in [1]. For the total $\pi^- p$ cross section $\sigma_t = 64\,\text{GeV}^{-2}$ is used and the slope parameter is set to $a = 8\,(\text{GeV}/c)^{-2}$. In order to describe the observed t dependence around $m_{3\pi} = 1\,\text{GeV}/c^2$, an additional exponential factor $e^{b(t_\pi - m_\pi^2)}$ with $b = 0.45\,(\text{GeV}/c)^{-2}$ was introduced. The $\pi\pi$ scattering amplitude is taken from [34], which

includes the dominant isobars of the partial-wave decomposition model [$[\pi\pi]_S$, $\rho(770)$, $f_0(980)$, $f_2(1270)$ and $\rho_3(1690)$]. With this Deck amplitude, a set of 10^8 Monte Carlo (MC) events has been generated. In order to calculate the projections of the Deck amplitude into the different partial waves, the Deck MC events have been partial-wave decomposed using the same wave set and method as for the data (see chapter 3). In each wave, the square-root of the Deck MC intensity is used to describe the shape of the non-resonant contribution. Still, this shape is multiplied with a complex-valued coupling constant, for each t' bin, such that the fit can adapt the strength and t'-dependent phase of the non resonant component in each partial wave. However, as in the Main fit, the phase of the non-resonant term is assumed to be constant.

Using this parameterization for all non-resonant terms, a resonance-model fit has been performed in study (O). The obtained resonance parameters are compared to the Main fit in figure 6.7. The largest impact is observed on the π_2 parameters. The $\pi_2'(2005)$ becomes extremely broad and hits the upper width limit of $1\,\mathrm{GeV}/c^2$. By making the $\pi_2'(2005)$ this broad, the fit essentially flattens the $\pi_2'(2005)$ phase motion and misuses it as a non-resonant term. As an example, this is shown in figure 6.8a for the intensity of the $2^{-+}\,0^+\,\rho(770)\,\pi\,F$ wave in the high t' region. One clearly finds the $\pi_2'(2005)$ component extended over the full mass range, destructively interfering with the other resonances which appears to be unphysical. The non-resonant term, parameterized using the Deck MC, is not used at all by the fit. The reason for this behavior is, that the Deck MC does not match well with the experimentally observed spectrum (see figure 6.8b). Therefore, the fit omits this term and misuses the $\pi_2'(2005)$ as the non-resonant contribution without achieving a good description of this partial-wave intensities. Although the $f_2(1270)$ isobar is included in the Deck model, the Deck intensity distribution in partial waves with $f_2(1270)$ isobar does not agree well with the data. This shows the need for a further improvement of the Deck model. Finally, this effects also the $\pi_2(1670)$ and $\pi_2(1880)$ resonances which both become broader. The a_2' additionally becomes lighter. To prevent this unphysical behavior, study (P) was performed, where the $\pi_2'(2005)$ resonance was removed from the 2^{-+} waves in addition to using the Deck MC as parameterization for the non-resonant terms. The results are shown as rectangles in figure 6.7 and are in good agreement with the previous study for the non-π_2 parameters. The $\pi_2(1880)$ parameters show a shift to larger widths w.r.t. the Main solution, which is similar to study (U) in which the $\pi_2'(2005)$ was also left out (see section 5.3). Using the Deck MC as non-resonant parameterization, the $\pi_2(1670)$ parameters are in good agreement with the Main fit.

A significant impact of the parameterization of the non-resonant terms is also observed for the $a_1(1420)$, which becomes $40\,\mathrm{MeV}/c^2$ narrower. Similar to the situation in the 2^{-+} waves, the Deck MC in waves with $f_0(980)$ isobar is in disagreement with the observed data. In the $1^{++}\,0^+$ $f_0(980)\,\pi\,P$ wave (see figure 6.9) the Deck MC shows a broad enhancement (orange) starting at $1.2\,\mathrm{GeV}/c^2$ and extending beyond the mass range included in the fit. This shape is neither consistent with the observed intensity spectra nor with the non-resonant shape from the Main fit (green). As this obviously unrealistic parameterization of the non-resonant term biases the $a_1(1420)$ parameters, the Deck MC study is not considered in their systematic uncertainties.

Since the $1^{++}\,0^+\,\rho(770)\,\pi\,S$ wave has significant contributions from non-resonant processes, the influence of their parameterization on the description of this wave is expected to be large. However, the obtained $a_1(1260)$ parameters are in good agreement with the Main fit. The a_1'

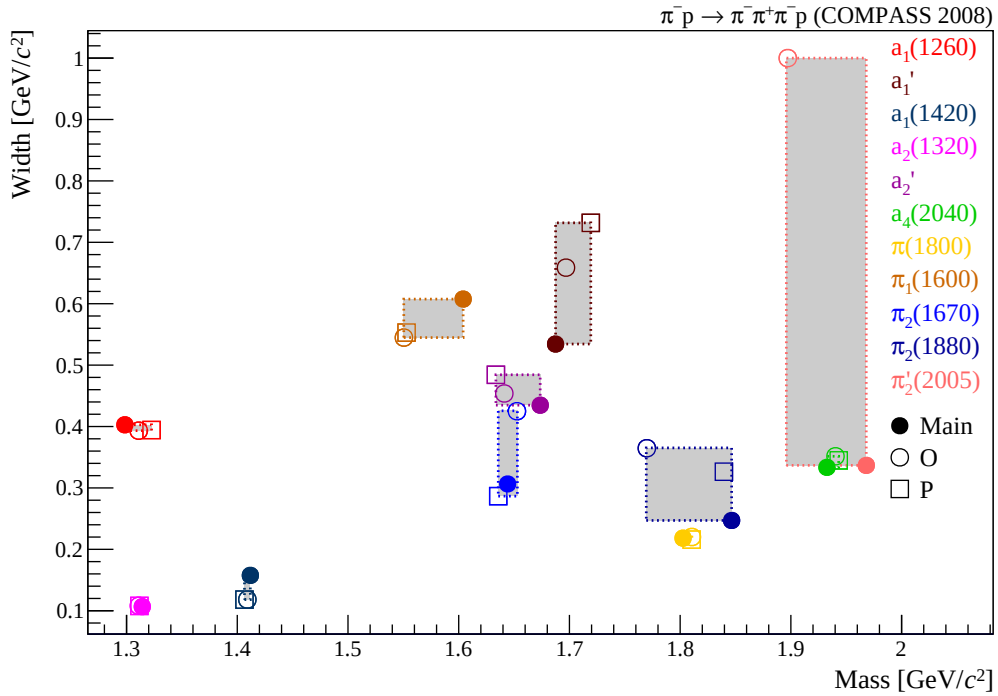

Figure 6.7: Resonance parameters obtained from study (O) using partial-wave projections of the Deck MC as non-resonant terms. Study (P) additionally omits the $\pi_2'(2005)$ resonance in order to avoid the observed instabilities. The reader should note the larger scale of the vertical axis to visualize the large width of the $\pi_2'(2005)$.

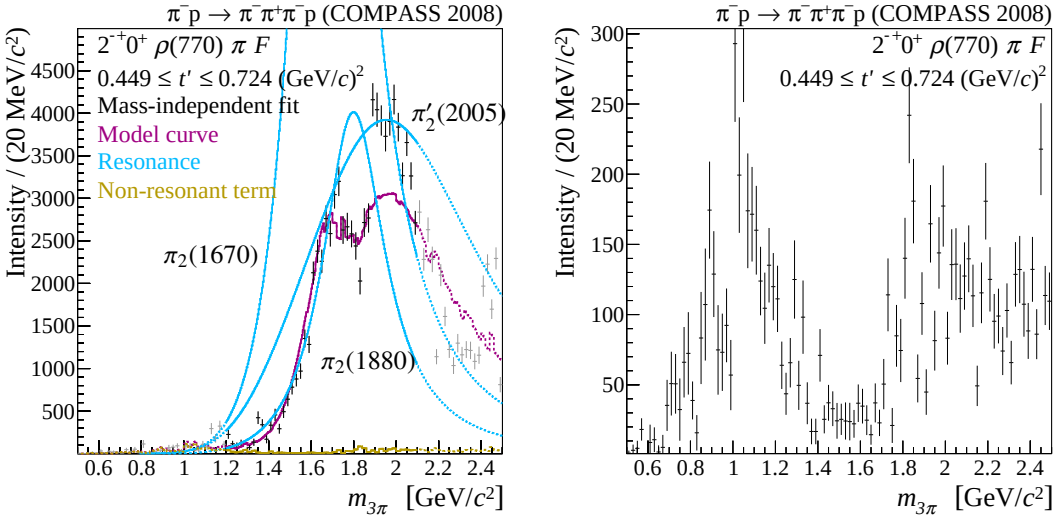

(a) Result of study (O)

(b) Partial-wave projection of Deck MC

Figure 6.8: Fit result of study (O) using the partial-wave projection of the Deck MC as parameterization for the non-resonant term in the $2^{-+}\,0^+\,\rho(770)\,\pi\,F$ wave in the high t' region (left). The orange histogram in the left plot and the right plot show the intensity of the Deck MC in this wave.

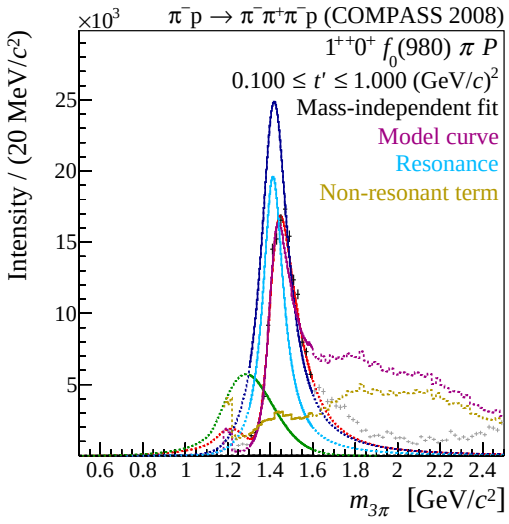

Figure 6.9: The fit result of study (O) using the Deck MC as parameterization for the non-resonant term (see figure 6.8) in the $1^{++}\,0^{+}\,f_0(980)\,\pi\,P$ wave.

becomes $120\,\mathrm{MeV}/c^2$ broader. The intensity spectra are shown in figure 6.10a. The shape of the Deck MC (orange) is similar to the result from the Main fit (green). The maximum is approximately at the same position but the two intensity distributions deviate in their high-mass tails. Especially in the high-t' region, shown in figure 6.10b, the fit assigns much less intensity to the non-resonant term in study (O) and is now able to describe the narrow peak, however with the same $a_1(1260)$ parameters as in the Main fit.

Also in the spin-exotic $1^{-+}\,1^{+}\,\rho(770)\,\pi\,P$ wave, a major contribution of the non-resonant term is found. The Deck MC and the non-resonant term obtained from the Main fit have a remarkably similar shape (see figure 6.11a). Using the Deck MC, the intensity of the non-resonant term is slightly reduced, while that of the $\pi_1(1600)$ component increases. Compare to the systematic uncertainties the $\pi_1(1600)$ parameters change only slightly. It becomes $50\,\mathrm{MeV}/c^2$ lighter and $60\,\mathrm{MeV}/c^2$ narrower. Furthermore, the high-mass part of the phases is better described using the Deck MC as non-resonant parameterization, as illustrated in figure 6.11b for the relative phase between the $1^{-+}\,1^{+}\,\rho(770)\,\pi\,P$ wave and the dominant 1^{++} wave.

Using the Deck model as non-resonant parameterization offers a great possibility to test the influence of the non-resonant parameterization on the resonance parameters. Especially the $a_1(1260)$ resonance shows stable characteristics despite the large non-resonant contribution to the 1^{++} waves.

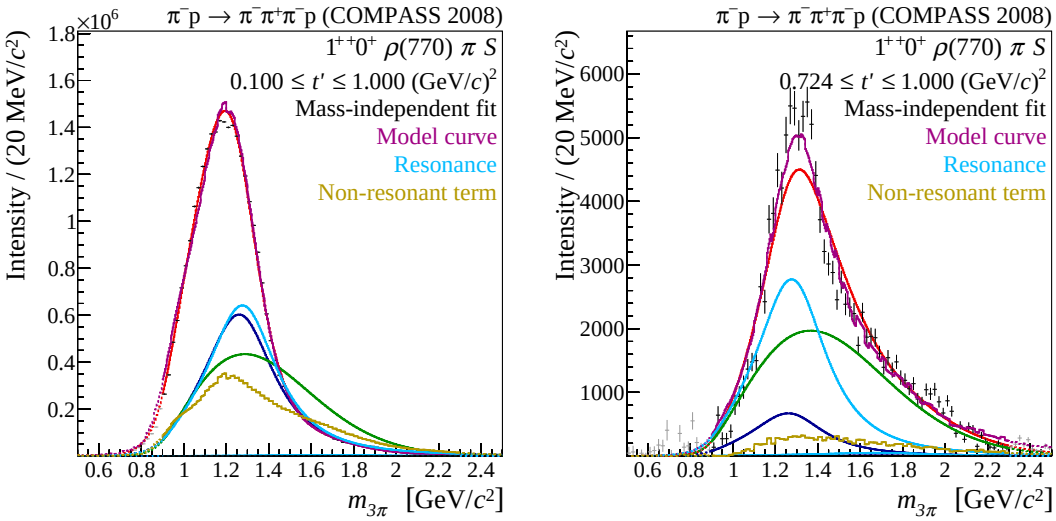

(a) t'-summed intensity (b) High-t' region

Figure 6.10: Fit result of study (O) (violet/cyan/orange) using the Deck MC as parameterization for the non-resonant term (see figure 6.8), compared to the Main fit (red/blue/green) in the $1^{++}\,0^+\,\rho(770)\,\pi\,S$ wave for all t' bins (left) and in the highest t' bin (right).

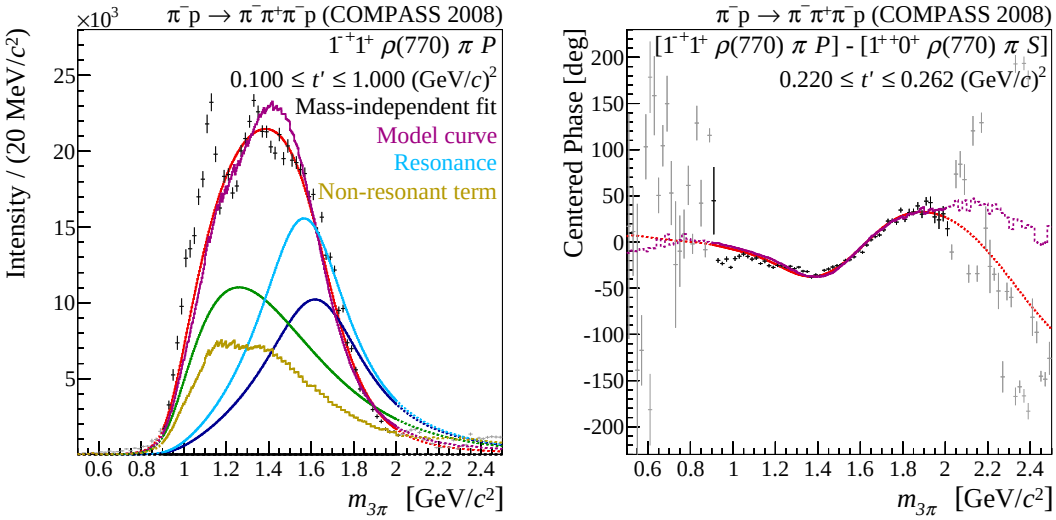

(a) t'-summed intensity (b) Relative phase w.r.t. $1^{++}\,0^+\,\rho(770)\,\pi\,S$ wave

Figure 6.11: The fit result of study (O) using the Deck MC as parameterization for the non-resonant term (see figure 6.8) in the $1^{-+}\,1^+\,\rho(770)\,\pi\,P$ wave.

6.1.6 Influence of the χ^2-Definition

The χ^2 definition used in the resonance-model fit is not unique. In the Main fit, the χ^2 measures the deviation of the description of all spin-density matrix elements ${}^{\mathrm{RM}}\rho_{\alpha\beta} = {}^{\mathrm{RM}}\mathcal{T}_{\alpha}\,{}^{\mathrm{RM}}\mathcal{T}^{*}_{\beta}$ by the resonance model from the data (see equation (4.13)). Therefore, in each mass and t' bin, the fit minimizes the distance to N^2_{waves} data points[1]. However, the result of the mass-independent fit are the transition amplitudes, which give $2N_{\mathrm{waves}} - 1$[2] independent data points per mass and t' bin. This clearly shows that there are mathematical correlations between the spin-density matrix elements, which are ignored in the standard χ^2 definition. Furthermore, also the transition amplitudes among themselves are correlated, which is encoded in the covariance matrix $C_{\zeta\kappa}$ of the mass-independent fit. Also this information is not used in the χ^2 formulation used in the Main fit. Neglecting these correlations between the data points in the standard χ^2 definition, means that the obtained χ^2 value does not strictly follow the χ^2 distribution in a T-statistical sens. Therefore, it is neither expected to be centered around the number of degrees of freedom (Ndf) nor is its deviation from Ndf a quantitative goodness-of-fit criterion. However, it will be shown below, that the χ^2 is in qualitatively agreement with formulations that include the correlations.

To account for this difficulty, other χ^2 definitions have been introduced by [35] and [29]. The first requirement on an alternative χ^2 is to get rid of the artificial increase in the number of data points. The simplest approach is to fit only one row of a specific reference wave of the spin-density matrix ($\rho_{\mathrm{ref}\,\alpha} = \mathcal{T}_{\mathrm{ref}}\mathcal{T}^{*}_{\alpha}$) which contains exactly $2N_{\mathrm{waves}} - 1$ real elements. Thus one row contains the full information of all 14 partial waves of the mass-independent fit. To take into account also the correlations between the transition amplitudes, all amplitudes of one mass and t' bin have to be combined with their real and imaginary parts. This can be represented by the $2N_{\mathrm{waves}}$-dimensional vector

$$\mathcal{T}_{\zeta} = (\mathcal{T}_{1,\Re}, \mathcal{T}_{1,\Im}, \mathcal{T}_{2,\Re}, \mathcal{T}_{2,\Im}, \dots,) \tag{6.3}$$

with the corresponding covariance matrix $C_{\zeta\kappa}$. Since in the first analysis stage, the mass and t' bins are independently fitted, the transition amplitudes of different bins have by definition no correlations. In this formalism, the residuals of the spin-density matrix elements between the resonance model (RM) and the data can be calculated as follows

$$\Delta_{\alpha,\Re} = \Re\left[\mathcal{T}_{\mathrm{ref}}\mathcal{T}^{*}_{\alpha}\right] - \Re\left[{}^{\mathrm{RM}}\mathcal{T}_{\mathrm{ref}}\,{}^{\mathrm{RM}}\mathcal{T}_{\alpha}{}^{*}\right] \tag{6.4}$$

$$\Delta_{\alpha,\Im} = \Im\left[\mathcal{T}_{\mathrm{ref}}\mathcal{T}^{*}_{\alpha}\right] - \Im\left[{}^{\mathrm{RM}}\mathcal{T}_{\mathrm{ref}}\,{}^{\mathrm{RM}}\mathcal{T}_{\alpha}{}^{*}\right] \tag{6.5}$$

$$\Delta_{\mathrm{ref}} = |\mathcal{T}_{\mathrm{ref}}|^2 - |{}^{\mathrm{RM}}\mathcal{T}_{\mathrm{ref}}|^2 \tag{6.6}$$

$$\tag{6.7}$$

and collected in a $(2N_{\mathrm{waves}} - 1)$ - dimensional vector

$$\Delta_i = (\Delta_{1,\Re}, \Delta_{1,\Im}, \Delta_{2,\Re}, \Delta_{2,\Im}, \dots, \Delta_{\mathrm{ref}}). \tag{6.8}$$

[1] Partial-wave intensities and real- and imaginary-part of the interference terms.
[2] Real and imaginary part of amplitudes minus one global phase.

Using standard error propagation, the covariance matrix of the production amplitudes $C_{\zeta\kappa}$ can be transformed into the new basis of residuals Δ using the Jacobian matrix of the transformation:

$$J_{i\zeta} = \frac{\partial \Delta_i}{\partial \mathcal{T}_\zeta} \tag{6.9}$$

$$\tilde{C}_{ij} = \sum_{\zeta,\kappa} J_{i\zeta} C_{\zeta\kappa} J_{\kappa j}. \tag{6.10}$$

With this formalism, the χ^2 value is defined via the Mahalanobis distance [36] as

$$\chi^2 = \sum_{t'} \sum_{m_{3\pi}} \sum_{ij} \left[\Delta_i \tilde{C}^{-1}_{ij} \Delta_j \right]_{(m_{3\pi}, t')} . \tag{6.11}$$

This χ^2 definition takes into account all correlations. A further advantage of it is, that all coupling parameters, except the couplings for the reference wave, enter at most quadratically in the χ^2 formula. Thus, the coupling parameters could be determined analytically by calculating the zeros of the first derivatives of χ^2 w.r.t. the couplings, $\partial\chi^2/\partial C$, which are linear functions in the couplings. This feature was not used for this analysis.

To investigate the influence of the χ^2 formulation on the resonance parameters, study (S) has been performed, using the χ^2 definition in equation (6.11). As a reference wave, the $1^{++}\,0^+\,\rho(770)\,\pi\,S$ wave was used, because it is the only wave of all 14 partial waves that can be described over the full mass range of 0.9 to 2.3 GeV/c^2 used in the fit. The resulting resonance parameters are shown in figure 6.12. A significant change in the description of the 1^{++} waves is observed. The $a_1(1260)$ resonance is shifted to a mass of around 1.1 GeV/c^2, while the a_1' parameters have changed to that of the $a_1(1260)$ in the Main fit. This means, that using the alternative χ^2 formulation, the fit needs an a_1 resonance in the low-mass region of the $1^{++}\,0^+\,\rho(770)\,\pi\,S$ wave, instead of an excited a_1'. The $a_1(1260)$ resonance parameters stay almost unchanged, but now described by the a_1' term in the parameterization. Looking into the description of the $1^{++}\,0^+\,\rho(770)\,\pi\,S$ intensity (figure 6.13a), one finds a possible reason of this behavior. The interpretation of the $a_1(1260)$ and the non-resonant component is similar to the Main fit. However, the fit uses now the resonance structure at 1.1 GeV/c^2 to compensate the imperfections in the description of the intensity of this wave. Similar unphysical effects are also observed in other studies. The reason why this occurs with the χ^2 definition of equation (6.11) is, that this formulation is unsymmetrical in the partial waves. The transition amplitude of the reference wave enters in all data points used by the fit, while the amplitudes of the other waves only enter in two per mass and t' bin. Furthermore, the fit is more driven by the intensities as each wave, except the reference wave, contributes to exactly one interference term. Thus, the fit tends to describe the reference wave as good as possible to minimize the χ^2 value. Together with the imperfections of the resonance model, this may lead to unphysical solutions, as observed for study (S). The bad description of the $1^{++}\,0^+\,f_2(1270)\,\pi\,P$ wave, shown in figure 6.13b, further supports this hypothesis. Also the resulting parameters of the other resonances are affected. The $\pi_1(1600)$ becomes 65 MeV/c^2 broader and slightly lighter, resulting in the largest $\pi_1(1600)$ width, observed in all studies that enter the systematic uncertainty. The $a_2(1320)$ width increases by 3.3 MeV/c^2, which determines the upper limit of its systematic error. Using the alternative χ^2 formulation of equation (6.11), the resulting

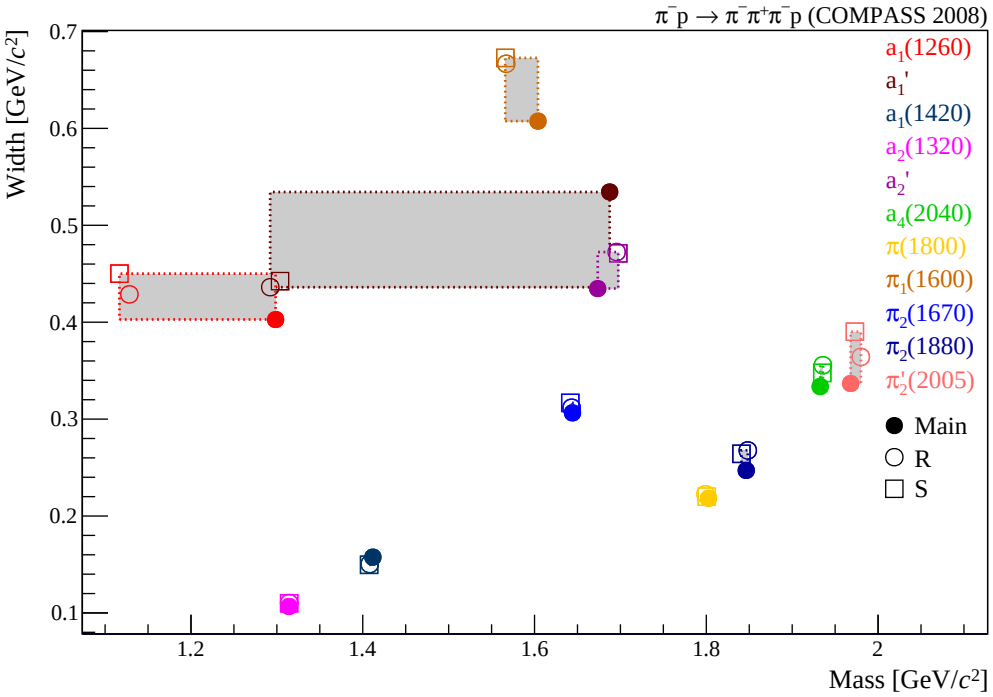

Figure 6.12: Resonance parameters obtained from the fits with a χ^2 formulation that takes into account the correlations of the spin-density matrix elements. In study (S) only one row of the spin-density matrix is used to calculate χ^2 [see equations (6.4) to (6.6)]. In study (R) the deviation between data and resonance-model is directly calculated on the bases of the production amplitudes [see equations (6.13) to (6.15)].

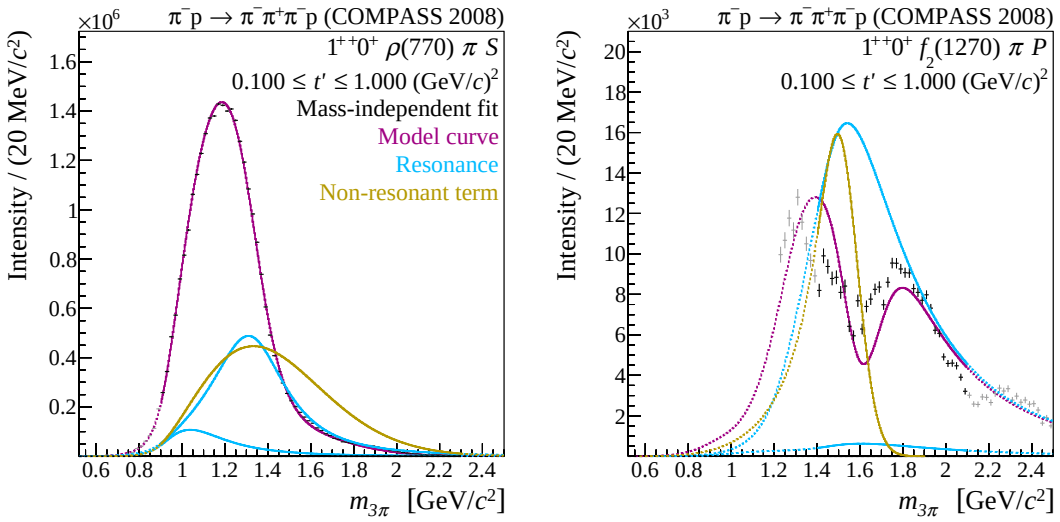

(a) $1^{++}\,0^{+}\,\rho(770)\,\pi\,S$ (b) $1^{++}\,0^{+}\,f_2(1270)\,\pi\,P$

Figure 6.13: The fit result of the 1^{++} waves using the χ^2 formulation of equation (6.11) [study (S)].

χ^2 value is 60 124 units. Together with the decreased number of data points (13 596) and the number of free fit parameters (722), the fit obtains a $\chi^2/\mathrm{Ndf} = 4.7$. This reflects the extremely high statistical precision of the data, due to which even small imperfections in the resonance model lead to a large increase in χ^2. The Main fit obtains a similar $\chi^2/\mathrm{Ndf} = 3.82$. This indicates, that the correlations have no huge influence on interpretation of the obtained χ^2 value.

Another approach for the χ^2 definition is to directly fit the real and imaginary parts of the production amplitudes. In order to get rid of the global phase, again a reference wave has to be selected whose phase is subtracted from all other amplitudes

$$\tilde{\mathcal{T}}^*_\alpha = \mathcal{T}^*_\alpha e^{i\varphi_{\mathrm{ref}}} = \mathcal{T}^*_\alpha \frac{\mathcal{T}_{\mathrm{ref}}}{|\mathcal{T}_{\mathrm{ref}}|} \tag{6.12}$$

using $e^{i\varphi_{\mathrm{ref}}} = \mathcal{T}_{\mathrm{ref}}/|\mathcal{T}_{\mathrm{ref}}|$. Therefore, directly fitting the production amplitudes can be formulated similar to equations (6.4) to (6.6) substituting $\mathcal{T}_{\mathrm{ref}}\mathcal{T}^*_\alpha \to \frac{\mathcal{T}_{\mathrm{ref}}\mathcal{T}^*_\alpha}{|\mathcal{T}_{\mathrm{ref}}|}$

$$\Delta_{\alpha,\Re} = \Re\left[\tilde{\mathcal{T}}^*_\alpha\right] - \Re\left[{}^{\mathrm{RM}}\tilde{\mathcal{T}}^*_\alpha\right] = \Re\left[\frac{\mathcal{T}_{\mathrm{ref}}\mathcal{T}^*_\alpha}{|\mathcal{T}_{\mathrm{ref}}|}\right] - \left[\Re\frac{{}^{\mathrm{RM}}\mathcal{T}_{\mathrm{ref}}\,{}^{\mathrm{RM}}\mathcal{T}_\alpha}{|{}^{\mathrm{RM}}\mathcal{T}_{\mathrm{ref}}|}\right] \tag{6.13}$$

$$\Delta_{\alpha,\Im} = \Im\left[\tilde{\mathcal{T}}^*_\alpha\right] - \Im\left[{}^{\mathrm{RM}}\tilde{\mathcal{T}}^*_\alpha\right] = \Im\left[\frac{\mathcal{T}_{\mathrm{ref}}\mathcal{T}^*_\alpha}{|\mathcal{T}_{\mathrm{ref}}|}\right] - \Im\left[\frac{{}^{\mathrm{RM}}\mathcal{T}_{\mathrm{ref}}\,{}^{\mathrm{RM}}\mathcal{T}_\alpha{}^*}{|{}^{\mathrm{RM}}\mathcal{T}_{\mathrm{ref}}|}\right] \tag{6.14}$$

$$\Delta_{\mathrm{ref}} = |\mathcal{T}_{\mathrm{ref}}| - |{}^{\mathrm{RM}}\mathcal{T}_{\mathrm{ref}}|. \tag{6.15}$$

In contrast to the previously discussed alternative approach, only the phase of the reference wave enters in all residuals but not the intensity. As expected, the obtained resonance parameters using this χ^2 formulation [study (R)] are in good agreement with the results of the previous study as shown in figure 6.12 (rectangles).

The alternative χ^2 definitions have the draw-back of a dedicated reference wave. This seemingly lead to a unphysical description in the partial-waves. Furthermore, recent progress in the mass-independent fit revealed some non-Gaussian correlations between the fitted parameters which break the assumptions of the two alternative χ^2 formulations [37]. On the other hand, the standard χ^2 definition, even if not interpretable in a T-statistical sense, is a perfectly valid measurement of deviation between the data and the resonance model.

6.1.7 Change in Angular-Momentum Barrier Factor

The interaction radius of the centrifugal-barrier potential, entering in the angular-momentum barrier factors (see section 3.2), represents a further source of systematics of the resonance model. To study the influence of this model parameter, two fits have been performed with a slightly decreased value of $R = 0.75\,\mathrm{fm}$ [study (M)] and a marginally enlarged value of $R = 1.29\,\mathrm{fm}$ [study (N)], w.r.t. the interaction radius used in the Main fit ($R = 1\,\mathrm{fm}$). The solutions of these studies are compared with the Main fit in figure 6.14. Considering the $\pi_1(1600)$ parameters, reducing the radius slightly increases the resonance width, while increasing R leads to the

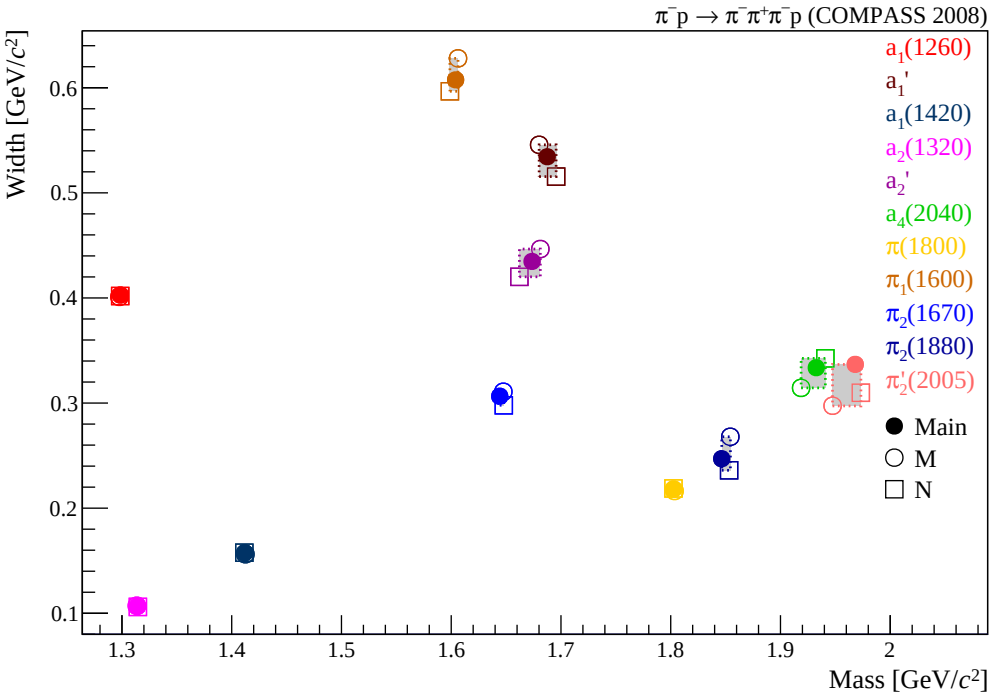

Figure 6.14: Resonance parameters obtained from the fits with slightly reduced [(M) / open circles] or slightly increased [(N) / open rectangles] interaction-radius parameter in the angular-momentum barrier factors, compared to the Main solution (full circles).

opposite effect. This consistent behavior can also be observed for almost all other resonances. The arising deviations from the Main solution are negligible compared to the overall systematics. One can conclude from these studies that the outcome of the resonance-model fit does not depend on the exact value of the interaction radius in the angular-momentum barrier factors.

6.2 Resonance Parameters and their Systematic Uncertainty

An extensive set of studies has been performed to cover a broad range of systematic effects and to estimate the systematic uncertainty of the resonance parameters. Various studies have been discussed in the previous sections and are summarized in the following. Table 6.3 summarizes all performed systematic studies.

Not all performed studies produced a physically meaningful result. For instance, removing resonances from the resonance model drastically changes the results. Furthermore, most of these studies have yielded clearly unphysical results. Therefore, these studies [(U), (V), (W), (X), (Y), (Z) and (P)] are not considered for the systematic errors. Additionally, the study, using a dynamic-width parameterization for the $\pi_1(1600)$ component [study (AC)] does not enter the

systematic error as the obtained parameters are not directly comparable. For some studies not all obtained resonance parameters enter the systematics. Study (O) using the Deck MC for the non-resonant terms yield unphysical π_2 and $a_1(1420)$ parameters (compare section 6.1.5) and is not considered for the systematic errors of these resonance parameters accordingly. Based on the same argument, the solutions for the a_1 parameters, obtained from the studies with the alternative χ^2 definitions (see section 6.1.6), do not enter the systematics. Which study defines the systematic uncertainties of which resonance parameter is summarized in table 6.4.

The Main solution (full circles) and the results of the systematic studies (open circles), are summarized in figure 6.15 for the a_J-like (1^-J^{++}) and π_J-like (1^-J^{-+}) resonances. For each resonance, only the systematic studies that were selected to define the systematic uncertainties (see table 6.4) are plotted. The obtained resonance parameters with their systematic uncertainties are collected in table 6.1. As the statistical errors are more than one order of magnitude smaller, compared to the systematics, they have been omitted from the table.

In the a_J-like sector (figure 6.15a), the $a_2(1320)$, $a_1(1420)$ and $a_4(2040)$ resonances are well-defined which is reflected by the small systematic uncertainty of their resonance parameters. The mass of the $a_1(1260)$ resonance could be extracted with a relatively small systematic uncertainty. Its width, however, is not well determined. The excited a_j states, a_1' and a_2', show the largest instabilities. To discuss the uncertainty of the $a_2(1320)$ parameters, a zoom into its parameter region is shown as an inset in figure 6.15a. Most studies give results close to the Main solution. The systematic uncertainties are mostly defined by outliers. The smallest $a_2(1320)$ mass was observed in study (O), using the Deck MC as non-resonant parameterization and results in an $3.1\,\mathrm{MeV}/c^2$ lighter $a_2(1320)$. All other studies yield an $a_2(1320)$ mass within $\pm 1\,\mathrm{MeV}/c^2$ around the Main solution. The studies (R) and (S), which used an alternative χ^2 formulation, lead to the broadest $a_2(1320)$ with $\Gamma_0 = 110.2\,\mathrm{MeV}/c^2$, while the smallest observed width originates from study (E), where all 2^{++} waves, except the $2^{++}\,1^+\,\rho(770)\,\pi\,D$ wave where removed. Due to the small width of the $a_2(1320)$ and the low non-resonant contribution in its mass region (compare section 5.2), its resonance parameters can be extracted with a small systematic uncertainty. The $a_2(1320)$ is the best defined three-pion resonance. As the a_2' resonance interferes with the non-resonant component and the high-mass tail of the much more dominant $a_2(1320)$ resonance in a complicated way, its resonance parameters show a larger spread. Especially the studies without the $2^{++}\,1^+\,f_2(1270)\,\pi\,P$ wave [(E) and (J)] show a significant larger mass of $1.8\,\mathrm{GeV}/c^2$. The $a_1(1260)$ mass is extracted with a small uncertainty. The largest deviation ($22\,\mathrm{MeV}/c^2$ lighter) was observed using looser cuts in the event-selection [study (K)]. The larger asymmetric spread in the $a_1(1260)$ width comes from a bimodal behavior of the fit, where, depending on the concrete model, a narrow $a_1(1260)$ solution with less resonant and a dominant non-resonant contribution in the $1^{++}\,0^+\,\rho(770)\,\pi\,S$ wave is found (see section 5.4). This narrow $a_1(1260)$ solution, with an up to $100\,\mathrm{MeV}/c^2$ smaller width, is observed, for example, when omitting the 2^{++} waves. Excluding these studies with the narrow $a_1(1260)$, the $a_1(1260)$ width is determined within $\pm 30\,\mathrm{MeV}/c^2$. Like for the a_2' resonance, the excited 1^{++} state a_1' is rather unstable and shows a larger spread in its resonance parameters. The broadest solutions are obtained from the studies (K) and (O) with looser cuts in the event-selection and the non-resonant terms from the Deck MC, respectively. The resonance parameters of the narrow $a_1(1420)$ structure show only little systematic uncertainties. The largest impact on its parameters originate from the

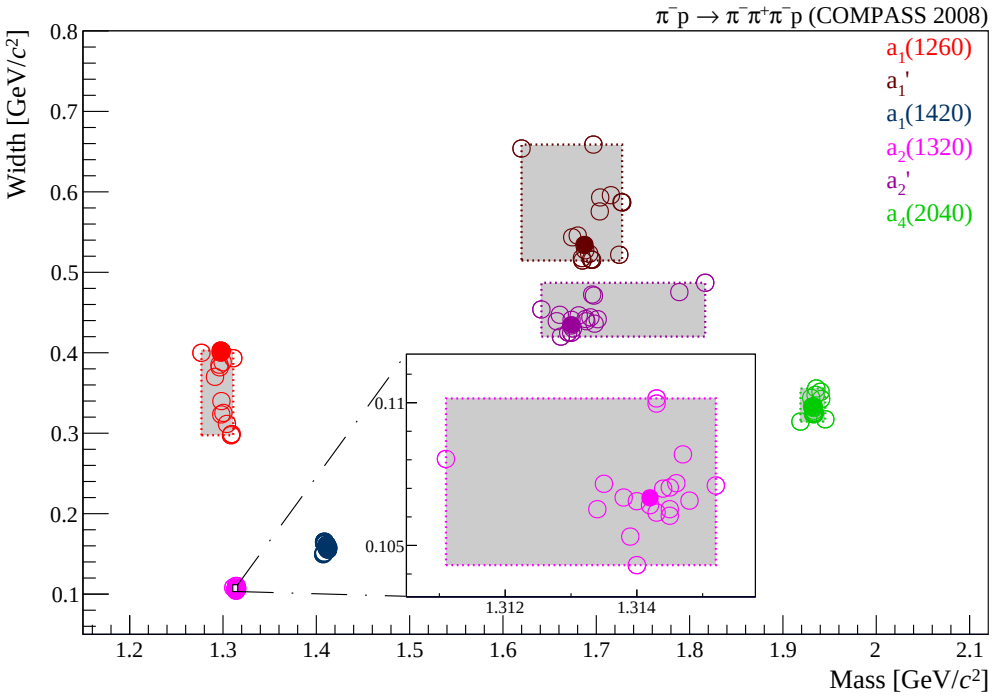

(a) a_J -like resonances

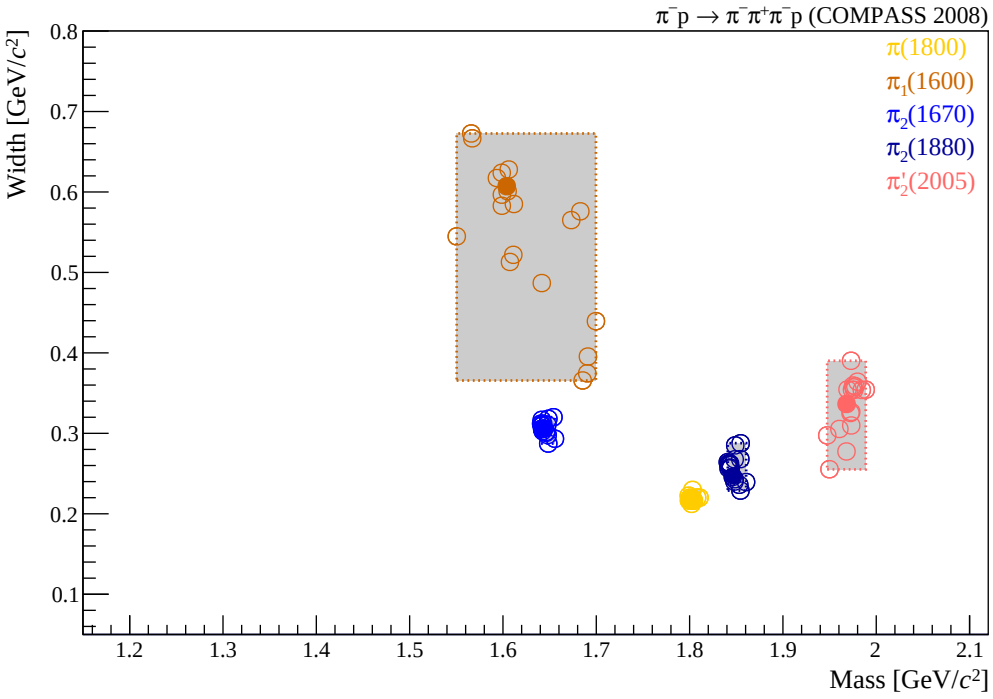

(b) π_J -like resonances

Figure 6.15: Resonance parameters obtained from the Main fit (full circles) and systematic studies entering in the systematic error (open circles). The gray boxes represent the systematic uncertainties of the corresponding resonance, defined by the extremal values of the studies.

alternative χ^2 definition [studies (R) and (S)] and study (D) without the 2^{++} waves. Similar to the $a_2(1320)$ resonance, the narrow structure and its small correlations other terms allow for a precise extraction of the $a_1(1420)$ parameters. Finally, the $a_4(2040)$ parameters can reliably be extracted from the data considering that it has a width approximately three times that of the $a_2(1320)$.

Among the analyzed π_J-like resonances, illustrated in figure 6.15b, the $\pi(1800)$ parameters show the smallest systematic uncertainty. The largest increase of $11\,\mathrm{MeV}/c^2$ of its width is observed in study (AB) with a tighter fit range in the 0^{-+} wave (see section 5.1), while the other studies reproduce the Main solution within $\pm 6\,\mathrm{MeV}/c^2$. Similar to the situation for the a_2-like resonances, the systematic uncertainties for the π_2-like resonances increase for the parameters of the higher excited states. Furthermore, a strong correlation of the π_2 parameters is observed. In study (T) without branchings and in study (AB) with a tighter 0^{-+} fit range, the broadest solutions for the $\pi_2(1670)$ and $\pi_2(1880)$ are observed, while the $\pi_2'(2005)$ component was obtained $80\,\mathrm{MeV}/c^2$ narrower in these studies. In contrast, studies (S) and (R) with an alternative χ^2 formulation lead to the largest $\pi_2'(2005)$ width and also yield broader $\pi_2(1670)$ and $\pi_2(1880)$ resonances. Considering all systematics, the $\pi_2(1670)$ parameters can be extracted with the smallest uncertainties and the $\pi_2(1880)$ has a relatively small spread in its width. The large systematic errors of the $\pi_2'(2005)$ parameters reflect the smaller evidence for this signal in the data. The overall largest systematic effects are observed in the Breit-Wigner parameters of a possible $\pi_1(1600)$ resonance. A cluster of solutions is found, centered around the Main solution. However, many studies deviate from the Main fit. The studies (S) and (R) with the alternative χ^2 formulations mark the upper limit of the $\pi_1(1600)$ width. All other studies obtain a narrower $\pi_1(1600)$, which leads to a highly asymmetric uncertainty. The narrowest and heaviest $\pi_1(1600)$ solutions, which appear as a vertical band in figure 6.15b, are obtained from four systematic studies, where various combinations of 2^{++} waves have been omitted. All of these studies also feature the narrow $a_1(1260)$ solution, as discussed in section 5.4. This reveals a strong correlation between the 1^{++} and 1^{-+} sector. In study (L) with coarser t' binning and study (AA) with the tightened 1^{-+} fit range, the $\pi_1(1600)$ has a width similar to that of the Main fit but with an around $70\,\mathrm{MeV}/c^2$ larger mass. With almost the same width but a $50\,\mathrm{MeV}/c^2$ lower mass, the Deck MC study (O) defines the low limit of the extracted $\pi_1(1600)$ mass parameter. The large spread in the $\pi_1(1600)$ parameters reflects the difficulty in separating the $\pi_1(1600)$ from the dominant non-resonant term.

Figure 6.16 compares the resonance parameters of the Main fit (full circles) and their systematic uncertainties (gray boxes) with the PDG estimates of the resonance parameters (colored boxes and white circles) [6]. A good agreement is found for the well-known $\pi(1800)$ resonance parameters. The PDG lists the $a_4(2040)$ resonance with larger mass and smaller width, compared to the results of this analysis. However, such a systematic shift was already observed in an earlier analysis of this channel of a smaller data set using a lead target instead of liquid hydrogen by the COMPASS collaboration [17]. This is in agreement with the findings of this analysis and also consistent with measurements of the $a_4(2040)$ resonance in the $\eta\,\pi^-$ and $\eta'\pi^-$ final state by the COMPASS collaboration [38]. Furthermore, similar parameters have been observed by the VES experiment in $\pi^- A \to \omega\,\pi^-\,\pi^0\,A^*$ [39]. The extracted mass of the $a_2(1320)$ resonance is $4.8\,\mathrm{MeV}/c^2$ smaller than listed by the PDG, but still within the range of other observations.

Table 6.1: Resonance parameters and systematic errors of this analysis (COMPASS). For a comparison, the central values and estimated uncertainties of the PDG [6] are listed. For the $\pi_2'(2005)$ parameters, the observations of the B852 experiment [10] are shown, as the PDG lists no average for this further state.

(a) a_J-like resonances

		$a_1(1260)$	$a_1(1420)$	a_1'	$a_2(1320)$	a_2'	$a_4(2040)$
COMPASS	Mass [MeV/c^2]	$1298\,^{+13}_{-22}$	$1411.8\,^{+1.0}_{-4}$	$1680\,^{+40}_{-60}$	$1314.2\,^{+1.0}_{-3.1}$	$1674\,^{+140}_{-32}$	$1933\,^{+13}_{-14}$
	Width [MeV/c^2]	$400\,^{+0}_{-100}$	$158\,^{+8}_{-8}$	$534\,^{+120}_{-20}$	$106.7\,^{+3.5}_{-2.4}$	$435\,^{+50}_{-15}$	$334\,^{+22}_{-19}$
PDG	Mass [MeV/c^2]	$1230\,^{+40}_{-40}$	—	$1647\,^{+22}_{-22}$	$1318.3\,^{+0.5}_{-0.6}$	$1732\,^{+16}_{-16}$	$1996\,^{+10}_{-9}$
	Width [MeV/c^2]	$250 - 600$	—	$254\,^{+27}_{-27}$	$107\,^{+5}_{-5}$	$194\,^{+40}_{-40}$	$255\,^{+28}_{-24}$

(b) π_J-like resonances

		$\pi(1800)$	$\pi_1(1600)$	$\pi_2(1670)$	$\pi_2(1880)$	$\pi_2'(2005)$
COMPASS	Mass [MeV/c^2]	$1802.6\,^{+8}_{-3.5}$	$1600\,^{+100}_{-50}$	$1644.2\,^{+12}_{-3.4}$	$1847\,^{+14}_{-6}$	$1968\,^{+21}_{-21}$
	Width [MeV/c^2]	$218\,^{+11}_{-6}$	$600\,^{+60}_{-240}$	$306\,^{+14}_{-19}$	$247\,^{+40}_{-18}$	$330\,^{+50}_{-80}$
PDG	Mass [MeV/c^2]	$1812\,^{+12}_{-12}$	$1662\,^{+8}_{-9}$	$1672.2\,^{+3.0}_{-3.0}$	$1895\,^{+16}_{-16}$	$1974\,^{+97}_{-97}$
	Width [MeV/c^2]	$208\,^{+12}_{-12}$	$241\,^{+40}_{-40}$	$260\,^{+9}_{-9}$	$235\,^{+34}_{-34}$	$341\,^{+200}_{-200}$

The PDG also lists an excited a_2 state, the $a_2(1700)$ in the same mass region as the a_2', found in this analysis, but with a significantly smaller width. Similarly for the a_1', the PDG lists the $a_1(1640)$ in a similar mass region but with a smaller width. For the $a_1(1260)$, the a_1 ground state, a diversity of different resonance widths and, to a lesser degree, masses are observed by different experiments. For this reason the PDG only gives parameter ranges for the $a_1(1260)$ width and no central value. This reflects the systematic problems with this resonance, also observed in this analysis. A slightly heavier $a_1(1260)$ mass is found in this analysis, compared to the PDG range. Also the parameters of the π_2-like resonances, deviate from the PDG listings. The $\pi_2(1670)$ is found systematically lighter, compared to other experiments. In this analysis, its width is found to be larger than the PDG value, but there are other experiments like BNL E582 [10], VES [39] or HBC[3] [40] which found also a similar broad $\pi_2(1670)$. In the previous COMPASS analysis of this channel [39], the same trend in the $\pi_2(1670)$ parameters is observed. The width of the $\pi_2(1880)$ resonance, found in this analysis, agrees well with the PDG, while its mass is lower. A possible $\pi_2'(2005)$ state with similar parameters has also been observed

[3] Hydrogen bubble chamber (HBC) experiment at SLAC (1977).

by the BNL E852 experiment [10] in the reaction $\pi^- p \to \omega \pi^- \pi^0 p$, while a comparable state with a $33\,\mathrm{MeV}/c^2$ higher mass and $130\,\mathrm{MeV}/c^2$ smaller width was found by Anisovich, et al. [41] in proton-antiproton annihilations. The spin-exotic $\pi_1(1600)$ resonance is listed in the PDG with a similar mass as in this analysis but a significantly smaller width. Other experiments have measured a width of a possible $\pi_1(1600)$ in the range of 185 to $403\,\mathrm{MeV}/c^2$ [10, 42]. Even if the systematics for the $\pi_1(1600)$ show a clear trend for smaller widths, the result of this analysis is not in agreement with other findings. Also in the earlier COMPASS analysis [39] a narrower $\pi_1(1600)$ of $269 \pm 21\,^{+42}_{-62}\mathrm{MeV}/c^2$ was found. However, one should notice, that this measurement was performed with a lead in stead of a liquid hydrogen target.

Before concluding on the obtained results in chapter 8, a further piece of information, the t' dependences of the different components, is used in chapter 7 to shed some more light on some of the issues discussed above.

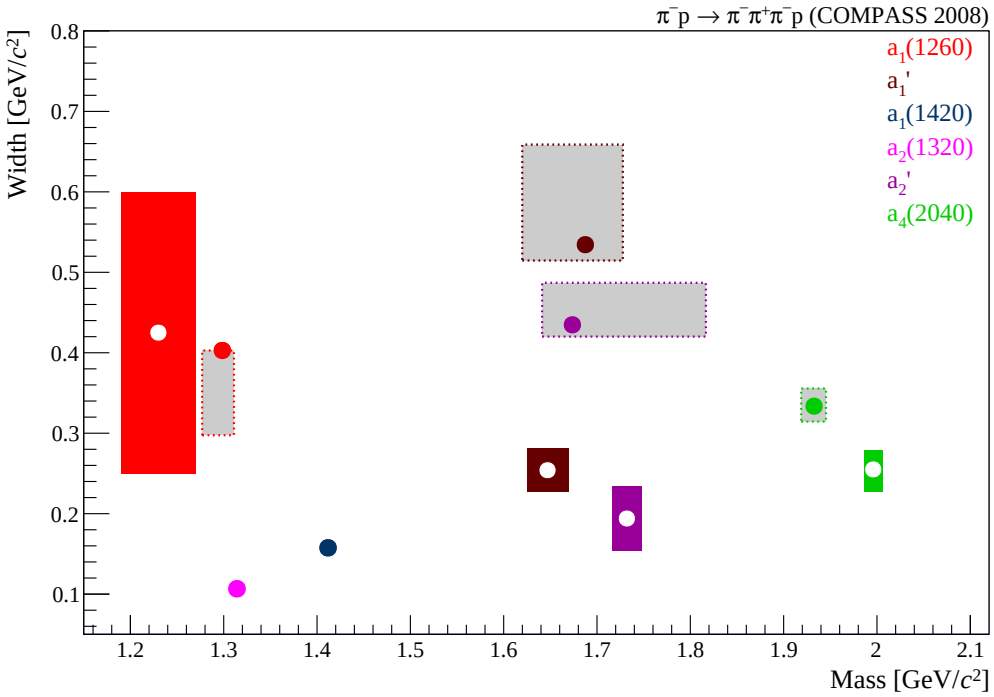

(a) a_J-like resonances

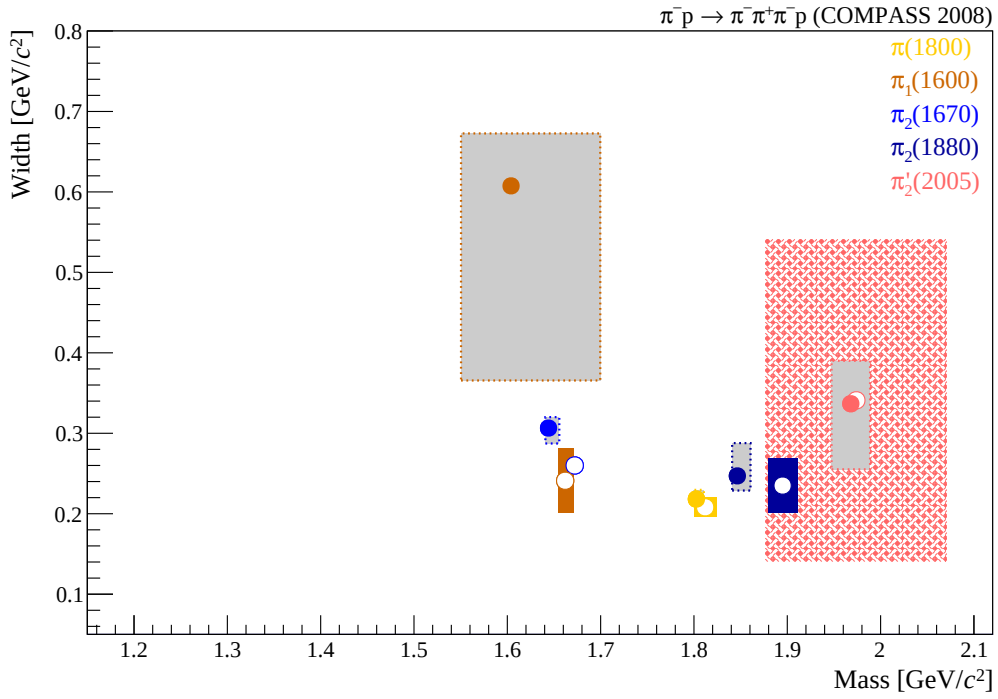

(b) π_J-like resonances

Figure 6.16: Resonance parameters of the Main solution (full circles) and the corresponding systematic uncertainties (gray boxes), compared to the average resonance parameters (white circles) and their estimated uncertainty (colored boxes), as listed by the PDG [6]. No PDG average exists for the further state $\pi_2'(2005)$. Therefore the measurement of the BNL E852 [10] experiment was used as reference.

Table 6.3: List of systematic studies.

Label	Description
Main	Main Fit
(A)	Fit without 2^{-+} waves
(B)	Fit without 1^{++} waves
(C)	Fit without 4^{++} waves
(D)	Fit without 2^{++} waves
(E)	Fit with $2^{++}\,1^{+}\,\rho(770)\,\pi\,D$ wave as only 2^{++} wave
(F)	Fit with $2^{++}\,2^{+}\,\rho(770)\,\pi\,D$ wave as only 2^{++} wave
(G)	Fit with $2^{++}\,1^{+}\,f_2(1270)\,\pi\,F$ wave as only 2^{++} wave
(H)	Fit without $2^{++}\,1^{+}\,\rho(770)\,\pi\,D$ wave
(I)	Fit without $2^{++}\,2^{+}\,\rho(770)\,\pi\,D$ wave
(J)	Fit without $2^{++}\,1^{+}\,f_2(1270)\,\pi\,F$ wave
(K)	Looser event selection (no central-production cut, no PID and RPD information)
(L)	Coarser t' binning (8 t' bins)
(M)	Reduced range parameter in angular-momentum barrier factors ($R = 0.75\,\text{fm}$)
(N)	Increased range parameter in angular-momentum barrier factors ($R = 1.29\,\text{fm}$)
(O)	Deck MC as non-resonant parameterization
(P)	Deck MC as non-resonant parameterization and no $\pi_2'(2005)$
(Q)	χ^2 with model integration over $m_{3\pi}$ bin width
(R)	Alternative χ^2-definition: directly fitting the production amplitude
(S)	Alternative χ^2-definition: fitting only one row of ρ-matrix
(T)	Fit without fixed relative spin-density branchings
(U)	Fit without $\pi_2'(2005)$ resonance
(V)	Fit with $a_1(1260)$ in $1^{++}\,0^{+}\,f_0(980)\,\pi\,P$ wave
(W)	Fit without $\pi_1(1600)$ resonance
(X)	Fit without $a_1(1420)$ resonance
(Y)	Fit without a_1' resonance
(Z)	Fit without a_2' resonance
(AA)	Fit with low-mass fit-range of $1.4\,\text{GeV}/c^2$ in $1^{-+}\,1^{+}\,\rho(770)\,\pi\,P$ wave
(AB)	Fit with low-mass fit-range of $1.6\,\text{GeV}/c^2$ in $0^{-+}\,0^{+}\,f_0(980)\,\pi\,S$ wave
(AC)	Dynamic-width parameterization assuming 100 % $\rho(770)\,\pi\,P$ decay for $\pi_1(1600)$

Table 6.4: Systematic studies, that were selected to define the systematic uncertainties of the various resonance parameters (X). Studies which are not considered for a certain resonance are marked with "O".

Study	$a_1(1260)$	$a_1(1420)$	a_1'	$a_2(1320)$	a_2'	$a_4(2040)$	$\pi(1800)$	$\pi_1(1600)$	$\pi_2(1670)$	$\pi_2(1880)$	$\pi_2'(2005)$
A	X	X	X	X	X	X	X	X	O	O	O
B	O	X	O	X	X	X	X	X	X	X	X
C	X	X	X	X	X	O	X	X	X	X	X
D	X	X	X	O	O	X	X	X	X	X	X
E	X	X	X	X	X	X	X	X	X	X	X
G	X	X	X	X	X	X	X	X	X	X	X
H	X	X	X	X	X	X	X	X	X	X	X
I	X	X	X	X	X	X	X	X	X	X	X
J	X	X	X	X	X	X	X	X	X	X	X
K	X	X	X	X	X	X	X	X	X	X	X
L	X	X	X	X	X	X	X	X	X	X	X
M	X	X	X	X	X	X	X	X	X	X	X
N	X	X	X	X	X	X	X	X	X	X	X
O	X	O	X	X	X	X	X	X	O	O	O
Q	X	X	X	X	X	X	X	X	X	X	X
R	O	X	O	X	X	X	X	X	X	X	X
S	O	X	O	X	X	X	X	X	X	X	X
T	X	X	X	X	X	X	X	X	X	X	X
AA	X	X	X	X	X	X	X	X	X	X	X
AB	X	X	X	X	X	X	X	X	X	X	X

CHAPTER 7

t' Dependences of Model Components

One of the most challenging aspects of this analysis is the separation between the various model components, contributing to one partial wave. In addition to the interference patterns between the partial waves, the binning in t' plays an important role. It not only helps to better separate resonances from non-resonant contributions, but also gives the possibility to extract the t' dependences of the different model components. The t'-dependent intensities (t' spectra) and production phases will be discussed in this chapter, together with their systematic uncertainties. A complete list of the t' slope parameters can be found in table 7.1. Plots of the t' dependences of all model components are summarized in appendix G.

The t' spectra of the well-known resonances like the $\pi(1800)$, the $a_4(2040)$ or the $a_2(1320)$ are in good agreement with a single exponential dependence and show a resonance-like slope parameter in the range of 8 to 9 $(\mathrm{GeV}/c)^{-2}$ with a small systematic uncertainty. Also the t' spectra of the π_2 resonances are in agreement with those well-known resonances. In contrast, the t' slope of the $a_1(1260)$ resonance shows a unusually large value of $12.68\,^{+0.25}_{-5}$ $(\mathrm{GeV}/c)^{-2}$ compared to the other resonances with large systematic uncertainties. Especially the appearance of the narrow $a_1(1260)$ solution leads to a significant change in its t' slope towards a value of 8 to 9 $(\mathrm{GeV}/c)^{-2}$. The investigation of the t' dependence of the $a_1(1420)$ resonance signal further supports its resonance character. For the spin-exotic $\pi_1(1600)$, a resonance-like slope of 7.2 $(\mathrm{GeV}/c)^{-2}$ is observed. However, the systematic studies reveal a large uncertainty and correlation with the $a_1(1260)$ parameters. Except for the $a_1(1260)$ where large systematic effects are observed when removing the fixed relative branchings, the assumption of fixed relative branchings can either be confirmed in study (T) without branchings or it is obvious that removing the branchings leads to unphysical solutions.

7.1 Extraction of the t' Dependences of the Model Components

To obtain the t' dependence of the intensity of a certain component k in a certain wave α, called t' spectrum in the rest of the text, the total intensity is calculated in each t' bin by integrating over

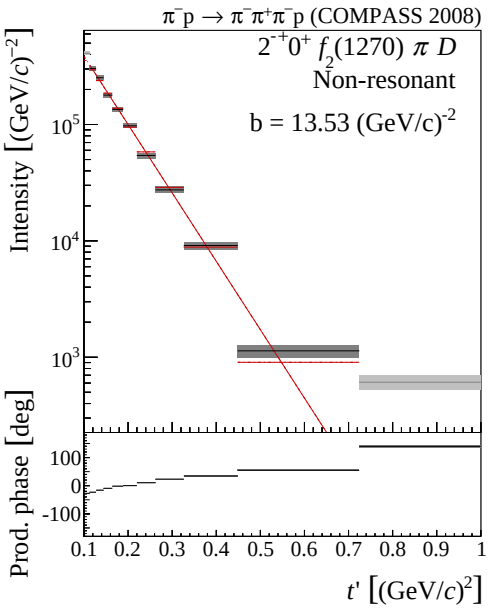

Figure 7.1: (For illustration) t' spectrum and production phase of the non-resonant component in the 2^{-+} 0^+ $f_2(1270)\,\pi\,D$ wave.

the theory curve of the corresponding component of the resonance-model fit. As the resonance model is valid only within the fitted mass-range, the integration is performed over this range. The t' binning is not equidistant. Therefore the intensity of each t' bin is normalized to the t' bin width $\Delta t'$:

$$\text{Intensity}^k_\alpha(t') = \frac{1}{\Delta t'} |C^k_\alpha(t')|^2 \int_{m_{\text{start}}}^{m_{\text{end}}} \mathrm{d}m_{3\pi}\, |\mathcal{D}^k(m_{3\pi}, t'; \zeta_k)|^2 \varphi_\alpha(m_{3\pi}) \Psi(m_{3\pi}). \tag{7.1}$$

One should notice, that for a resonance in a wave with fixed relative branchings, the coupling $C^k_\alpha(t')$ is replace by a fixed relative branching factor ${}_\alpha B^k_\beta$ and the coupling of the reference wave $C^k_\beta(t')$ according to equation (4.10). In order to estimate the statistical uncertainty of the intensities $\text{Intensity}^k_\alpha(t')$, a set of 10 000 Monte Carlo samples is generated according to the covariance matrix of the fit parameters of the resonance-model fit, assuming Gaussian errors for the fit parameters. For each sample, the intensity is calculated and the variance of the intensities determines the errors. Details can be found in appendix G. Figure 7.1 shows the t' spectrum (top) of the non-resonant term in the 2^{-+} 0^+ $f_2(1270)\,\pi\,D$ for illustration. The errors are drawn as gray boxes with a black line indicating the central value. However, usually these statistical uncertainties are very small and only the black lines are visible in the figures. The t' dependence of the production phase, which is the phase of the coupling constant $C^k_\alpha(t')$, is shown in figure 7.1 (bottom). The uncertainties of the production phase are calculated in the same way as those for the t' spectra. To resolve the ambiguity of the global phase, the production phase of the $a_1(1260)$ in the 1^{++} 0^+ $\rho(770)\,\pi\,S$ wave is fixed to 0°. Thus, all production phases are measured relative to this component.

Assuming single Pomeron exchange between the beam pion and target proton (see section 1.2), Regge theory predicts an exponentially falling cross section with t' [26]. This behavior can be motivated by treating diffractive scattering, in the optical analogy as scattering on a gray disk. In this picture the slope parameter is related to the radius of the disk [26]. Assuming a proton radius of around 0.85 fm, the slope parameter would be in the order of $10\,(\mathrm{GeV}/c)^{-2}$. For waves with spin projection $M \neq 0$, the decay amplitude depends on the azimuthal angle ϕ, measured around the beam axis. For forward scattering ($t' = 0$) the production plain and thus ϕ is not defined. Thus the amplitude has to vanish in the very forward direction. This kinematic effect introduces an additional $t'^{|M|}$ factor [1]. The t' spectrum is parameterized in the following way:

$$\frac{\mathrm{d}\,\mathrm{Intensity}(t')}{\mathrm{d}\,t'} = I_0 \left(t'\right)^{|M|} e^{-bt'} \tag{7.2}$$

with the slope parameter b. Figure 7.1 shows the χ^2 fit of this model (red line) to the data. In the fit, the exponential function is integrated over the t' bins (red bars) and compared to the extracted t' spectrum from the resonance-model fit (black bars). As the single-exponential assumption holds only in a limited t' range, the first and last t' bin is excluded from the fit such that the fit is performed in the range

$$0.113 < t' < 0.724\,(\mathrm{GeV}/c)^2. \tag{7.3}$$

All obtained slope parameters are summarized in table 7.1. The listed systematic uncertainties were determined from the studies discussed in chapters 5 and 6. As for the resonance parameters, the statistical uncertainties are negligible and therefore omitted from the table. The same studies as for the resonance parameters were selected. In two additional studies, (Main.a) and (Main.b), the influence of the t' fit range is investigated. In (Main.a) also the last t' bin is included in the fit, while study (Main.b) additionally covers the first bin.

7.2 t' Spectrum and Production Phase in the 0^{-+} Wave

The t' spectrum and the production phase as a function of t' of the $\pi(1800)$ resonance in the 0^{-+} $0^+ f_0(980)\,\pi\,S$ wave are shown in figure 7.2a.

The t' spectrum of the $\pi(1800)$ component is in good agreement with the single-exponential fit within the fit range. Only in the last t' bin, the observed intensity deviates from the exponential model. This behavior is observed in most of the t' spectra and shows the limitations of the single-exponential approximation. The extracted slope parameter of $b = 8.72\,(\mathrm{GeV}/c)^{-2}$ is within the range, typically expected for resonant structures in pion-proton scattering [33].

The production phase of the $\pi(1800)$, measured with respect to the $a_1(1260)$, shows a slowly rising phase of 50° over the full t' range. For a resonance, no phase motion with t' of the production phase is expected. A rising phase motion between 40° to 60° is observed for most

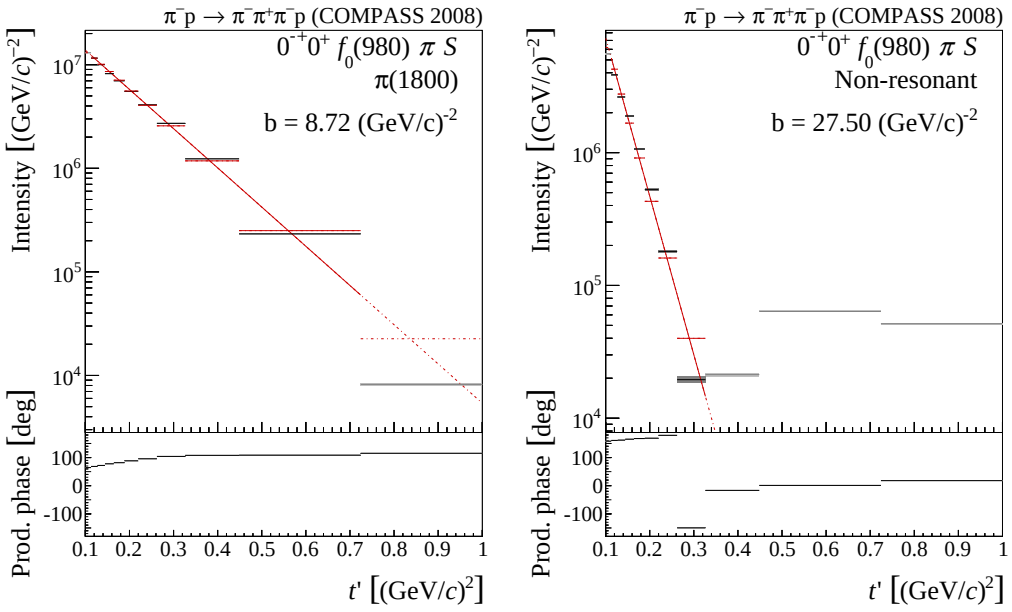

(a) $\pi(1800)$ (b) Non-resonant component

Figure 7.2: t' spectrum and production phase of the resonant and non-resonant components in the $0^{-+}\,0^{+}$ $f_0(980)\,\pi\,S$ wave.

of the resonances. Since they are all measured w.r.t. the $a_1(1260)$, it is more likely, that the production phase of the $a_1(1260)$ component in the $1^{++}\,0^{+}\,\rho(770)\,\pi\,S$ wave falls with t'. This would also support the observation, that the separation between the resonant and non-resonant term in the $1^{++}\,0^{+}\,\rho(770)\,\pi\,S$ wave needs further improvement. But as no absolute phases can be measured, this is only a hypothesis.

In the same way as for the resonances also the spectra of the non-resonant terms can be extracted from the resonance-model fit. The t' spectrum and the production phase of the non-resonant component in the $0^{-+}\,0^{+}\,f_0(980)\,\pi\,S$ are shown in figure 7.2b. The t' spectrum has a dip, so that the highest three t' bins disagree with a single exponential shape. The low-t' region shows a large slope of $27\,(\mathrm{GeV}/c)^{-2}$. This indicates, that resonant and non-resonant contributions in the $0^{-+}\,0^{+}\,f_0(980)\,\pi\,S$ potentially describe components from different production processes. This interpretation is further supported by the large phase motion of the production phase with t' of the non-resonant term of 220°. The different t' dependencies of resonant and non-resonant contributions support the separation between these components in the resonance-model fit.

7.3 The $a_4(2040)$ Resonance and the Influence of fixed relative Branchings

The fixing of the relative branchings of the same resonance in different partial waves with the same $J^{PC}\, M^{\varepsilon}$ quantum numbers force the t' dependences of this resonance to be the same in all branched waves (see section 4.2). Therefore, the extracted slope parameters of the resonances are the same in different branched waves, as it can be seen in table 7.1. An example is the slope of the $a_4(2040)$ resonance in the $4^{++}\ 1^+\ \rho(770)\,\pi\, G$ and $4^{++}\ 1^+\ f_2(1270)\,\pi\, F$ waves (see table 7.2f). However, small deviations are possible as the statistical errors of the extracted t' spectra are different for different partial waves, which affects the single-exponential fits.

A slope of $9.22\,(\mathrm{GeV}/c)^{-2}$ is observed for the $a_4(2040)$, which is consistent with a resonance interpretation. The systematic effects on the slope parameter are summarized in figure 7.3b. The different data points show the outcomes of the various systematic studies. The color encodes the difference in χ^2 of the single-exponential fit of the corresponding study w.r.t. the Main solution. Like its resonance parameters, the t' slope parameter of the $a_4(2040)$ resonance shows a small systematic uncertainty. The largest deviations are observed for study (K) with looser cuts in the event selection and study (O) using the Deck-MC for the non-resonant terms. The t' spectrum of the non-resonant terms of both 4^{++} waves has a larger slope of $14\,(\mathrm{GeV}/c)^{-2}$, which is in agreement with the non-resonant interpretation.

To test whether the assumption of fixed relative branchings is supported by the data, in study (T) the relative branchings are removed from the fit (see section 6.1.3). Figure 7.3a compares the t' spectra of the $a_4(2040)$ resonance in the $4^{++}\ 1^+\ \rho(770)\,\pi\, G$ wave from the Main fit (data: black, model: red) wit those obtained from study (T) (green/orange). Both fit results show essentially the same t' dependence and their extracted slope parameters b are in good agreement. As the $4^{++}\ 1^+\ \rho(770)\,\pi\, G$ wave has spin projection $M = 1$, the fitted model includes the suppression factor $t'^{|M|}$. In the three lowest t' bins, more intensity is observed as predicted by the single-exponential model. This could be a hint for a still imperfect separation between the resonant and non-resonant components in this wave, as the non-resonant contribution is larger in the low-t' region. A slow phase motion of the production phase w.r.t. the $a_1(1260)$ of around 60° is observed over the analyzed t' range.

In the $4^{++}\ 1^+\ f_2(1270)\,\pi\, F$ wave, the t' spectrum shows a marginally different slope without relative branchings (compare black/red with green/orange in figure 7.4a) . However, this deviation is within the systematics, observed in the other studies, which are summarized in figure 7.4b. Thus one can conclude that the assumptions of the relative branchings holds for the $a_4(2040)$ in the two analyzed 4^{++} waves.

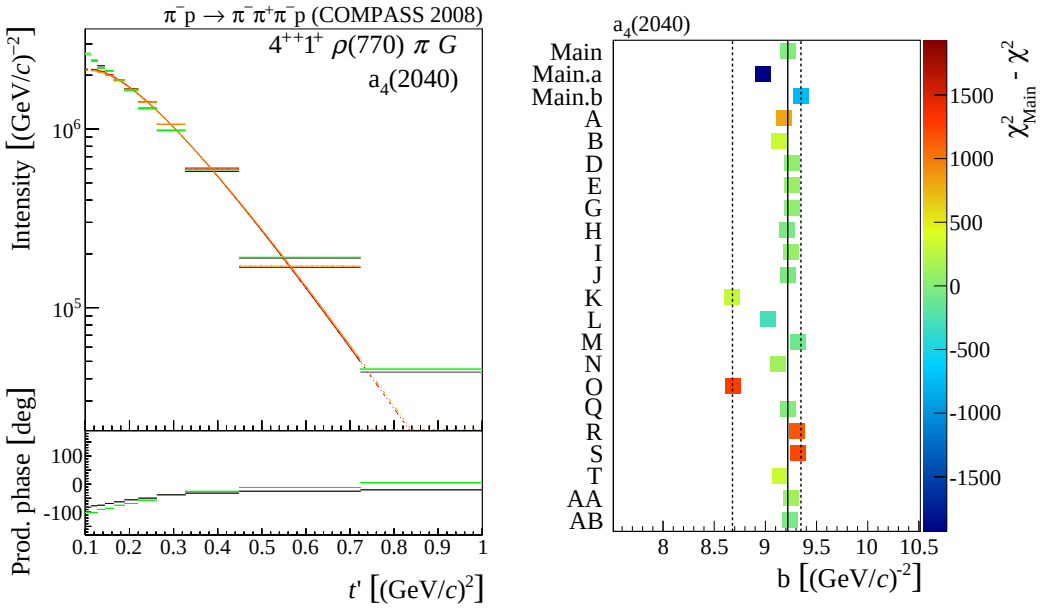

(a) $a_4(2040)$ (b) t' slope parameter

Figure 7.3: t' spectrum and production phase of the $a_4(2040)$ in the $4^{++}\ 1^+\ \rho(770)\,\pi\,G$ wave with (black/red) and without (green/orange) fixed relative branchings (a) and the slope parameter estimated in the systematic studies (b). The dashed lines represent the estimate for the systematic uncertainties.

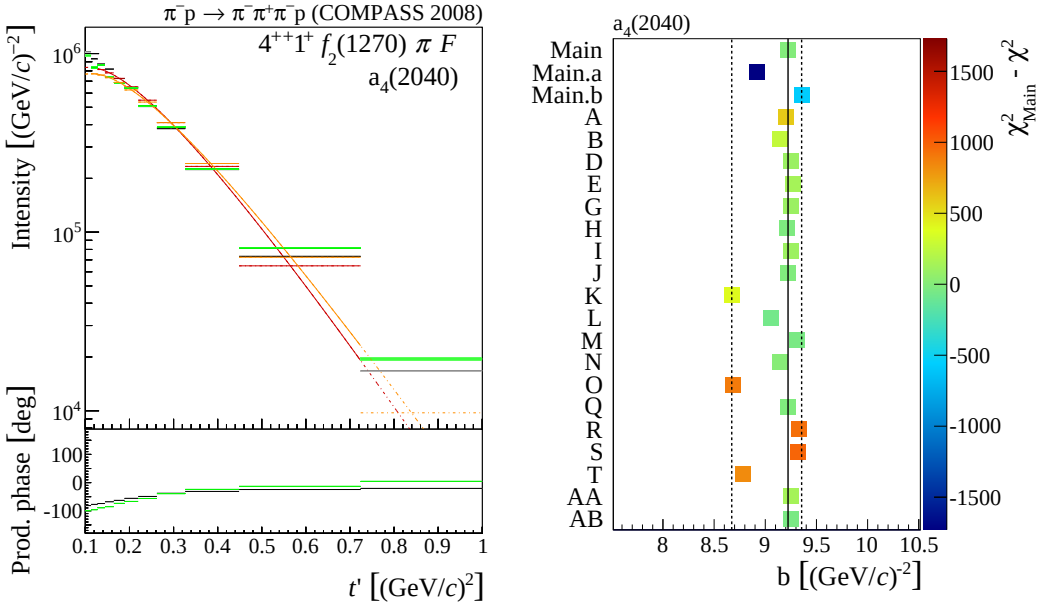

(a) $a_4(2040)$ (b) t' slope parameter

Figure 7.4: Like in figure 7.3 but for the $a_4(2040)$ in the $4^{++}\ 1^+\ f_2(1270)\,\pi\,F$ wave.

7.4 2^{++} Waves and Different Spin Projections

Similar to the already discussed $a_4(2040)$, the $a_2(1320)$ slope in the $2^{++}\,1^+\,\rho(770)\,\pi\,D$ wave, which is the dominant 2^{++} wave, can be extracted with small systematic uncertainties [$b = 7.88\,^{+0.24}_{-0.6}(\mathrm{GeV}/c)^{-2}$]. The observed t' spectrum is reproduced by the single-exponential model, except for an increased intensity in the three lowest t' bins (see figure 7.5a). In this analysis, the $a_2(1320)$ component is also included in the $2^{++}\,2^+\,\rho(770)\,\pi\,D$ wave. As both waves have different spin projection M, the fixed relative branchings cannot be applied. Thus the $a_2(1320)$ has independent t' spectra in the $2^{++}\,M^+\,\rho(770)\,\pi\,D$ waves, as shown in figure 7.5b. Also in the $M = 2$ wave, the shape is in fair agreement with the single-exponential model. However, the slope of $9.05(\mathrm{GeV}/c)^{-2}$ is slightly larger compared to the $M = 1$ waves. This is still within the systematic uncertainties, but may be an indication for an imperfect separation between the components in the $2^{++}\,2^+\,\rho(770)\,\pi\,D$ wave. In all 2^{++} waves, the $a_2(1320)$ resonance shows a slowly rising phase motion of 30° to 40°w.r.t. the $a_1(1260)$. Considering study (T) without fixed branchings and studies (D) through (J), where various combinations of 2^{++} waves are omitted from the resonance model, the $a_2(1320)$ t' slope is in good agreement in the $2^{++}\,1^+\,\rho(770)\,\pi\,D$ and $2^{++}\,1^+\,f_2(1270)\,\pi\,P$ waves. Thus the application of fixed relative branchings is valid.

The situation is more complicated for the excited a_2 state, the a_2'. The slope of $b = 6.8\,(\mathrm{GeV}/c)^{-2}$ in the $2^{++}1^+$ waves is smaller than that of the $a_2(1320)$, which is expected for an excited higher-mass state. In the $2^{++}\,1^+\,f_2(1270)\,\pi\,P$ wave (see figure 7.6a) where a significant contribution of the a_2' is observed, the slope is extracted with small systematic uncertainties. However, in the $2^{++}\,1^+\,\rho(770)\,\pi\,D$ wave with only a small contribution of the a_2', larger deviations are observed, especially in the studies without the $2^{++}\,1^+\,f_2(1270)\,\pi\,P$ wave and in study (T) without fixed relative branchings. This shows, that for a proper extraction of a possible a_2' resonance, the additional information of the $2^{++}\,1^+\,f_2(1270)\,\pi\,P$ wave is needed. This means that the fixed branchings do not only reduce the number of fit parameters, but also stabilize the fit. The extracted t' spectra in the $2^{++}\,2^+\,\rho(770)\,\pi\,D$ wave shows large fluctuations and yield a rather steep slope of $15\,^{+5}_{-7}(\mathrm{GeV}/c)^{-2}$. The large systematic error reflects the weak evidence of a possible a_2' in the $2^{++}\,2^+\,\rho(770)\,\pi\,D$ wave.

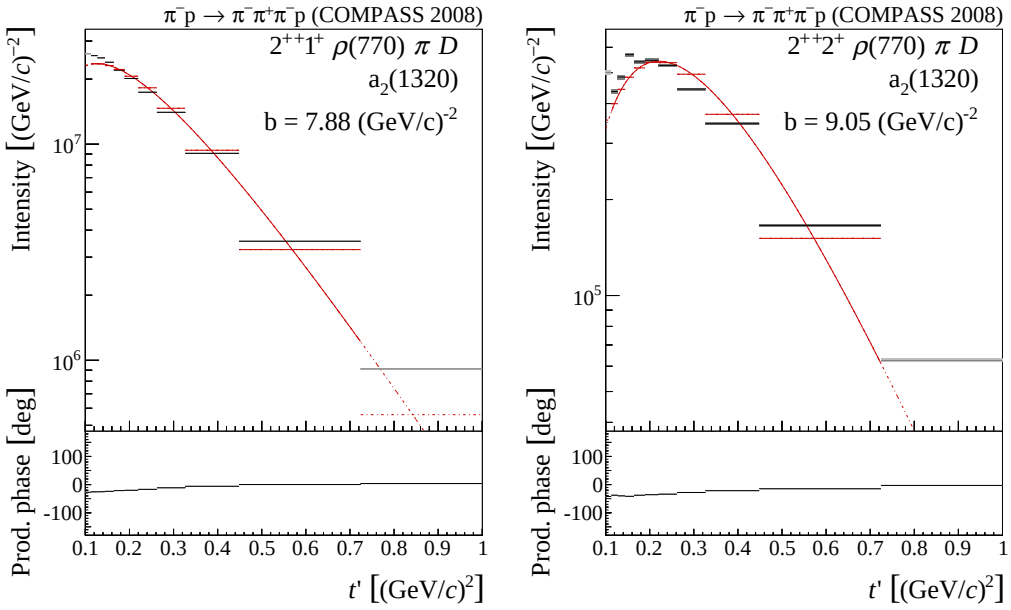

(a) $M = 1$ (b) $M = 2$

Figure 7.5: t' spectra and production phases of the $a_2(1320)$ in the 2^{++} $\rho(770)\pi D$ waves with spin projections one and two.

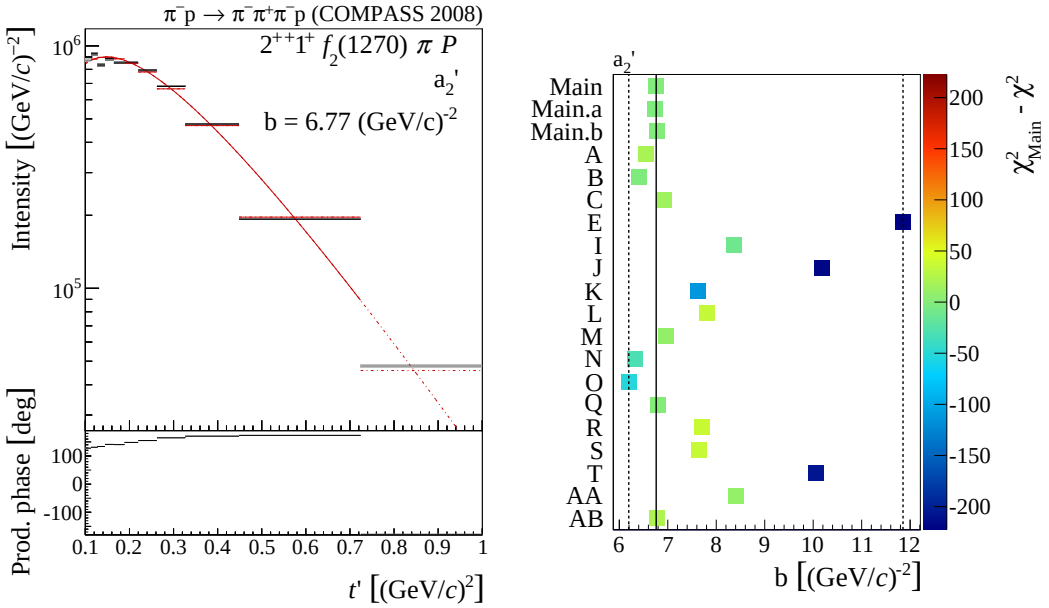

(a) a_2' (b) t' slope parameter

Figure 7.6: t' spectrum and production phases of the a_2' in the 2^{++} 1^+ $f_2(1270)\pi P$ wave (a) and the systematic uncertanties of the a_2' t' slope parameter in the 2^{++} 1^+ $\rho(770)\pi D$ wave (b). The dashed lines represent the estimate for the systematic uncertainties.

7.5 The 2^{-+} Waves

The 2^{-+} sector contributes with the largest number of waves to the resonance-model fit. Three waves with spin projection $M = 0$ are used and one with $M = 1$. Each of the π_2 resonances has fixed relative branchings in the $M = 0$ waves and therefore the same t' dependences in these waves.

The t' dependence of all three resonant components in the $2^{-+}\,0^+\,f_2(1270)\,\pi\,S$ wave are shown in figure 7.7. The t' spectra are well described by the single-exponential model. Similar to a_2 states, the higher excitations show a shallower slope. The largest systematic effect on the $\pi_2(1670)$ slope is observed in study (T) without fixed relative branchings. Without branchings, in all the 2^{-+} waves with $M = 0$ the t' slope of the $\pi_2(1670)$ becomes smaller. This means that there is no tension between these waves concerning the $\pi_2(1670)$ t' dependence, but, due to the correlation with other parameters, the $\pi_2(1670)$ t' slope becomes shallower.

The $\pi_2(1880)$ t' dependence in the $2^{-+}\,0^+\,f_2(1270)\,\pi\,D$ and $2^{-+}\,0^+\,\rho(770)\,\pi\,F$ waves is almost unchanged when omitting fixed branchings. However, a much steeper t' spectrum is observed in the $2^{-+}\,0^+\,f_2(1270)\,\pi\,S$ wave in study (T) (see figure 7.8a). This coincides with a vast increase of the total phase motion of the production phase, which leads to the conclusion, that without the additional constraints of the other 2^{-+} waves with $M = 0$, the fit uses the $\pi_2(1880)$ component to improve the description of the non-resonant contribution in the $2^{-+}\,0^+\,f_2(1270)\,\pi\,S$ wave. This is consistent with the small contribution of the $\pi_2(1880)$ to this wave, as discussed in section 5.3, and demonstrates the yield in stability when using fixed relative branchings. As the result of study (T) for the $\pi_2(1880)$ t' slope in the $2^{-+}\,0^+\,f_2(1270)\,\pi\,S$ wave is clearly unphysical, it is not included into the systematic uncertainty for the slope of this component.

The situation for the $\pi_2'(2005)$ is similar to that of the $\pi_2(1880)$. Without fixed relative branchings, the t' slope in the $2^{-+}\,0^+\,f_2(1270)\,\pi\,S$ wave becomes $1.4\,(\mathrm{GeV}/c)^{-2}$ shallower, while it is similar to the Main fit in the $2^{-+}\,0^+\,f_2(1270)\,\pi\,D$ wave. In the $2^{-+}\,0^+\,\rho(770)\,\pi\,F$ wave, a steep drop of the intensity of the $\pi_2'(2005)$ component in the lowest five t' bins is observed without branchings (see figure 7.9), which is not in agreement with the single-exponential model. However, the production phase remains flat, in agreement with the resonance hypothesis. It can be speculated, that it is not a problem of separating the resonant and non-resonant components, but of the separation between the resonances, especially as three resonance components are used to describe the 2^{-+} waves. However, combining the different information from the different 2^{-+} waves via fixed relative branchings stabilizes the fit.

In the 2^{-+} $f_2(1270)\,\pi\,S$ wave with spin projection $M = 1$, the fit assigns less intensity to the $\pi_2(1880)$ and $\pi_2'(2005)$ components compared to the $M = 0$ wave. This leads to larger fluctuations in their t' spectra. The extracted slopes of $b_{\pi_2(1880)} = 8.4\,(\mathrm{GeV}/c)^{-2}$ and $b_{\pi_2'(2005)} = 7.4\,(\mathrm{GeV}/c)^{-2}$ are slightly larger, compared to the $M = 0$ waves. A similar increase of the t' slope, when going to higher spin projections, is also observed for the 2^{++} waves (see section 7.4). One should also notice, that the $\pi_2(1880)$ component in the $2^{-+}\,1^+\,f_2(1270)\,\pi\,S$ wave shows a large phase motion of the production phase of around 150° w.r.t. the $a_1(1260)$.

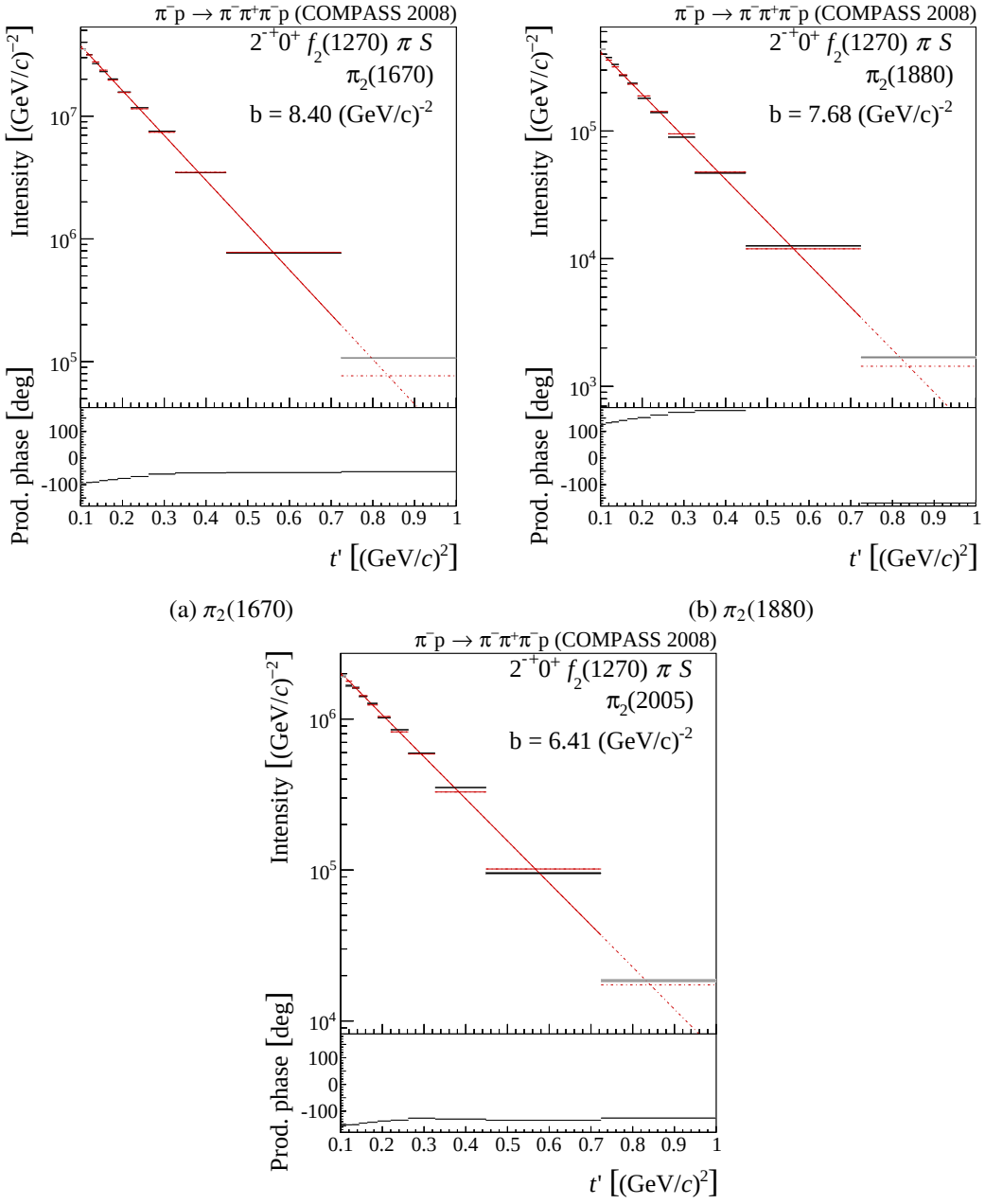

(a) $\pi_2(1670)$ (b) $\pi_2(1880)$

(c) $\pi_2'(2005)$

Figure 7.7: t' spectra and production phases of all three π_2 resonances in the $2^{-+}\,0^+\,f_2(1270)\,\pi\,S$ wave.

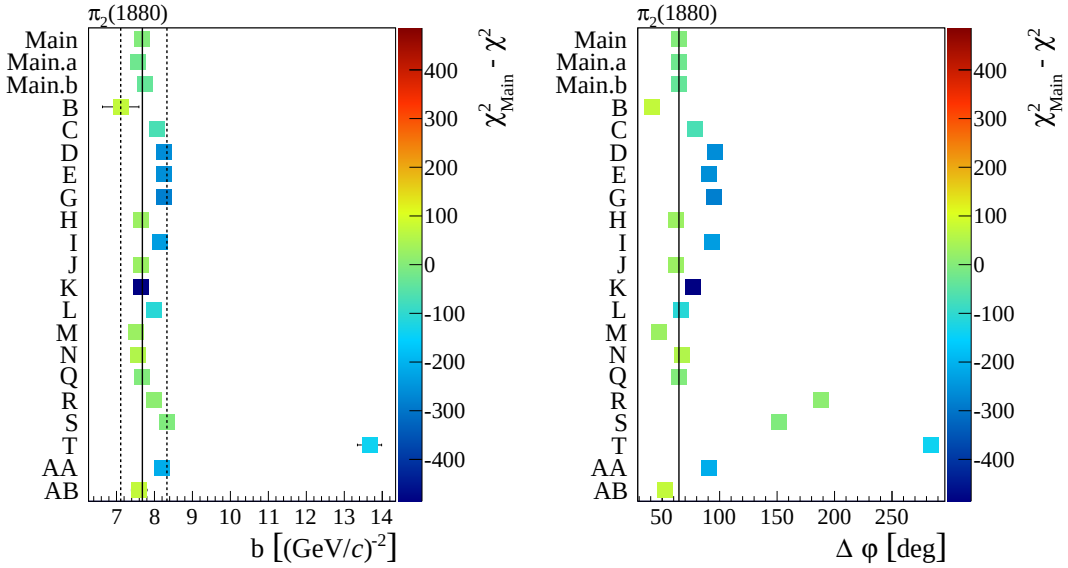

(a) Systematics of the t' slope parameter (b) Systematics of the maximal phase-motion

Figure 7.8: Systematic studies of the t' slope for the $\pi_2(1880)$ in the $2^{-+}0^+ f_2(1270)\pi S$ wave. The dashed lines in (a) represent the estimate for the systematic uncertainties. (b) compares the maximal phase-motion of the production phase with t' of the $\pi_2(1880)$ obtained from the different studies.

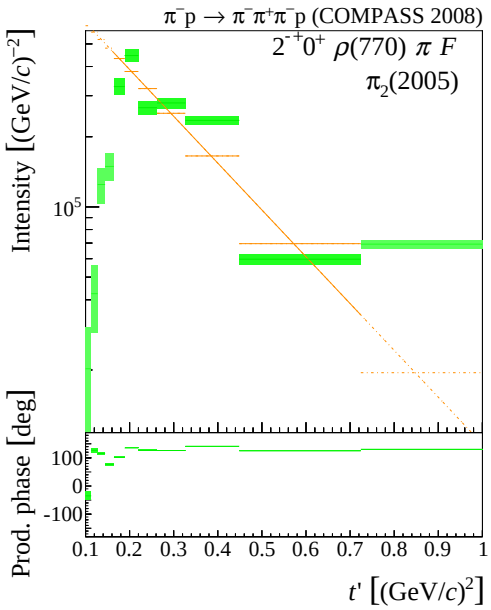

Figure 7.9: t' spectrum and production phase of the $\pi_2'(2005)$ in the $2^{-+}\,0^+\,\rho(770)\,\pi\,F$ wave of the study without branchings.

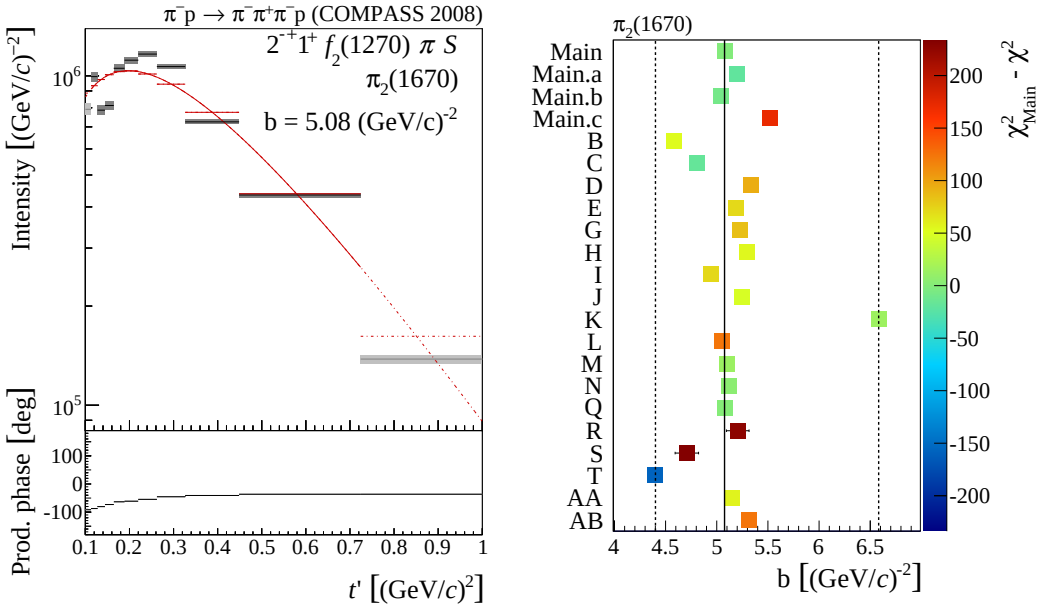

(a) t' spectrum and production phase

(b) t' slope parameter

Figure 7.10: t' spectrum and production phase of the $\pi_2(1670)$ resonance in the $2^{-+}\,1^+\,f_2(1270)\,\pi\,S$ wave (a) and the systematic uncertanties on the $\pi_2(1670)$ t' slope parameter in this wave (b). The dashed lines represent the estimate for the systematic uncertainties.

The t' spectrum of the $\pi_2(1670)$ resonance in the $2^{-+}\,1^+\,f_2(1270)\,\pi\,S$ wave (see figure 7.10a) has a much smaller slope of $5.1\,(\mathrm{GeV}/c)^{-2}$. The shape in the low-$t'$ region cannot be reproduced by the single-exponential model. When fitting only the intermediate t' region (study Main.c) from 0.220 to 0.724 $(\mathrm{GeV}/c)^2$, the slope increases to $5.5\,(\mathrm{GeV}/c)^{-2}$ but is still around $3\,(\mathrm{GeV}/c)^{-2}$ smaller compared to that in the $M = 0$ waves. Study (K) with the looser cuts in the event selection yields the largest slope of $6.6\,(\mathrm{GeV}/c)^{-2}$ for the $\pi_2(1670)$ in this wave. The large change in the production phase of the $\pi_2(1880)$ component, discussed above, indicates a change in the interference pattern between the resonant components in the $2^{-+}\,1^+\,f_2(1270)\,\pi\,S$ wave. This interference effects could lead to the unusually shallow t' dependence of the $\pi_2(1670)$ resonance in this wave.

The t' spectra of the non-resonant components in the 2^{-+} waves are collected in figure 7.11. In the $2^{-+}\,0^+\,\rho(770)\,\pi\,S$ wave, the non-resonant term shows a steep slope of $10\,(\mathrm{GeV}/c)^{-2}$ in the low-t' region, while in the high-t' region its slope of $5\,(\mathrm{GeV}/c)^{-2}$ is unusually shallow for a non-resonant term (see figure 7.11a). However, the production phase shows a large phase motion of more than 100°. Figure 7.11b shows the t' spectrum of the non-resonant term in the $2^{-+}\,0^+\,f_2(1270)\,\pi\,D$ wave. The extracted slope of $13.5\,(\mathrm{GeV}/c)^{-2}$ and the large phase motion of the production phase of 170° are in agreement with the non-resonant hypothesis. In the $2^{-+}\,0^+\,\rho(770)\,\pi\,F$ wave, the t' spectrum of the non-resonant term deviates from the expected single-exponential shape as shown in figure 7.11c. The non-resonant term does contribute only little to the $2^{-+}\,0^+\,\rho(770)\,\pi\,F$ wave and only in the high-t' region. Thus the observed t' spectrum

seems to be driven by imperfections of the model. Figure 7.11d shows the t' spectrum of the non-resonant term in the $2^{-+}\,1^{+}\,f_2(1270)\,\pi\,S$ wave. Except for some fluctuations in the lowest t' bins the single-exponential fit can reproduce the shape. The resonance-like t' slope of 7.3 $(\mathrm{GeV}/c)^{-2}$ and the small phase motion of the production phase of 40° indicate a still imperfect separation between resonant and non-resonant terms, also seen for the $\pi_2(1670)$ in this wave.

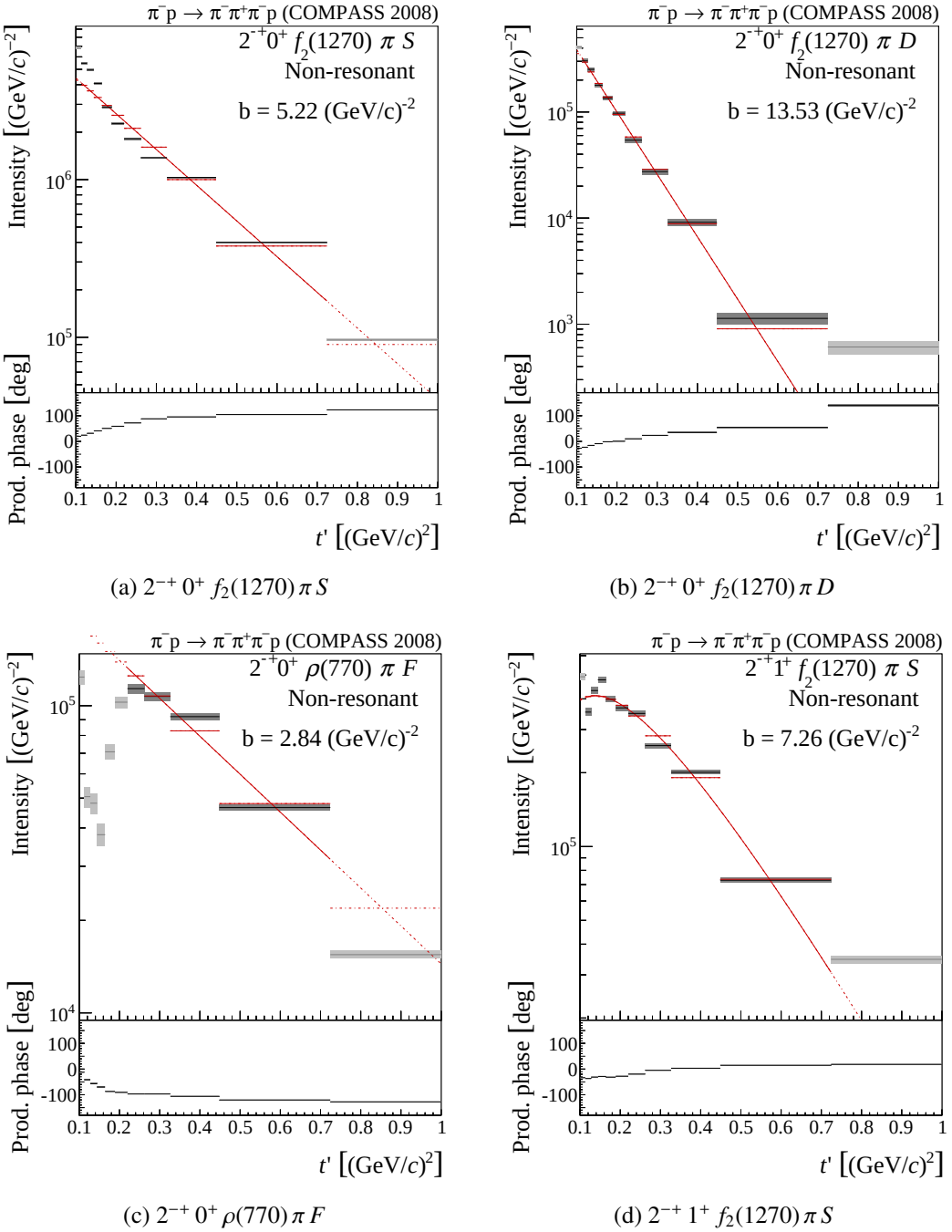

(a) $2^{-+}\,0^{+}\,f_2(1270)\,\pi\,S$

(b) $2^{-+}\,0^{+}\,f_2(1270)\,\pi\,D$

(c) $2^{-+}\,0^{+}\,\rho(770)\,\pi\,F$

(d) $2^{-+}\,1^{+}\,f_2(1270)\,\pi\,S$

Figure 7.11: t' spectra and production phases of the non-resonant components in the 2^{-+} waves.

7.6 The 1^{++} Waves

The t'-resolved partial-wave analysis of the $1^{++}\,0^+\,\rho(770)\,\pi\,S$ wave shows interesting features like the movement of the peak position with t', as discussed in section 5.4. To investigate this further, the t' dependence of its components is discussed in the following. The t' spectrum of the $a_1(1260)$ resonance in the $1^{++}\,0^+\,\rho(770)\,\pi\,S$ wave, obtained from the Main fit, is shown in figure 7.12a. As this component was chosen as the reference for all production phases, its relative production phase is fixed to zero. The shape of the t' spectrum can be reproduced by the single-exponential model with a slope of $12.68\,(\mathrm{GeV}/c)^{-2}$. The t'-spectrum of the non-resonant term in the $1^{++}\,0^+\,\rho(770)\,\pi\,S$ wave shows a very similar slope of $12.9\,(\mathrm{GeV}/c)^{-2}$. However, the relative production phase between both components has a large phase motion of 110°. This large change of the production phase between both components with t' leads to different interference patterns in the low- and high-t' regions, which manifests themselves as a shift of the peak position in the intensity spectrum with t'.

The t' slope parameter of the $a_1(1260)$ in the $1^{++}\,0^+\,\rho(770)\,\pi\,S$ wave has a large systematic uncertainty, as shown in figure 7.12b. Especially the studies (D), (E), (G), (I) and (AA) which result in the narrow $a_1(1260)$ solution (see section 5.4), where more of the $1^{++}\,0^+\,\rho(770)\,\pi\,S$ intensity is assigned to the non-resonant term, show a much shallower $a_1(1260)$ t' slope of 7.5 to $8.5\,(\mathrm{GeV}/c)^{-2}$. The same effect is observed in study (T) without fixed relative branchings (see figure 7.13a). With the increased $a_1(1260)$ intensity in the high-t' region the narrow peak is better described by the resonance model, as illustrated in figure 7.13b, which is not possible in the Main fit. In contrast, without fixed relative branchings, the t' slope of the $a_1(1260)$ in the $1^{++}\,0^+\,f_2(1270)\,\pi\,P$ wave becomes almost $3\,(\mathrm{GeV}/c)^{-2}$ steeper w.r.t. the one in the $1^{++}\,0^+\,\rho(770)\,\pi\,S$ wave. This shows, that there is some tension between the two 1^{++} waves. This tension could cause the bimodal behavior with the narrow $a_1(1260)$ solution, appearing in some studies.

The t' spectrum of the a_1' component in the $1^{++}\,0^+\,\rho(770)\,\pi\,S$ wave is shown in figure 7.14a. Except for the observed slight bending towards lower intensities in the low-t' region, the shape can be fitted well by the single-exponential model. The extracted t' slope of $7.2\,(\mathrm{GeV}/c)^{-2}$ shows relatively small systematic uncertainties (see figure 7.14b). Only in study (T) without fixed relative branchings, the slope parameter becomes significantly larger. This goes together with a large increase in the production phase motion from 20° in the Main solution to 180° in study (T), similar to the situation for the $\pi_2(1880)$ in the $2^{-+}\,0^+\,f_2(1270)\,\pi\,S$ wave, discussed in section 7.5. With a similar argument, the solution of study (T) is excluded from the systematic uncertainty of the a_1' t' slope. Removing the branchings in the $1^{++}\,0^+\,f_2(1270)\,\pi\,P$ wave, where the a_1' is dominant, only slightly decreases the t' slope of the a_1'. The resonance-like t' slope of $7.3\,(\mathrm{GeV}/c)^{-2}$ and the flat production phase w.r.t. the $a_1(1260)$ supports the resonance interpretation of a possible a_1' state.

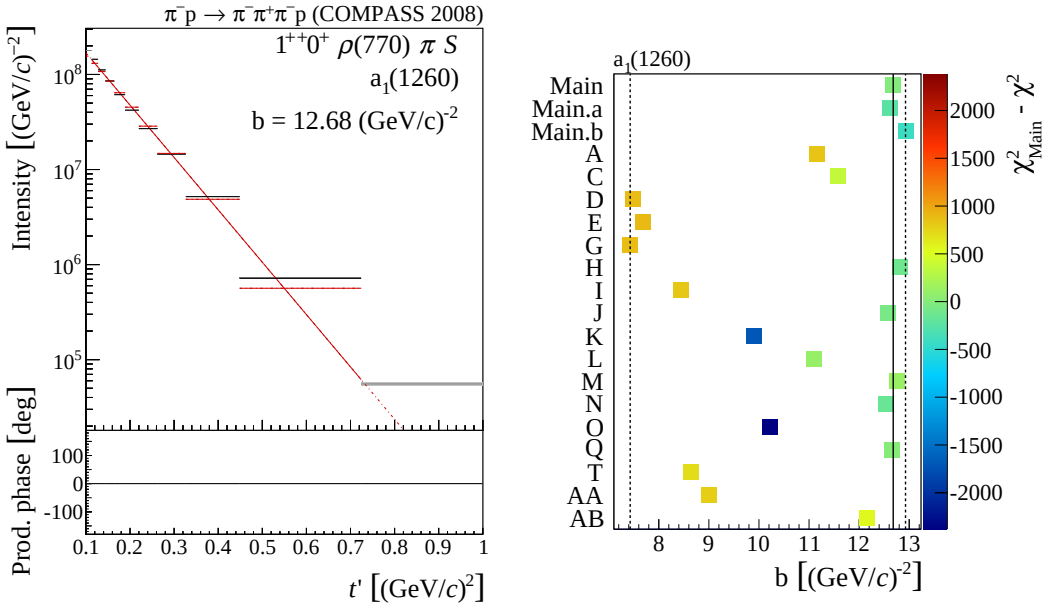

(a) t' spectrum and production phase

(b) t' slope parameter

Figure 7.12: t' spectrum and production phase of the $a_1(1260)$ resonance in the $1^{++}\,0^+\,\rho(770)\,\pi\,S$ wave (a) and the systematic uncertanties of the $a_1(1260)$ t' slope in this wave (b). The dashed lines represent the estimate for the systematic uncertainties.

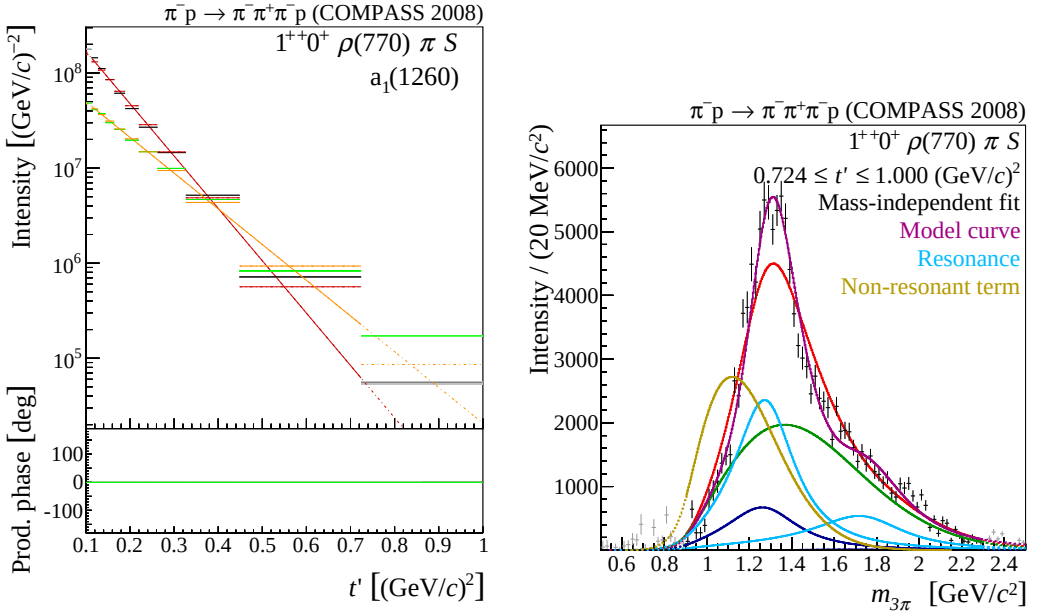

(a) t' spectrum

(b) Intensity spectrum

Figure 7.13: t' spectrum and production phase of the $a_1(1260)$ resonance in the $1^{++}\,0^+\,\rho(770)\,\pi\,S$ wave of the Main fit (black/red) compared to study (T) without fixed branchings (green/orange) (a) and the intensity spectrum of this wave in the highest t' bin (b) of the Main solution (red/blue/green) in comparison with study (T) without relative branchings (violet/cyan/orange).

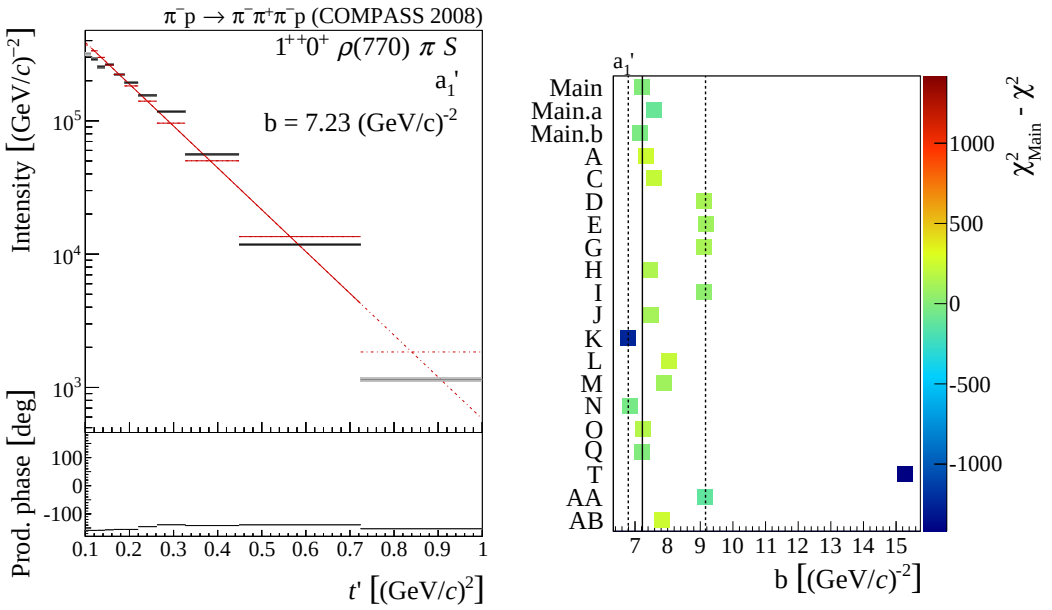

(a) t' spectrum and production phase

(b) t' slope parameter

Figure 7.14: t' spectrum and production phase of the a_1' resonance in the $1^{++}\,0^+\,\rho(770)\,\pi\,S$ wave (a) and the systematic uncertanties of the a_1' t' slope in this wave (b). The dashed lines represent the estimate for the systematic uncertainties.

7.7 The $1^{++}\,0^+\,f_0(980)\,\pi\,P$ Wave

The $1^{++}\,0^+\,f_0(980)\,\pi\,P$ exhibits a novel narrow signal, slightly above $1.4\,\mathrm{GeV}/c^2$. The interpretation of this signal as independent 1^{++} resonance, the $a_1(1420)$, was discussed in section 5.5. Figure 7.15a shows the t' spectrum and the production phase of this component. The extracted spectrum follows clearly the single-exponential model. The systematics of the extracted slope parameter of $9.47\,^{+0.24}_{-1.0}\,(\mathrm{GeV}/c)^{-2}$ (see figure 7.15b) show only one significant deviation from the Main fit. In study (K) with looser cuts in the event selection, a $1\,(\mathrm{GeV}/c)^{-2}$ shallower t' spectrum is found, but with a worse χ^2 of the single-exponential fit as compared to that of the Main solution (see color of the data point in figure 7.15a). The t' dependence of the $a_1(1420)$ is similar to those of well-known resonances like the $\pi(1800)$, which supports its resonance interpretation. There are speculations that the $a_1(1420)$ signal is not an independent resonance, but arises from a singularity in the $a_1(1260)$ decay into $K\overline{K}^*$ (see section 8.1 or [43]). It should be noticed, that the $a_1(1420)$ component shows a different t' spectrum and a slow phase motion in the production phase of 50° compared to the $a_1(1260)$. However, due to the large systematic uncertainties of the t' dependence of the $a_1(1260)$, a common source of both structures cannot be excluded. The non-resonant term in the $1^{++}\,0^+\,f_0(980)\,\pi\,P$ wave shows a steeper t' slope of $11.6\,(\mathrm{GeV}/c)^{-2}$ and a large phase motion of the production phase of 150°, which is similar to the observations for the non-resonant components in other waves.

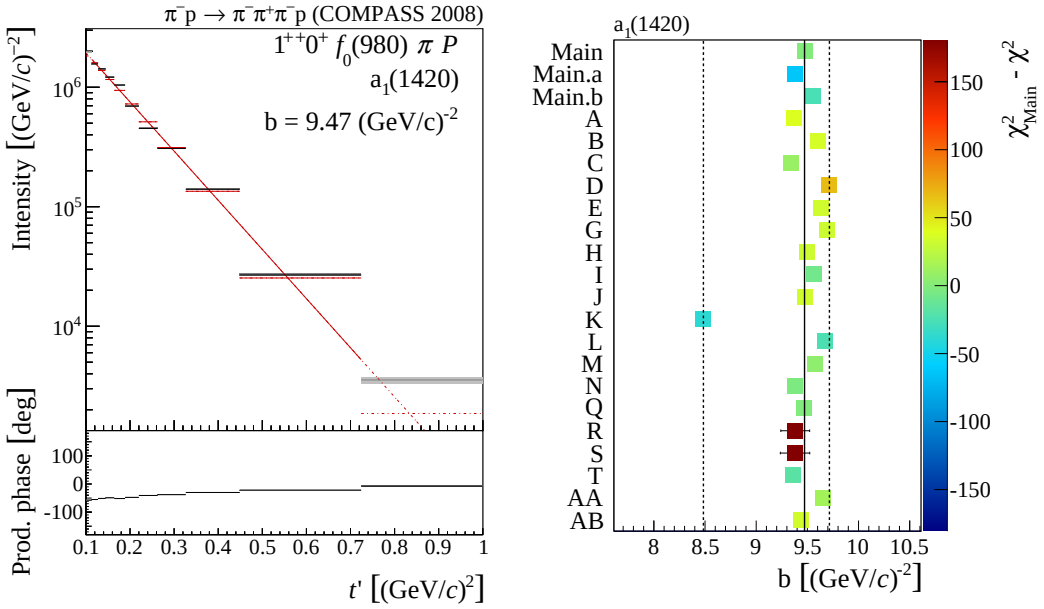

(a) t' spectrum and production phase

(b) t' slope parameter

Figure 7.15: t' spectrum and production phase of the $a_1(1420)$ in the $1^{++}\,0^+\,f_0(980)\,\pi\,P$ wave (a) and the systematic uncertainties on the $a_1(1420)$ t' slope parameter in this wave (b). The dashed lines represent the estimate for the systematic uncertainties.

7.8 The $\pi_1(1600)$ Spin-Exotic Resonance

One of the main aims of this analysis is the investigation of a possible $\pi_1(1600)$ resonance in the $1^{-+}\,1^+\,\rho(770)\,\pi\,P$ wave with spin-exotic quantum numbers. Concerning the $\pi_1(1600)$ resonance parameters, large systematic uncertainties are observed, as shown in chapter 6. In the following, the t' dependence of the $\pi_1(1600)$ component is investigated to gain further insight into its complicated structure.

The t' spectrum and production phase of the $\pi_1(1600)$ are shown in figure 7.16a. The shape is not in agreement with the single-exponential assumption for $M = 1$ and cannot be reproduced by the fit. The maximum is shifted towards higher t' values w.r.t. the single-exponential assumption (red line) with a too steep drop going to lower t'. The extracted t' slope is $7.2\,^{+1.0}_{-3.1}(\mathrm{GeV}/c)^{-2}$, with a large systematic uncertainty. The systematic studies show two clusters of solutions (see figure 7.16b). One centered around the solution of the Main fit within $1.0\,(\mathrm{GeV}/c)^{-2}$ and a second cluster around a slope of $4.5\,(\mathrm{GeV}/c)^{-2}$. The studies in the second cluster are associated with the narrow $a_1(1260)$ solutions. This illustrates the strong correlation between the $\pi_1(1600)$ and the a_1 resonances within the resonance model, also observed for the resonance parameters (see chapter 6). The production phase shows a slow phase-motion w.r.t. the $a_1(1260)$ of only 25°. In contrast to the $\pi_1(1600)$, the non-resonant component in the spin-exotic wave exhibits a much steeper t' slope of $19.0\,(\mathrm{GeV}/c)^{-2}$ with a large phase motion in the production phase of more than 200°. This shows that the $1^{-+}\,1^+\,\rho(770)\,\pi\,P$ wave presumably has different components

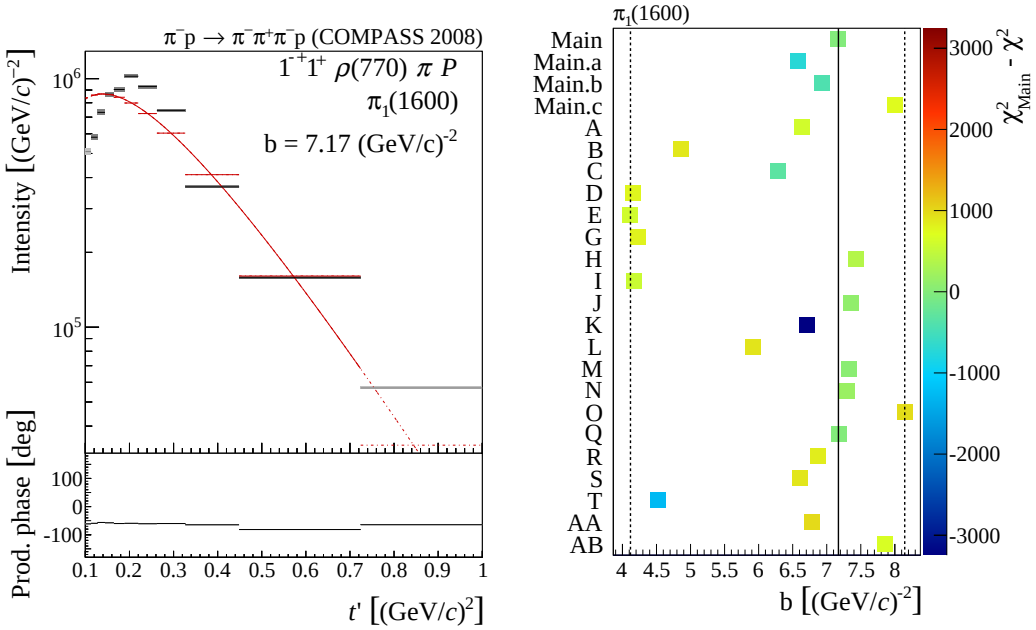

(a) t' spectrum and production phase

(b) t' slope parameter

Figure 7.16: t' spectrum and production phase of a possible $\pi_1(1600)$ resonance in the $1^{-+}\,1^{+}\,\rho(770)\,\pi\,P$ wave (a) and the systematic uncertanties on the $\pi_1(1600)$ t' slope parameter in this wave (b). The dashed lines represent the estimate for the systematic uncertainties.

with different t' characteristics. Due to the t'-resolved information, the fit is able to separate these components to a large degree. However, the large systematic uncertainties indicate, that the model needs to be improved. Especially a more realistic parameterization of the non-resonant term is required, in order to be able to make conclusive statements abut the existence of the $\pi_1(1600)$.

Table 7.1: Extracted t' slope parameters in units of $(\mathrm{GeV}/c)^{-2}$ and their systematic uncertainties.

(a) 0^{-+} Waves

Wave	$\pi(1800)$	Non-Resonant
$0^{-+}0^{+}f_0(980)\pi S$	$8.72\,^{+0.7}_{-0.28}$	$27.5\,^{+1.9}_{-8}$

(b) 1^{++} Waves

Wave	$a_1(1260)$	$a_1(1420)$	a_1'	Non-Resonant
$1^{++}0^{+}\rho(770)\pi S$	$12.68\,^{+0.25}_{-5}$	—	$7.2\,^{+1.9}_{-0.4}$	$12.9\,^{+3.5}_{-2.7}$
$1^{++}0^{+}f_2(1270)\pi P$	$12.3\,^{+2.4}_{-5}$	—	$7.3\,^{+1.8}_{-0.6}$	$12.3\,^{+2.5}_{-2.9}$
$1^{++}0^{+}f_0(980)\pi P$	—	$9.47\,^{+0.24}_{-1.0}$	—	$11.6\,^{+0.8}_{-1.2}$

(c) 1^{-+} Waves

Wave	$\pi_1(1600)$	Non-Resonant
$1^{-+}1^{+}\rho(770)\pi P$	$7.2\,^{+1.0}_{-3.1}$	$19.0\,^{+0.7}_{-5}$

(d) 2^{++} Waves

Wave	$a_2(1320)$	a_2'	Non-Resonant
$2^{++}1^{+}\rho(770)\pi D$	$7.88\,^{+0.24}_{-0.6}$	$6.8\,^{+5}_{-0.6}$	$13.4\,^{+0.5}_{-1.3}$
$2^{++}1^{+}f_2(1270)\pi P$	$7.87\,^{+0.21}_{-0.5}$	$6.8\,^{+1.7}_{-0.6}$	$9.5\,^{+4}_{-1.4}$
$2^{++}2^{+}\rho(770)\pi D$	$9.05\,^{+0.11}_{-0.5}$	$15\,^{+5}_{-7}$	$8.5\,^{+2.4}_{-0.5}$

(e) 2^{-+} Waves

Wave	$\pi_2(1670)$	$\pi_2(1880)$	$\pi_2'(2005)$	Non-Resonant
$2^{-+}0^{+}f_2(1270)\pi S$	$8.40\,^{+0.34}_{-0.7}$	$7.7\,^{+0.6}_{-0.6}$	$6.41\,^{+0.26}_{-1.3}$	$5.2\,^{+5}_{-0.5}$
$2^{-+}0^{+}f_2(1270)\pi D$	$8.40\,^{+0.33}_{-1.7}$	$7.7\,^{+0.7}_{-0.6}$	$6.43\,^{+0.21}_{-0.9}$	$13.5\,^{+5}_{-2.2}$
$2^{-+}0^{+}\rho(770)\pi F$	$8.40\,^{+0.33}_{-0.4}$	$7.7\,^{+0.6}_{-0.6}$	$6.42\,^{+0.24}_{-0.9}$	$2.8\,^{+2.8}_{-4}$
$2^{-+}1^{+}f_2(1270)\pi S$	$5.1\,^{+1.5}_{-0.7}$	$8.4\,^{+4}_{-1.8}$	$7.4\,^{+3.4}_{-1.4}$	$7.3\,^{+1.1}_{-2.0}$

(f) 4^{++} Waves

Wave	$a_4(2040)$	Non-Resonant
$4^{++}1^{+}\rho(770)\pi G$	$9.22\,^{+0.13}_{-0.5}$	$14\,^{+4}_{-4}$
$4^{++}1^{+}f_2(1270)\pi F$	$9.22\,^{+0.13}_{-0.6}$	$14.4\,^{+1.9}_{-4}$

CHAPTER 8

Conclusions and Outlook

8.1 Conclusions

The investigation of meson resonances in diffractive production and the extraction of their resonance parameters is a major challenge. In this analysis, the a_J and π_J light meson resonances were investigated in the $\pi^-\pi^-\pi^+$ final state, in the reaction $\pi^- + p \to \pi^-\pi^-\pi^+ + p_{\text{recoil}}$. Their masses and widths were extracted performing the largest resonance-model fit ever used in this channel, which consistently describes more than 50 % of the total intensity. Due to the high statistical precision of the COMPASS data, an extensive investigation of the systematic uncertainties is indispensable, as done in this thesis.

The resonance parameters of the $a_2(1320)$, $a_4(2040)$ and $\pi(1800)$ resonances can be extracted with small uncertainties. They are in fair agreement with previous observations. Furthermore, the stability of the t' spectra of these components and the extracted slope parameters of 8 to 9 $(\text{GeV}/c)^{-2}$ demonstrate, that these signals are robust against systematic effects. Therefore, these components are used as well-defined interferometers for other components in the resonance model.

For the $a_1(1260)$ resonance, large systematic effects on the resonance parameters and the t' dependence are observed. These instabilities are mostly driven by the large non-resonant contribution in the $1^{++}\,0^+\,\rho(770)\,\pi\,S$ wave and the inability of the model to reproduce the fine details of the peak shape. Due to the high statistical precision in this wave, even small changes in its description by the resonance model lead to large increases in χ^2. Together with the flexibility of the non-resonant parameterization, this potentially amplifies model artifacts and leads to a bimodal behavior of the $a_1(1260)$ component with the appearance of solutions with wide and narrow $a_1(1260)$. These instabilities, limit a precise interpretation of the intensity peak in the $1^{++}\,0^+\,\rho(770)\,\pi\,S$ wave.

For a consistent description of the data, it is necessary to include a excited a_1 and a_2 resonance, the a_1' and the a_2', in the resonance model. While the PDG [6] lists excited a_1 and a_2 states

with masses, similar to those observed in this analysis, the widths obtained from COMPASS data are much larger compared to previous measurements. This could be an indication for an imperfect separation between the resonant and non-resonant contributions. There are no clear reference waves for the a_1' and a_2', because the mass region around $1.6\,\mathrm{GeV}/c^2$ is crowded with resonances in almost all partial waves. Together with the dominant ground states and the large non-resonant contributions, a separation between the different components is very difficult. On the other hand, the t' dependences of the a_1' and a_2' components are consistent with resonance structures. There is evidence for both resonances in the data, but a perfect separation from the other terms of the model is difficult. This is reflected in the large systematic uncertainties of the a_1' and a_2' parameters.

For the first time four 2^{-+} waves are analyzed simultaneously in a resonance-model fit. They show a variety of different features with different t' dependences. While the $\pi_2(1670)$ is dominant in the 2^{-+} $f_2(1270)\,\pi\,S$ waves and the $\pi_2(1880)$ is clearly visible in the $f_2(1270)\,\pi\,D$ decay mode, the strongest evidence for a $\pi_2'(2005)$ is observed mainly in the high-t' region of the $\rho(770)\,\pi\,F$ wave. Without this third π_2 resonance, not all features of the 2^{-+} waves are reproduced and the parameters of the $\pi_2(1880)$ are strongly shifted. Furthermore, the t' slope parameters of the different resonance components support the hypothesis of three π_2 resonances. On the other hand, the systematic studies show, that the overlap of the π_2 resonances and the uncertainty in the non-resonant description make an exact separation of these components difficult.

The novel signal in the $1^{++}\,0^+\,f_0(980)\,\pi\,P$ wave slightly above $1.4\,\mathrm{GeV}/c^2$ has also been observed in the $\pi^-\pi^0\pi^0$ final state by the COMPASS [32] and VES [44] experiments. The peak shows clear resonance characteristics and is consistently described by an independent narrow a_1 resonance named $a_1(1420)$. The extracted $a_1(1420)$ parameters are consistent with the results of a previous analysis of the COMPASS data with a resonance-model of only three partial waves [45]. Furthermore, the additional information of the extended wave set of 14 waves, used in this analysis, significantly reduces the systematic uncertainties of the $a_1(1420)$ by a factor of 3. The t' dependence of the $a_1(1420)$ is in good agreement with other resonances like the $\pi(1800)$. However, the interpretation of this signal is unclear. It is only $114\,\mathrm{MeV}/c^2$ heavier than the $a_1(1260)$ ground state, which would be unusually close for an excited quark-model state. Also the fact, that it is seen only in the $f_0(980)\,\pi\,P$ decay leads to speculations. The $f_0(980)$ is assumed to have significant strangeness content and was proposed to be a $K\overline{K}$ molecule or a tetraquark state [46, 47]. Accordingly, there are tetraquark interpretations of the $a_1(1420)$ proposed by Wang [48] or Chen et al. [49]. Another peculiar property of the $a_1(1420)$ is its proximity to the $K\overline{K}^*$ threshold at around $1390\,\mathrm{MeV}/c^2$. This inspired an alternative interpretation of the $a_1(1420)$ by Mikhasenko et al. [43]. They showed, that the general shape of the intensity spectrum in the $1^{++}\,0^+\,f_0(980)\,\pi\,P$ wave and its relative phase to the $a_1(1260)$ can be explained by a triangle singularity in the rescattering reaction $a_1(1260) \to K\overline{K}^* \to K\overline{K}\,\pi^- \to f_0(980)\,\pi^-$. As discussed in section 5.4, non-resonant processes contribute significantly to the 1^{++} waves. Therefore, Berger and Basdevant [50] interpreted the signal in the $1^{++}\,0^+\,f_0(980)\,\pi\,P$ wave as an interference and rescattering effect of the $a_1(1260)$ with the Deck-like non-resonant contributions. A discrimination between these various possible interpretations can only be done by direct comparison with the data.

One of the most disputed experimental findings in the light-meson sector is the observation of the $\pi_1(1600)$ resonance with spin-exotic quantum numbers $J^{PC} = 1^{-+}$. In this analysis, the broad bump in the $1^{-+}\,1^+\,\rho(770)\,\pi\,P$ wave, observed in the COMPASS data, is parameterized by a non-resonant term and a possible $\pi_1(1600)$ resonance. The resonance parameters show large systematic uncertainties. A strong correlation with the $a_1(1260)$ parameters is observed in the systematic studies. Especially the appearance of the narrow $a_1(1260)$ solution has dramatic influence on the $\pi_1(1600)$ width and its t' slope parameter, which both become smaller. The study without the $\pi_1(1600)$ in the resonance model shows a clear need for a resonance-like component mostly in the high-t' region. However, requiring analyticity of the amplitude [31], the peak-like structure of the non-resonant term formed by the fit should in principle have a certain phase motion with $m_{3\pi}$. Such a phase motion is not included in the employed model for the non-resonant term. Furthermore, the t' spectrum of the $\pi_1(1600)$ deviates from the expected single-exponential shape in the low-t' region. Nevertheless, the extracted t' slope parameter of $7\,(\mathrm{GeV}/c)^{-2}$ and the small phase motion of the production phase with t', together with the much steeper t' slope of the non-resonant term in the spin-exotic $1^{-+}\,1^+\,\rho(770)\,\pi\,P$ wave, are in favor of the resonance interpretation. Although the systematic uncertainties are large, the significant contribution of the $\pi_1(1600)$ component to the spin-exotic 1^{-+} wave is stable in all systematic studies. However, in order to be able to make conclusive statements, the understanding of the non-resonant contributions has to be improved.

8.2 Outlook

One of the major complications of this analysis is the treatment of the non-resonant contributions. To overcome this problem, an alternative approach is presented in [51], which, instead of treating the non-resonant contributions at the level of the resonance-model fit, includes an independent "partial-wave" amplitude $\mathcal{A}_{\mathrm{non}}$ already at the stage of the partial-wave decomposition. In this way, the non-resonant contributions should be mostly absorbed by the additional amplitude $\mathcal{A}_{\mathrm{non}}$, instead of being projected into other partial waves. However, also this approach is sensitive to the used model for the non-resonant contributions.

To avoid the explicit modeling of the non-resonant contributions, the general requirements of unitarity and analyticity of the amplitudes can be exploited to construct a general parameterization for the transition amplitudes. Instead of summing over various model components, all contributions are described with one parameterization. Finally, the results should be independent of the explicit parameterizations, as long as they satisfies unitarity and analyticity [31, 52]. This can be done in the framework of the K-matrix formalism, which has been used, for example, to describe the $J^{PC} = 0^{++}$ isoscalar sector [53]. A first attempt to describe the amplitude of the spin-exotic $1^{-+}\,1^+\,\rho(770)\,\pi\,P$ wave yields promising results, but further investigations and developments are needed.

The wave set used in the partial-wave decomposition consists of 88 partial waves, but only 14 have been investigated in the resonance-model fit so far. Especially the 2^{-+} sector, which includes

17 waves, shows a rich spectrum of interesting features. As demonstrated in this analysis, with a solid bases wave set, all these striking structures can be investigated.

In addition to the charged three-pion final state, the COMPASS experiment also collected a large data set with two neutral pions in the final state ($\pi^- + p \to \pi^- \pi^0 \pi^0 + p_{\text{recoil}}$) [32]. With the method presented in this analysis, the meson resonances can be investigated also in this channel. This would allow for a consistency check between both final states, which are related by isospin symmetry.

The COMPASS experiment has collected a data set with outstanding statistical precision. This is a great opportunity to deepen our knowledge about the light-meson sector, but it is also a major challenge for models. Upcoming experiments like GlueX [54] will even exceed this precision. Therefore, it is essential to now identify the imperfection in the used models, as done in this thesis, and improve the models further.

APPENDIX A

Calculation of the Beam Energy

The energy of the incident beam pion for the reaction $\pi^- + p \rightarrow \pi^-\pi^-\pi^+ + p_{\text{recoil}}$ can be directly calculated from the measured three-momenta of the $\pi^-\pi^-\pi^+$ final state[1]

$$\vec{p}_{\text{X}} = \sum_{i=1}^{3} \vec{p}_i \tag{A.1}$$

$$E_{\text{X}} = \sum_{i=1}^{3} E_i = \sum_{i=1}^{3} \sqrt{|\vec{p}_i|^2 + m_\pi^2} \tag{A.2}$$

without knowing the momentum of the recoil proton and under the assumption, that the target proton is at rest in the lab frame [1]. The squared four-momentum transfer can be calculated from the four-momenta of the target proton before p_{target} and after p_{recoil} the interaction

$$t = (p_{\text{recoil}} - p_{\text{target}})^2 = 2m_p^2 - 2p_{\text{recoil}} \cdot p_{\text{target}} = 2m_p^2 - 2m_p E_{\text{recoil}} \tag{A.3}$$

$$= 2m_p \left\{ m_p - \left[m_p + (E_{\text{beam}} - E_{\text{X}}) \right] \right\} \tag{A.4}$$

$$= 2m_p (E_{\text{X}} - E_{\text{beam}}) \tag{A.5}$$

using energy conservation $E_{\text{recoil}} + E_{\text{X}} = E_{\text{target}} + E_{\text{beam}}$ and $E_{\text{target}} = m_p$ for a proton at rest. Alternatively, t can be calculated from the momenta of the beam pion and the 3π system X

$$t = (p_{\text{beam}} - p_{\text{X}})^2 = m_\pi^2 + m_{\text{X}}^2 - 2E_{\text{beam}}E_{\text{X}} + 2\vec{p}_{\text{beam}} \cdot \vec{p}_{\text{X}} \tag{A.6}$$

$$= m_\pi^2 + m_{\text{X}}^2 - 2E_{\text{beam}}E_{\text{X}} + 2E_{\text{beam}}|\vec{p}_{\text{X}}| \sqrt{1 - \frac{m_\pi^2}{E_{\text{beam}}^2}} \cos\vartheta. \tag{A.7}$$

Setting equation (A.5) equal to equation (A.7) gives an equation for the assumed beam energy E_{beam}, dependent only on the kinematics of the three-pion system. This equation can be solved numerically or analytically using the approximation $\sqrt{1 - \frac{m_\pi^2}{E_{\text{beam}}^2}} \approx 1 - \frac{m_\pi^2}{2E_{\text{beam}}^2}$ for $E_{\text{beam}} \gg m_\pi$.

[1] For simplicity, natural units are used $\hbar = c = 1$ here.

APPENDIX B

Partial-Wave Model

In table B.1, the wave set used for the partial-wave decomposition is summarized. The $J^{PC}\,M^{\varepsilon}$ quantum numbers are listed together with the isobar and the angular momentum L between isobar and bachelor pion of the decay. The threshold is the lowest three-pion mass for which the wave is included in the wave set. If no threshold is given, the wave is used over the full analyzed mass range of $500 < m_{3\pi} < 2500\,\mathrm{MeV}/c^2$.

Table B.1: Wave set used for the mass-independent fit. The table is taken from [2].

$J^{PC}\,M^{\varepsilon}$	Isobar	L	Threshold [MeV/c^2]
$0^{-+}\,0^{+}$	$[\pi\pi]_S$	S	—
$0^{-+}\,0^{+}$	$\rho(770)$	P	—
$0^{-+}\,0^{+}$	$f_0(980)$	S	1200
$0^{-+}\,0^{+}$	$f_2(1270)$	D	—
$0^{-+}\,0^{+}$	$f_0(1500)$	S	1700
$1^{++}\,0^{+}$	$[\pi\pi]_S$	P	—
$1^{++}\,1^{+}$	$[\pi\pi]_S$	P	1100
$1^{++}\,0^{+}$	$\rho(770)$	S	—
$1^{++}\,1^{+}$	$\rho(770)$	S	—
$1^{++}\,0^{+}$	$\rho(770)$	D	—
$1^{++}\,1^{+}$	$\rho(770)$	D	—
$1^{++}\,0^{+}$	$f_0(980)$	P	1180
$1^{++}\,1^{+}$	$f_0(980)$	P	1140
$1^{++}\,0^{+}$	$f_2(1270)$	P	1220
$1^{++}\,1^{+}$	$f_2(1270)$	P	—
$1^{++}\,0^{+}$	$f_2(1270)$	F	—
$1^{++}\,0^{+}$	$\rho_3(1690)$	D	—
$1^{++}\,0^{+}$	$\rho_3(1690)$	G	—
$1^{-+}\,1^{+}$	$\rho(770)$	P	—
$2^{++}\,1^{+}$	$\rho(770)$	D	—
$2^{++}\,2^{+}$	$\rho(770)$	D	—
$2^{++}\,1^{+}$	$f_2(1270)$	P	1000
$2^{++}\,2^{+}$	$f_2(1270)$	P	1400
$2^{++}\,1^{+}$	$\rho_3(1690)$	D	800
$2^{-+}\,0^{+}$	$[\pi\pi]_S$	D	—
$2^{-+}\,1^{+}$	$[\pi\pi]_S$	D	—
$2^{-+}\,0^{+}$	$\rho(770)$	P	—
$2^{-+}\,1^{+}$	$\rho(770)$	P	—
$2^{-+}\,2^{+}$	$\rho(770)$	P	—
$2^{-+}\,0^{+}$	$\rho(770)$	F	—
$2^{-+}\,1^{+}$	$\rho(770)$	F	—
$2^{-+}\,0^{+}$	$f_0(980)$	D	1160
$2^{-+}\,0^{+}$	$f_2(1270)$	S	—
$2^{-+}\,1^{+}$	$f_2(1270)$	S	1100
$2^{-+}\,2^{+}$	$f_2(1270)$	S	—
$2^{-+}\,0^{+}$	$f_2(1270)$	D	—
$2^{-+}\,1^{+}$	$f_2(1270)$	D	—
$2^{-+}\,2^{+}$	$f_2(1270)$	D	—
$2^{-+}\,0^{+}$	$f_2(1270)$	G	—
$2^{-+}\,0^{+}$	$\rho_3(1690)$	P	1000
$2^{-+}\,1^{+}$	$\rho_3(1690)$	P	1300
$3^{++}\,0^{+}$	$[\pi\pi]_S$	F	1380
$3^{++}\,1^{+}$	$[\pi\pi]_S$	F	1380
$3^{++}\,0^{+}$	$\rho(770)$	D	—
$3^{++}\,1^{+}$	$\rho(770)$	D	—
$3^{++}\,0^{+}$	$\rho(770)$	G	—
$3^{++}\,1^{+}$	$\rho(770)$	G	—
$3^{++}\,0^{+}$	$f_2(1270)$	P	960
$3^{++}\,1^{+}$	$f_2(1270)$	P	1140
$3^{++}\,0^{+}$	$\rho_3(1690)$	S	1380
$3^{++}\,1^{+}$	$\rho_3(1690)$	S	1380
$3^{++}\,0^{+}$	$\rho_3(1690)$	I	—
$3^{-+}\,1^{+}$	$\rho(770)$	F	—
$3^{-+}\,1^{+}$	$f_2(1270)$	D	1340
$4^{++}\,1^{+}$	$\rho(770)$	G	—
$4^{++}\,2^{+}$	$\rho(770)$	G	—
$4^{++}\,1^{+}$	$f_2(1270)$	F	—
$4^{++}\,2^{+}$	$f_2(1270)$	F	—
$4^{++}\,1^{+}$	$\rho_3(1690)$	D	1700
$4^{-+}\,0^{+}$	$[\pi\pi]_S$	G	1400
$4^{-+}\,0^{+}$	$\rho(770)$	F	—
$4^{-+}\,1^{+}$	$\rho(770)$	F	—
$4^{-+}\,0^{+}$	$f_2(1270)$	D	—
$4^{-+}\,1^{+}$	$f_2(1270)$	D	—
$4^{-+}\,0^{+}$	$f_2(1270)$	G	1600
$5^{++}\,0^{+}$	$[\pi\pi]_S$	H	—
$5^{++}\,1^{+}$	$[\pi\pi]_S$	H	—
$5^{++}\,0^{+}$	$\rho(770)$	G	—
$5^{++}\,0^{+}$	$f_2(1270)$	F	980
$5^{++}\,1^{+}$	$f_2(1270)$	F	—
$5^{++}\,0^{+}$	$f_2(1270)$	H	—
$5^{++}\,0^{+}$	$\rho_3(1690)$	D	1360
$6^{++}\,1^{+}$	$\rho(770)$	I	—
$6^{++}\,1^{+}$	$f_2(1270)$	H	—
$6^{-+}\,0^{+}$	$[\pi\pi]_S$	I	—
$6^{-+}\,1^{+}$	$[\pi\pi]_S$	I	—
$6^{-+}\,0^{+}$	$\rho(770)$	H	—
$6^{-+}\,1^{+}$	$\rho(770)$	H	—
$6^{-+}\,0^{+}$	$f_2(1270)$	G	—
$6^{-+}\,0^{+}$	$\rho_3(1690)$	F	—
$1^{++}\,1^{-}$	$\rho(770)$	S	—
$1^{-+}\,0^{-}$	$\rho(770)$	P	—
$1^{-+}\,1^{-}$	$\rho(770)$	P	—
$2^{++}\,0^{-}$	$\rho(770)$	D	—
$2^{++}\,0^{-}$	$f_2(1270)$	P	1180
$2^{++}\,1^{-}$	$f_2(1270)$	P	1300
$2^{-+}\,1^{-}$	$f_2(1270)$	S	—
Flat			—

APPENDIX C

Start-Parameter Ranges and Fitting Schemes

The fit parameters in the resonance-model fit are released in the following sequence:

1. The coupling parameters $C_\alpha^k(t')$ are fitted, using two methods to determine the start values for the couplings and keeping the shape parameters ζ_k and branchings ${}_\alpha B_\beta^k$ fixed.

   I Randomized: 25 sets of random start-parameters for the couplings are generated, fitted and the best fit result with the lowest χ^2 is used. These fits are performed independently in each t' bin.

   II Propagated: 25 sets of random start-parameters for the couplings are generated only for the lowest t' bin. For the other t' bins, the result of the previous bin is used as start-parameter set.

2. The branching parameters ${}_\alpha B_\beta^k$ are fitted in two consecutive steps, keeping the shape parameters fixed.

   a) Fix the coupling parameters to the values determined in (1) and fit the branchings.

   b) Release additionally the couplings and fit branching and coupling parameters.

3. Using the outcome of (2) as start-parameter set for the couplings and branchings, the shape parameters ζ_k are released in four different orders (coupling and branching parameters are always released).

   I) All shape parameters are released at once.

   II) a) First the shape parameters of the non-resonant terms are released.

   b) Then the shape parameters of the resonances are released.

III) a) First the shape parameters of the non-resonant terms in the dominant J^{PC} sectors (1^{++} [except $1^{++}\,0^{+}\,f_0(980)\,\pi\,P$], 2^{++}, 2^{-+}) are released.

b) Then the ones of the resonances in the dominant waves.

c) In a third step, all shape-parameters of all components in the remaining waves are released.

IV) a) First the shape parameters of the non-resonant terms in the dominant J^{PC} sectors [see (III)] are released.

b) Then the ones of the non-resonant terms of the remaining waves.

c) In a third step, the shape parameters of the resonances of the dominant J^{PC} sectors are released.

d) Finally, the shape parameters of the resonances in the remaining waves are released.

Table C.1: Start-parameter ranges for all resonant components.

Resonance	Start-parameter ranges	
	Mass [GeV/c^2]	Width [GeV/c^2]
$a_1(1260)$	1.20 to 1.35	0.20 to 0.70
$a_1(1420)$	1.40 to 1.43	0.10 to 0.20
a_1'	1.85 to 2.00	0.10 to 0.50
$a_2(1320)$	1.31 to 1.32	0.05 to 0.15
a_2'	1.60 to 2.00	0.20 to 0.80
$a_4(2040)$	1.90 to 2.05	0.30 to 0.50
$\pi(1800)$	1.75 to 1.85	0.18 to 0.25
$\pi_1(1600)$	1.50 to 1.70	0.20 to 0.60
$\pi_2(1670)$	1.60 to 1.70	0.28 to 0.40
$\pi_2(1880)$	1.80 to 2.00	0.20 to 0.50
$\pi_2'(2005)$	1.95 to 2.20	0.20 to 0.40

Table C.2: Start-parameter ranges for the non-resonant terms.

Partial-wave	Start-parameter ranges				
	Simplified	Extended			
	c $[(\mathrm{GeV}/c)^{-2}]$	b	c_0 $[(\mathrm{GeV}/c)^{-2}]$	c_1 $[(\mathrm{GeV}/c)^{-4}]$	c_2 $[(\mathrm{GeV}/c)^{-6}]$
$0^{-+}\,0^{+}\,f_0(980)\,\pi\,S$	-10 to 0	—	—	—	—
$1^{++}\,0^{+}\,\rho(770)\,\pi\,S$	—	0 to 10	-30 to 10	-20 to 60	-60 to 10
$1^{++}\,0^{+}\,f_2(1270)\,\pi\,P$	-10 to 0	—	—	—	—
$1^{++}\,0^{+}\,f_0(980)\,\pi\,P$	-15 to 0	—	—	—	—
$1^{-+}\,1^{+}\,\rho(770)\,\pi\,P$	—	0 to 15	-20 to 10	-40 to 35	-30 to 40
$2^{++}\,1^{+}\,\rho(770)\,\pi\,D$	—	0 to 35	-20 to 20	-60 to 60	-80 to 80
$2^{++}\,1^{+}\,f_2(1270)\,\pi\,P$	-10 to 0	—	—	—	—
$2^{-+}\,1^{+}\,f_2(1270)\,\pi\,S$	-10 to 0	—	—	—	—
$2^{-+}\,0^{+}\,f_2(1270)\,\pi\,S$	—	0 to 15	-20 to 10	-40 to 35	-30 to 40
$2^{-+}\,0^{+}\,f_2(1270)\,\pi\,D$	-10 to 0	—	—	—	—
$2^{-+}\,0^{+}\,\rho(770)\,\pi\,F$	—	0 to 15	-20 to 10	-40 to 35	-30 to 40
$2^{-+}\,1^{+}\,f_2(1270)\,\pi\,S$	-10 to 0	—	—	—	—
$4^{++}\,1^{+}\,\rho(770)\,\pi\,G$	-10 to 0	—	—	—	—
$4^{++}\,1^{+}\,f_2(1270)\,\pi\,F$	-10 to 0	—	—	—	—

APPENDIX D

Parameterizations used in the Resonance Model

In this chapter, the parameterizations of the resonance model and the corresponding formulas are summarized. The transition amplitudes are parameterized as a coherent sum over the various model components k

$$^{\mathrm{RM}}\mathcal{T}_{\alpha}(m_{3\pi}, t') = \left[\sum_{k \in \mathrm{Comp}_{\alpha}} C_{\alpha}^{k}(t')\, \mathcal{D}^{k}(m_{3\pi}, t'; \zeta_k) \right] \sqrt{\varphi_{\alpha}(m_{3\pi})}\, \sqrt{\Psi(m_{3\pi})} \tag{D.1}$$

with the complex-valued coupling parameters $C_{\alpha}^{k}(t')$, the dynamic functions $\mathcal{D}^{k}(m_{3\pi}, t'; \zeta_k)$ of the corresponding components, the phase-space integrals $\varphi_{\alpha}(m_{3\pi})$ (see section 3.2) and the so-called production phase-space $\Psi(m_{3\pi})$.

Resonance Parameterizations

Resonances are parameterized using relativistic Breit-Wigner functions

$$^{\mathrm{R}}\mathcal{D}^{k}(m_{3\pi}; m_0, \Gamma_0) = \frac{\sqrt{m_0\, \Gamma_0}}{m_0^2 - m_{3\pi}^2 - i\, m_0\, \Gamma(m_{3\pi})} \tag{D.2}$$

with the dynamic width $\Gamma(m_{3\pi})$. For most of the resonant components, a fixed-width Breit-Wigner with $\Gamma(m_{3\pi}) \approx \Gamma_0$ is used. The $a_1(1260)$ is parameterized using the so-called Bowler parameterization [27]

$$\Gamma_{a_1}(m_{3\pi}) = \Gamma_0 \frac{\varphi_{\rho\pi}^{1^+S}(m_{3\pi})}{\varphi_{\rho\pi}^{1^+S}(m_{a_1})} \frac{m_{a_1}}{m_{3\pi}} \tag{D.3}$$

which accounts for the finite width of the $\rho(770)$ resonance in the $\rho(770)\,\pi$ decay. The other exception is the parameterization of the $a_2(1320)$ resonance. Its dynamic width

$$\Gamma_{a_2}(m_{3\pi}) = \Gamma_0 \frac{m_{a_2}}{m_{3\pi}} \left[(1-x) \frac{q_{\rho\pi}(m_{3\pi}) F_D^2\left(q_{\rho\pi}(m_{3\pi})\right)}{q_{\rho\pi}(m_{a_2}) F_D^2\left(q_{\rho\pi}(m_{a_2})\right)} + x \frac{q_{\eta\pi}(m_{3\pi}) F_D^2\left(q_{\eta\pi}(m_{3\pi})\right)}{q_{\eta\pi}(m_{a_2}) F_D^2\left(q_{\eta\pi}(m_{a_2})\right)} \right] \tag{D.4}$$

takes into account the $\rho(770)\,\pi$ and $\eta(548)\,\pi$ D-wave in the two-body approximation for the phase space

$$\varphi_{\xi\pi}(m_{3\pi}) \propto\!\!\sim \frac{q_{\xi\pi}(m_{3\pi}) F_L^2\left(q_{\xi\pi}(m_{3\pi})\right)}{m_{3\pi}} \tag{D.5}$$

with the two-body break-up momentum $q_{\xi\pi}(m_{3\pi})$ [see equation (D.8)] and the angular-momentum barrier factors $F_L(q)$ [24] [see section 3.2].

Non-Resonant Term

The non-resonant term is parameterized in the following way

$${}^{\mathrm{NR}}\mathcal{D}^k(m_{3\pi}, t'; b, c_0, c_1, c_2) = (m_{3\pi} - m_{\mathrm{thr}})^b e^{(c_0 + c_1 t' + c_2 t'^2)\cdot \widetilde{q}^{\,2}(m_{3\pi})} \tag{D.6}$$

with the shape parameters (b, c_0, c_1, c_2). The exponentially falling amplitude with the squared two-body break-up momentum $\widetilde{q}(m_{3\pi})$ was introduced in [55] and further developed to this final form [29]. The t' dependence of the slope parameter $c(t') \approx c_0 + c_1 t' + c_2 t'^2$ is approximated by a second order polynomial. The constant shift m_{thr} in the $(m_{3\pi} - m_{\mathrm{thr}})^b$ prefactor is empirically fixed to $0.5\,\mathrm{GeV}/c^2$. $\widetilde{q}(m_{3\pi})$ is a smooth approximation for the two-body break-up momentum, valid also below the two-body threshold. It takes the finite width of the isobar into account and is calculated in the following way

$$\widetilde{q}(m_{3\pi}) = m_{3\pi}\, \varphi_\alpha(m_{3\pi}) \frac{q_{\xi\pi}(m_{\mathrm{norm}})}{m_{\mathrm{norm}} \varphi_\alpha(m_{\mathrm{norm}})}. \tag{D.7}$$

The phase-space integral $\varphi_\alpha(m_{3\pi})$ [see equation (3.10)] is used as well as the fact, that the three-body phase-space can be approximated by the two-body break-up momentum

$$q_{\xi\pi}(m) = \frac{\sqrt{\left(m^2 - (m_\pi + m_\xi)^2\right)\left(m^2 - (m_\pi - m_\xi)^2\right)}}{2m} \tag{D.8}$$

in the following way [6]

$$\varphi_\alpha(m_{3\pi}) \propto \frac{q_{\xi\pi}(m_{3\pi})}{m_{3\pi}}. \tag{D.9}$$

Finally $\widetilde{q}(m_{3\pi})$ is normalized such that it agrees with $q(m_{3\pi})$ at a mass of $m_{\text{norm}} = 2.4\,\text{GeV}/c^2$.

For some of the non-resonant terms, a simplified version of equation (D.6) is used, where $b = 0$, $c_1 = 0\,(\text{GeV}/c)^{-4}$, $c_2 = 0\,(\text{GeV}/c)^{-6}$

$$^{\text{NR}}\mathcal{D}^k(m_{3\pi}; c_0) = e^{c_0 \cdot \widetilde{q}^{\,2}(m_{3\pi})}. \tag{D.10}$$

Production Phase-Space

To account for the decrease of the probability of producing intermediate states with higher 3π masses, an additional production phase-space term $\Psi(m_{3\pi})$ is introduced. Inspired by calculations of central production reactions in [56] and [57] a model for the suppression of high-mass states was developed [29]. Finally a parameterization of the form

$$\Psi(m_{3\pi}) = \left[\frac{A_1}{m_{3\pi}}\right]^{B_1} - \left[\frac{A_2}{m_{3\pi}}\right]^{B_2} \tag{D.11}$$

was fitted to Monte-Carlo data, generated according to the developed model. The obtained parameters are listed in the following table:

Table D.1: Parameters of the production phase-space term $\Psi(m_{3\pi})$ in equation (D.11).

A_1 [GeV/c^2]	B_1	A_2 [GeV/c^2]	B_2
151.9073	2.4749	69.5612	2.8420

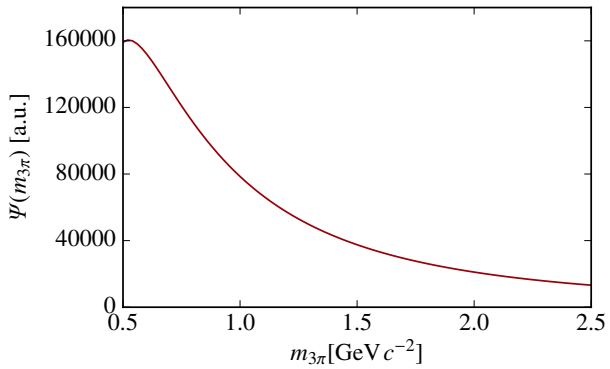

Figure D.1: 3π mass dependence the production phase-space according to equation (D.11).

APPENDIX E

Calculation of the t' Spectra and their Uncertainty

The t' dependence of the intensity (t' spectrum) of component k in partial wave α is determined by integrating the model component over its fitted mass range in the resonance-model fit (m_{start} to m_{end})

$$^{\mathcal{M}}\text{Intensity}^k_\alpha(t') = \frac{1}{\Delta t'} |C^k_\alpha(t')|^2 \int_{m_{\text{start}}}^{m_{\text{end}}} \mathrm{d}m_{3\pi}\, |\mathcal{D}^k(m_{3\pi}, t'; \zeta_k)|^2 \varphi_\alpha(m_{3\pi}) \Psi(m_{3\pi}) \tag{E.1}$$

where $\Delta t'$ is the t'-bin width. All other elements are described in section 4.1. The t' dependence of the production phase can directly be extracted from the phase of the coupling constants. One should notice, that for a resonance in a wave with fixed relative branchings, the coupling $C^k_\alpha(t')$ is replace by a fixed relative branching factor ${}_\alpha B^k_\beta$ and the coupling of the reference wave $C^k_\beta(t')$ according to (4.10). A discussion of the obtained t' spectra can be found in chapter 7.

The fit parameters

$$x_i = (C^k_\alpha(t'), {}_\alpha B^k_\beta, \zeta_k) \tag{E.2}$$

are the coupling parameters $C^k_\alpha(t')$, the branching parameters ${}_\alpha B^k_\beta$ and the shape parameters of the dynamic functions ζ_k. They enter in a complex way in the integration of the intensities. Therefore, a Monte Carlo method is used to determine the statistical error of the t' spectrum. A set of 10000 samples of random fit parameters, drawn according to the covariance matrix of the resonance-model fit, is generated. Then, for each sample $\mathcal{S}$, the integrated intensities $^{\mathcal{S}}\text{Intensity}^k_\alpha(t')$ are calculated. The error of the intensity is finally given by the variance of the 10000 MC samples around the central value of the fit $^{\mathcal{M}}\text{Intensity}^k_\alpha(t')$

$$\Delta\text{Intensity}^k_\alpha(t') = \sqrt{\left\langle \left({}^{\mathcal{S}}\text{Intensity}^k_\alpha(t') - {}^{\mathcal{M}}\text{Intensity}^k_\alpha(t') \right)^2 \right\rangle}. \tag{E.3}$$

The error of the production phase if given in the same way

$$\Delta\left[{}_{\text{Prod}}\varphi_\alpha^k(t')\right] = \sqrt{\left\langle\left({}^{\mathcal{S}}_{\text{Prod}}\varphi_\alpha^k(t') - {}^{\mathcal{M}}_{\text{Prod}}\varphi_\alpha^k(t')\right)^2\right\rangle}. \tag{E.4}$$

To draw random fit parameters ${}^{\mathcal{S}}x_i$ from the covariance matrix $\mathfrak{C}_{ij}$ of the resonance-model fit, a eigendecomposition of the covariance matrix is performed [29]. Therefore, a new matrix

$$\mathcal{V}_{ij} = \sqrt{\lambda_i}\, V_{ij} \tag{E.5}$$

is introduced, where λ_i are the eigenvalues of the covariance matrix and V_{ij} is a matrix of normalized eigenvectors v_j of the corresponding eigenvalues λ_i. In this way,

$$\mathfrak{C}_{ij} = \sum_l \mathcal{V}_{li}\mathcal{V}_{lj}. \tag{E.6}$$

To generate a set of random samples of the fit parameters ${}^{\mathcal{S}}x_i$ from the covariance matrix, assuming a Gaussian distribution of the fit parameters, Gaussian distributed random values r_j with standard deviation $\sigma = 1$ and mean $< r_j >= 0$ are multiplied by the $\mathcal{V}_{ij}$ matrix and shifted according to the main solution for the fit parameters ${}^{\mathcal{M}}x_i$

$${}^{\mathcal{S}}x_i = {}^{\mathcal{M}}x_i + \sum_j \mathcal{V}_{ji}\, {}^{\mathcal{S}}r_j. \tag{E.7}$$

This guarantees that the ${}^{\mathcal{S}}x_i$ are distributed according to the uncertainty of the fit parameter as

$$\begin{aligned}
\mathfrak{C}_{ij} &= \frac{1}{N_{\text{samples}}} \sum_{\mathcal{S}} \left({}^{\mathcal{S}}x_i - {}^{\mathcal{M}}x_i\right)\left({}^{\mathcal{S}}x_j - {}^{\mathcal{M}}x_j\right) \\
&= \frac{1}{N_{\text{samples}}} \sum_{\mathcal{S}} \left(\sum_l \mathcal{V}_{li}\, {}^{\mathcal{S}}r_l\right)\left(\sum_m \mathcal{V}_{mj}\, {}^{\mathcal{S}}r_m\right) \\
&= \sum_l \sum_m V_{li}\, V_{mj} \underbrace{\left(\frac{1}{N_{\text{samples}}} \sum_{\mathcal{S}} {}^{\mathcal{S}}r_l\, {}^{\mathcal{S}}r_m\right)}_{\delta_{lm}} \\
&= \sum_l V_{li}\, V_{lj}
\end{aligned} \tag{E.8}$$

where we used that $\frac{1}{N_{\text{samples}}} \sum_{\mathcal{S}} {}^{\mathcal{S}}r_l\, {}^{\mathcal{S}}r_m$ is the covariance matrix of the r_l random values which we generated from a Gaussian distribution with covariance δ_{lm}.

APPENDIX F

Results of the Main Fit

F.1 Spin-Density Matrices

On the following pages, the full results of the Main fit (see section 4.2), i.e. the spin-density matrix elements for all eleven t' bins, are shown. The shown relative phases, represent the phase of the wave of the corresponding row minus that of the wave of the corresponding column. For a better visualization, the relative phases were shifted such that they are centered around 0°.

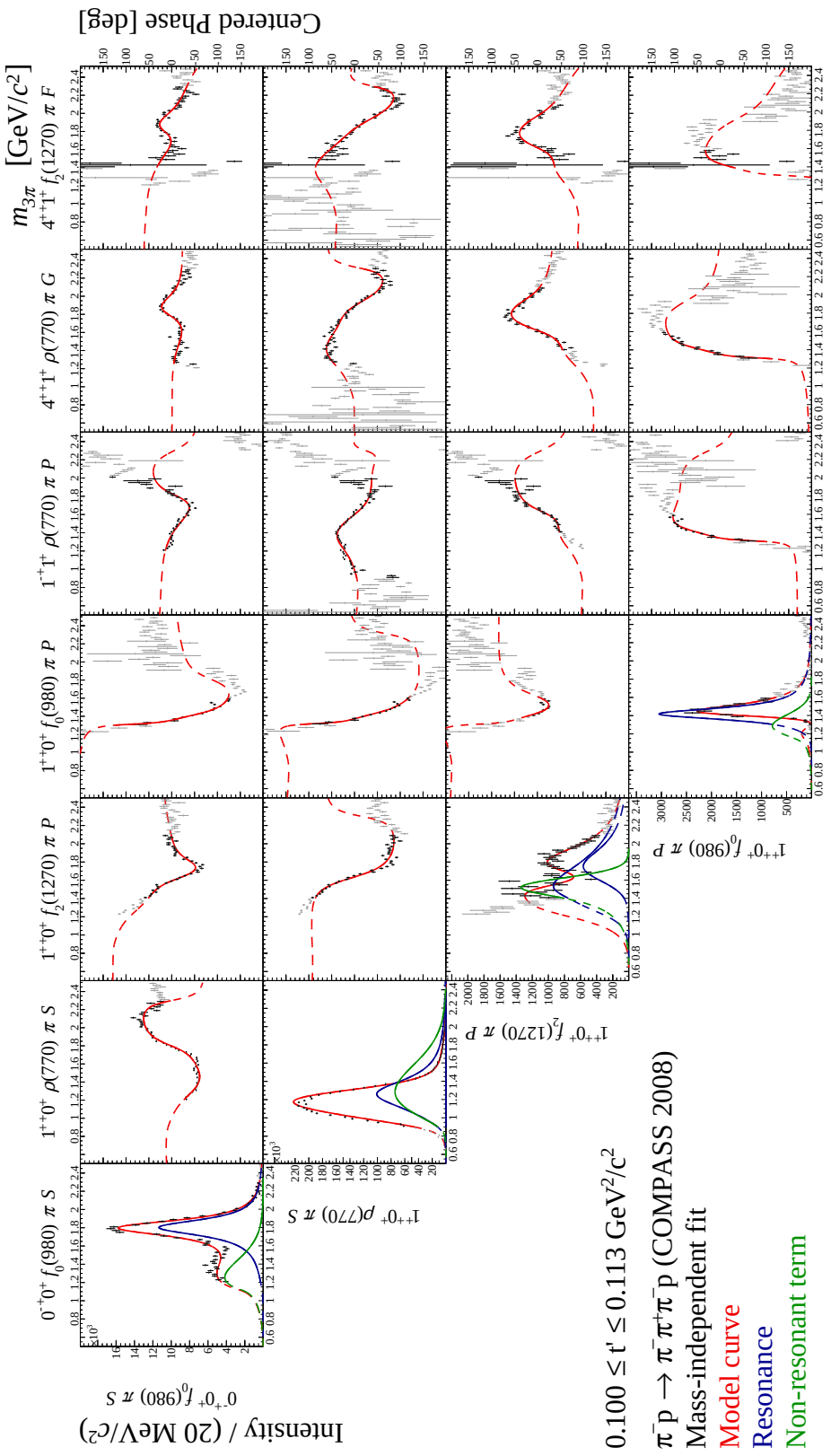

Figure F.1: Spin-density sub-matrix in the range of $0.100 < t' < 0.113\ (\mathrm{GeV}/c)^2$.

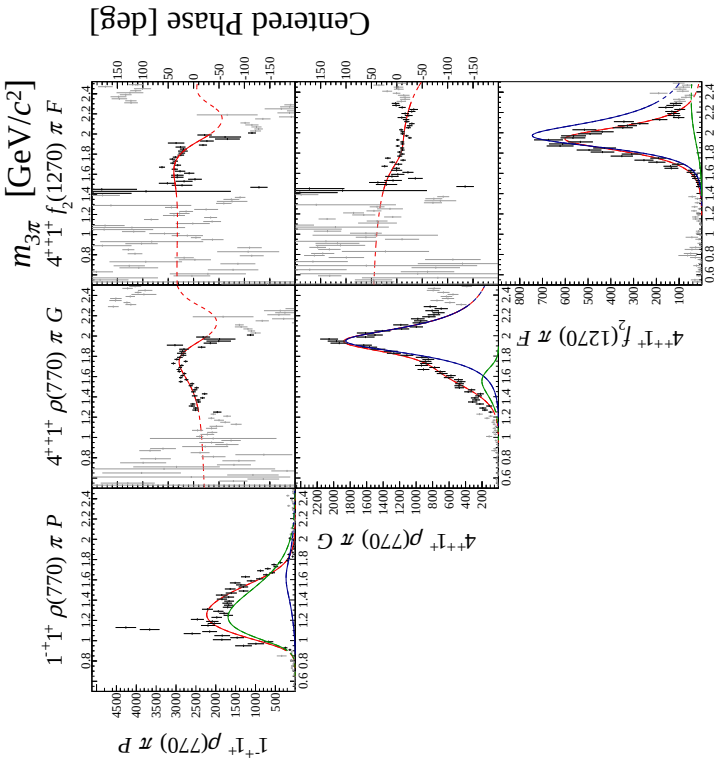

Figure F.2: Spin-density sub-matrix in the range of $0.100 < t' < 0.113\,(\mathrm{GeV}/c)^2$.

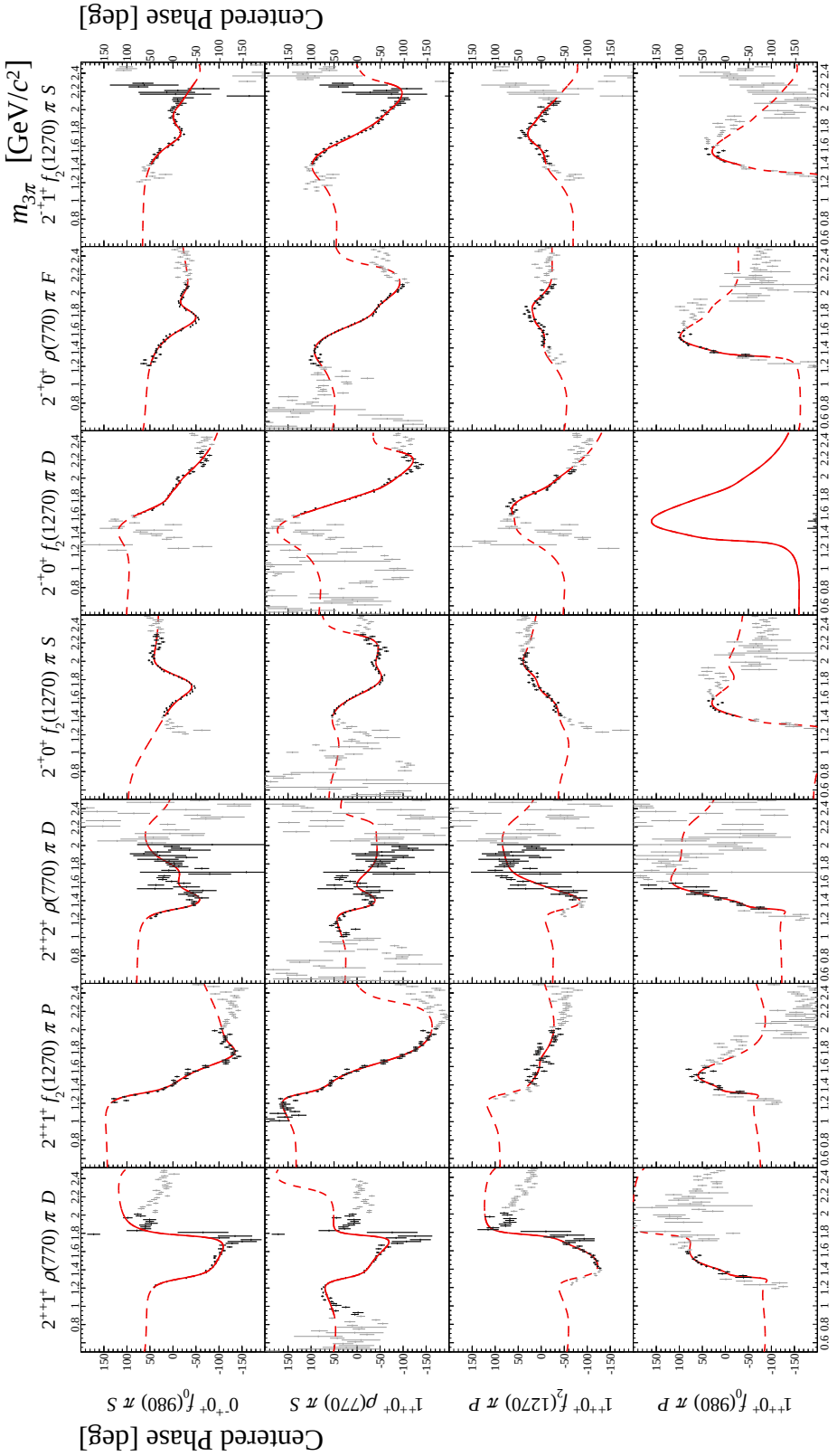

Figure F.3: Spin-density sub-matrix in the range of $0.100 < t' < 0.113$ (GeV/c)^2.

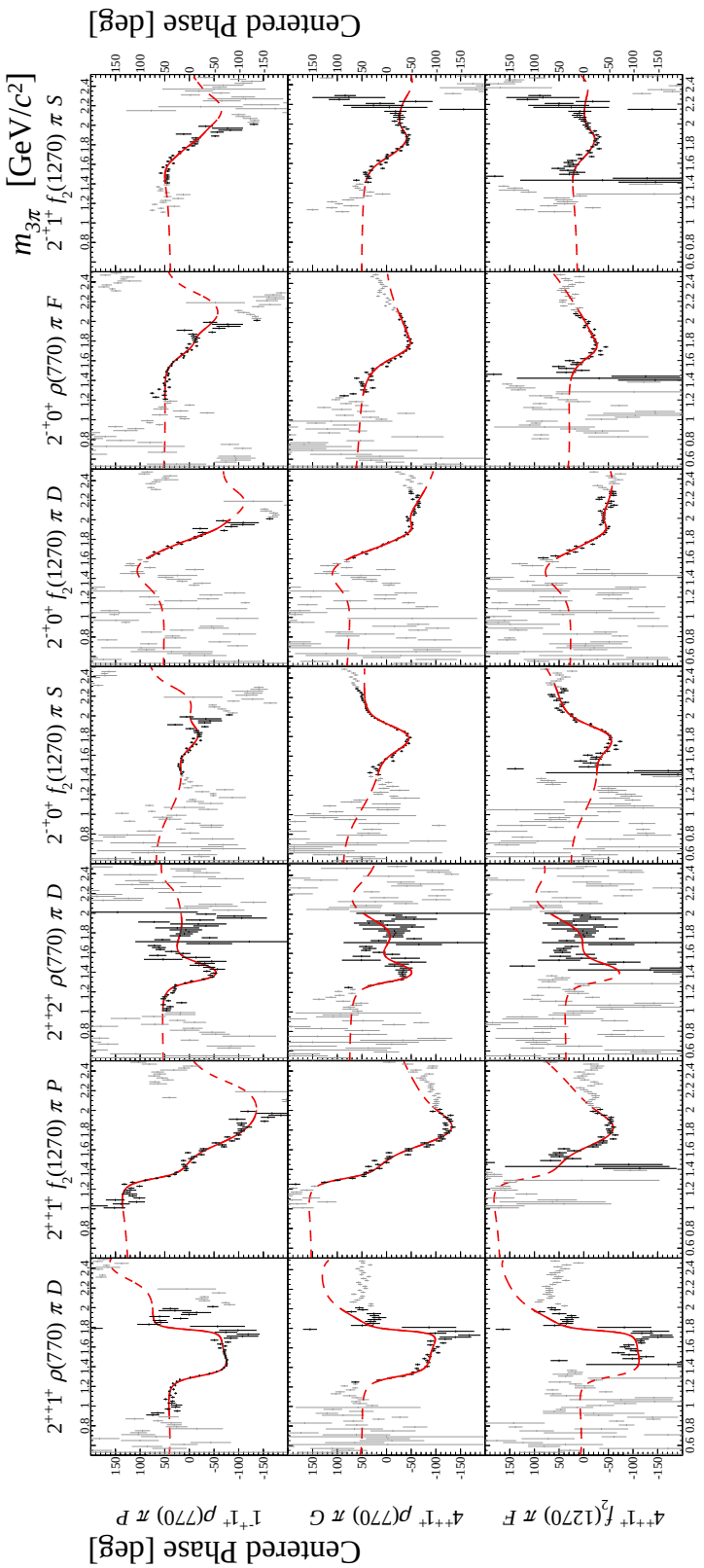

Figure F.4: Spin-density sub-matrix in the range of $0.100 < t' < 0.113\ (\mathrm{GeV}/c)^2$.

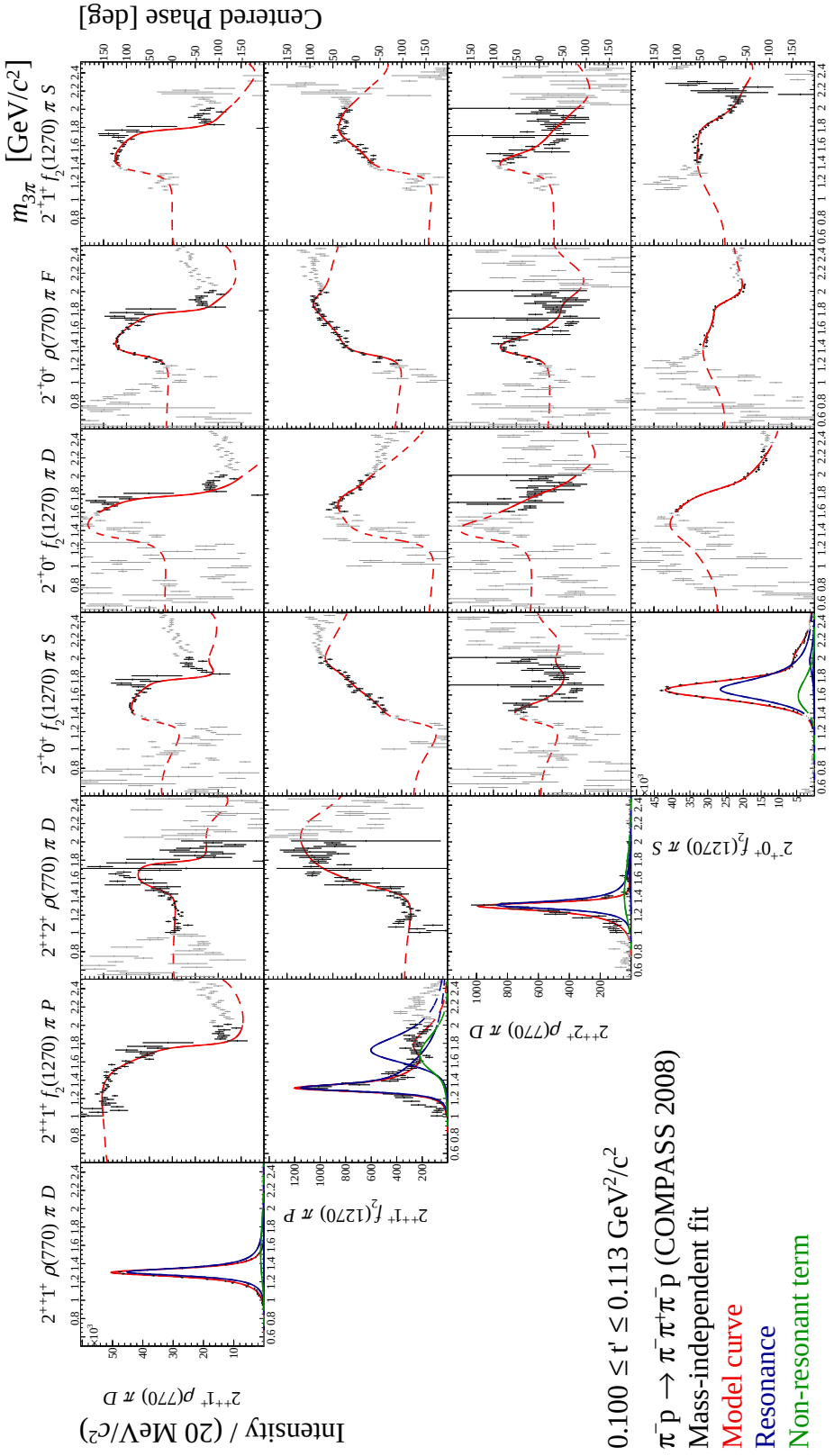

Figure F.5: Spin-density sub-matrix in the range of $0.100 < t' < 0.113$ (GeV/c)^2.

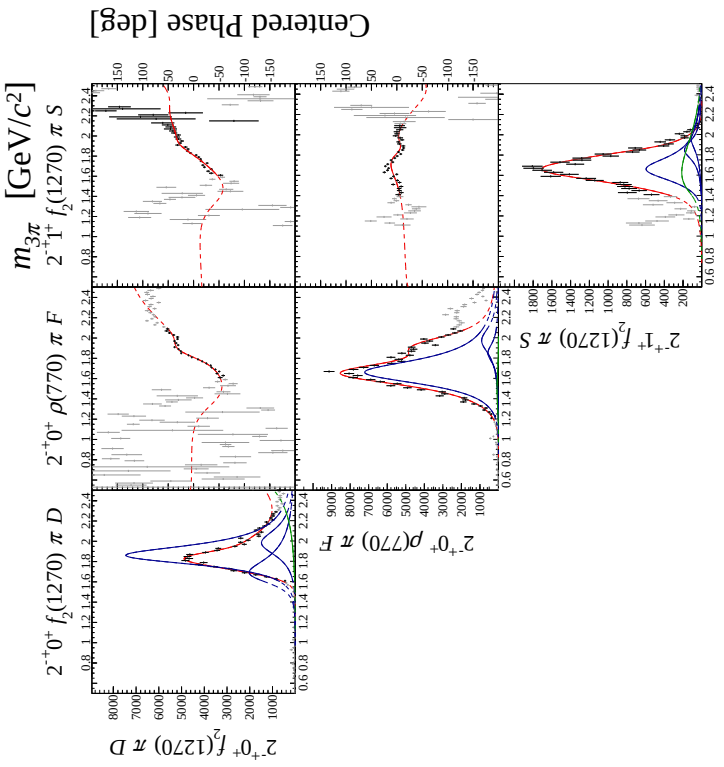

Figure F.6: Spin-density sub-matrix in the range of $0.100 < t' < 0.113\,(\mathrm{GeV}/c)^2$.

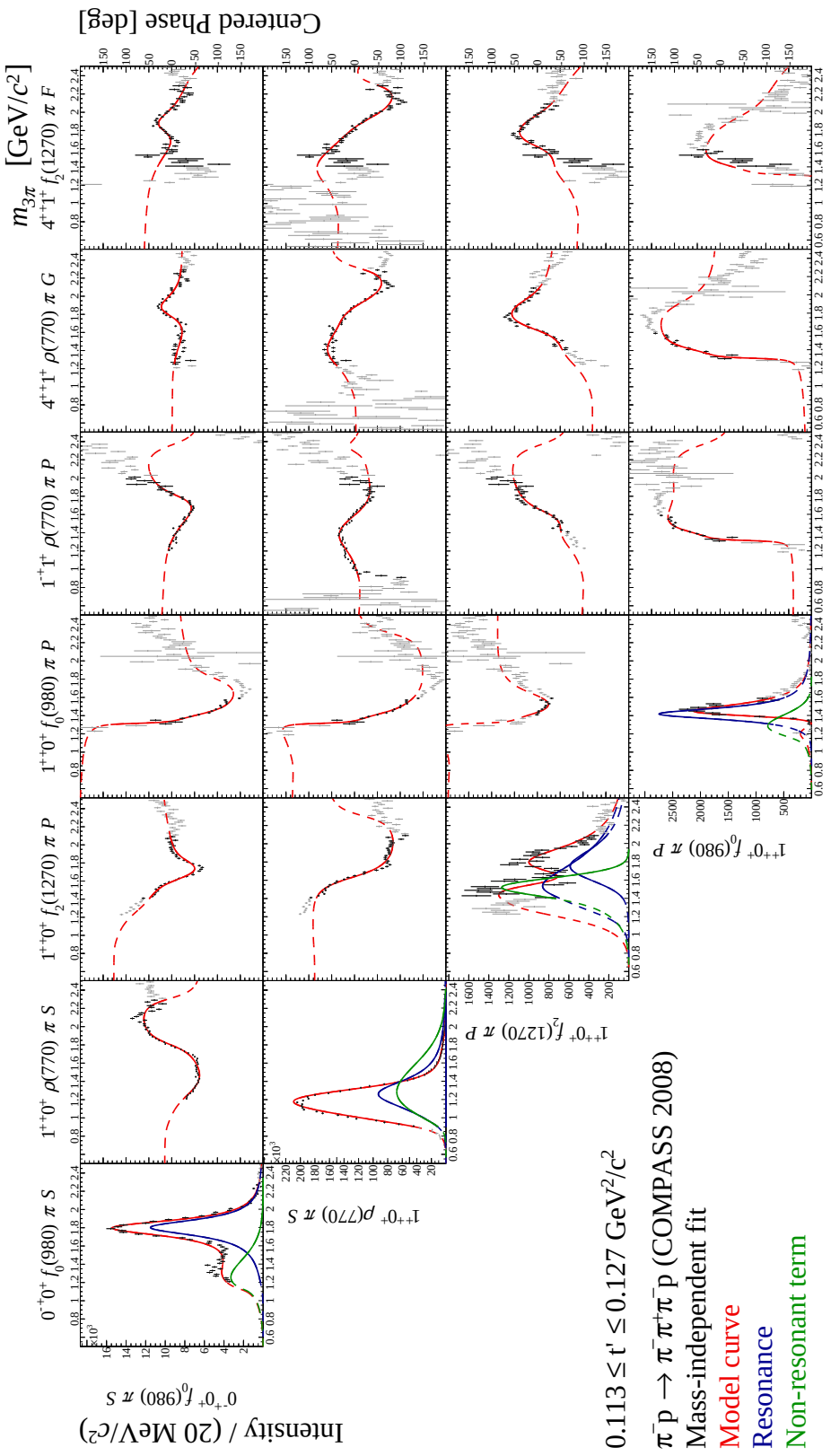

Figure F.7: Spin-density sub-matrix in the range of $0.113 < t' < 0.127$ (GeV/c)^2.

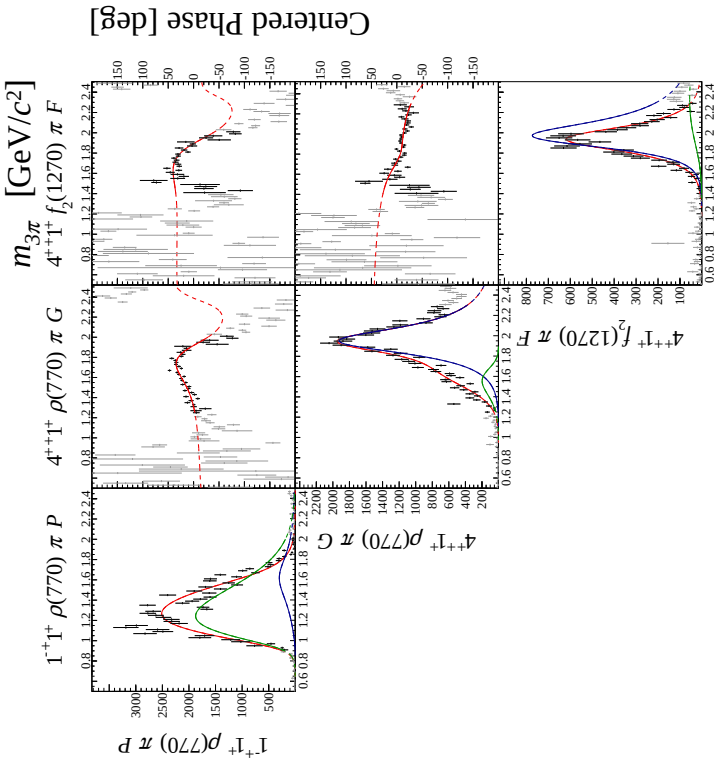

Figure F.8: Spin-density sub-matrix in the range of $0.113 < t' < 0.127$ (GeV/c)^2.

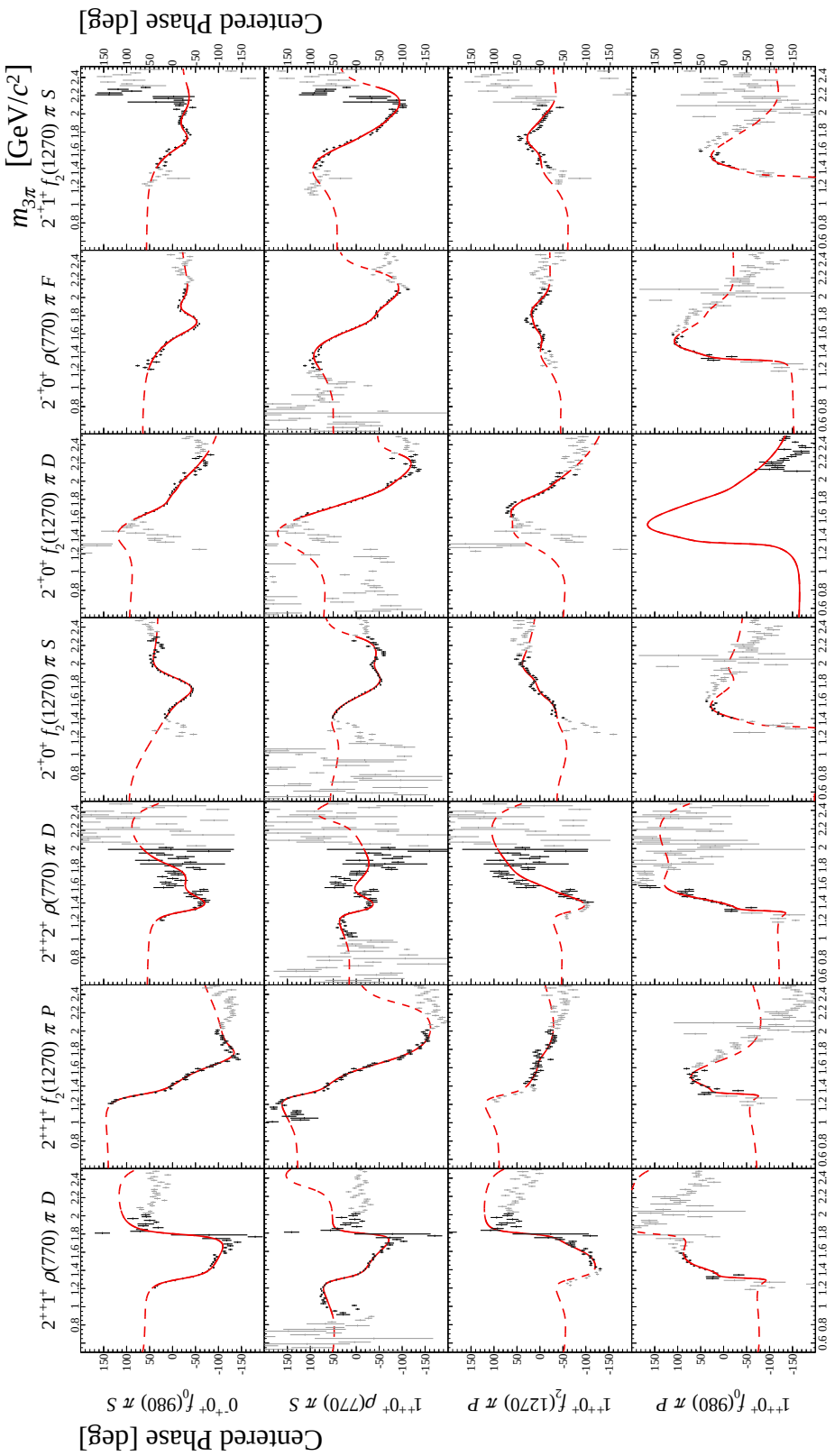

Figure F.9: Spin-density sub-matrix in the range of $0.113 < t' < 0.127$ (GeV/c)^2.

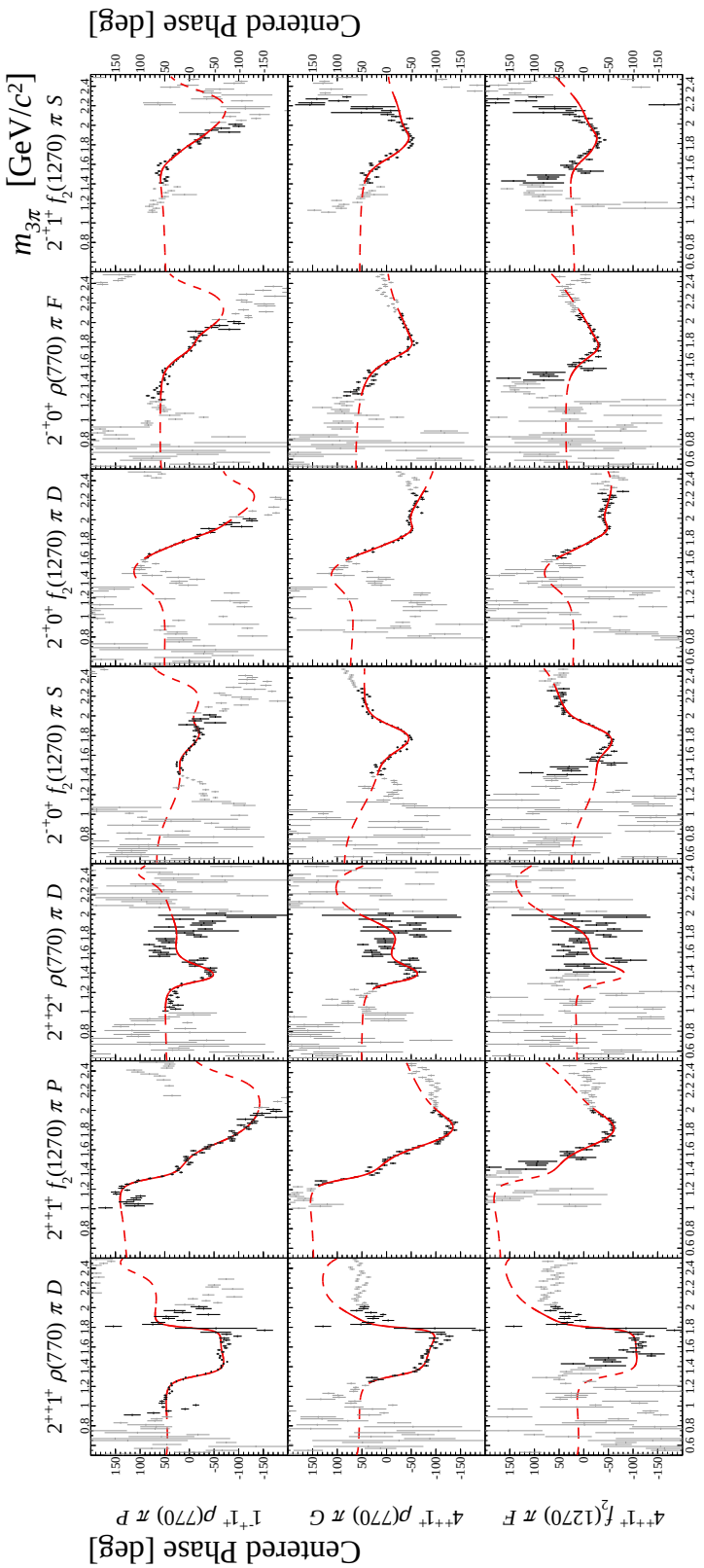

Figure F.10: Spin-density sub-matrix in the range of $0.113 < t' < 0.127$ (GeV/c)^2.

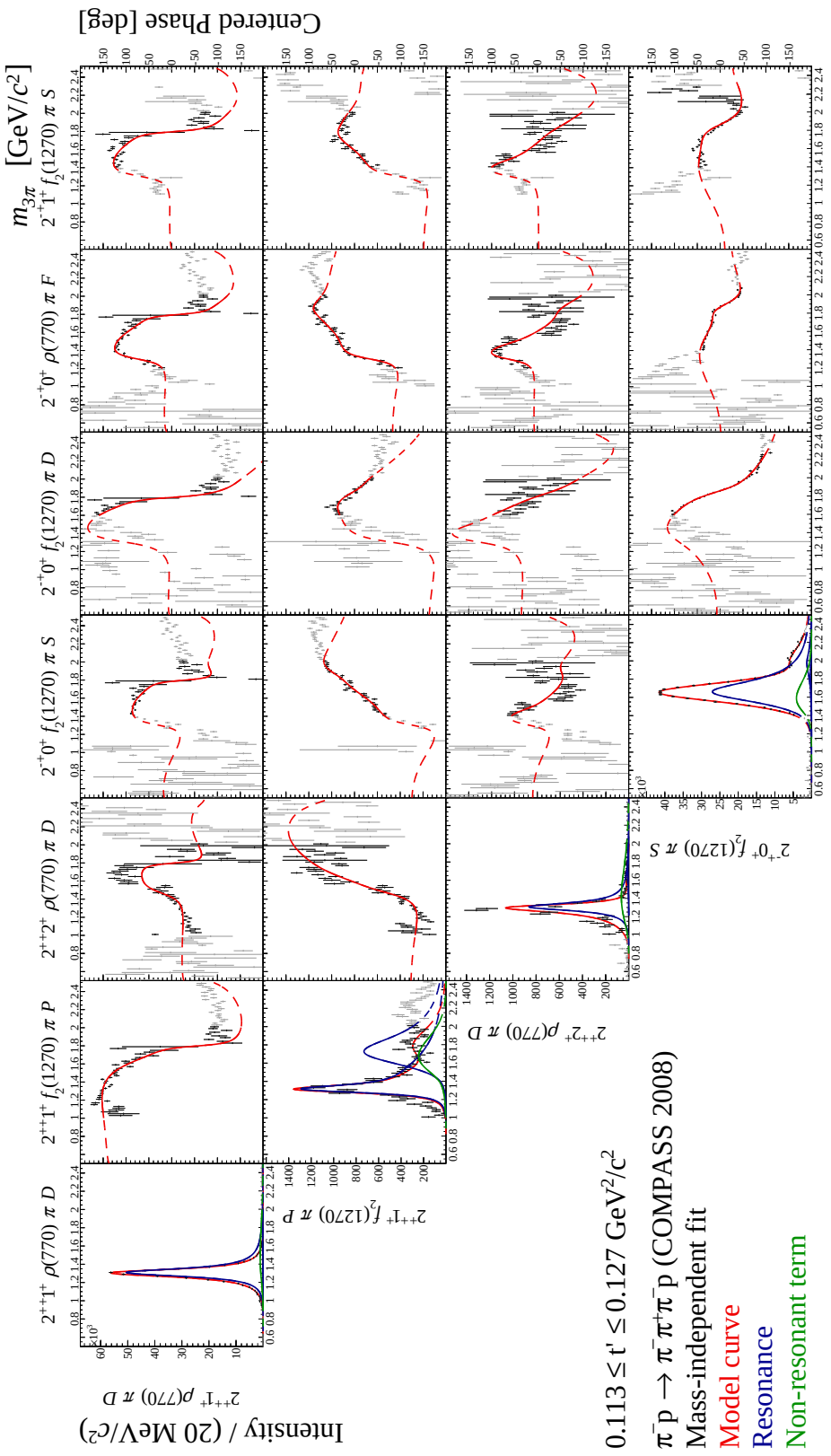

Figure F.11: Spin-density sub-matrix in the range of $0.113 < t' < 0.127$ (GeV/c)^2.

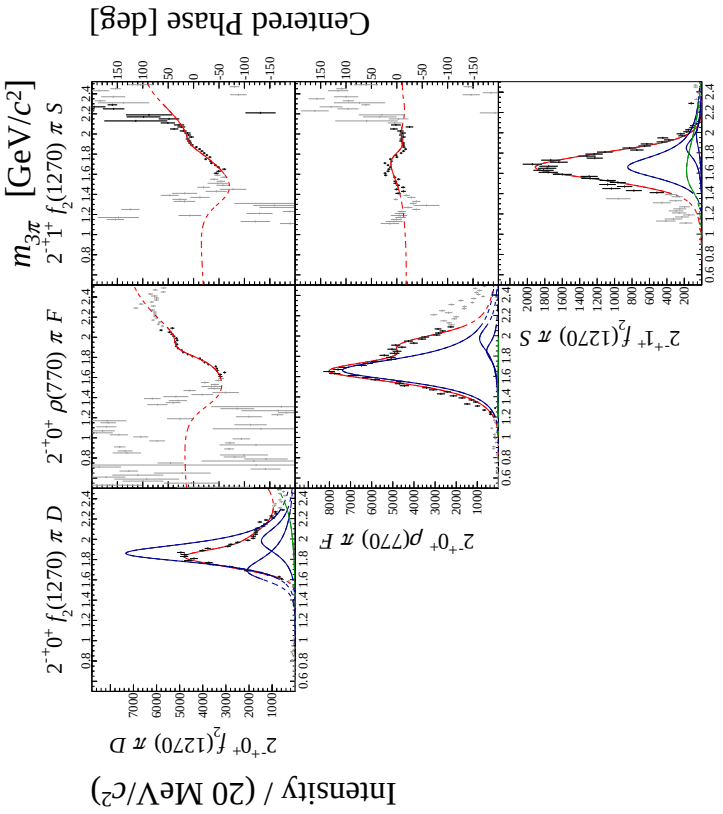

Figure F.12: Spin-density sub-matrix in the range of $0.113 < t' < 0.127$ (GeV/c)^2.

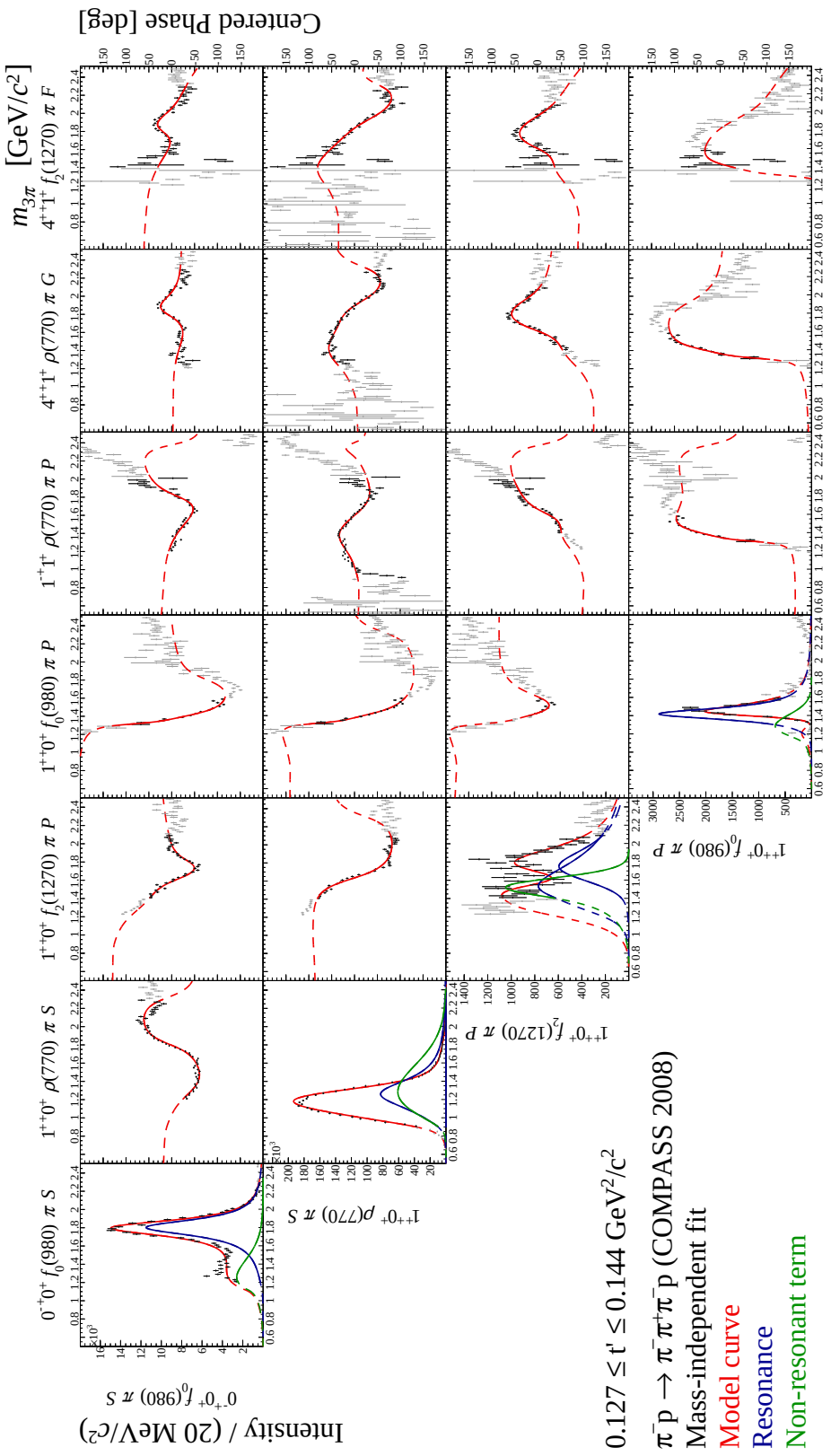

Figure F.13: Spin-density sub-matrix in the range of $0.127 < t' < 0.144$ (GeV/c)^2.

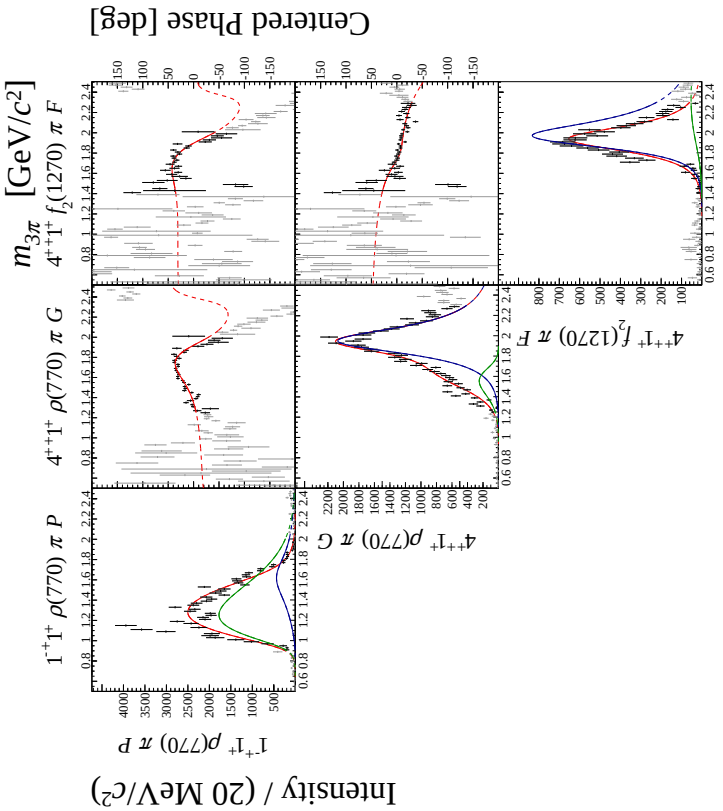

Figure F.14: Spin-density sub-matrix in the range of $0.127 < t' < 0.144$ (GeV/c)^2.

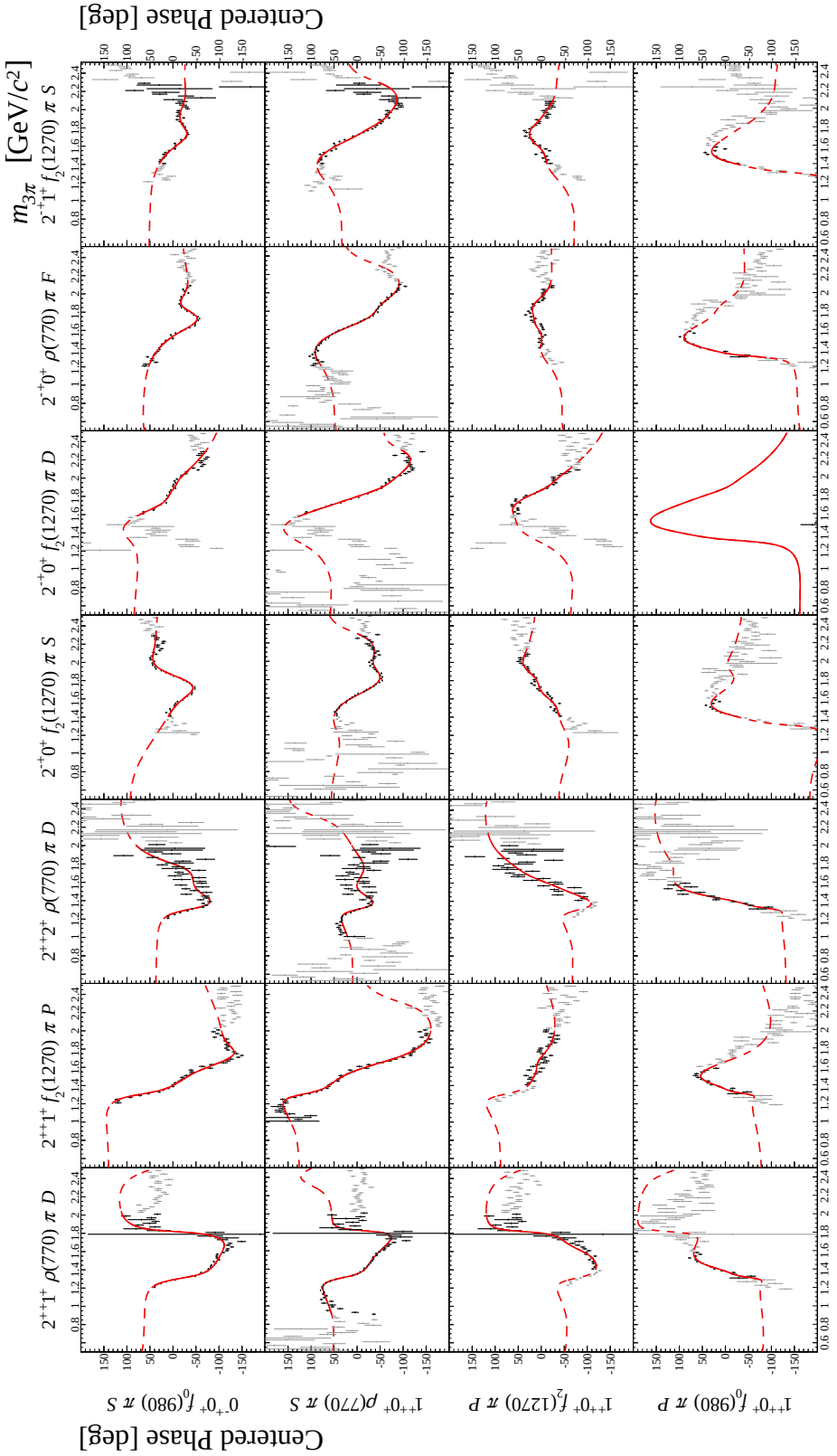

Figure F.15: Spin-density sub-matrix in the range of $0.127 < t' < 0.144\,(\mathrm{GeV}/c)^2$.

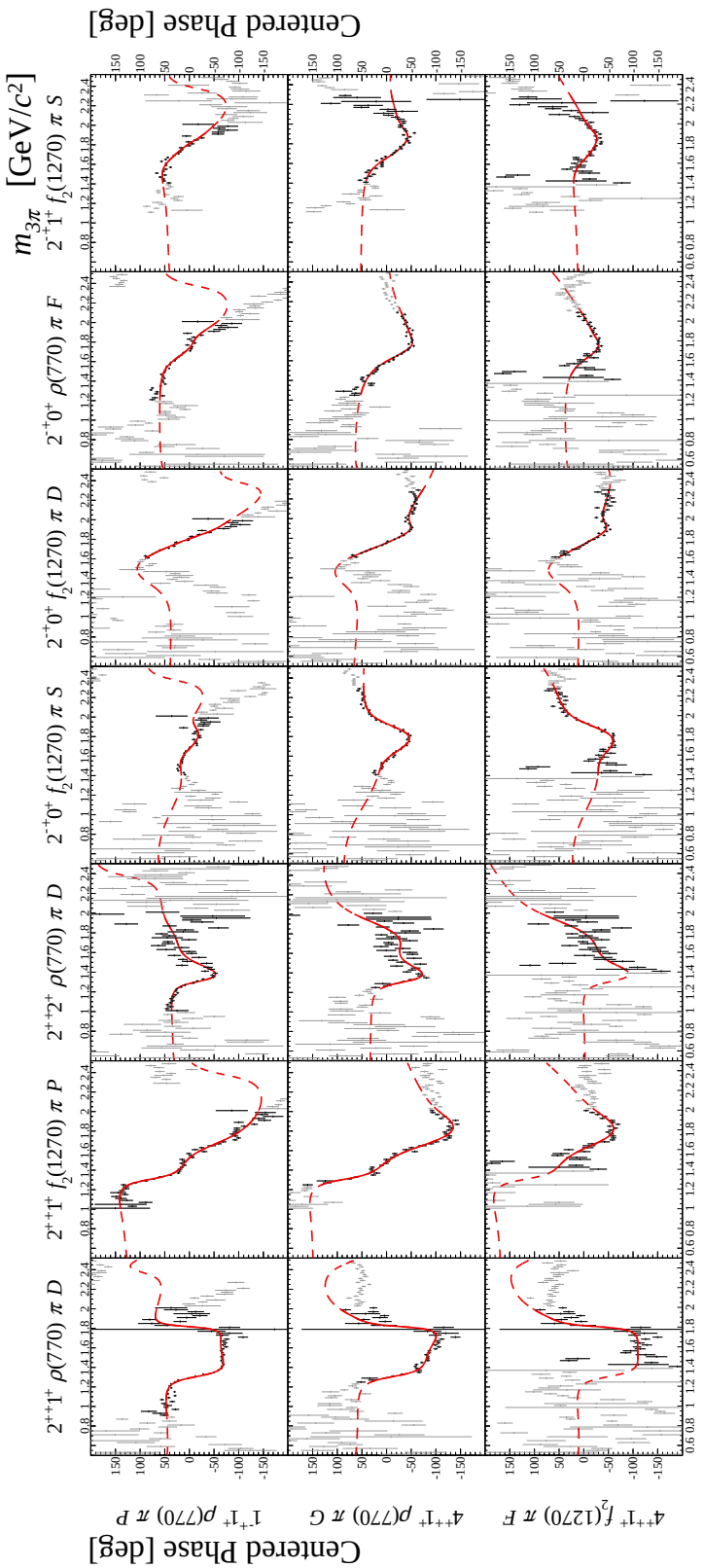

Figure F.16: Spin-density sub-matrix in the range of $0.127 < t' < 0.144$ (GeV/c)^2.

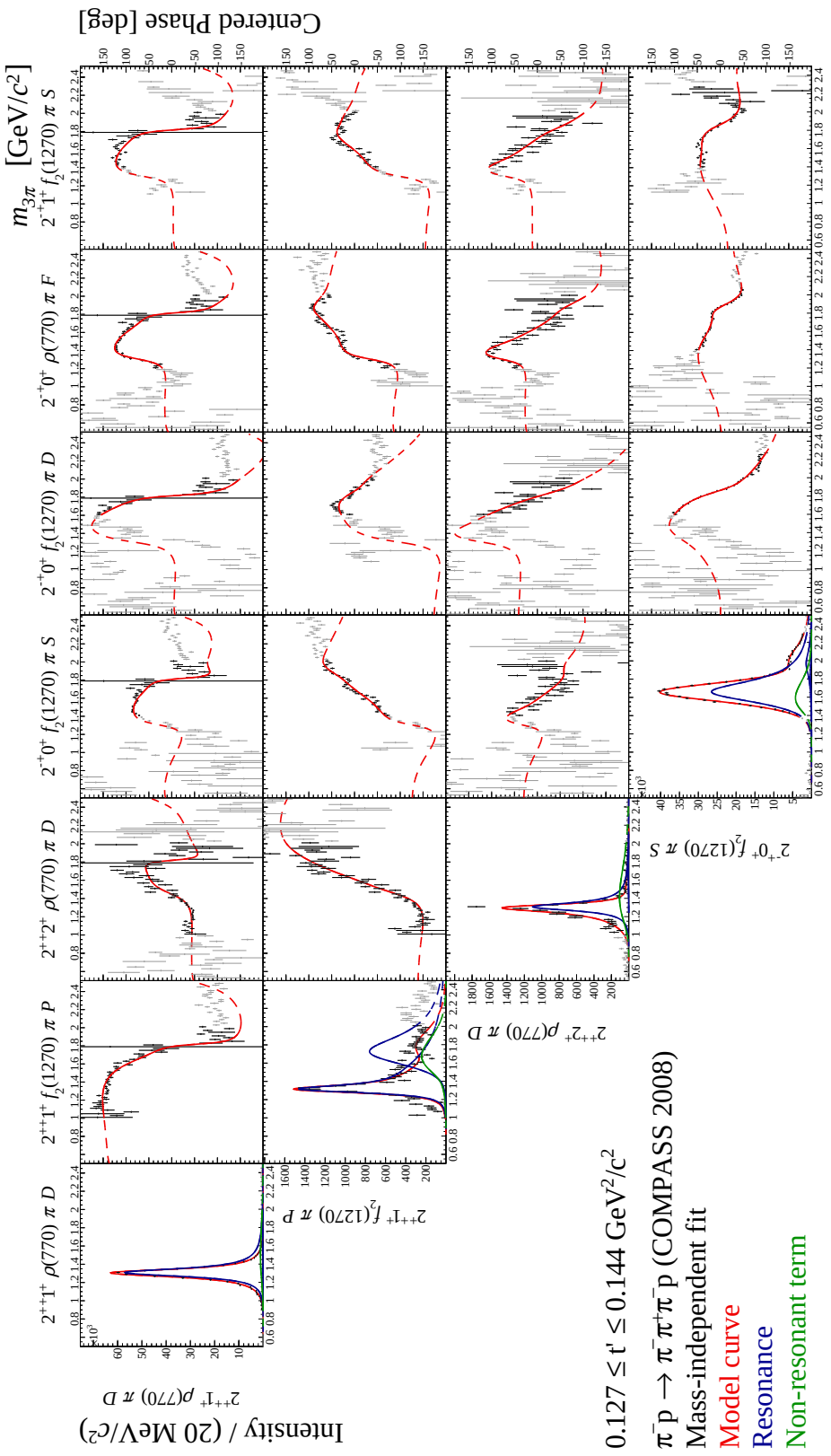

Figure F.17: Spin-density sub-matrix in the range of $0.127 < t' < 0.144$ (GeV/c)^2.

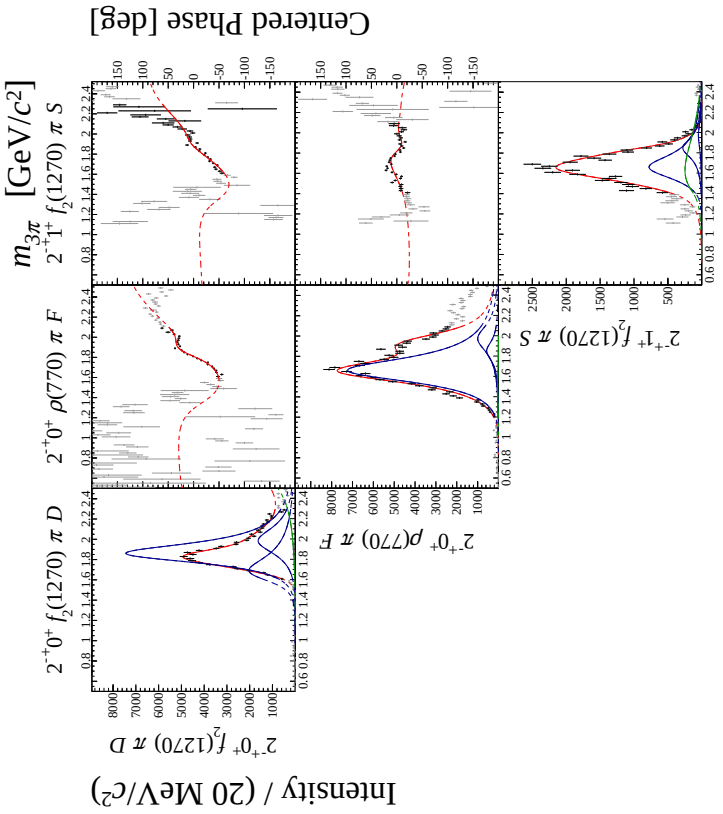

Figure F.18: Spin-density sub-matrix in the range of $0.127 < t' < 0.144$ (GeV/c)^2.

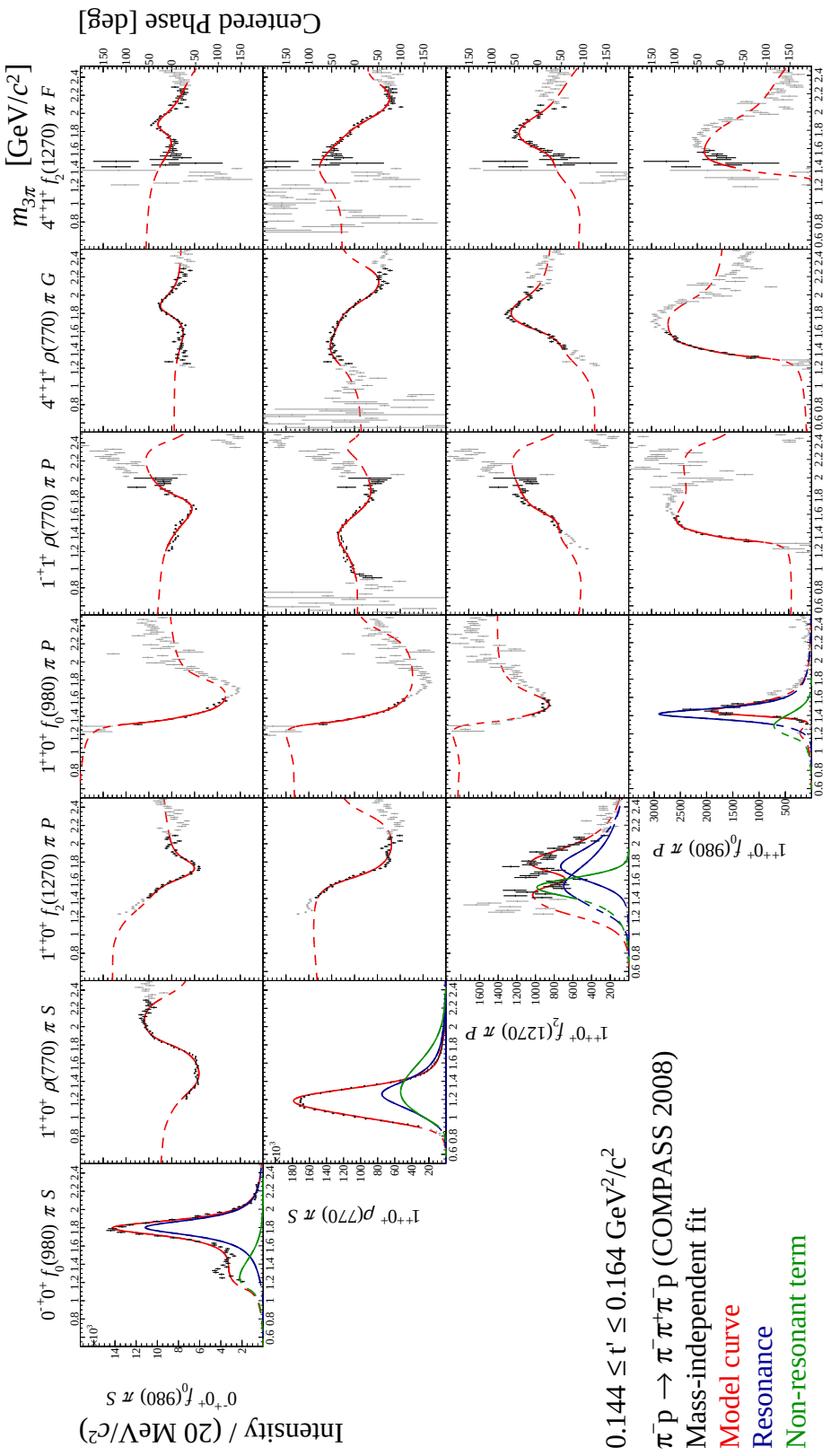

Figure F.19: Spin-density sub-matrix in the range of $0.144 < t' < 0.164$ (GeV/c)^2.

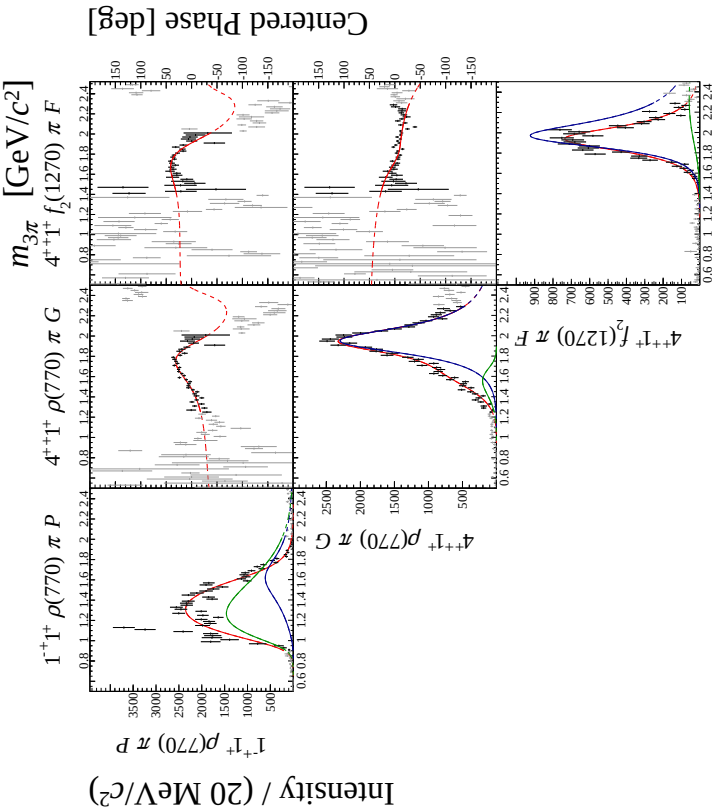

Figure F.20: Spin-density sub-matrix in the range of $0.144 < t' < 0.164\,(\mathrm{GeV}/c)^2$.

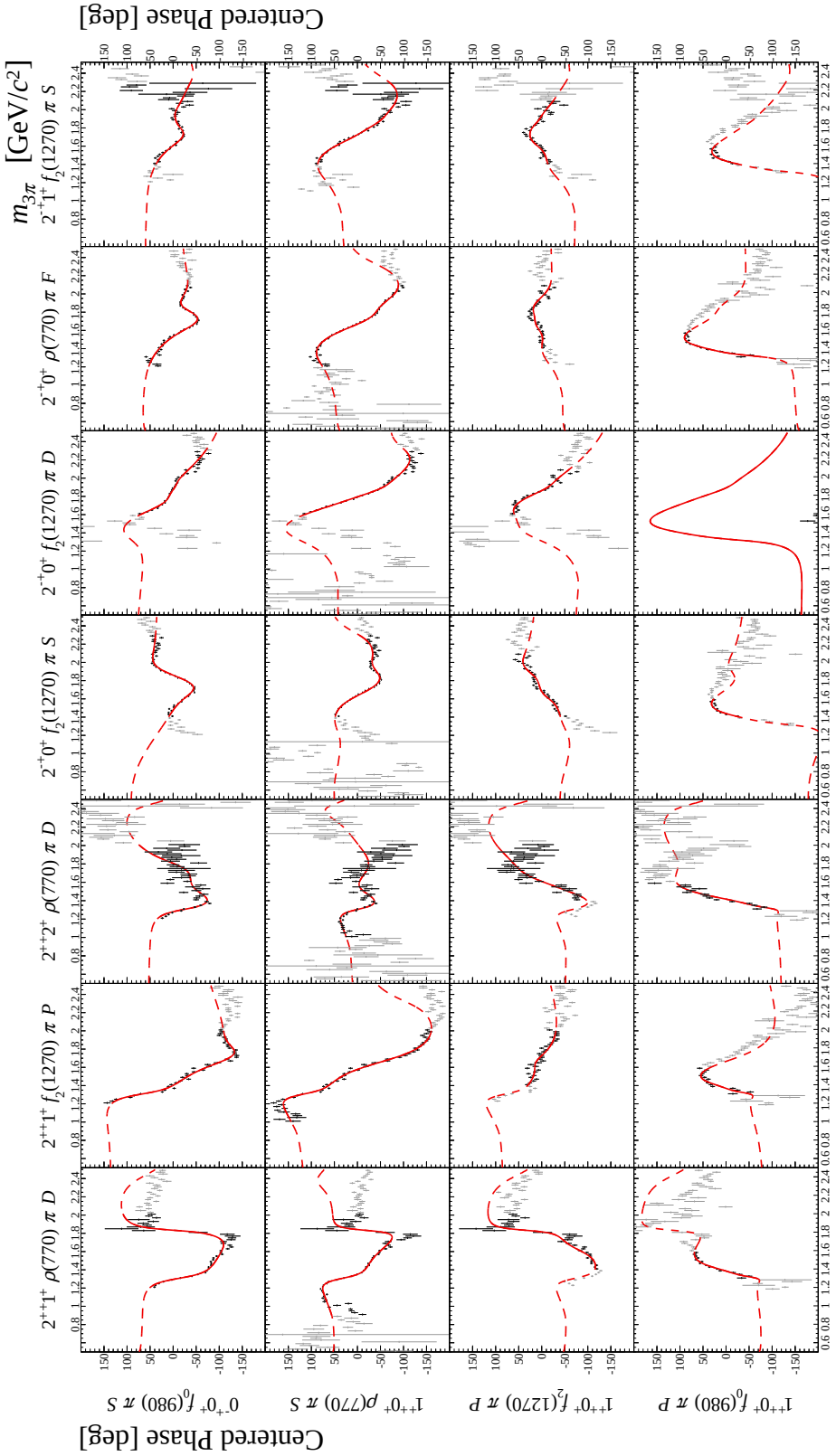

Figure F.21: Spin-density sub-matrix in the range of $0.144 < t' < 0.164\,(\mathrm{GeV}/c)^2$.

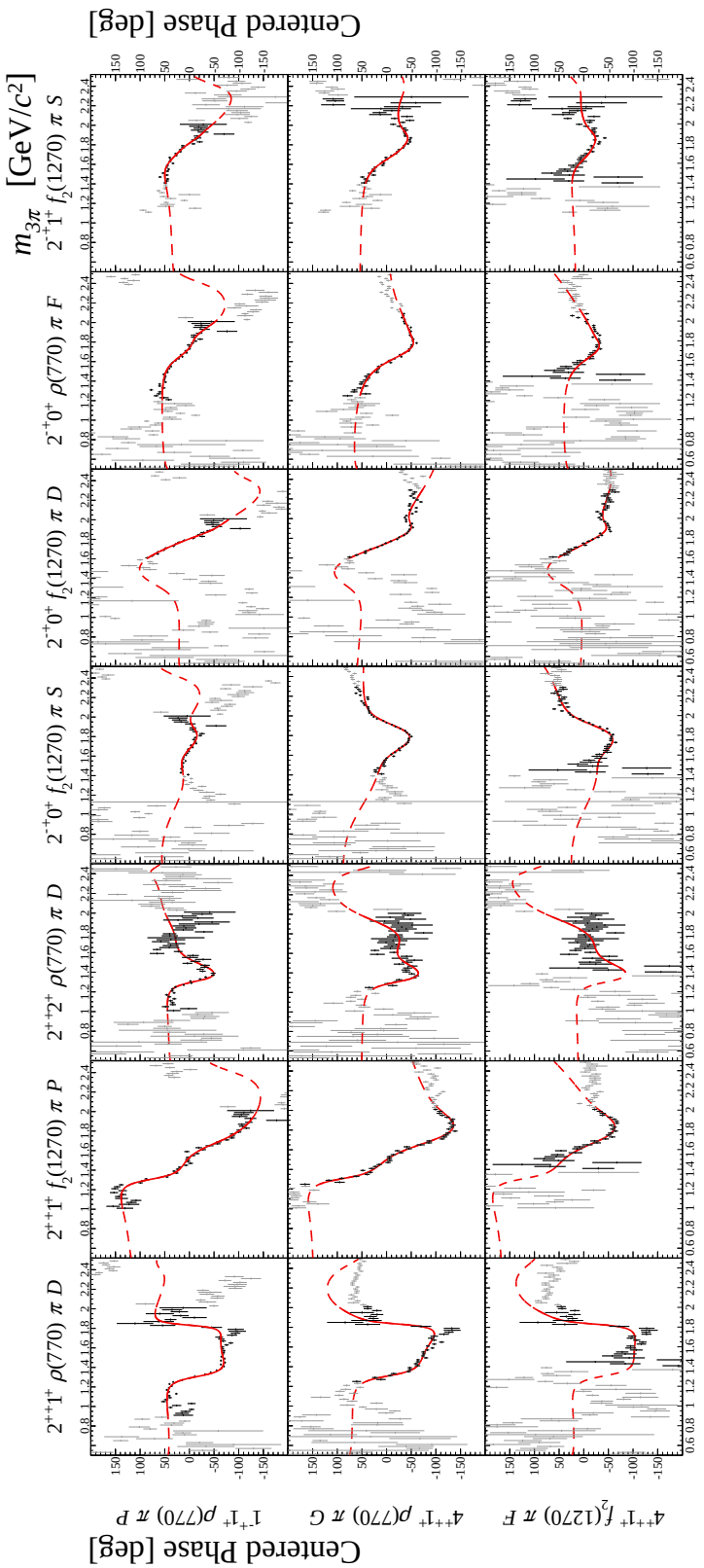

Figure F.22: Spin-density sub-matrix in the range of $0.144 < t' < 0.164\,(\mathrm{GeV}/c)^2$.

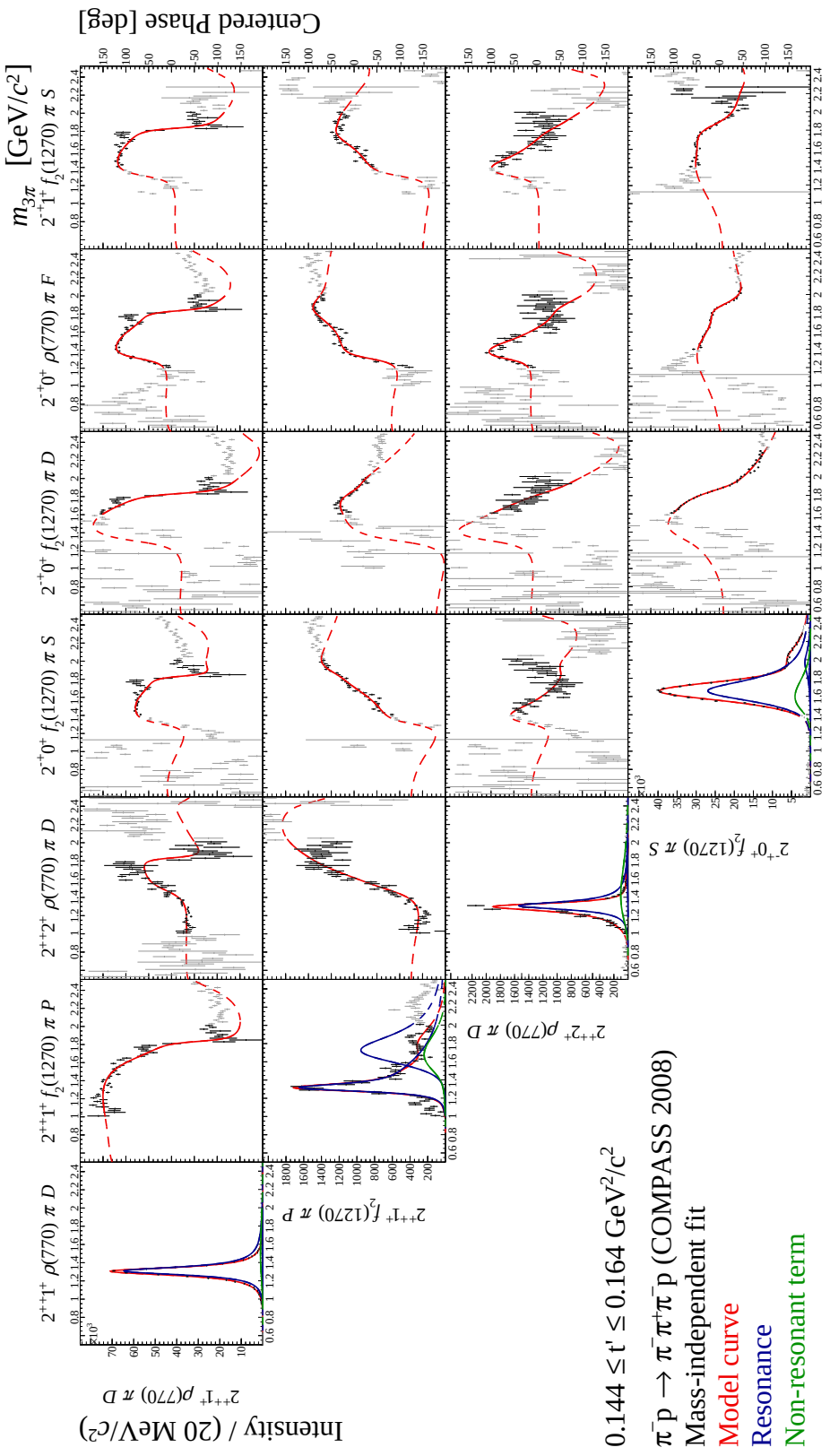

Figure F.23: Spin-density sub-matrix in the range of $0.144 < t' < 0.164\ (\mathrm{GeV}/c)^2$.

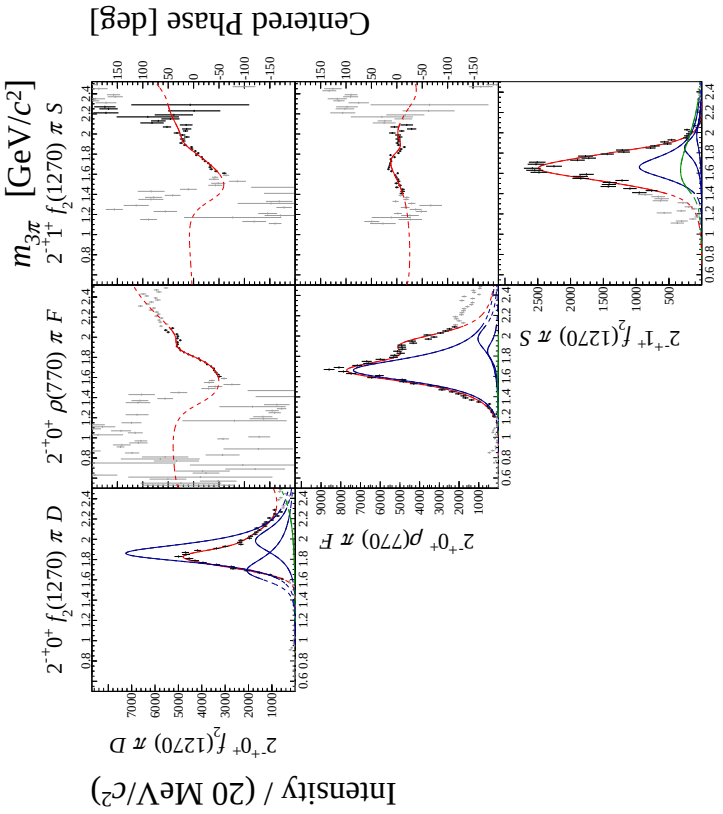

Figure F.24: Spin-density sub-matrix in the range of $0.144 < t' < 0.164\,(\mathrm{GeV}/c)^2$.

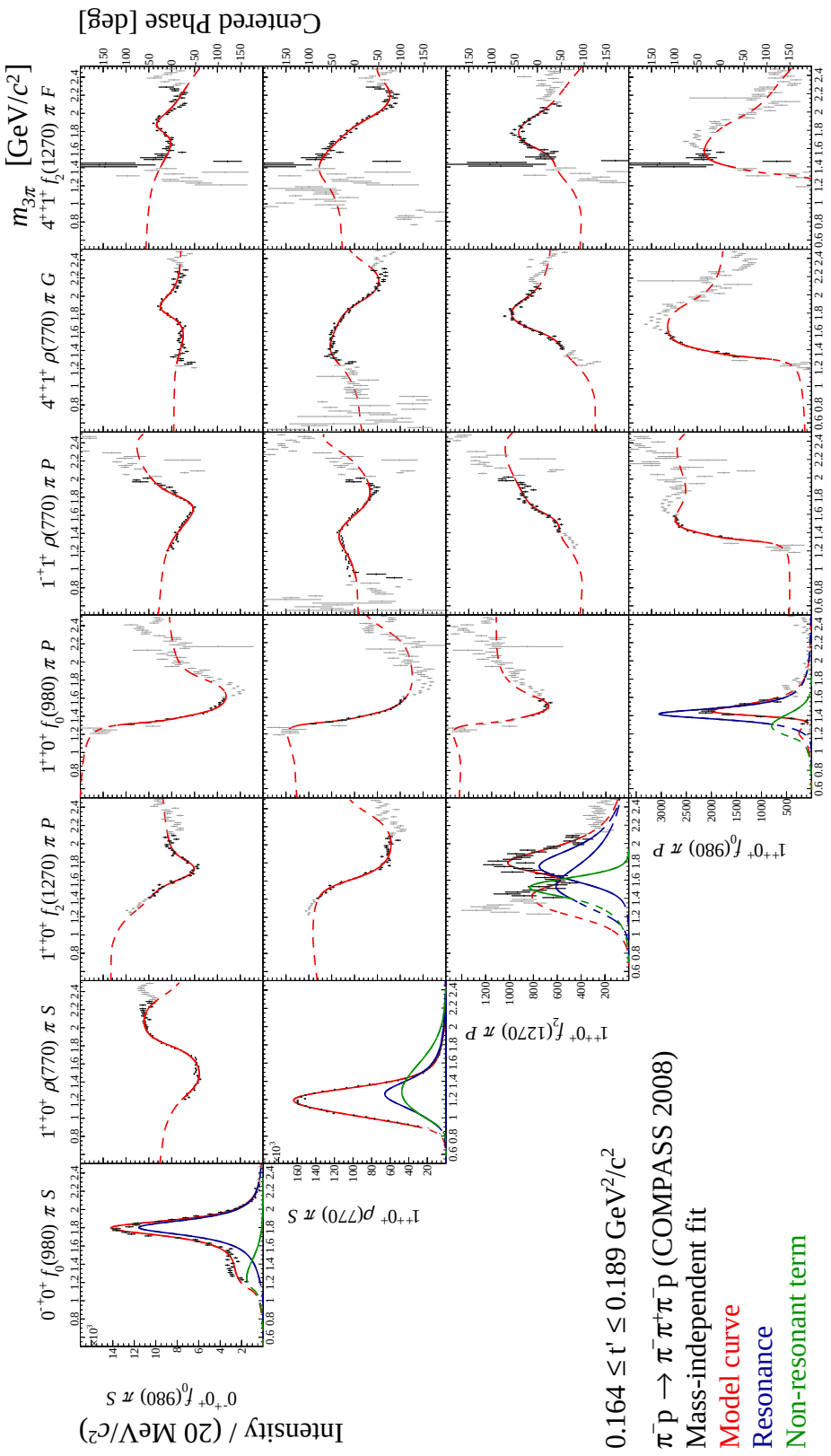

Figure F.25: Spin-density sub-matrix in the range of $0.164 < t' < 0.189$ (GeV/c)^2.

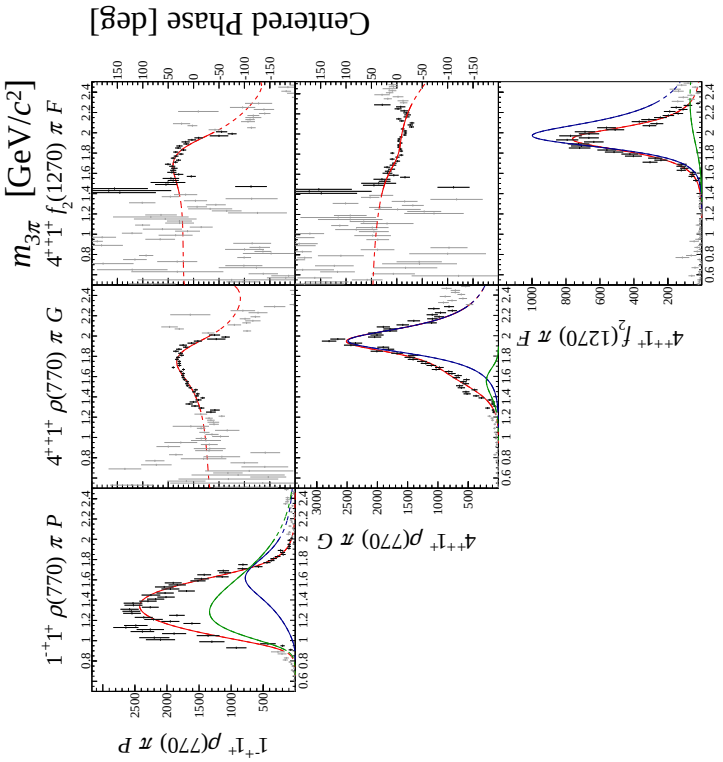

Figure F.26: Spin-density sub-matrix in the range of $0.164 < t' < 0.189$ (GeV/c)^2.

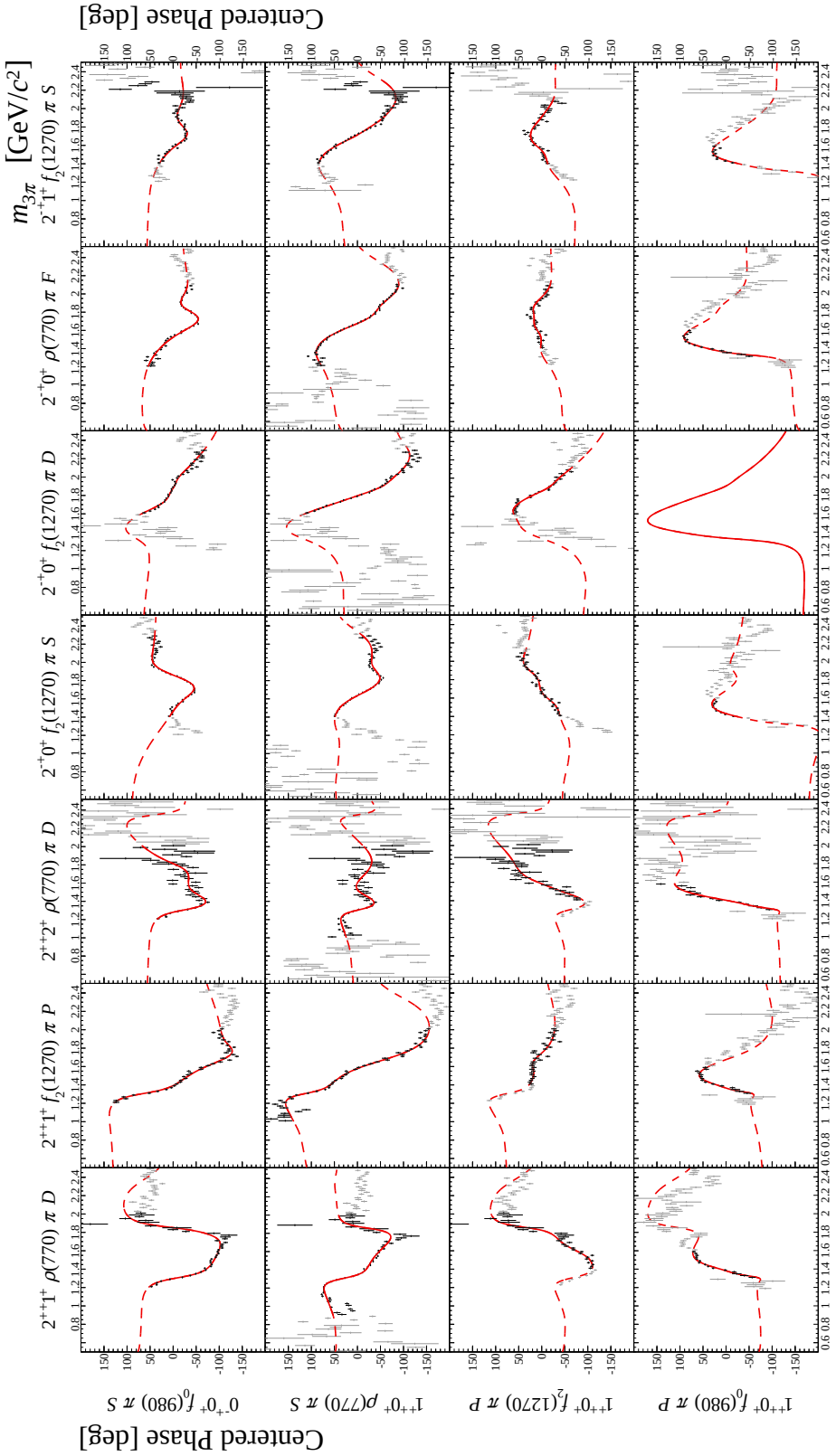

Figure F.27: Spin-density sub-matrix in the range of $0.164 < t' < 0.189$ (GeV/c)^2.

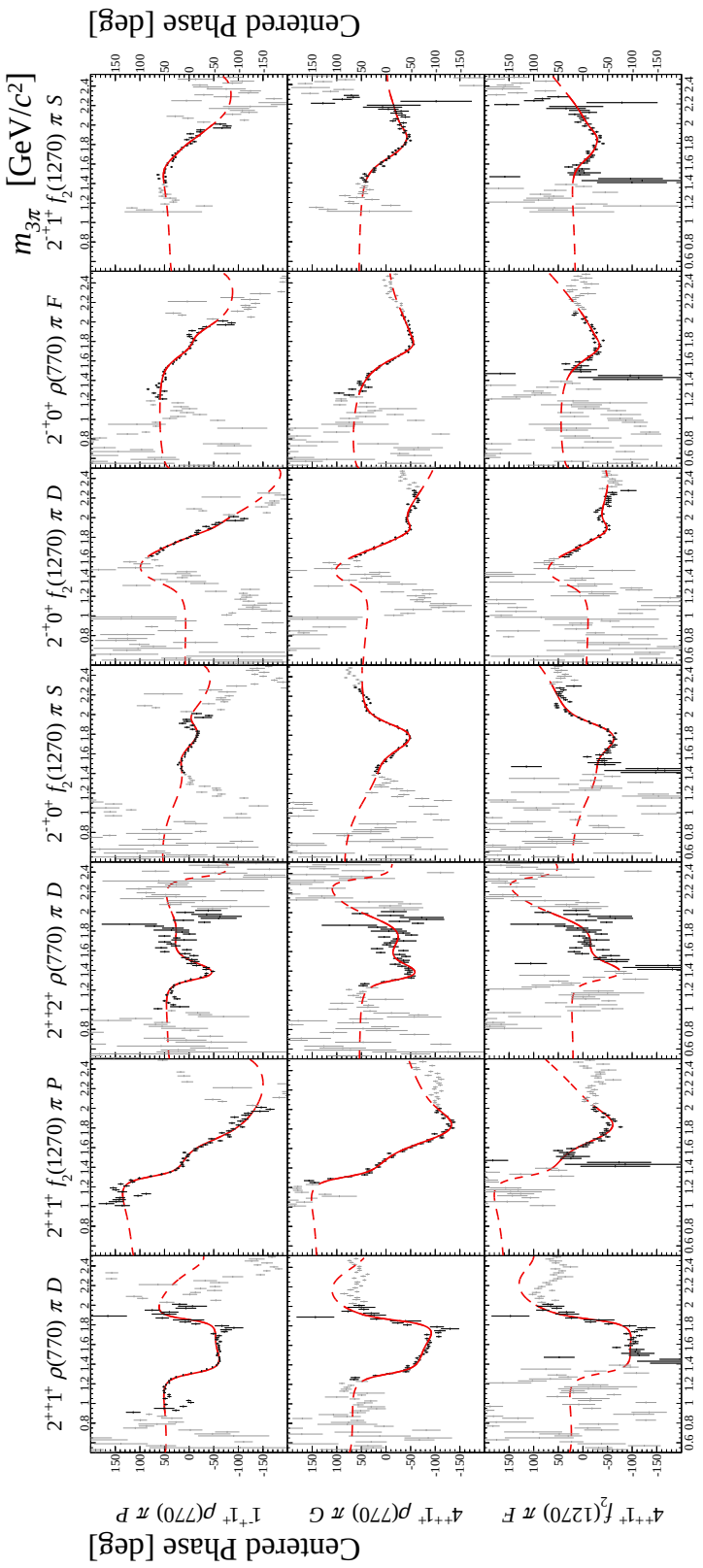

Figure F.28: Spin-density sub-matrix in the range of $0.164 < t' < 0.189$ (GeV/c)^2.

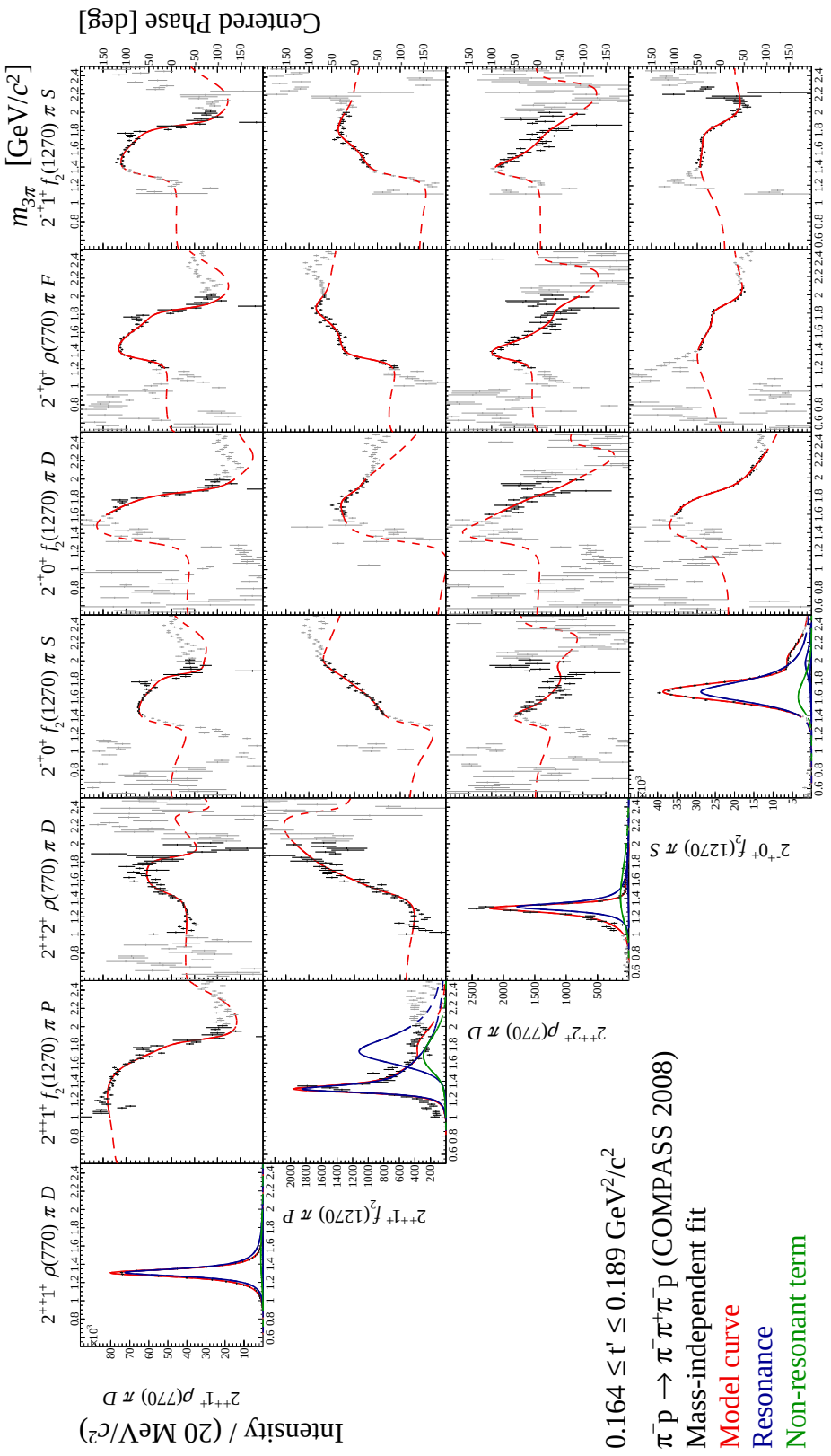

Figure F.29: Spin-density sub-matrix in the range of $0.164 < t' < 0.189$ (GeV/c)^2.

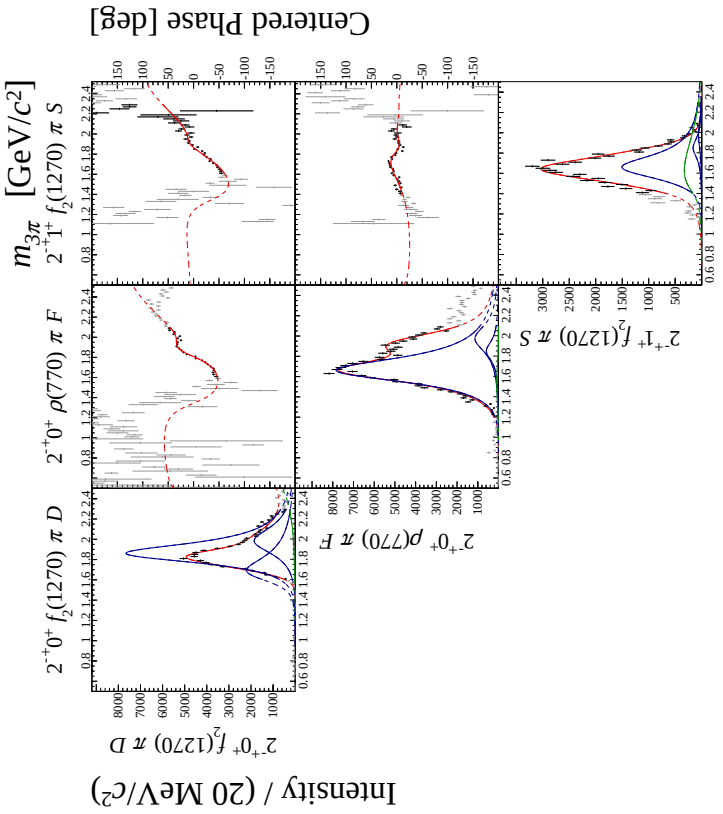

Figure F.30: Spin-density sub-matrix in the range of $0.164 < t' < 0.189\,(\mathrm{GeV}/c)^2$.

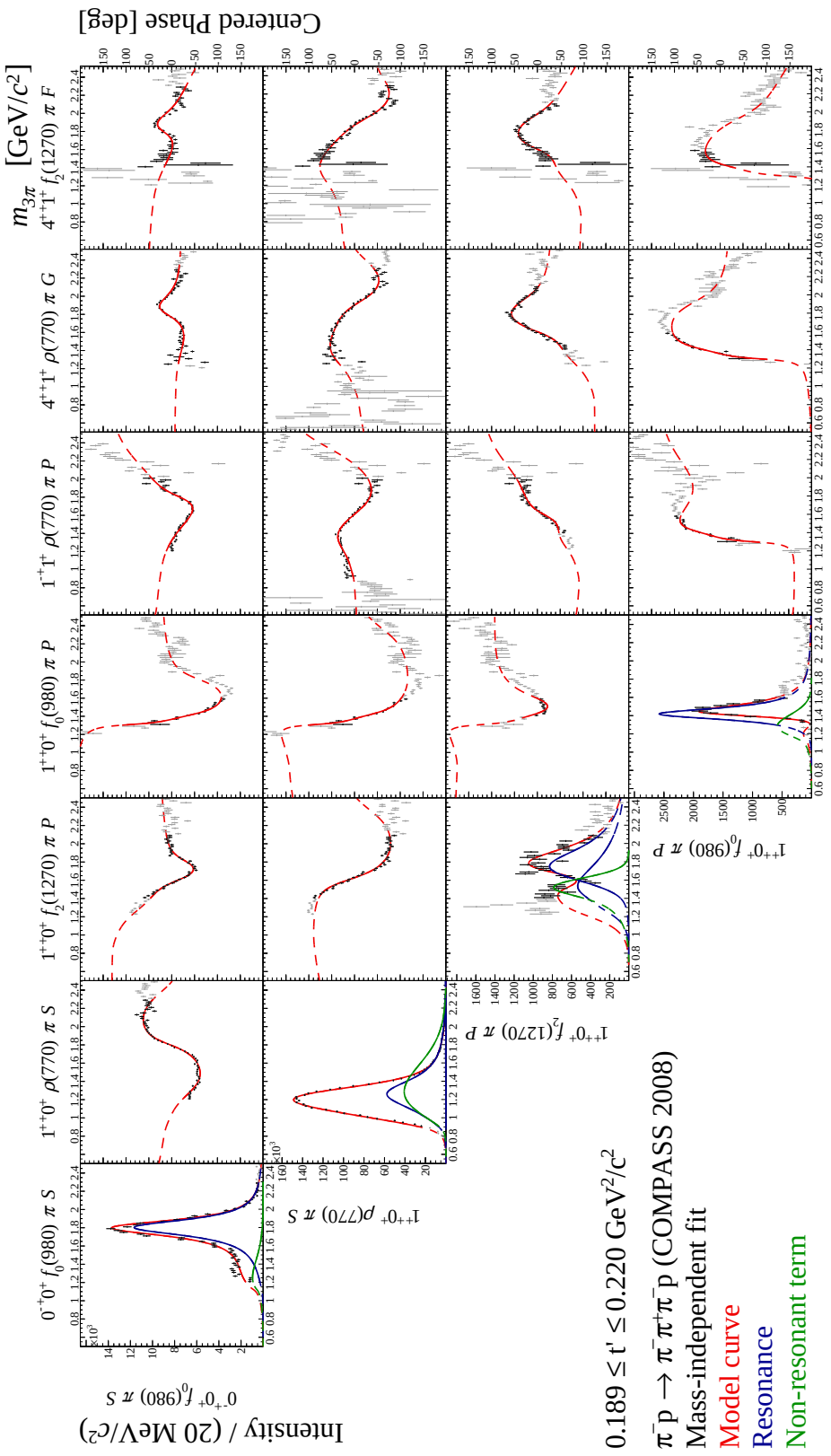

Figure F.31: Spin-density sub-matrix in the range of $0.189 < t' < 0.220\,(\mathrm{GeV}/c)^2$.

Figure F.32: Spin-density sub-matrix in the range of $0.189 < t' < 0.220\,(\mathrm{GeV}/c)^2$.

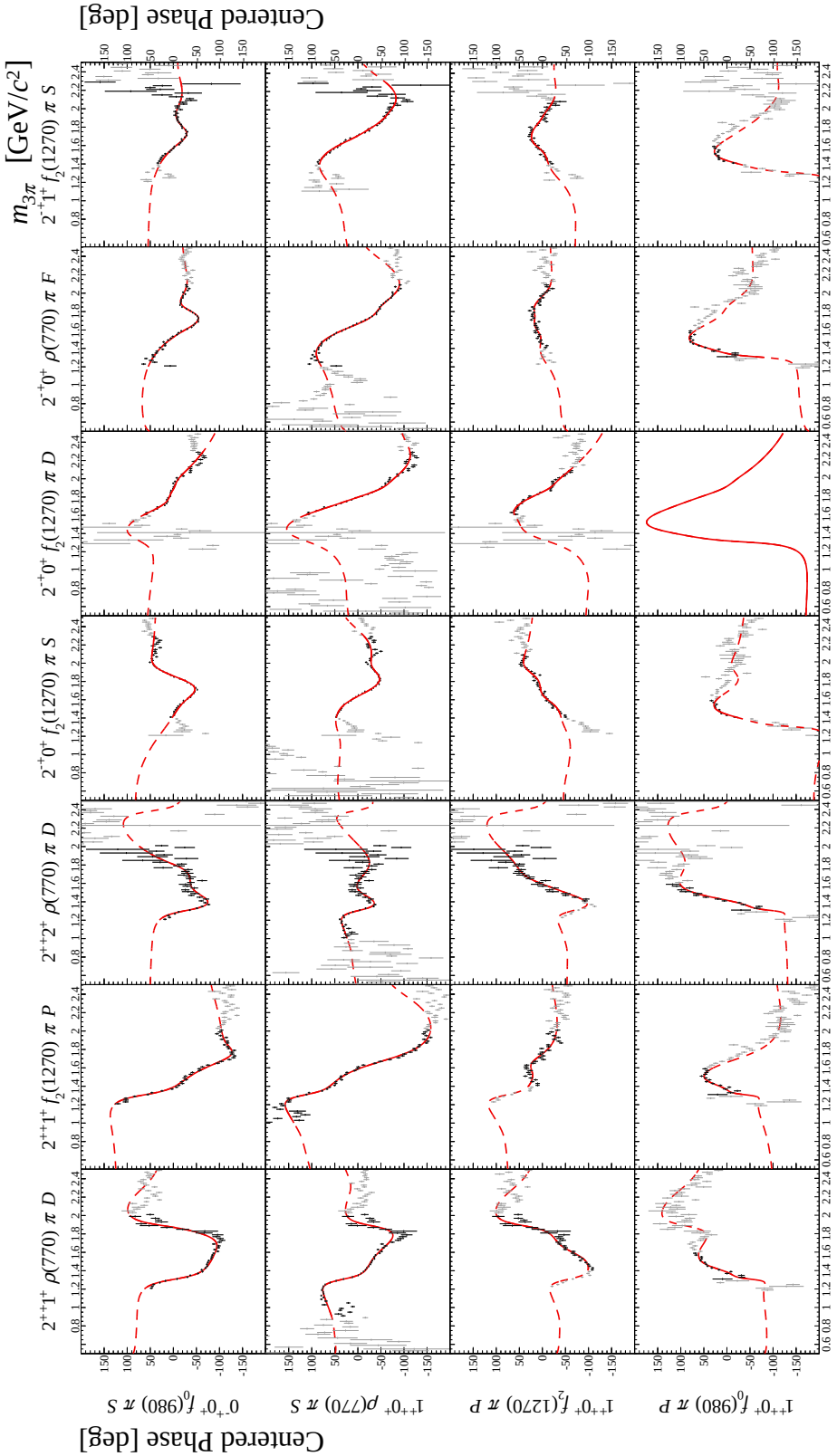

Figure F.33: Spin-density sub-matrix in the range of $0.189 < t' < 0.220\,(\mathrm{GeV}/c)^2$.

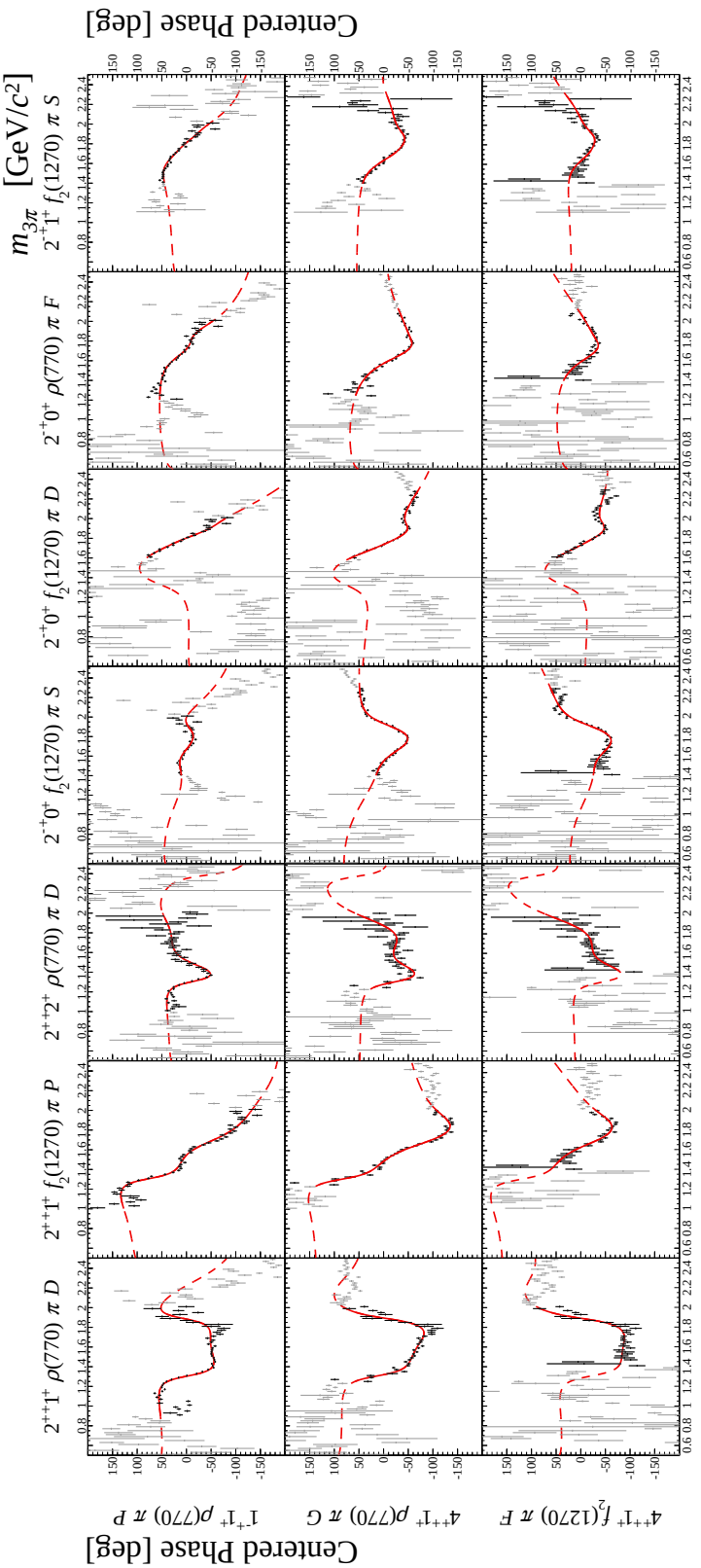

Figure F.34: Spin-density sub-matrix in the range of $0.189 < t' < 0.220\,(\mathrm{GeV}/c)^2$.

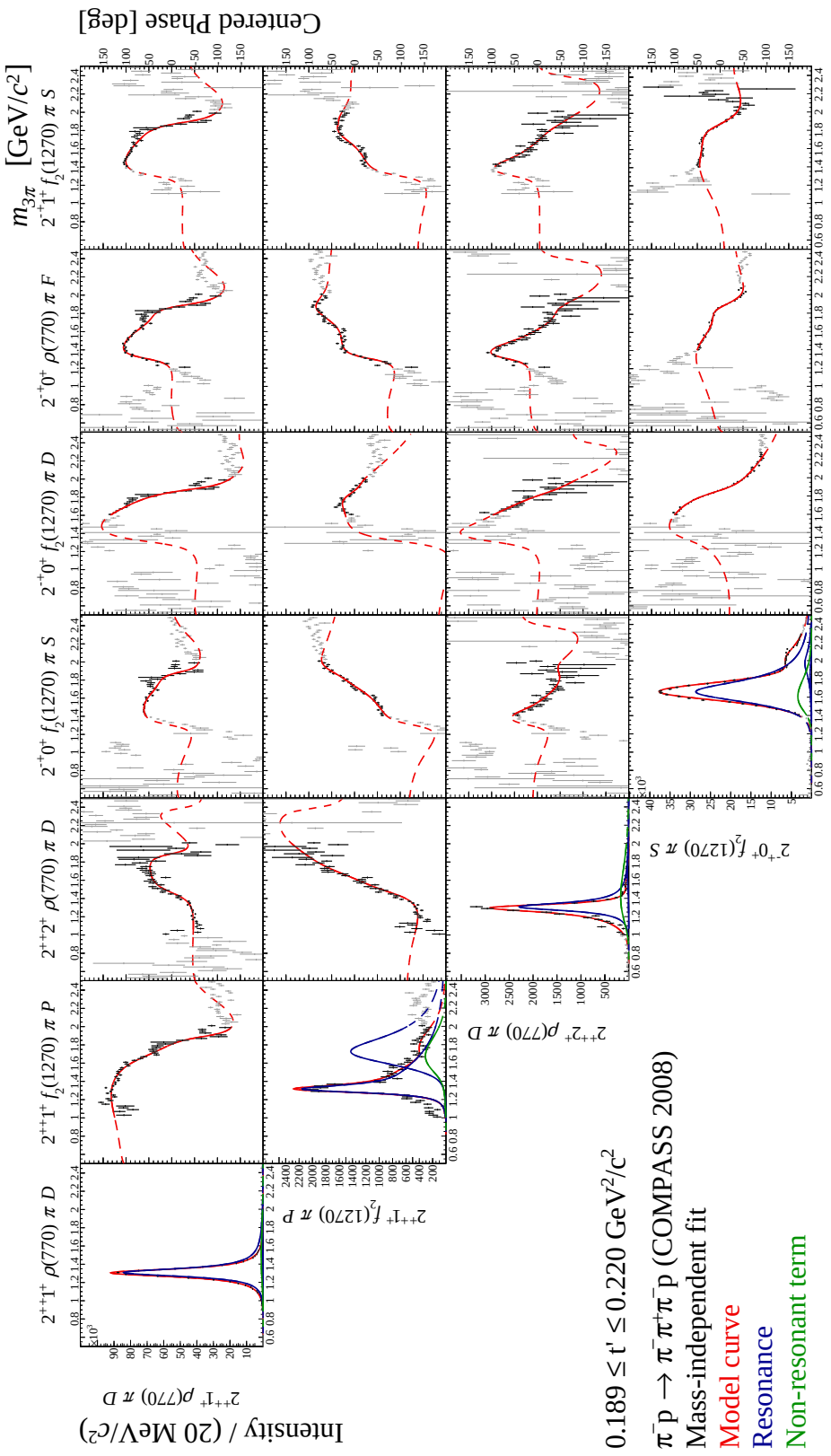

Figure F.35: Spin-density sub-matrix in the range of $0.189 < t' < 0.220\,(\mathrm{GeV}/c)^2$.

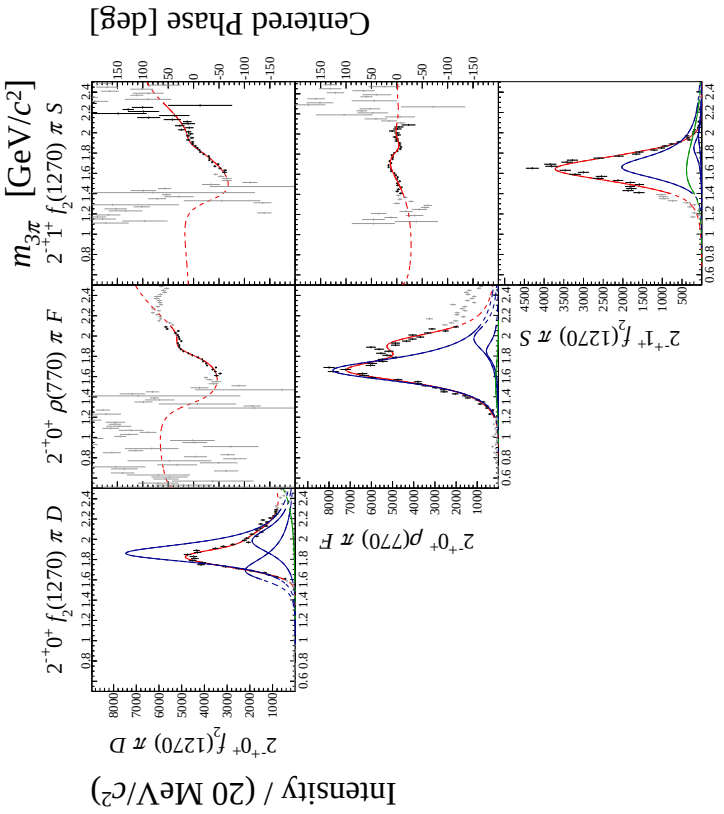

Figure F.36: Spin-density sub-matrix in the range of $0.189 < t' < 0.220\,(\mathrm{GeV}/c)^2$.

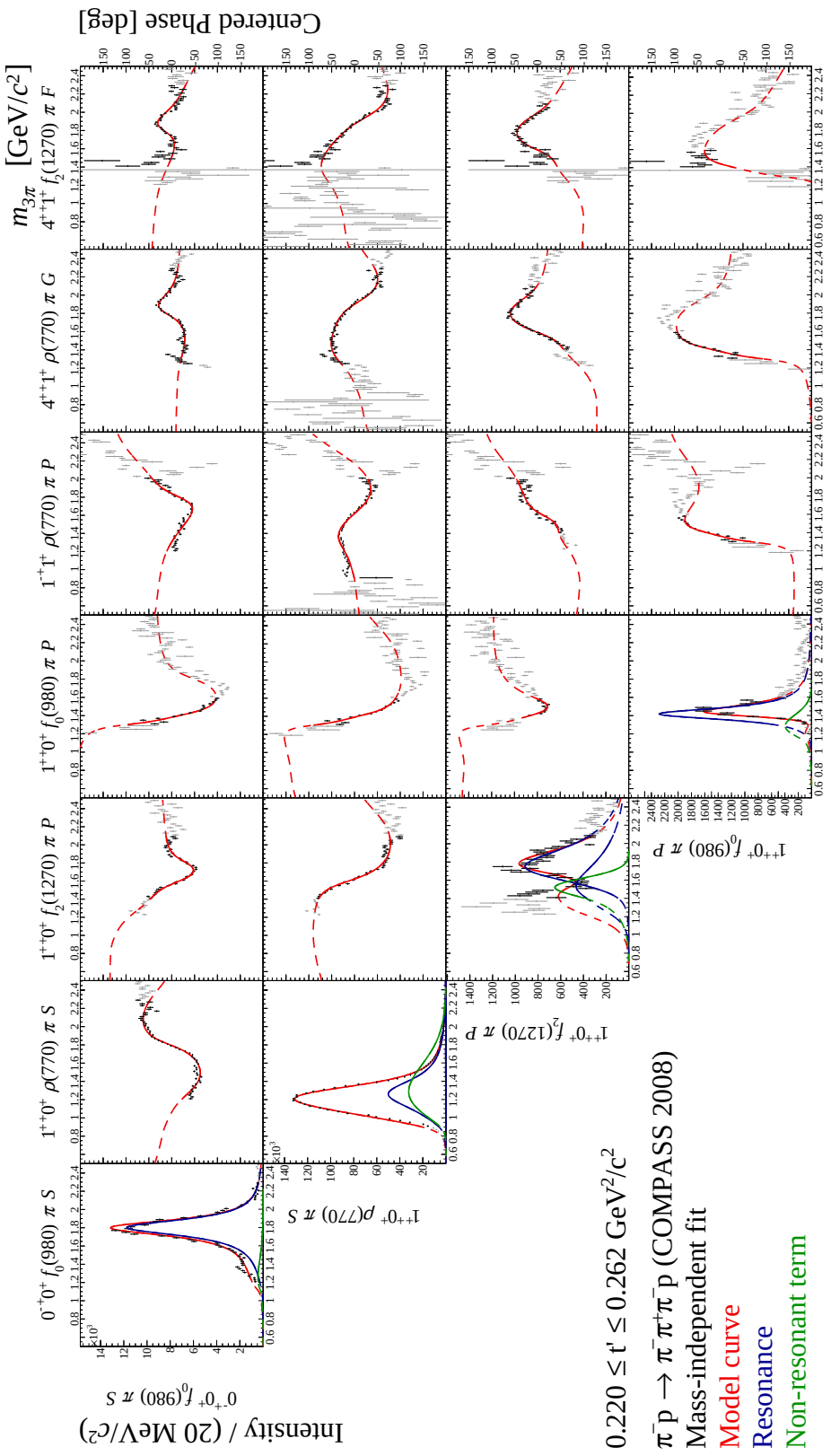

Figure F.37: Spin-density sub-matrix in the range of $0.220 < t' < 0.262$ (GeV/c)^2.

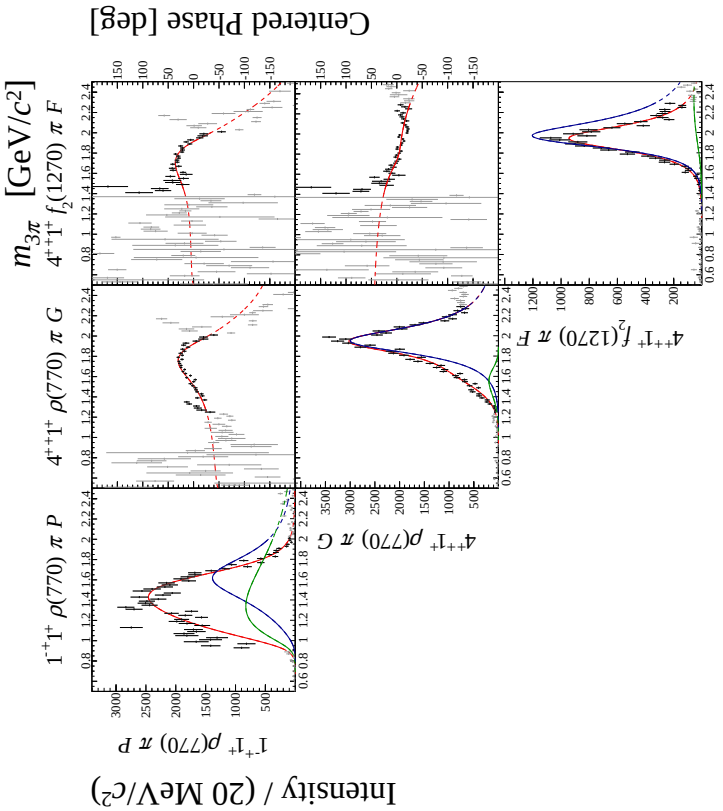

Figure F.38: Spin-density sub-matrix in the range of $0.220 < t' < 0.262$ (GeV/c)^2.

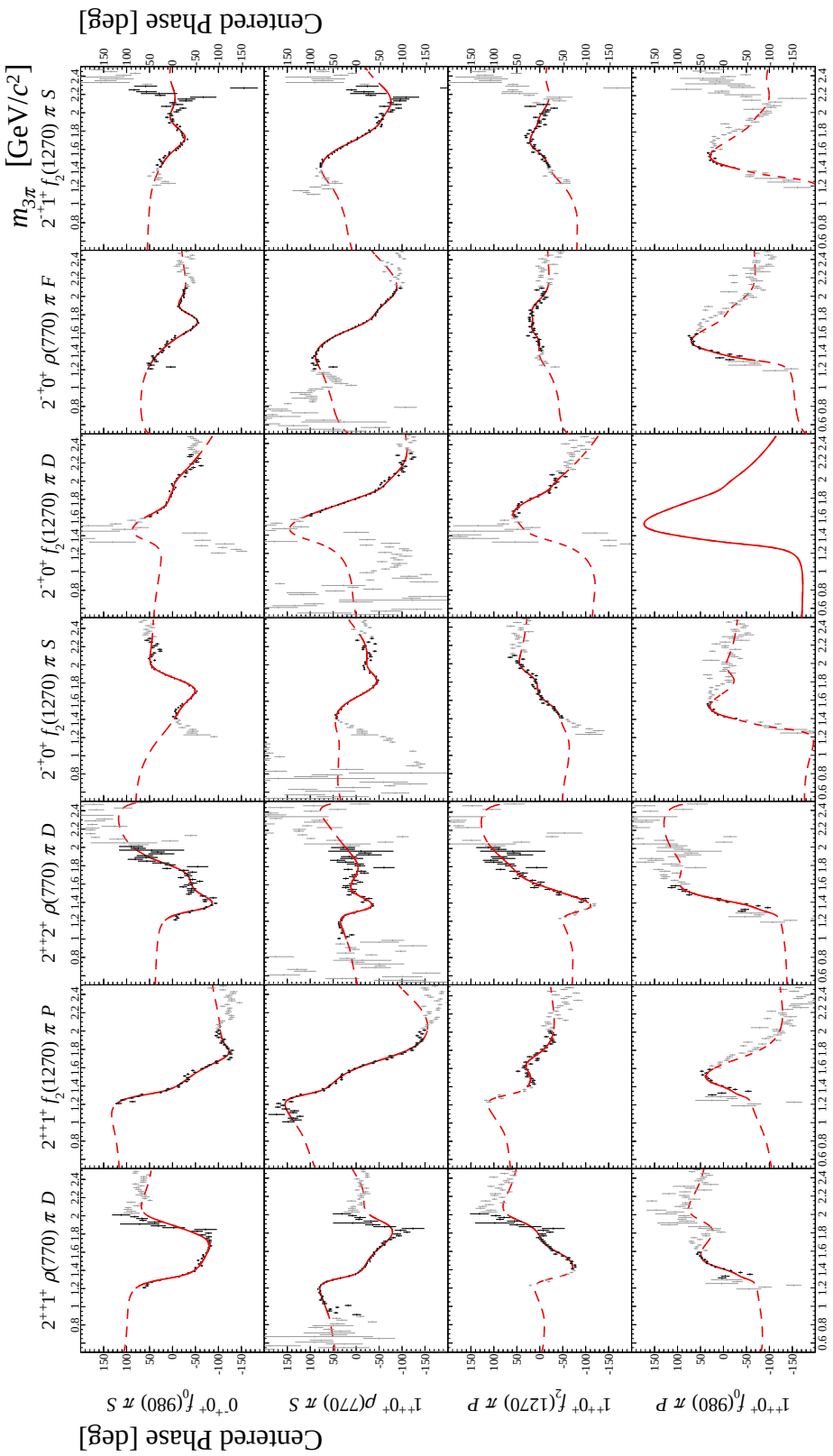

Figure F.39: Spin-density sub-matrix in the range of $0.220 < t' < 0.262\ (\mathrm{GeV}/c)^2$.

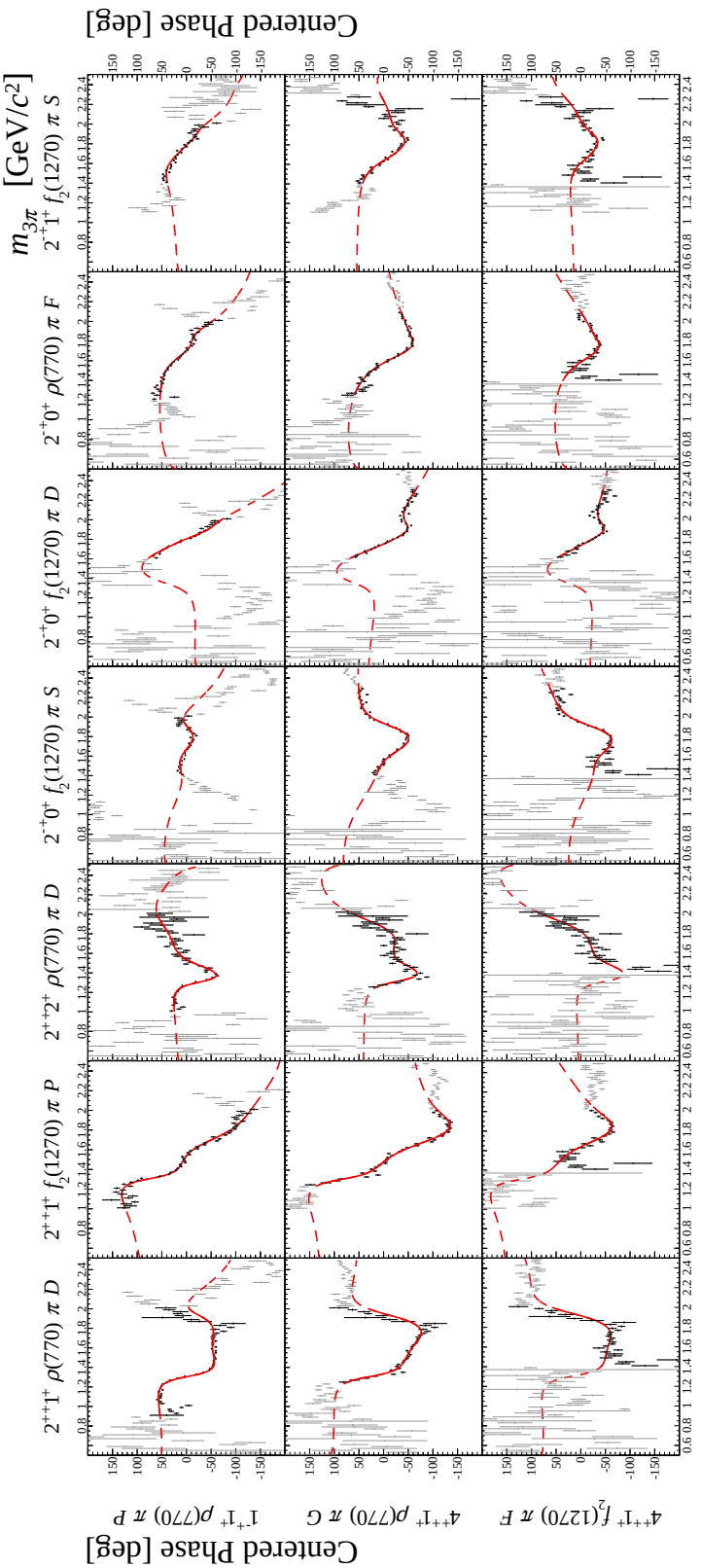

Figure F.40: Spin-density sub-matrix in the range of $0.220 < t' < 0.262$ (GeV/c)^2.

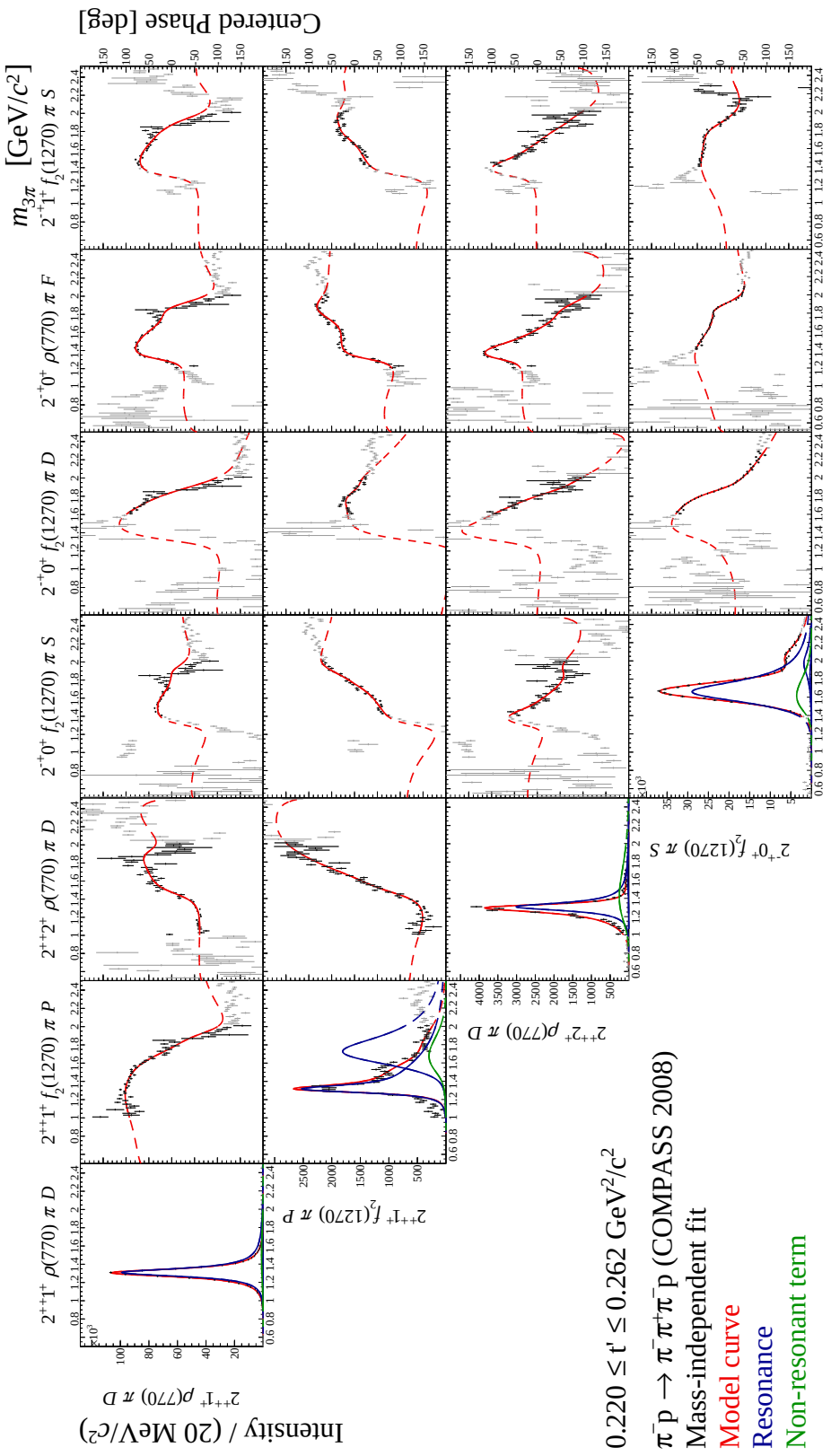

Figure F.41: Spin-density sub-matrix in the range of $0.220 < t' < 0.262$ (GeV/c)^2.

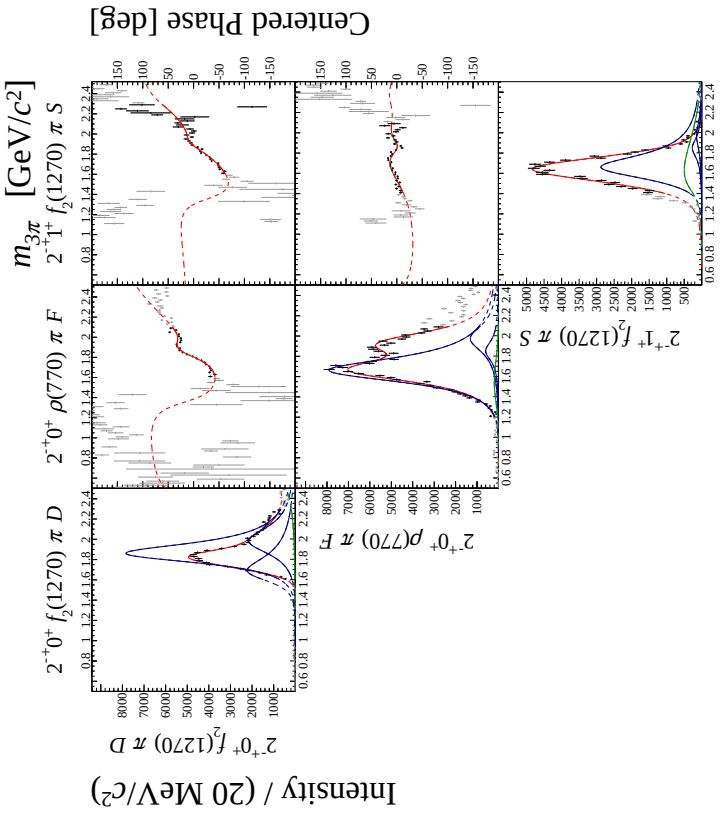

Figure F.42: Spin-density sub-matrix in the range of $0.220 < t' < 0.262\,(\mathrm{GeV}/c)^2$.

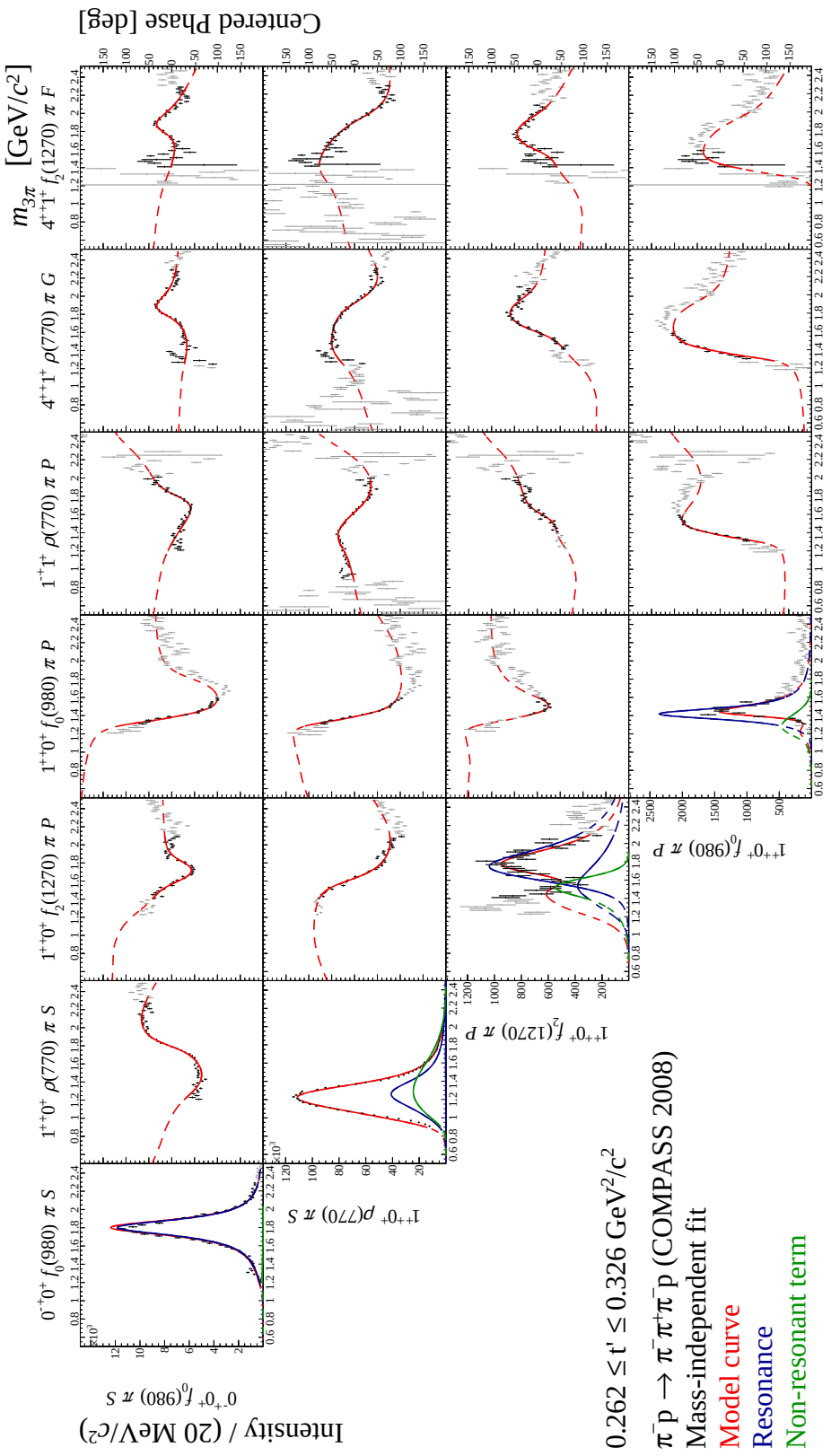

Figure F.43: Spin-density sub-matrix in the range of $0.262 < t' < 0.326\,(\mathrm{GeV}/c)^2$.

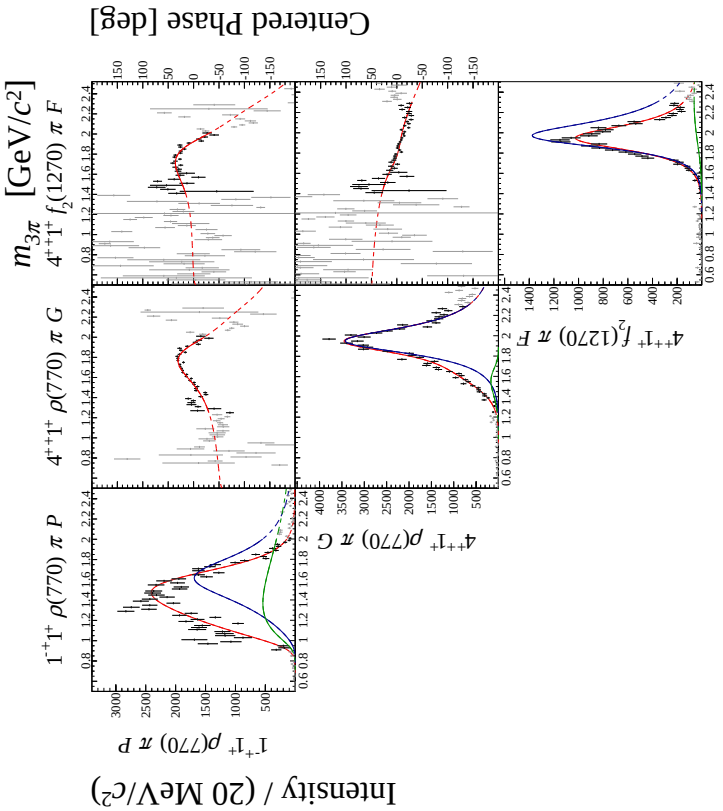

Figure F.44: Spin-density sub-matrix in the range of $0.262 < t' < 0.326\,(\mathrm{GeV}/c)^2$.

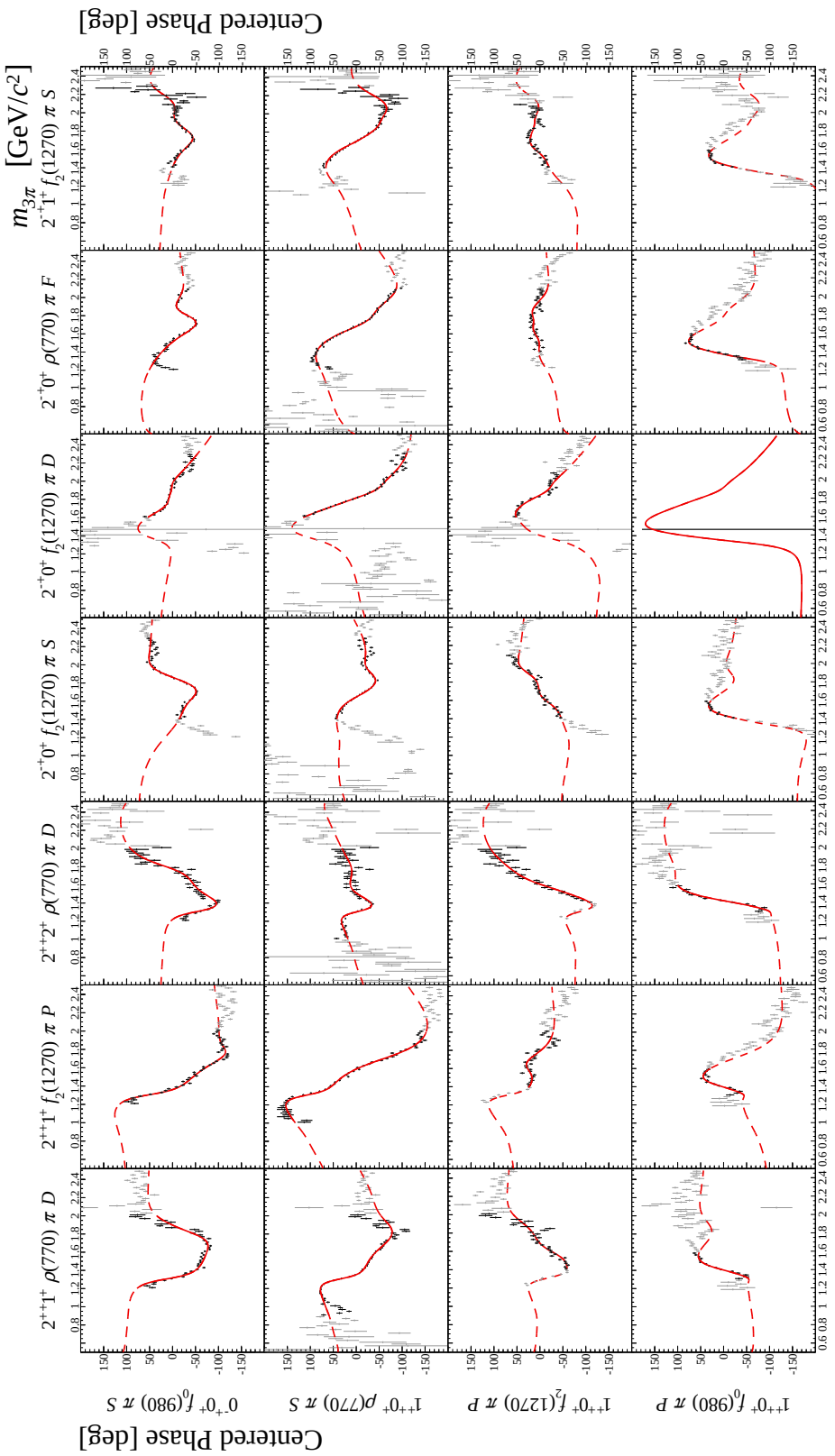

Figure F.45: Spin-density sub-matrix in the range of $0.262 < t' < 0.326\,(\mathrm{GeV}/c)^2$.

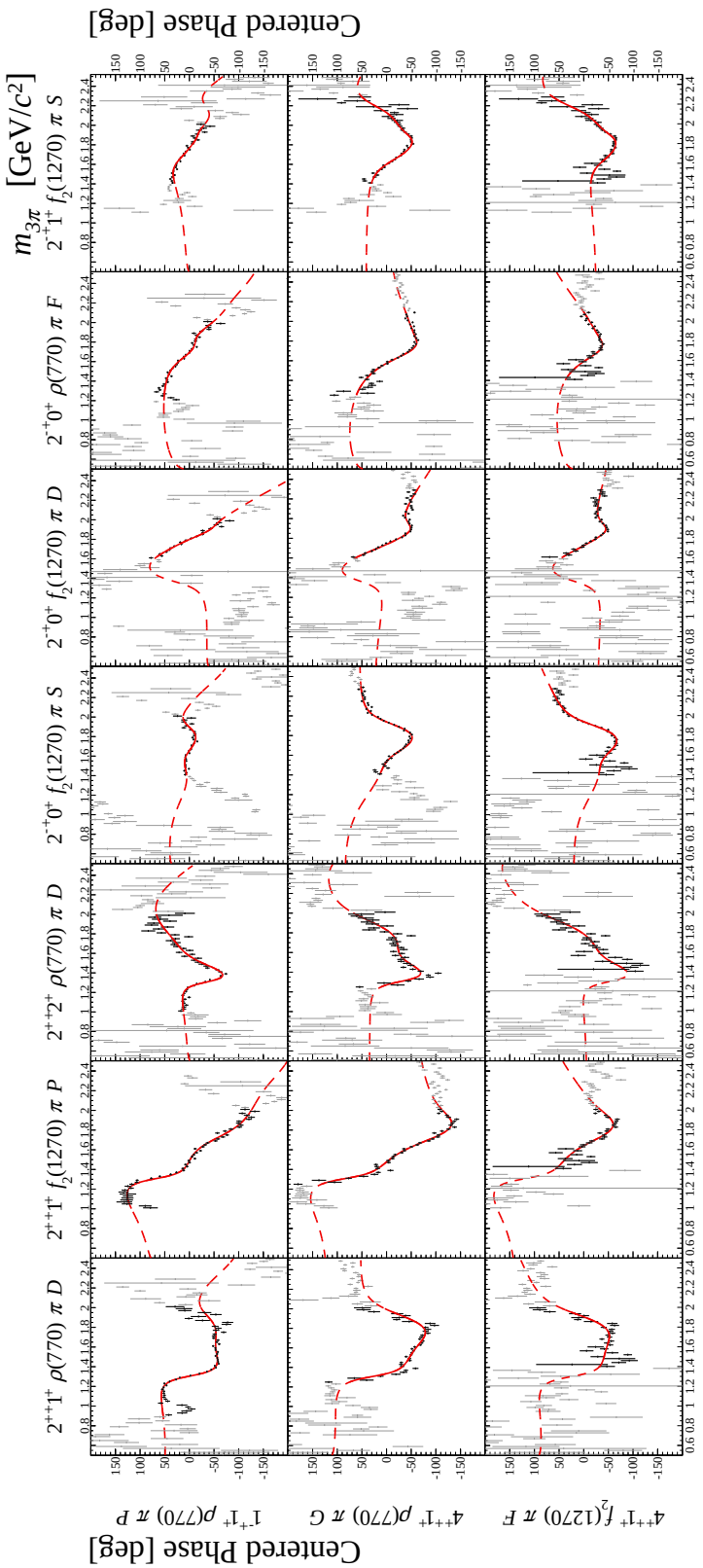

Figure F.46: Spin-density sub-matrix in the range of $0.262 < t' < 0.326\,(\mathrm{GeV}/c)^2$.

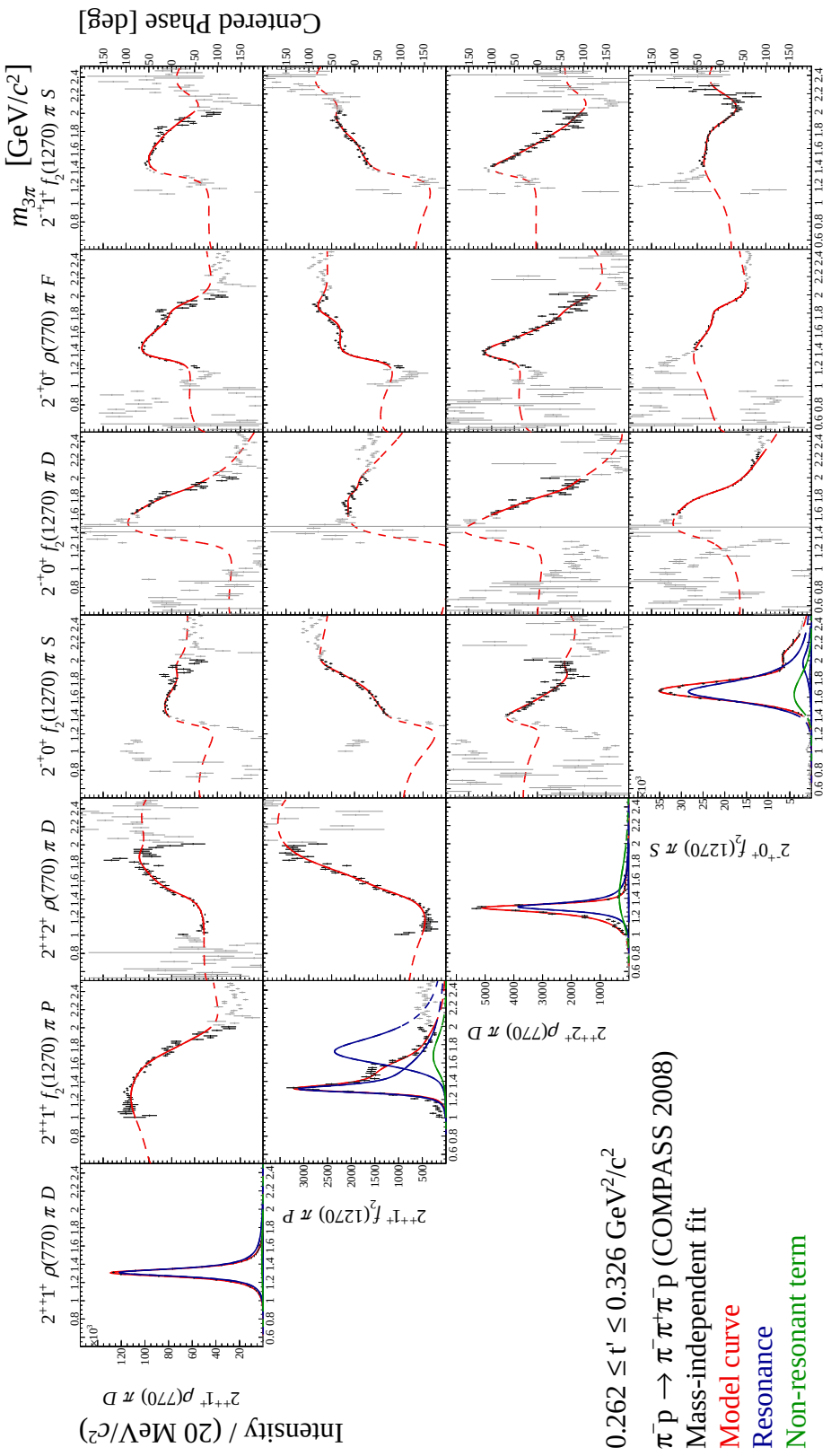

Figure F.47: Spin-density sub-matrix in the range of $0.262 < t' < 0.326\,(\mathrm{GeV}/c)^2$.

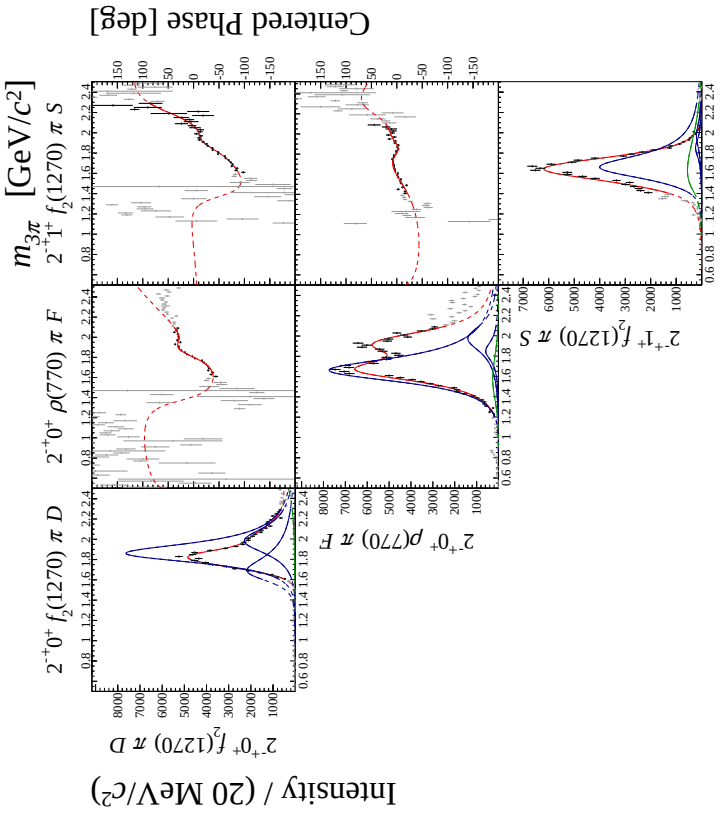

Figure F.48: Spin-density sub-matrix in the range of $0.262 < t' < 0.326\,(\mathrm{GeV}/c)^2$.

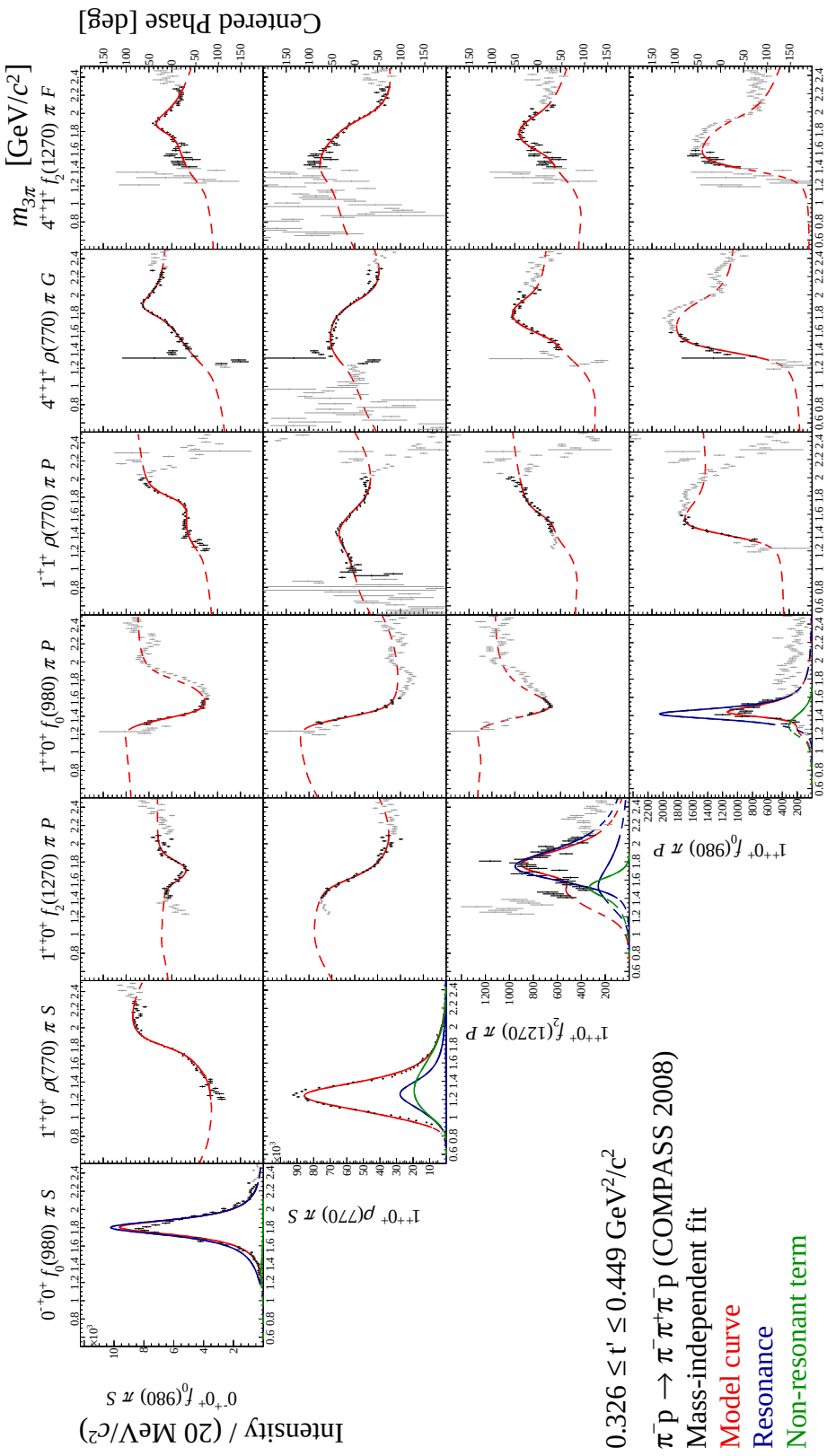

Figure F.49: Spin-density sub-matrix in the range of $0.326 < t' < 0.449$ (GeV/c)^2.

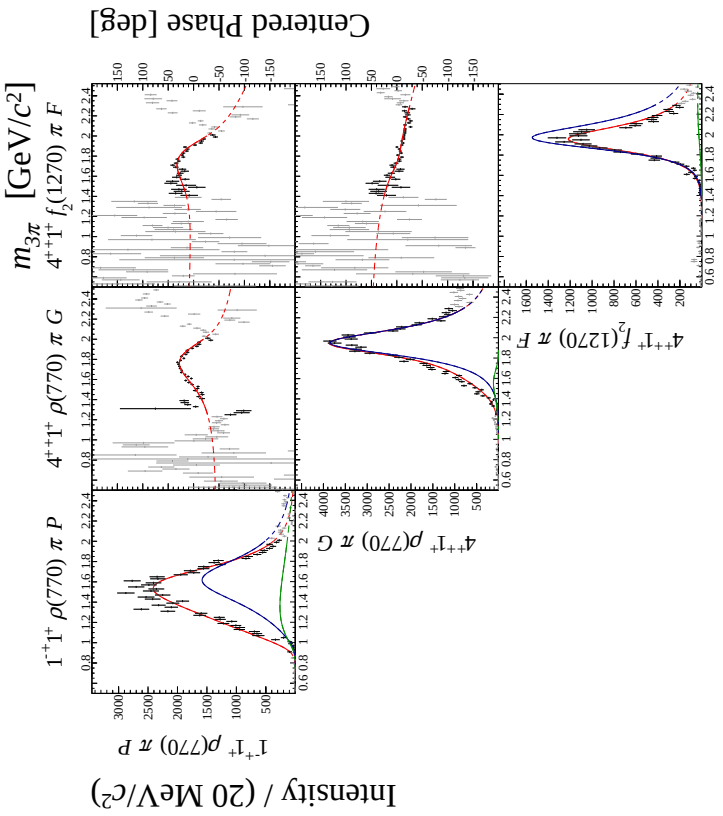

Figure F.50: Spin-density sub-matrix in the range of $0.326 < t' < 0.449$ (GeV/c)^2.

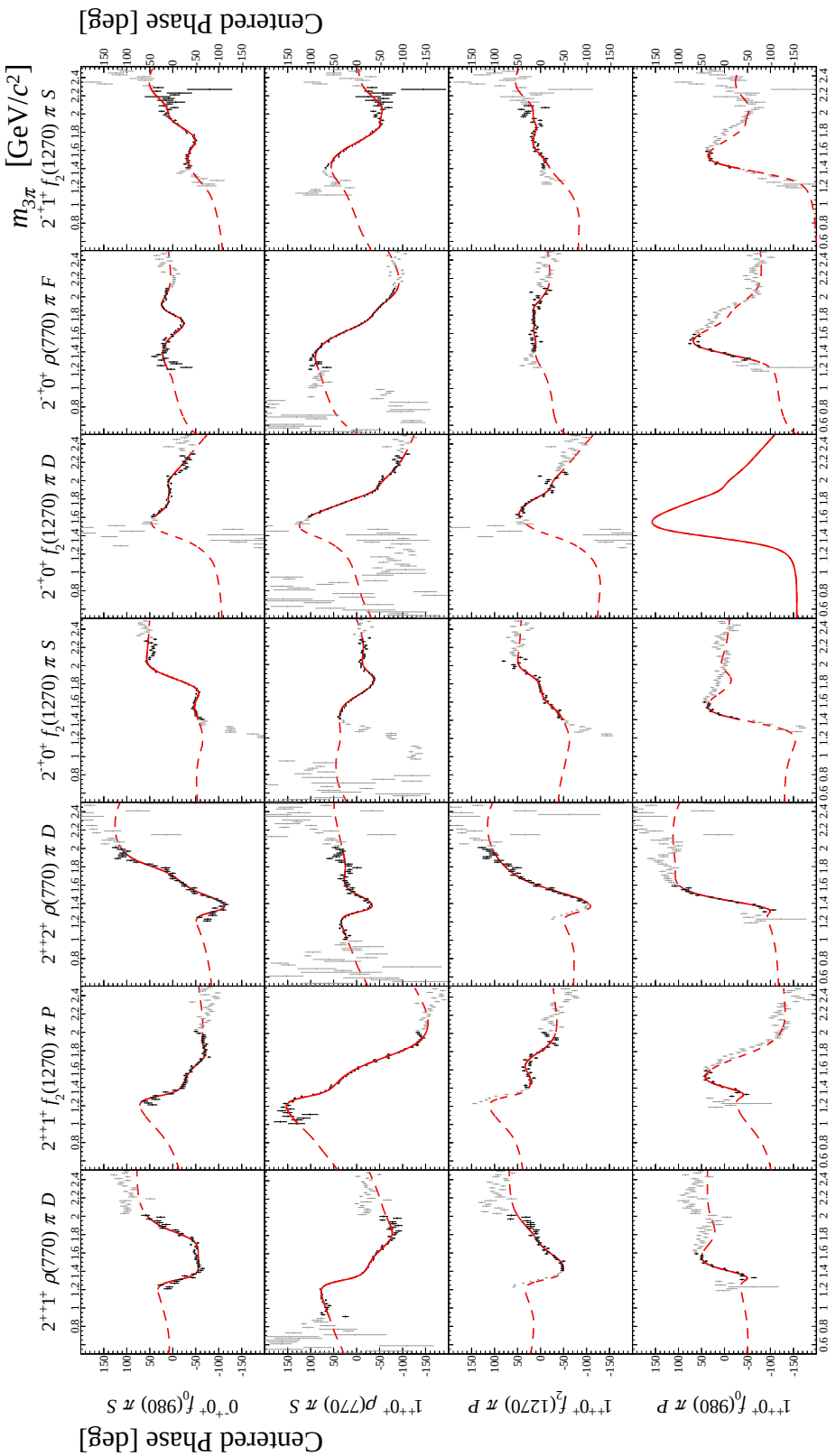

Figure F.51: Spin-density sub-matrix in the range of $0.326 < t' < 0.449$ (GeV/c)^2.

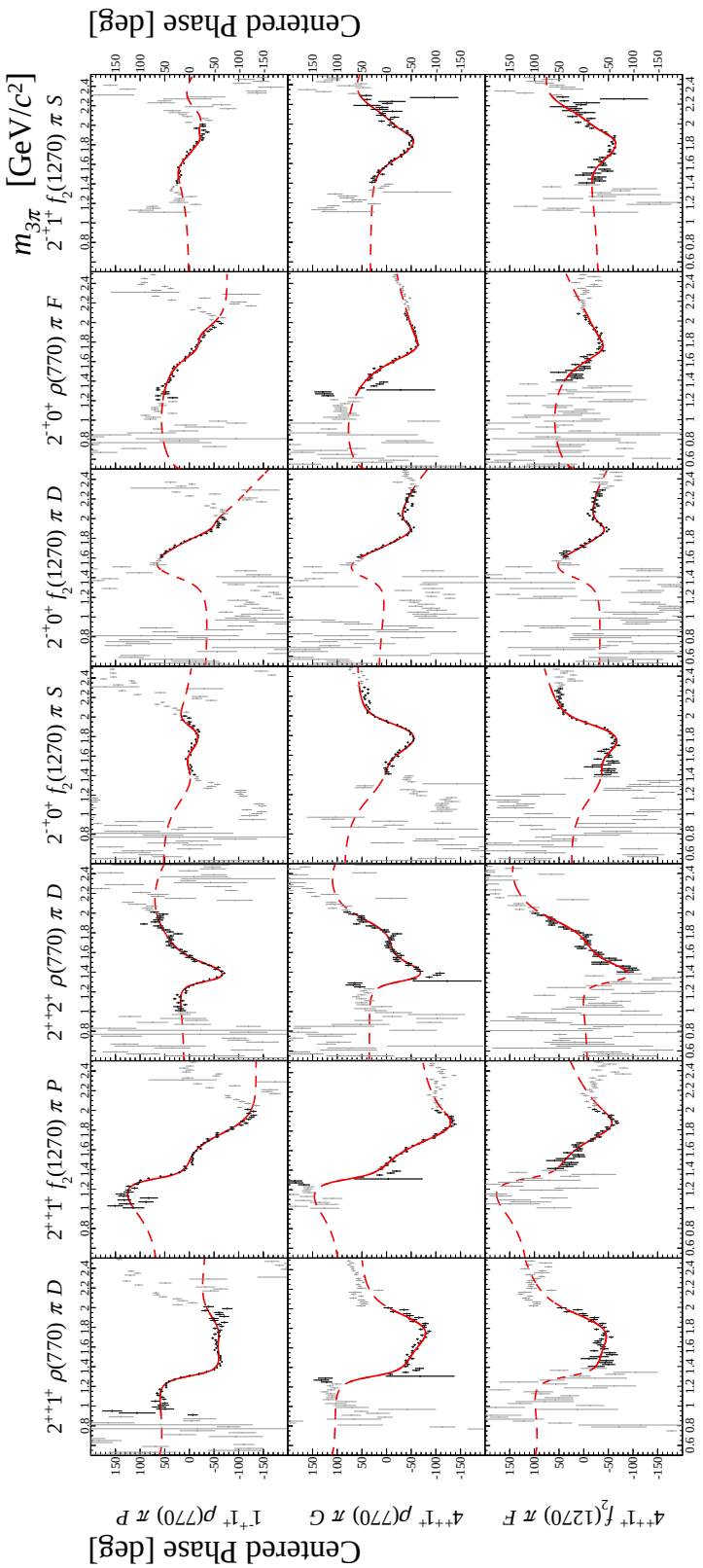

Figure F.52: Spin-density sub-matrix in the range of $0.326 < t' < 0.449\,(\mathrm{GeV}/c)^2$.

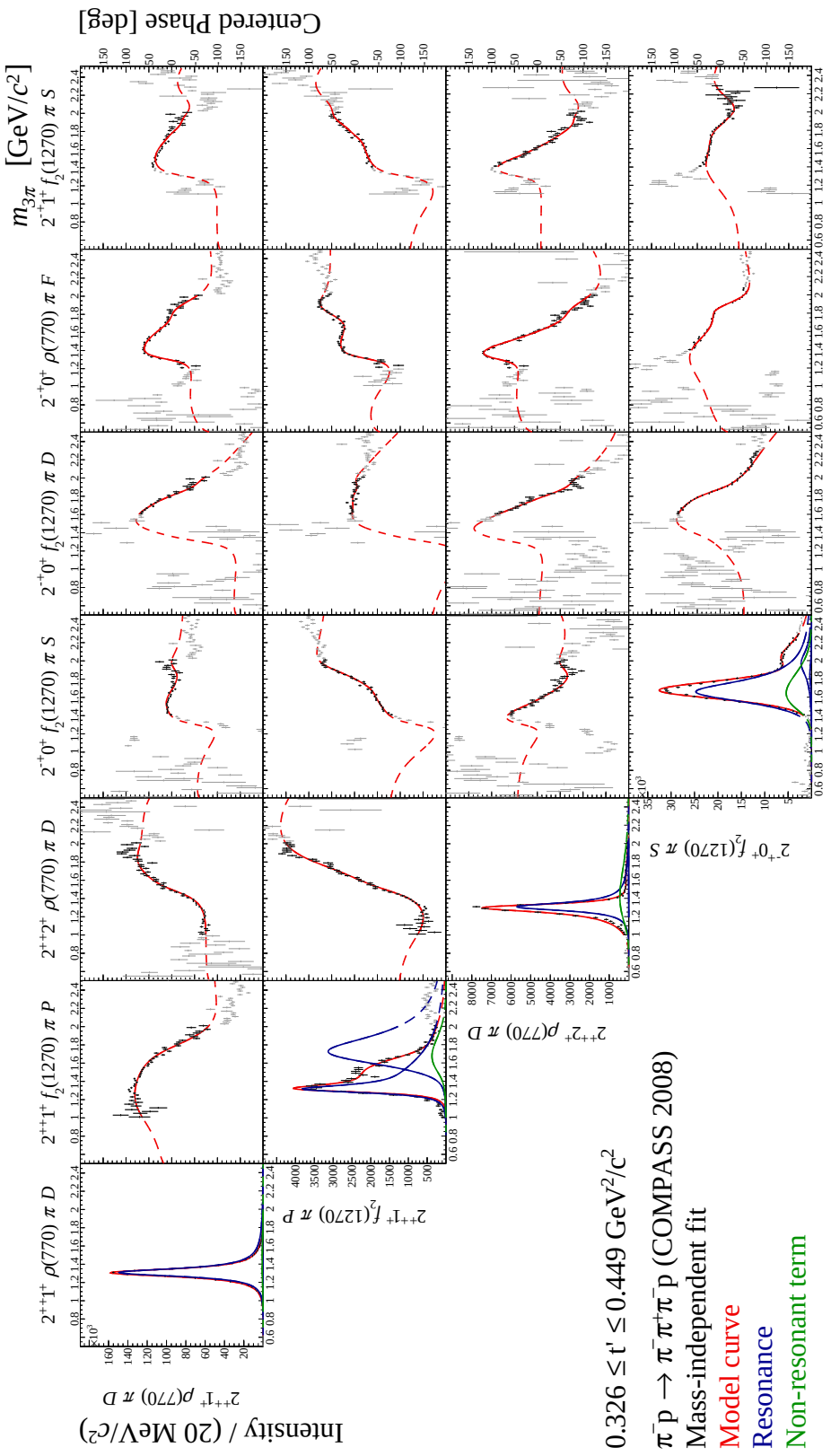

Figure F.53: Spin-density sub-matrix in the range of $0.326 < t' < 0.449$ (GeV/c)^2.

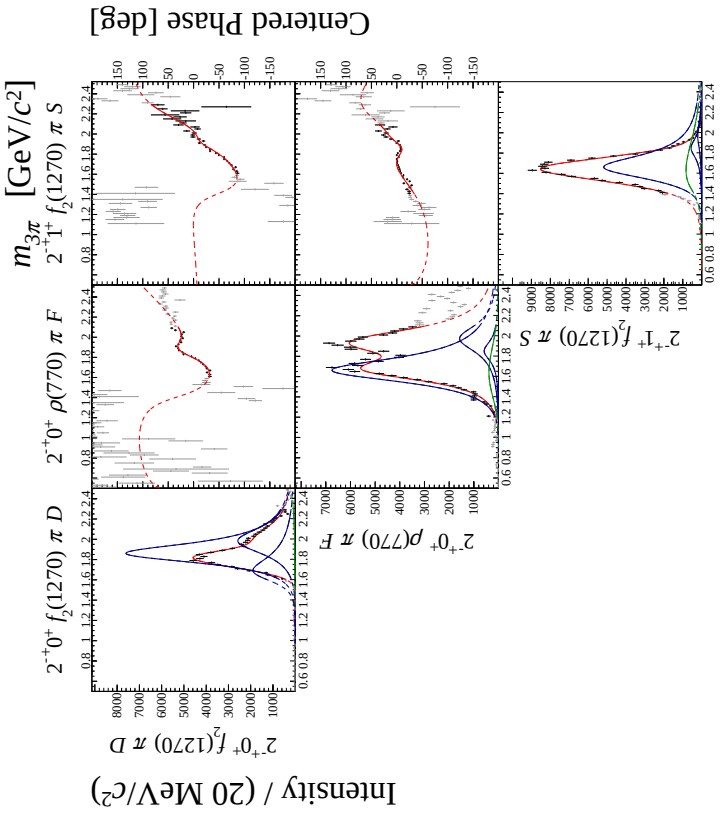

Figure F.54: Spin-density sub-matrix in the range of $0.326 < t' < 0.449\,(\mathrm{GeV}/c)^2$.

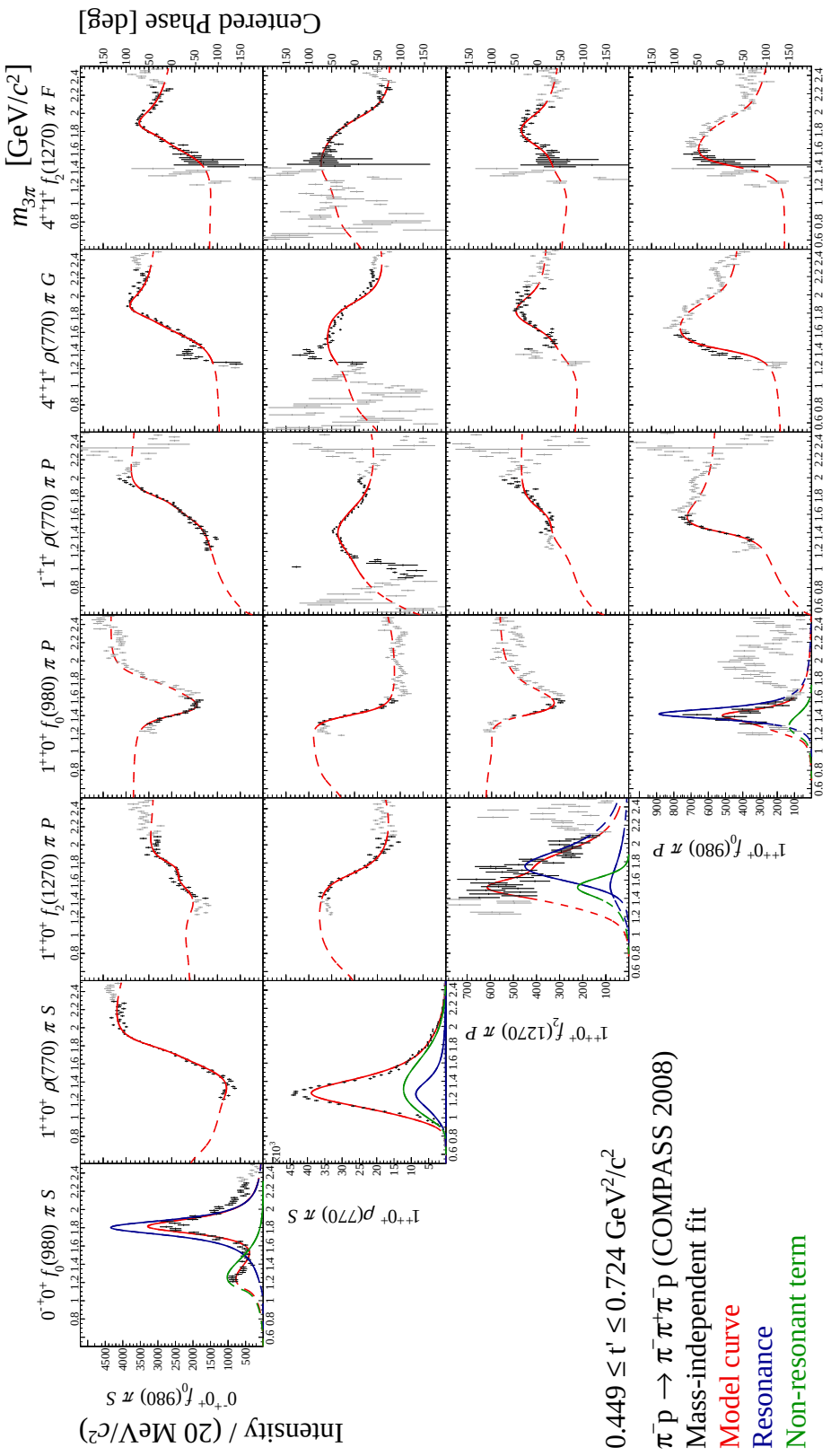

Figure F.55: Spin-density sub-matrix in the range of $0.449 < t' < 0.724\,(\mathrm{GeV}/c)^2$.

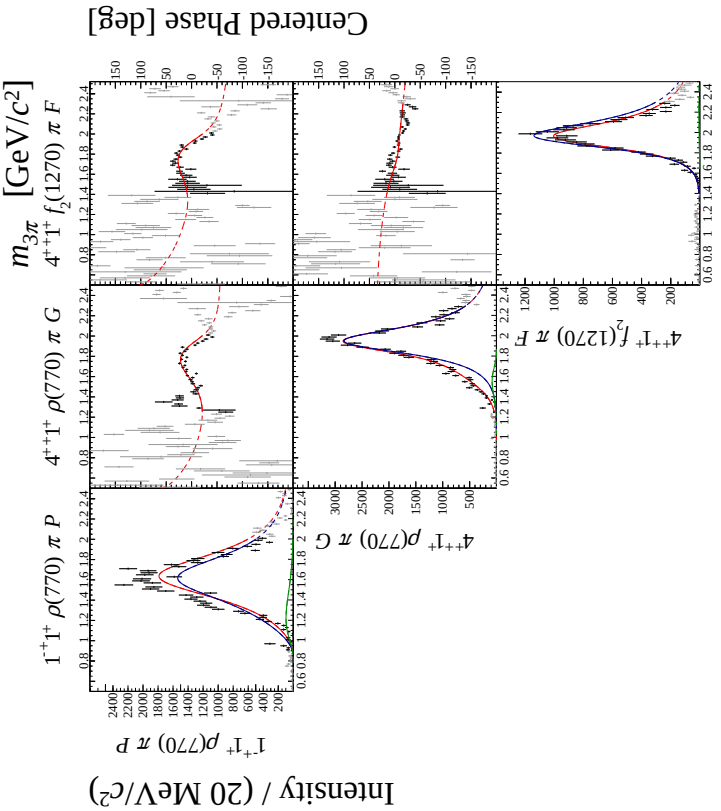

Figure F.56: Spin-density sub-matrix in the range of $0.449 < t' < 0.724$ (GeV/c)^2.

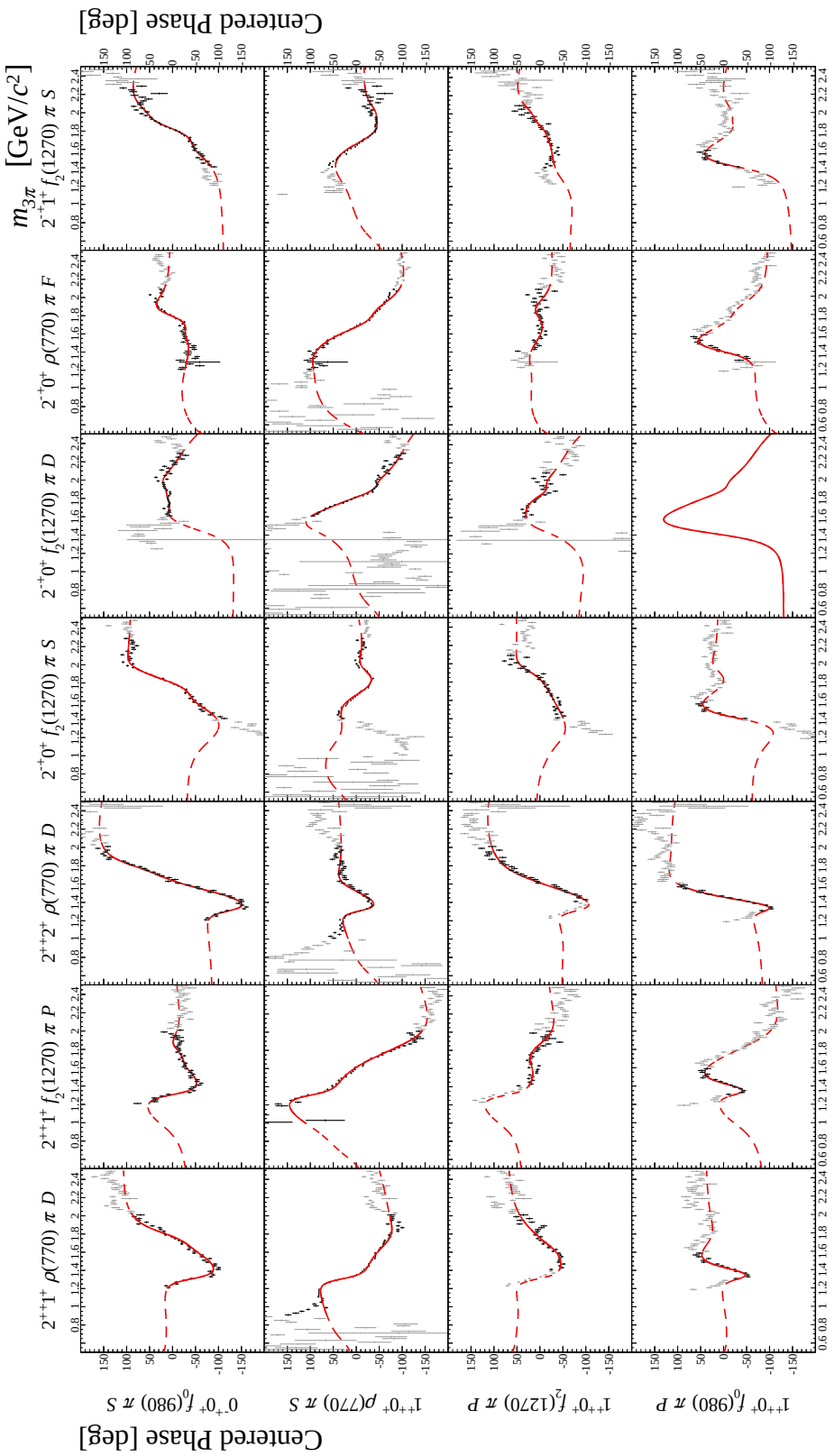

Figure F.57: Spin-density sub-matrix in the range of $0.449 < t' < 0.724\,(\mathrm{GeV}/c)^2$.

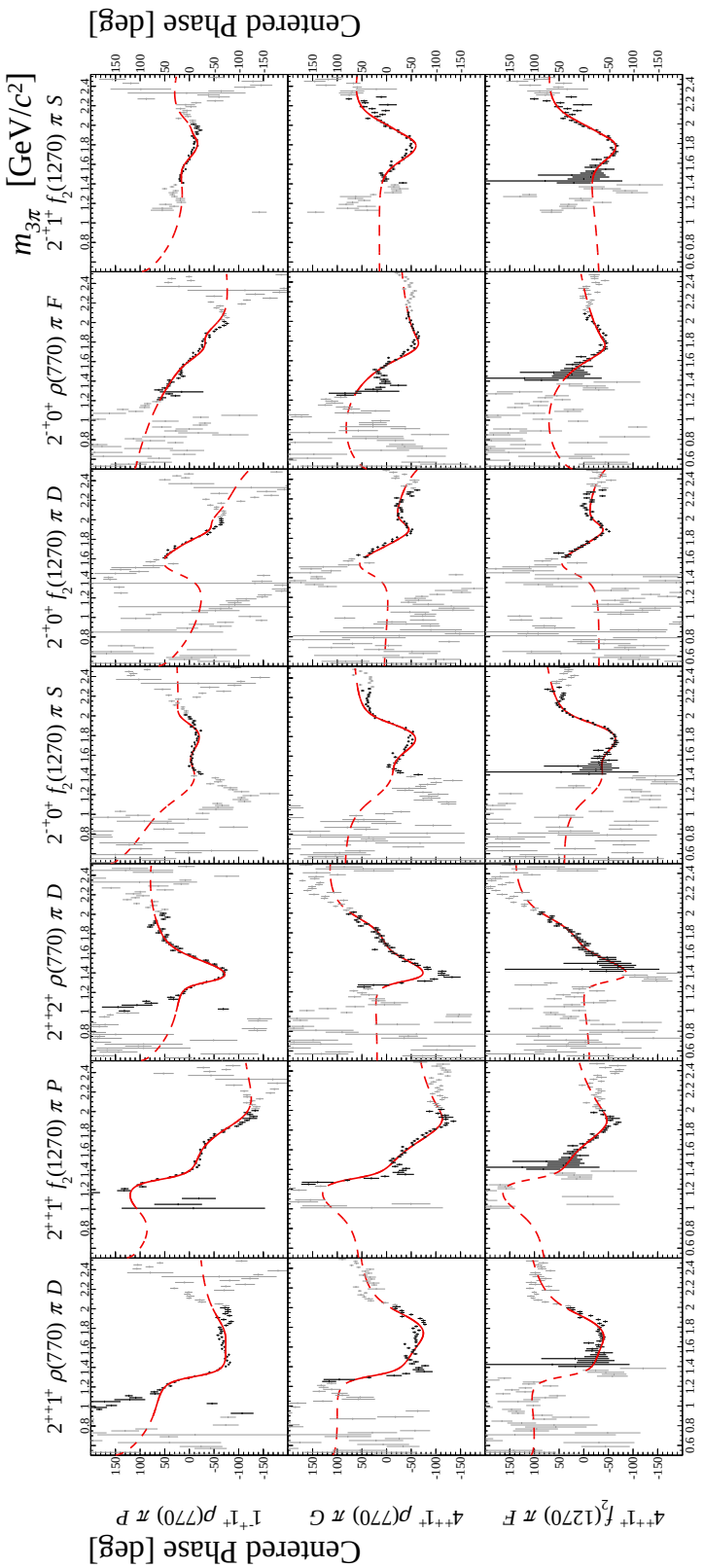

Figure F.58: Spin-density sub-matrix in the range of $0.449 < t' < 0.724\,(\mathrm{GeV}/c)^2$.

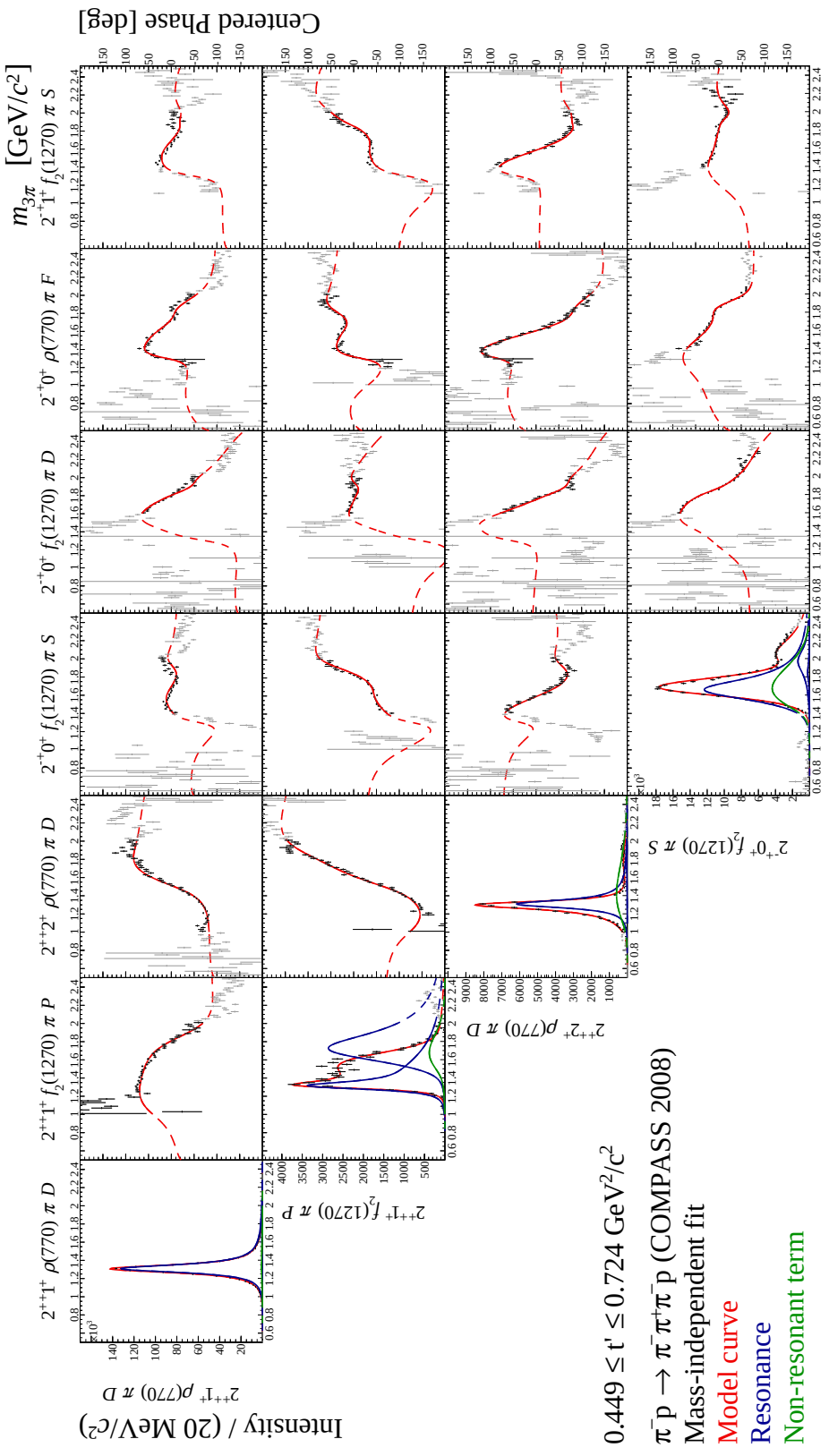

Figure F.59: Spin-density sub-matrix in the range of $0.449 < t' < 0.724$ (GeV/c)^2.

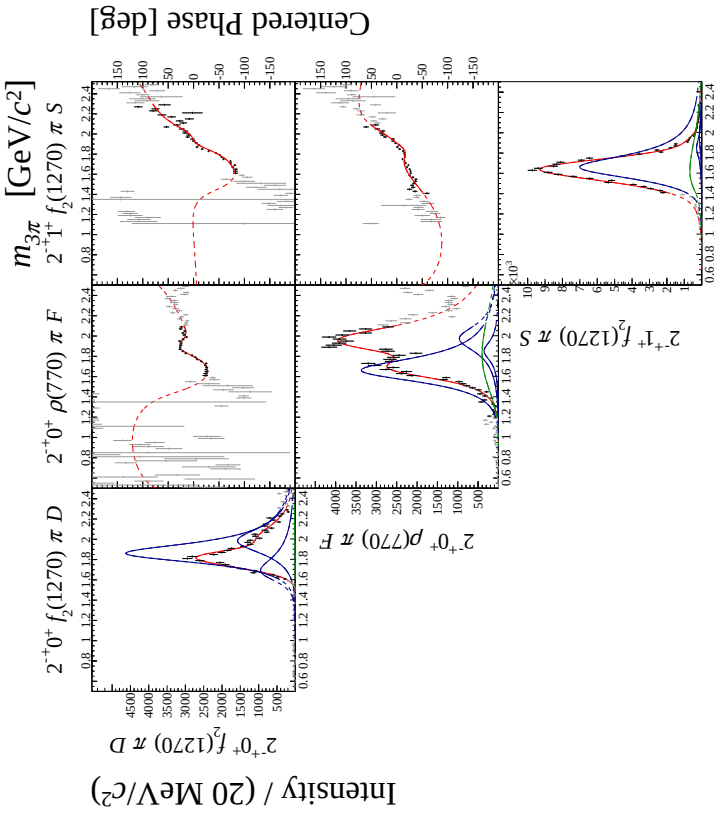

Figure F.60: Spin-density sub-matrix in the range of $0.449 < t' < 0.724\,(\mathrm{GeV}/c)^2$.

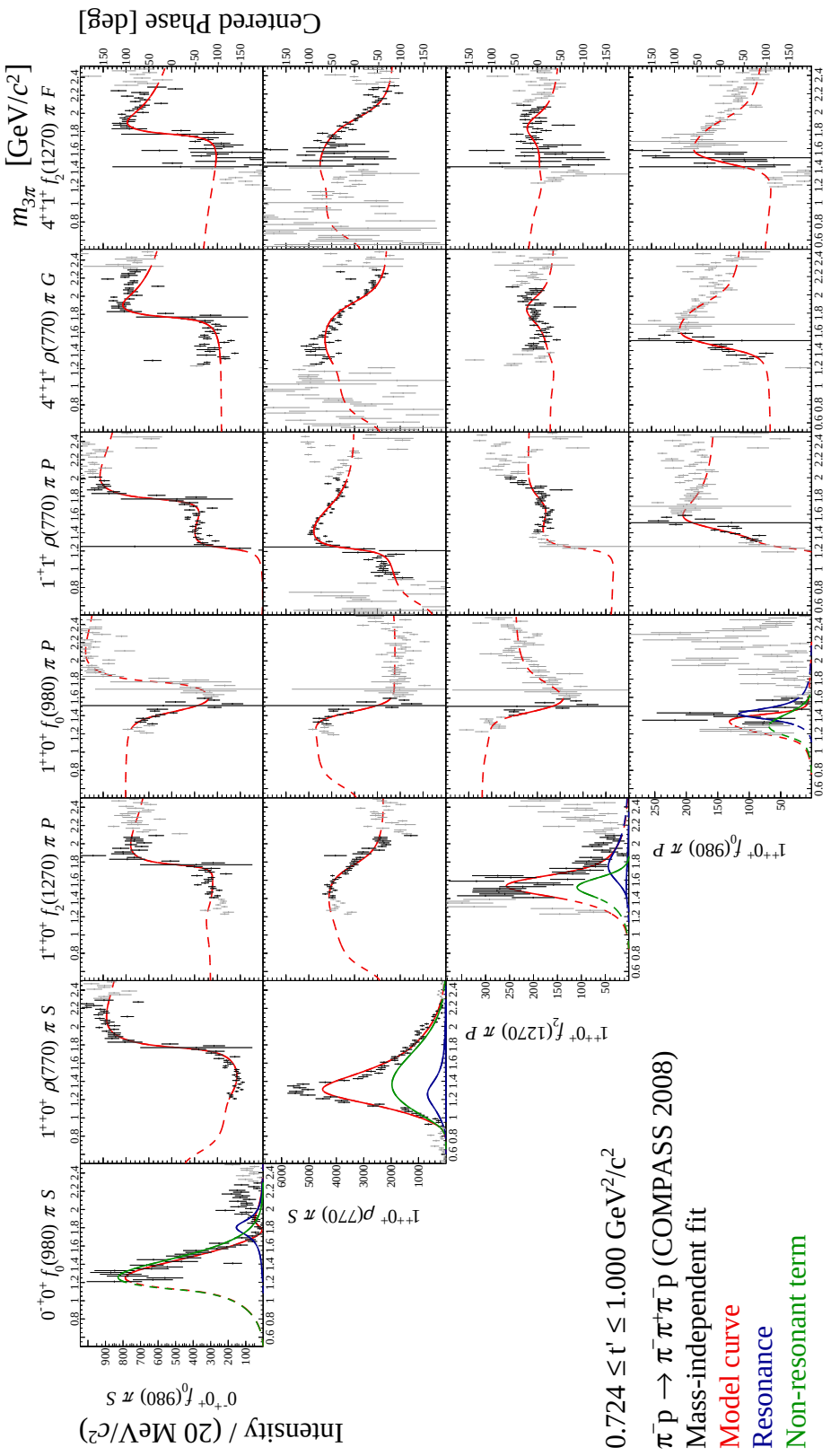

Figure F.61: Spin-density sub-matrix in the range of $0.724 < t' < 1.000\,(\mathrm{GeV}/c)^2$.

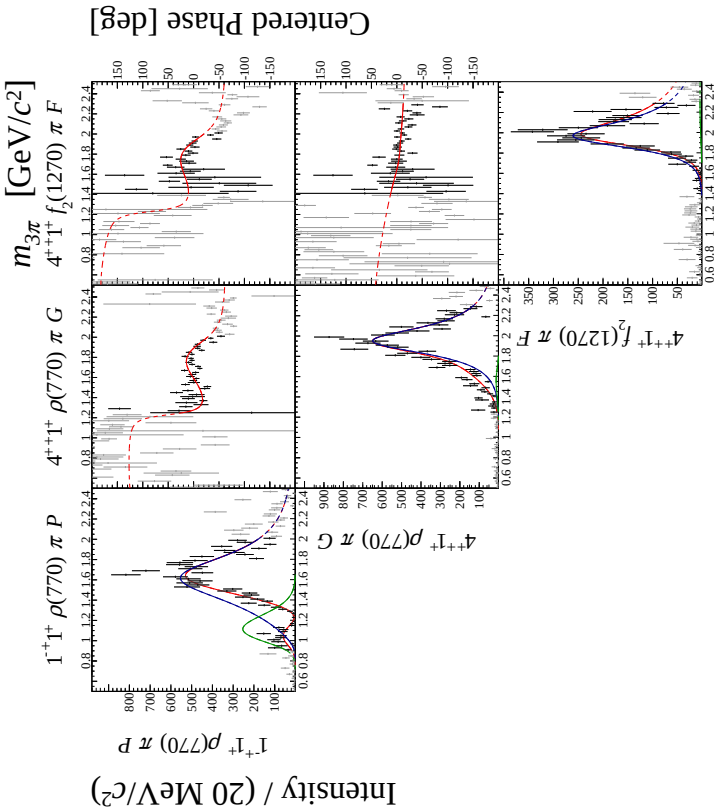

Figure F.62: Spin-density sub-matrix in the range of $0.724 < t' < 1.000\,(\mathrm{GeV}/c)^2$.

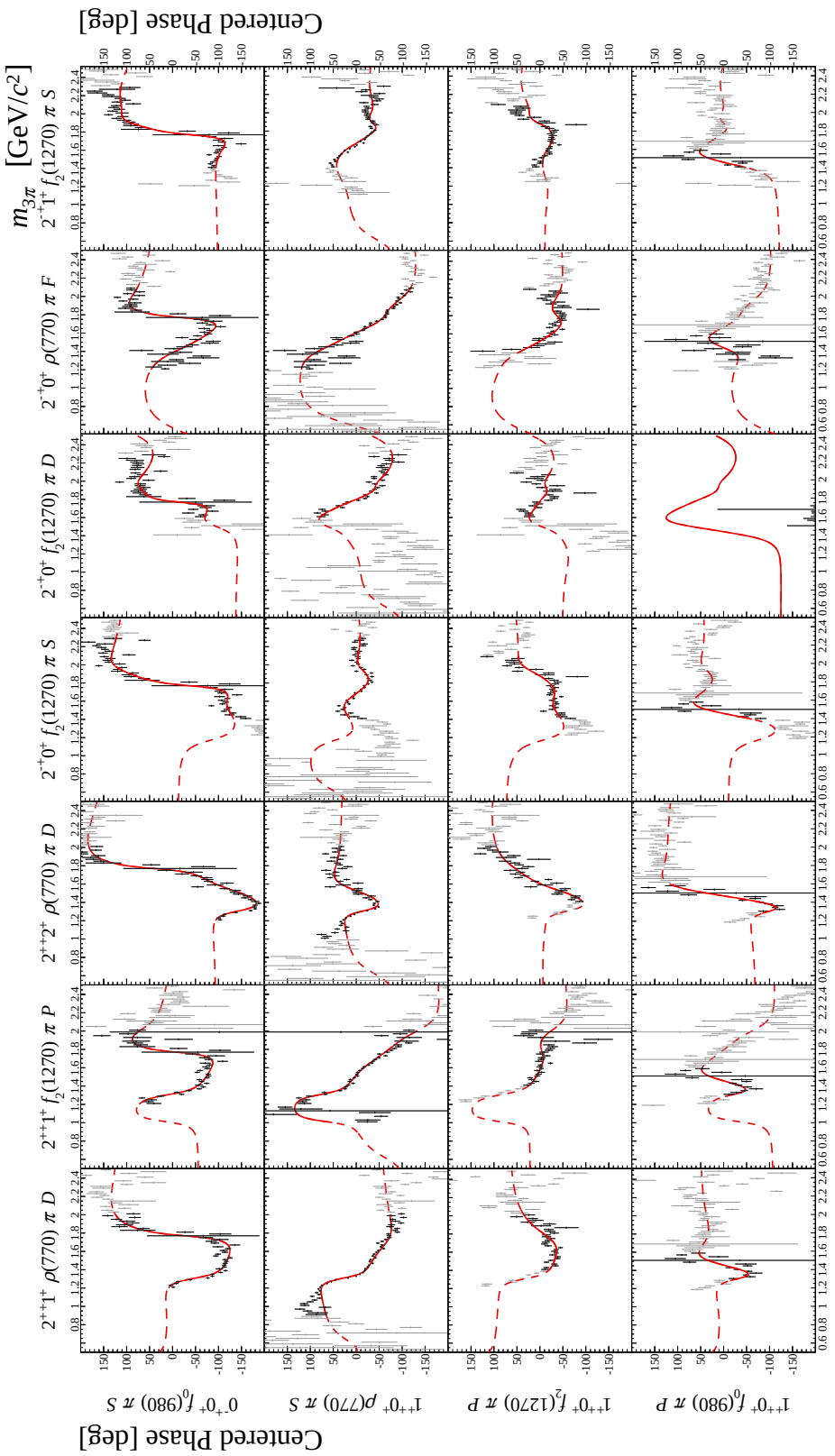

Figure F.63: Spin-density sub-matrix in the range of $0.724 < t' < 1.000\,(\mathrm{GeV}/c)^2$.

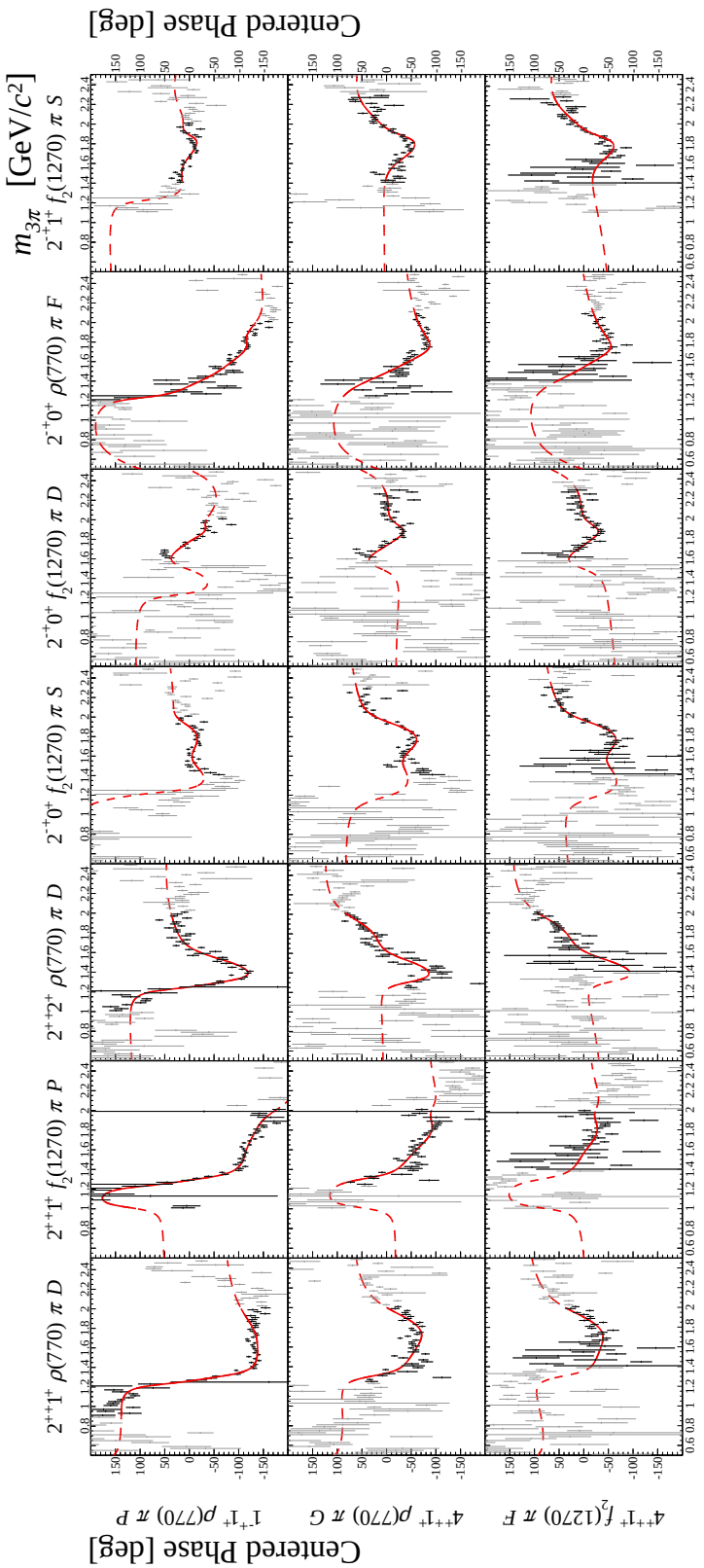

Figure F.64: Spin-density sub-matrix in the range of $0.724 < t' < 1.000\,(\mathrm{GeV}/c)^2$.

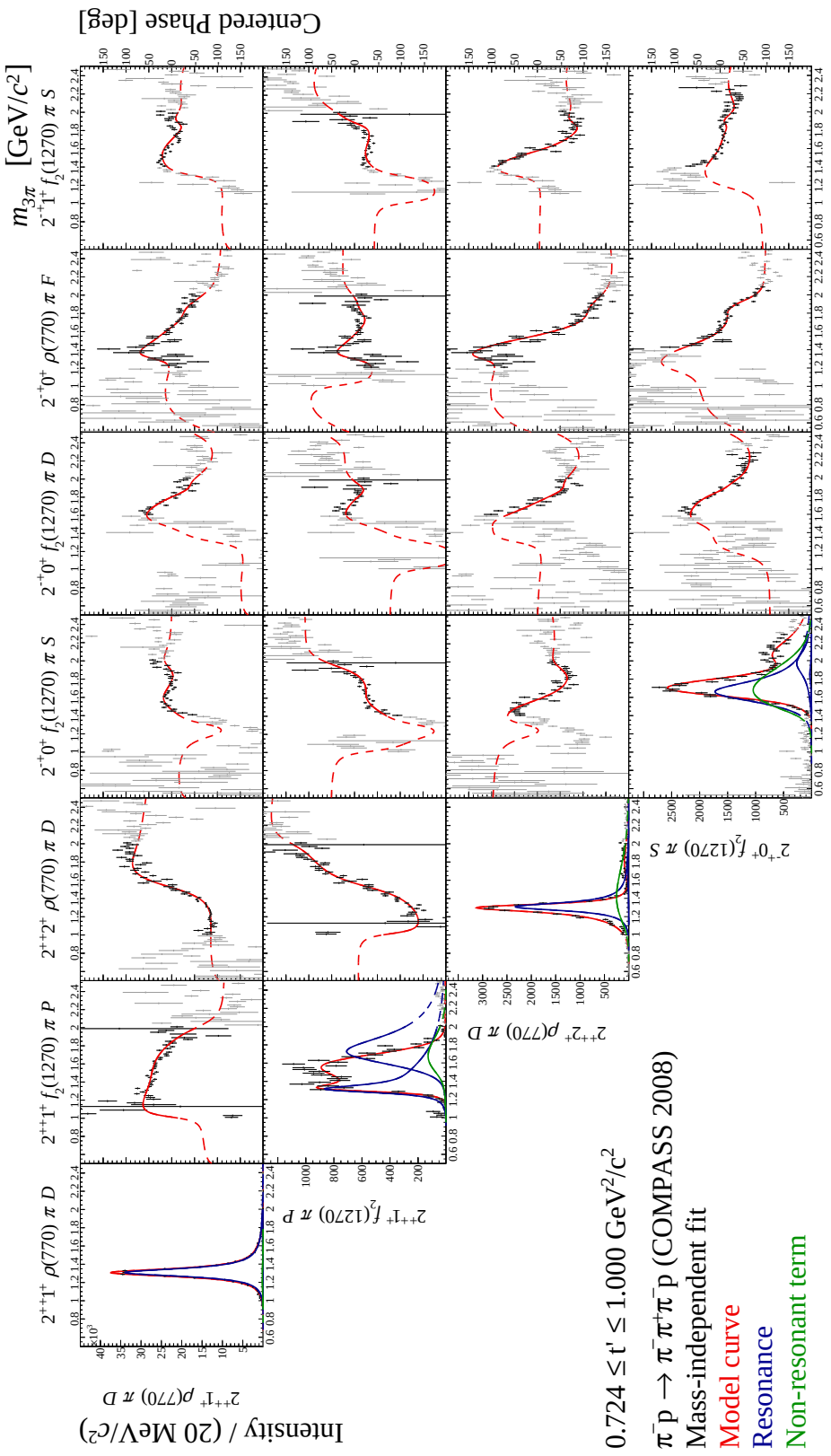

Figure F.65: Spin-density sub-matrix in the range of $0.724 < t' < 1.000\,(\mathrm{GeV}/c)^2$.

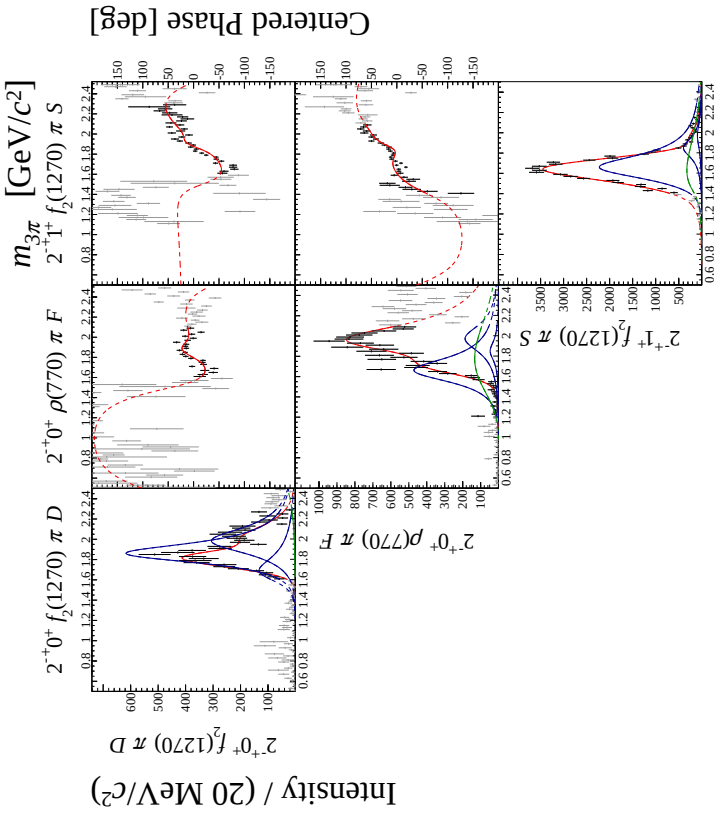

Figure F.66: Spin-density sub-matrix in the range of $0.724 < t' < 1.000\,(\mathrm{GeV}/c)^2$.

F.2 Overview over the Intensity Spectra in all t' Bins

In the following, the intensity spectra in all t' bins and the t'-summed intensity are summarized in one figure per partial wave.

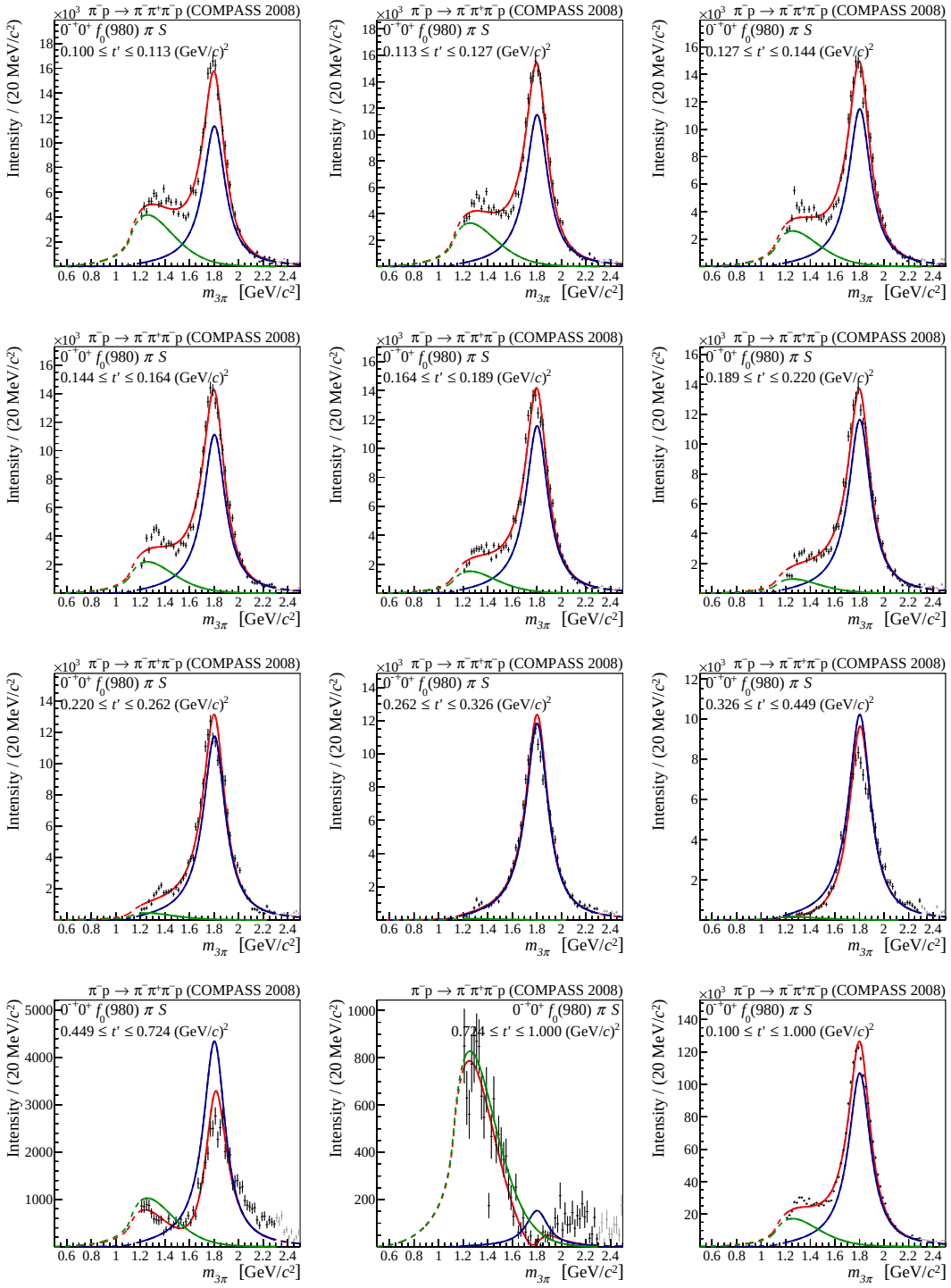

Figure F.67: Intensity spectra in the different t' bins of the $0^{-+}0^{+}f_0(980)\pi S$ wave.

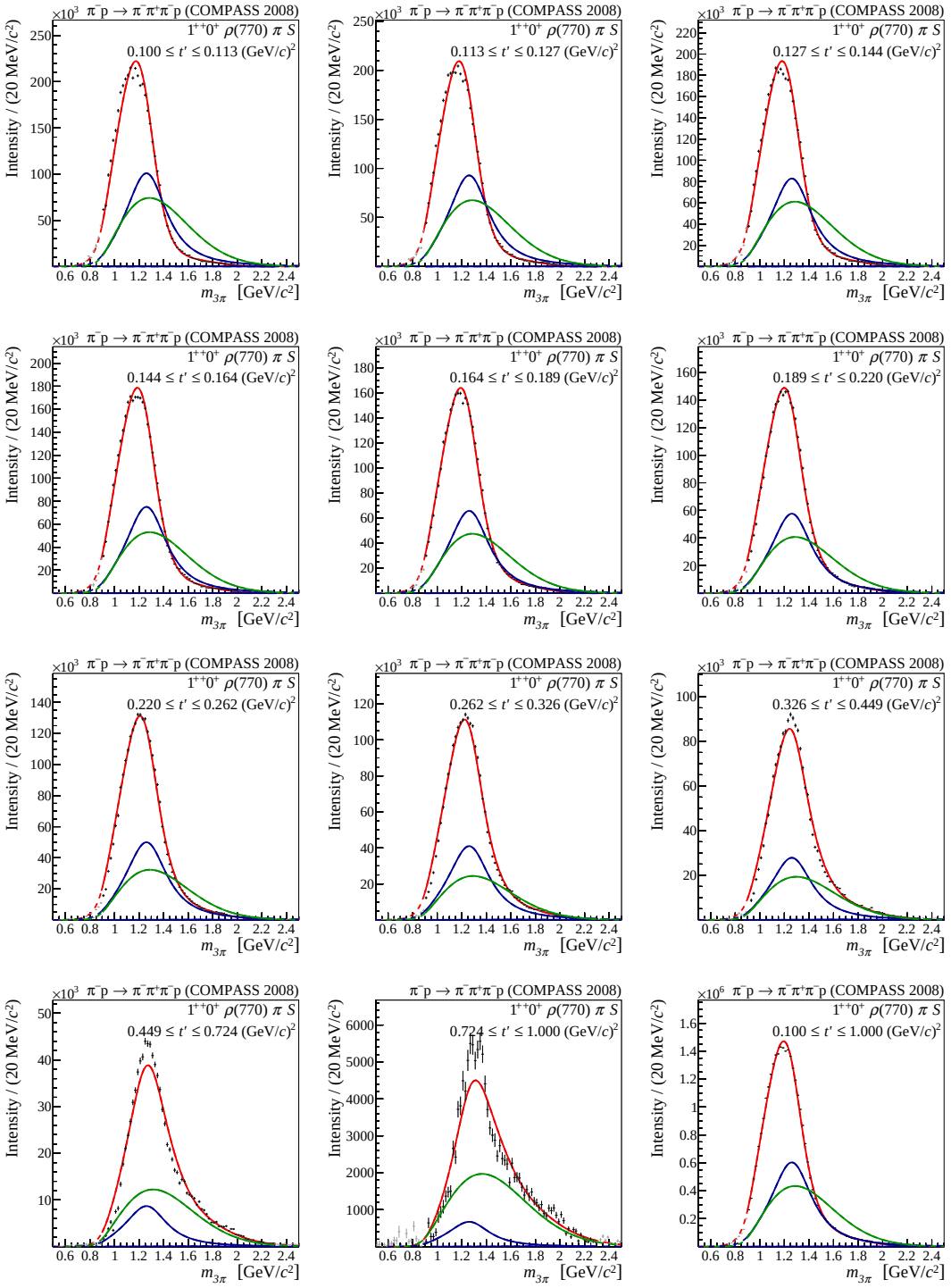

Figure F.68: Intensity spectra in the different t' bins of the $1^{++}0^+\rho(770)\pi S$ wave.

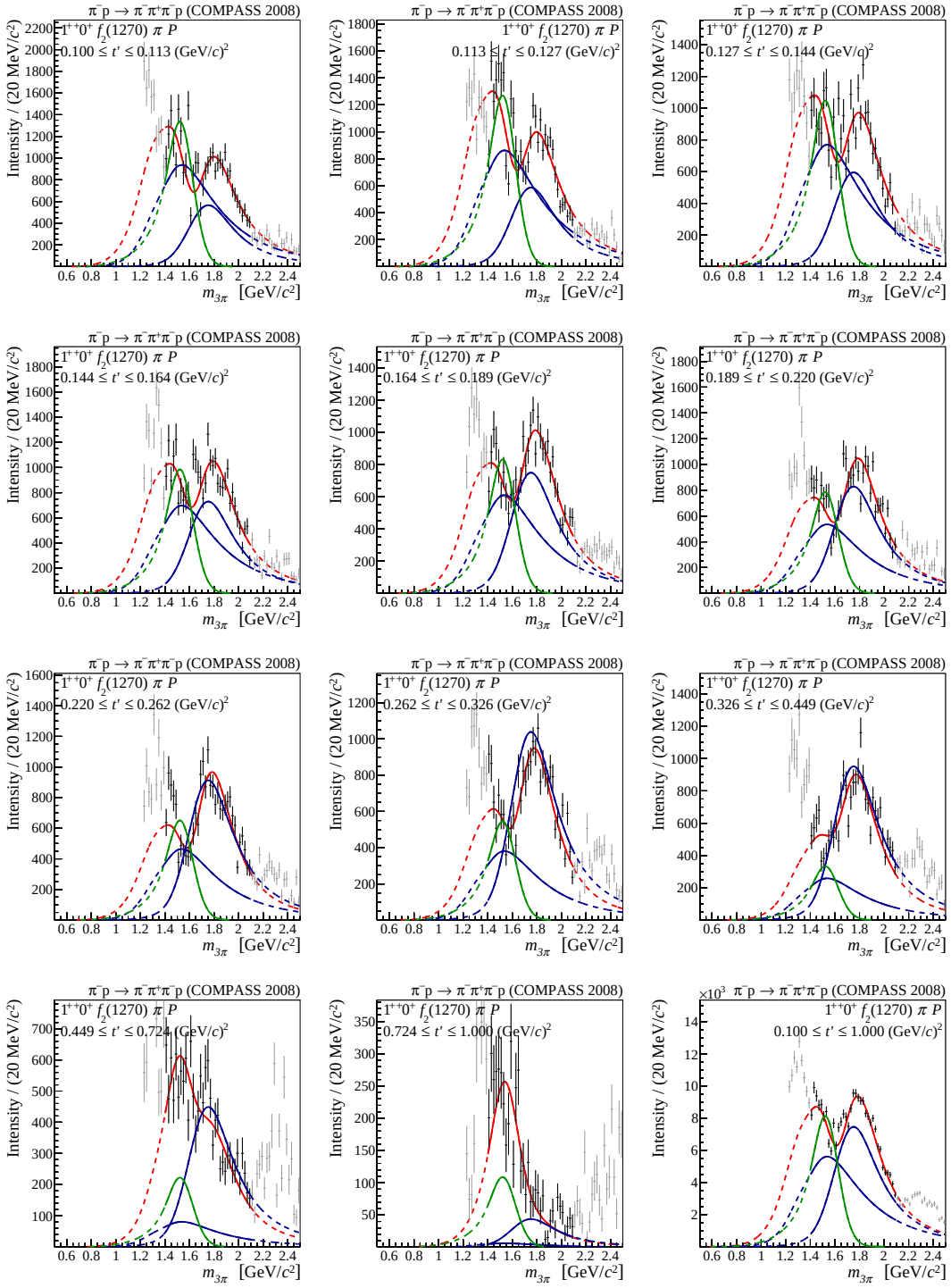

Figure F.69: Intensity spectra in the different t' bins of the $1^{++}0^+ f_2(1270)\pi P$ wave.

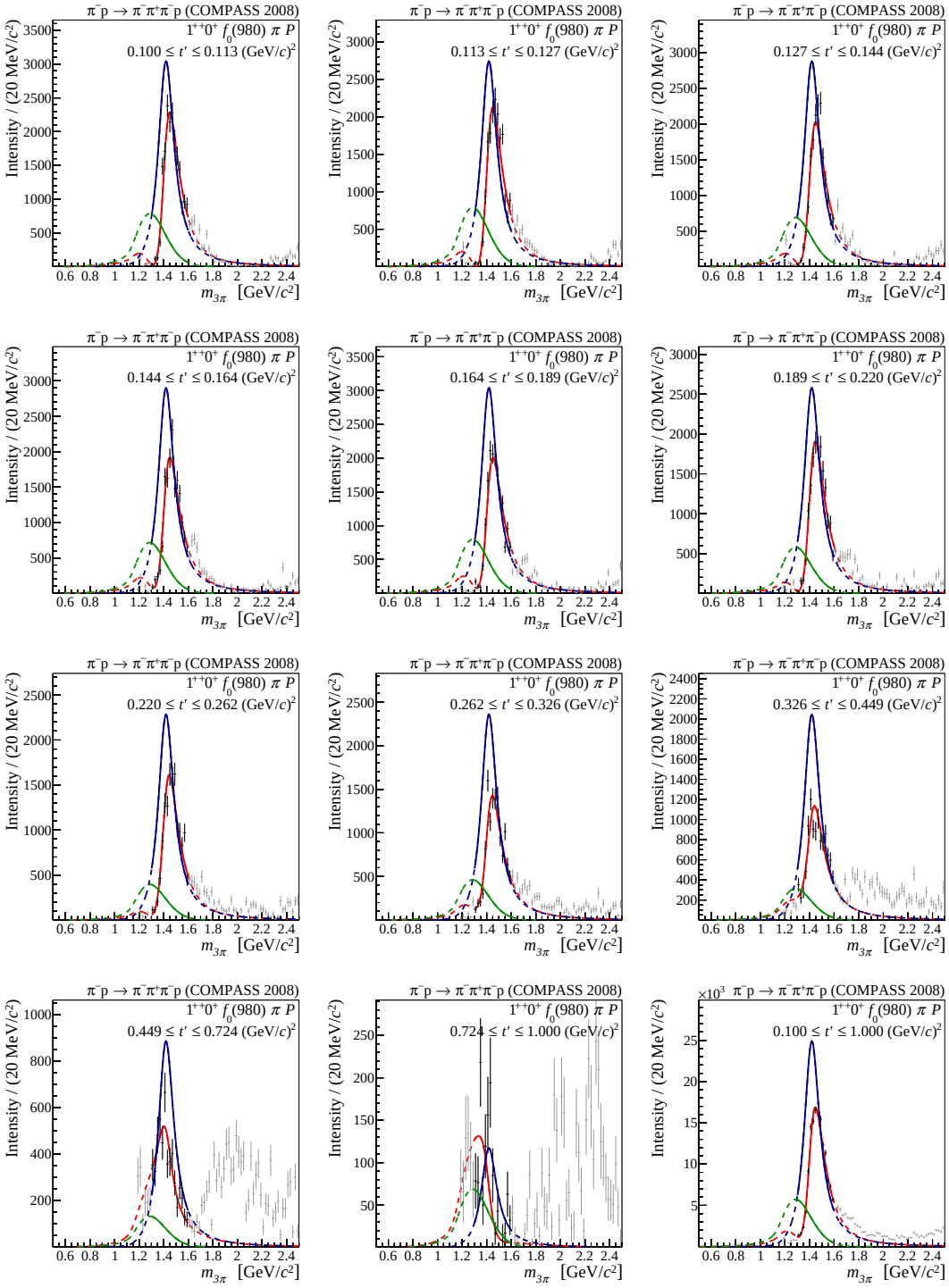

Figure F.70: Intensity spectra in the different t' bins of the $1^{++}0^+ f_0(980)\pi P$ wave.

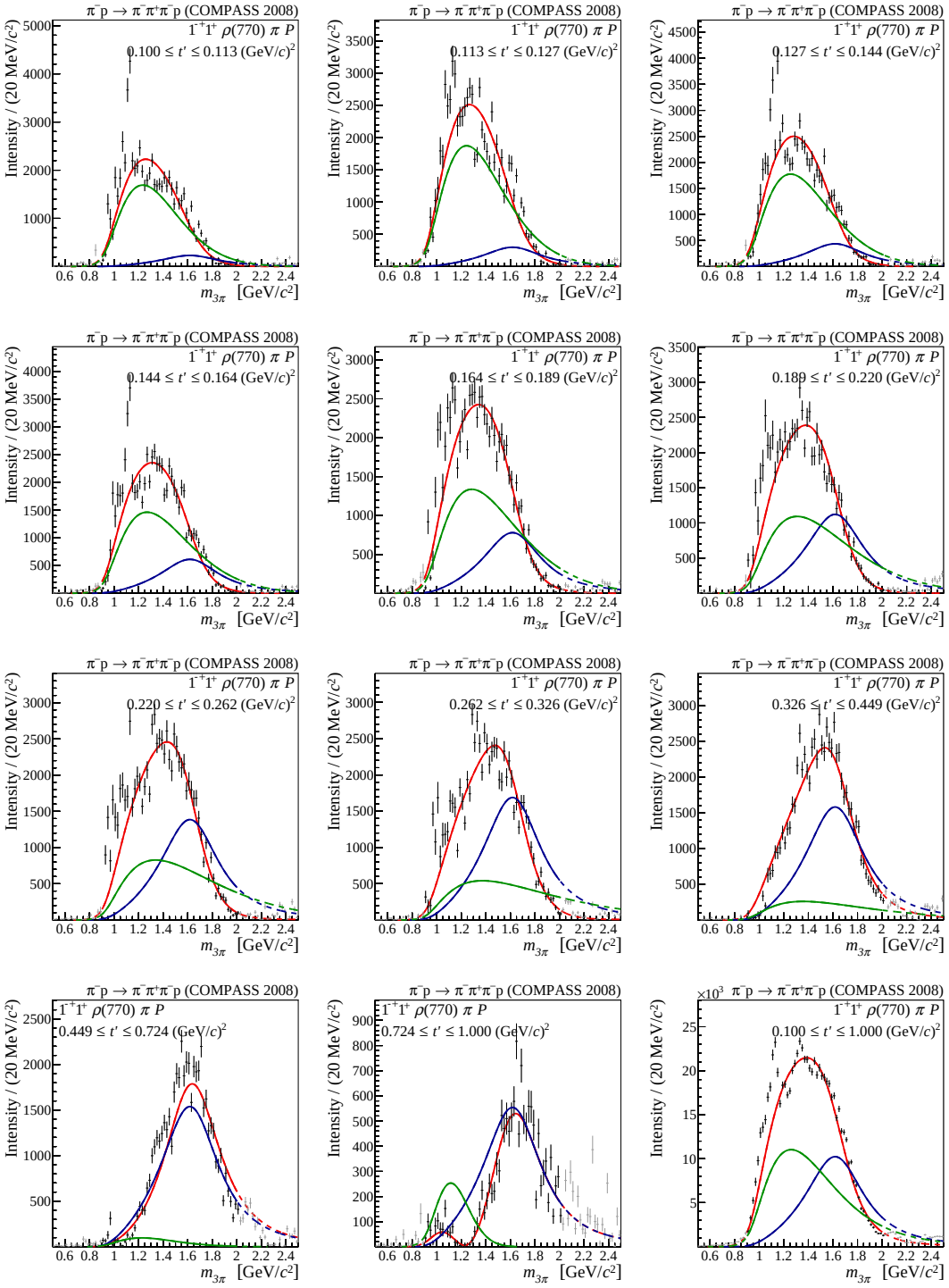

Figure F.71: Intensity spectra in the different t' bins of the $1^{-+}1^+\rho(770)\pi P$ wave.

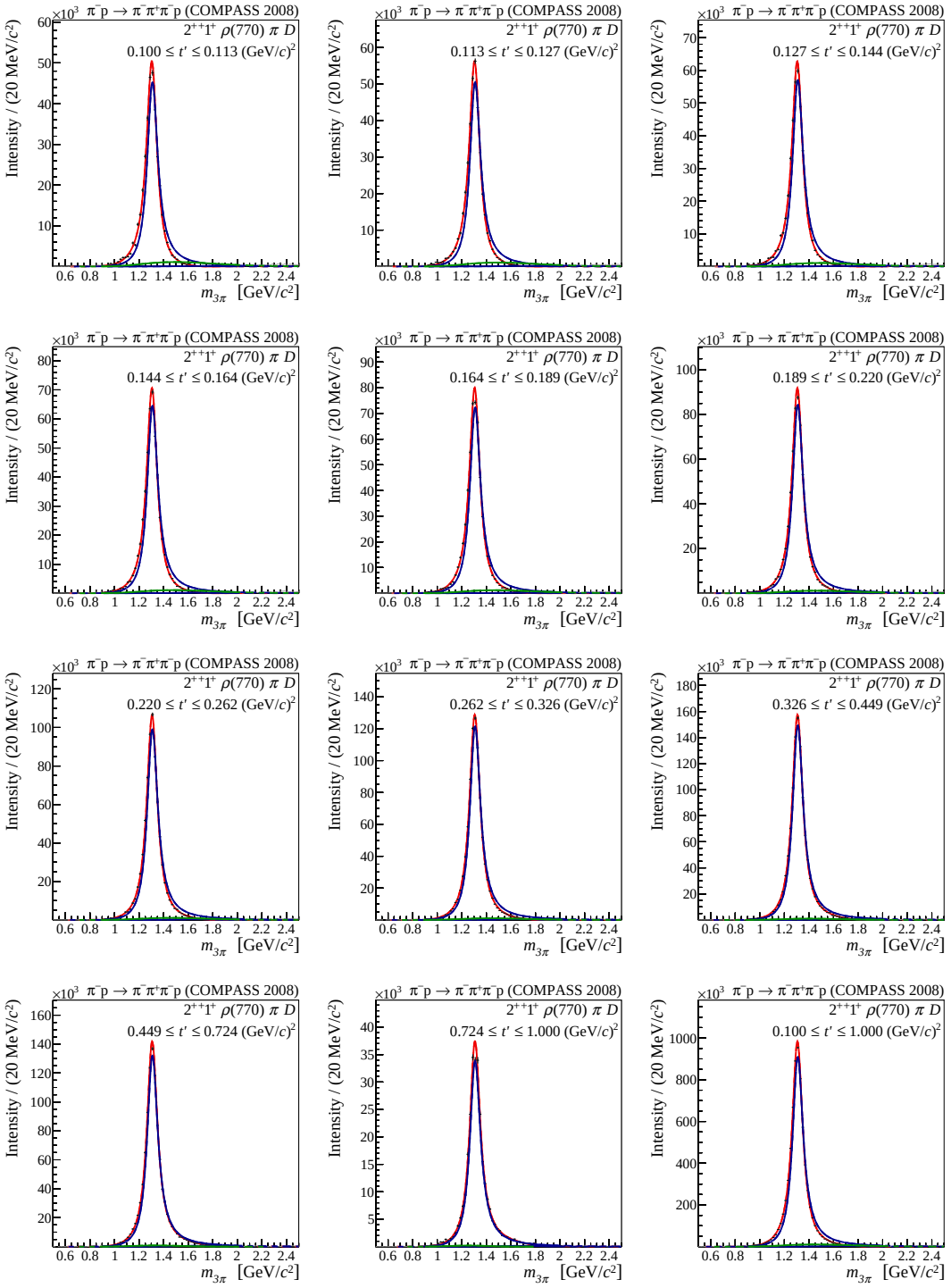

Figure F.72: Intensity spectra in the different t' bins of the $2^{++}1^{+}\rho(770)\pi D$ wave.

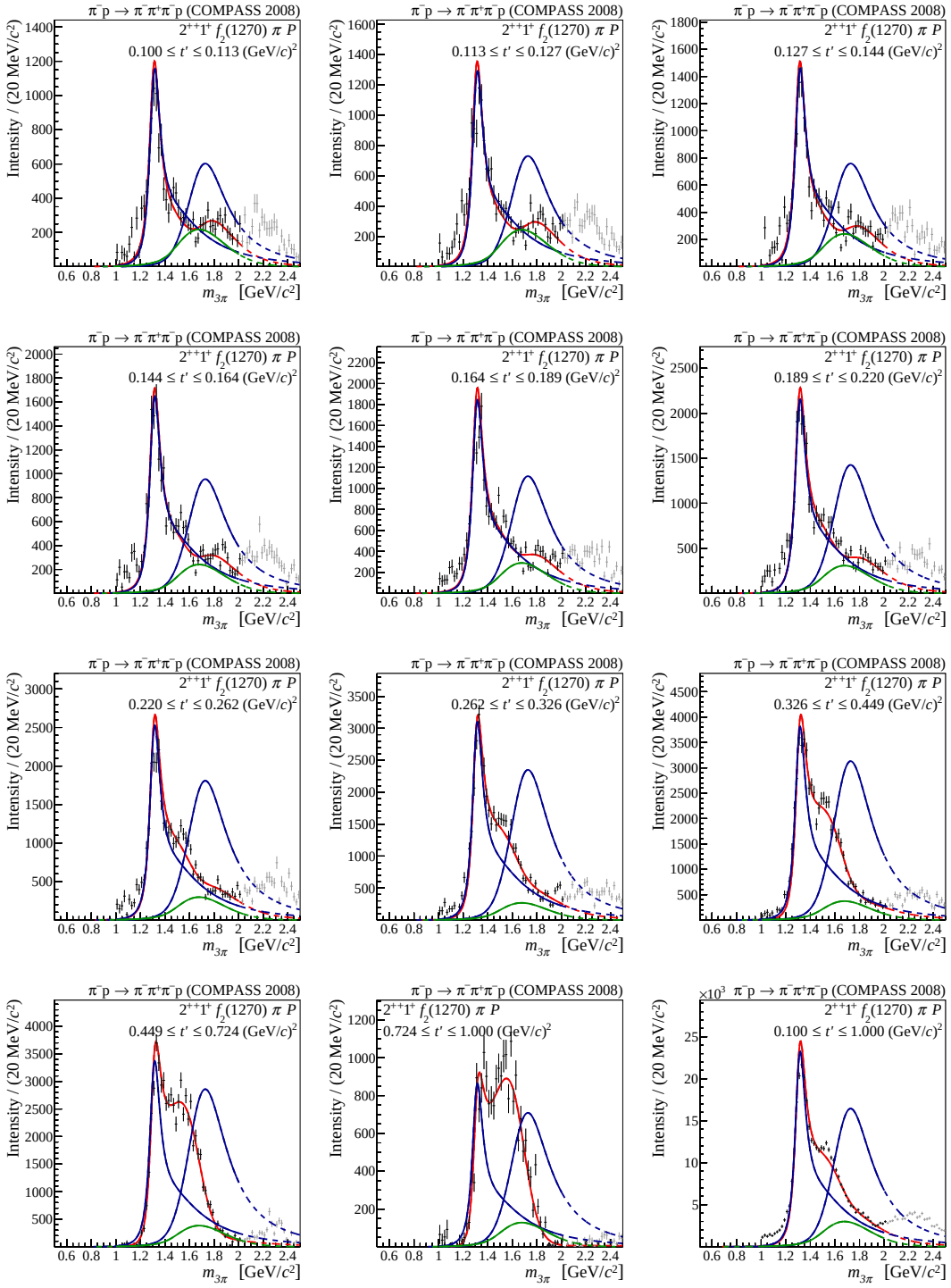

Figure F.73: Intensity spectra in the different t' bins of the $2^{++}1^+ f_2(1270)\pi P$ wave.

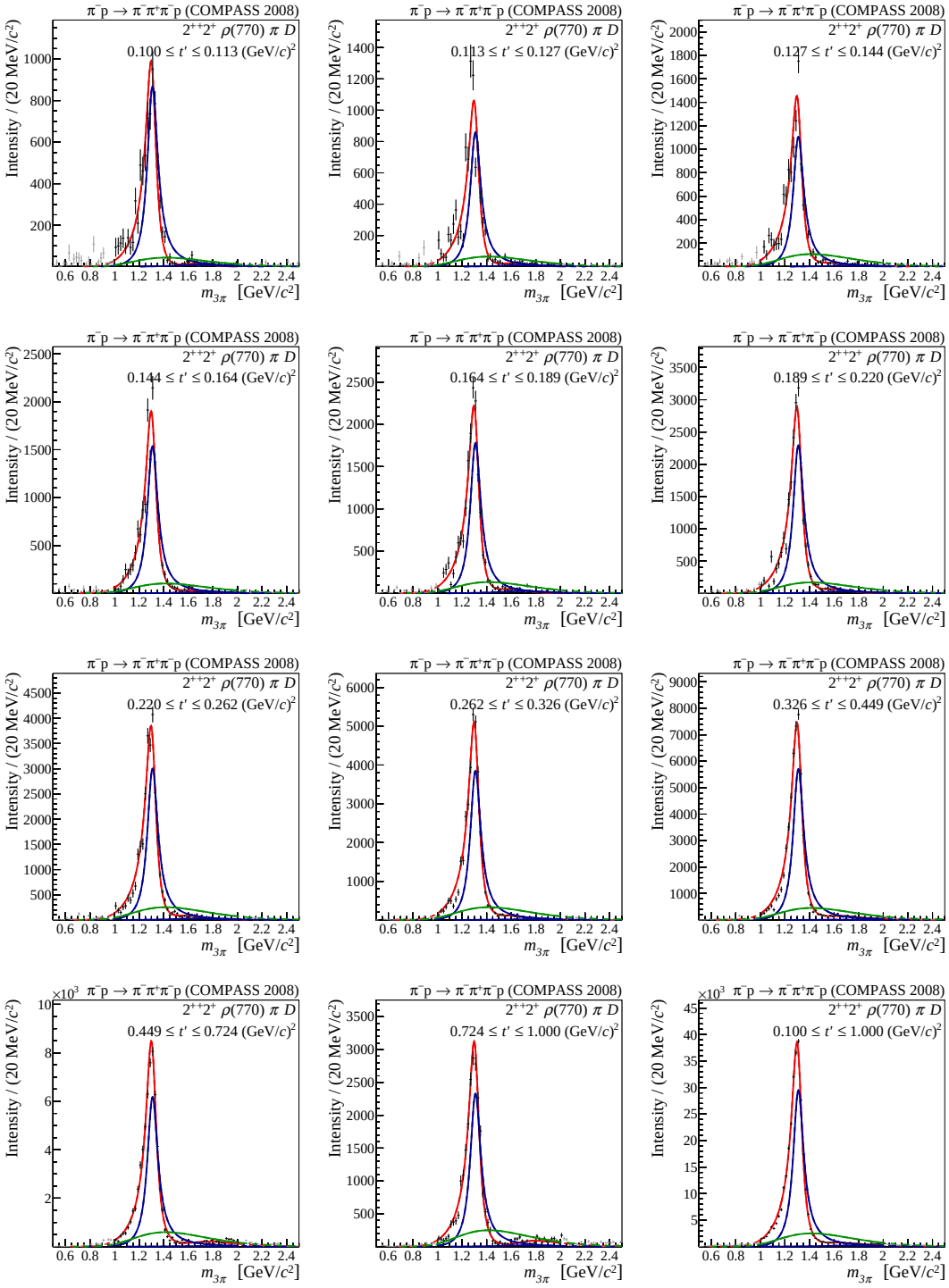

Figure F.74: Intensity spectra in the different t' bins of the $2^{++}2^+\rho(770)\pi D$ wave.

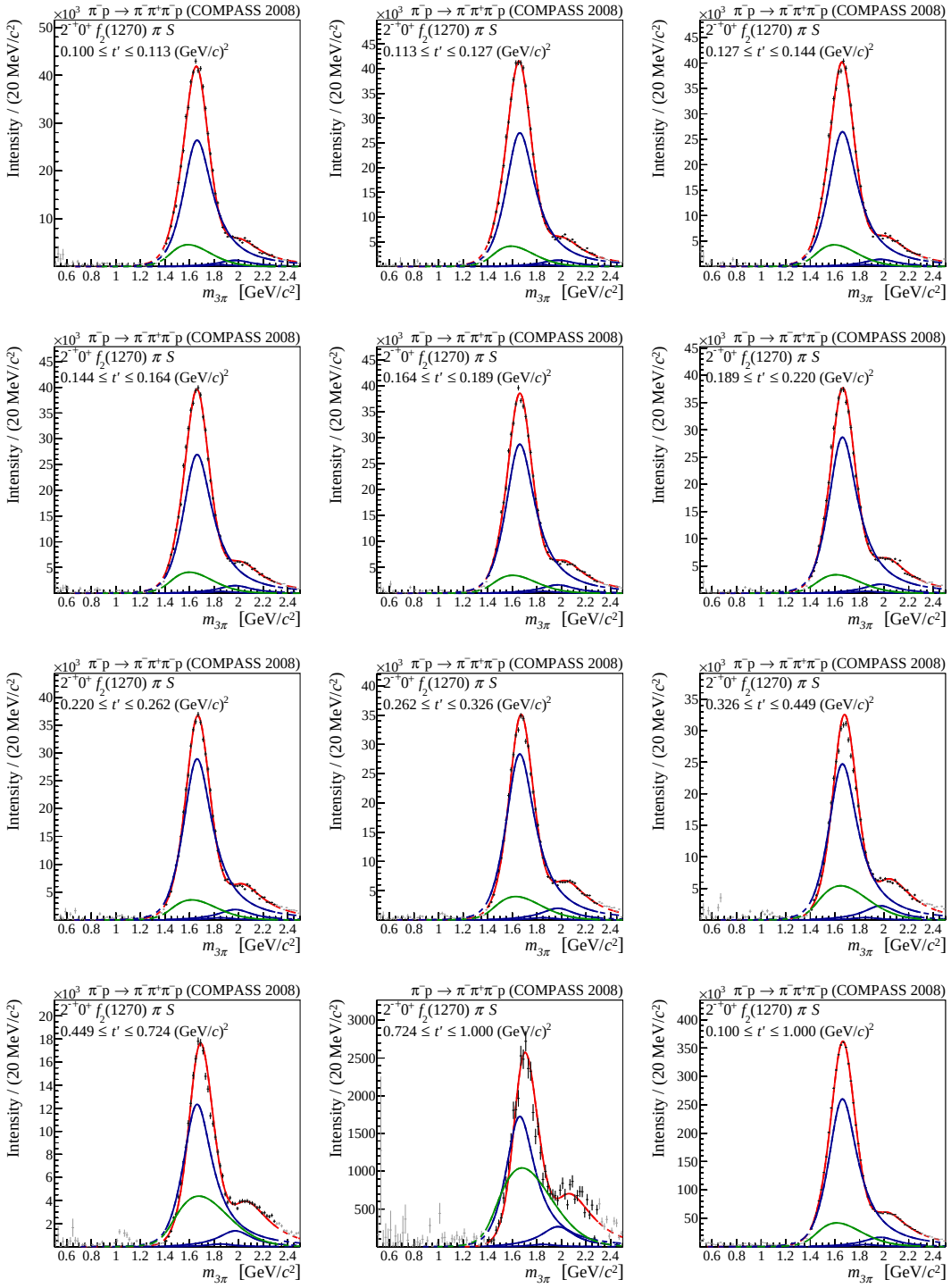

Figure F.75: Intensity spectra in the different t' bins of the $2^{-+}0^{+}f_2(1270)\pi S$ wave.

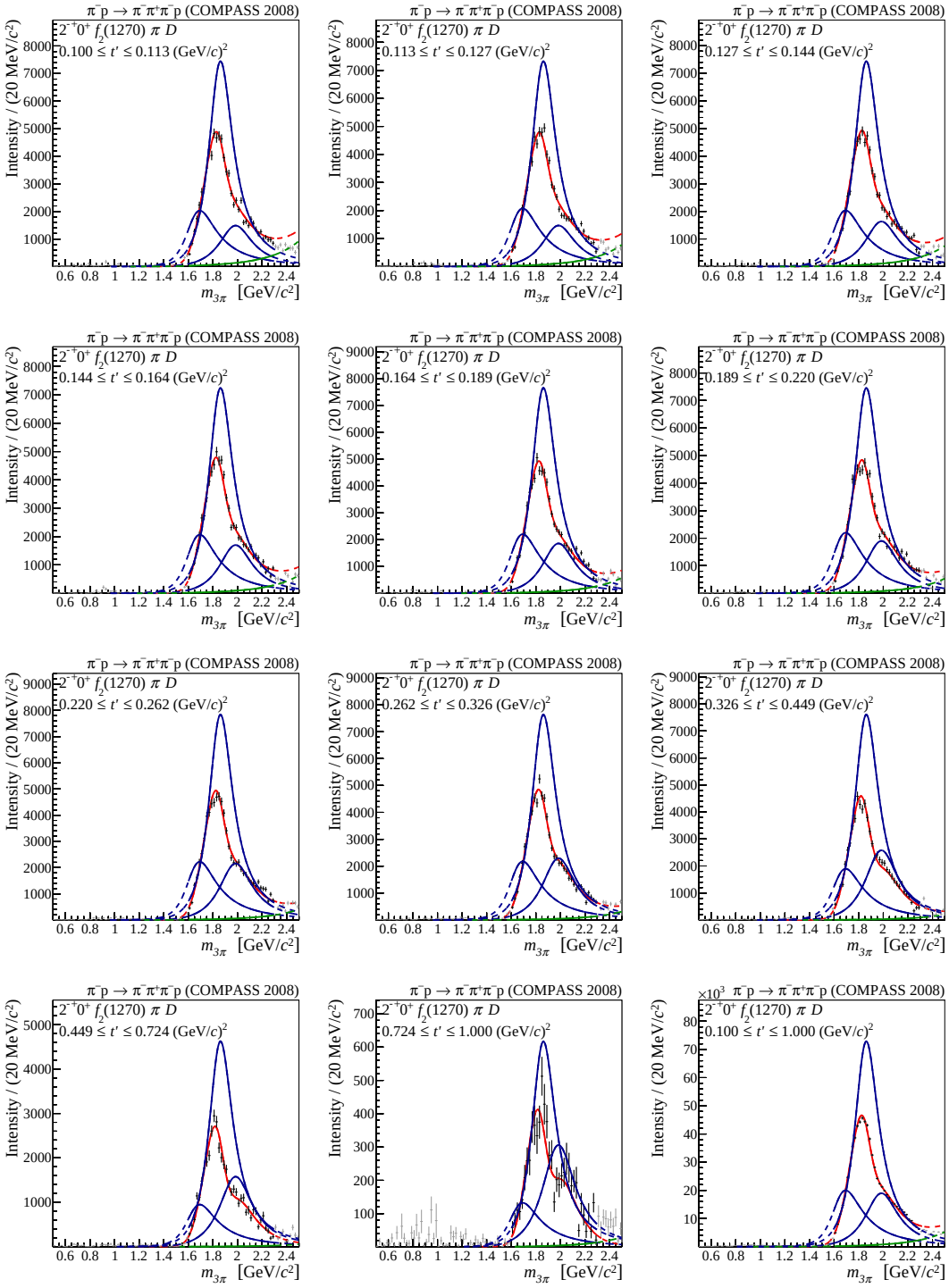

Figure F.76: Intensity spectra in the different t' bins of the $2^{-+}0^+ f_2(1270)\pi D$ wave.

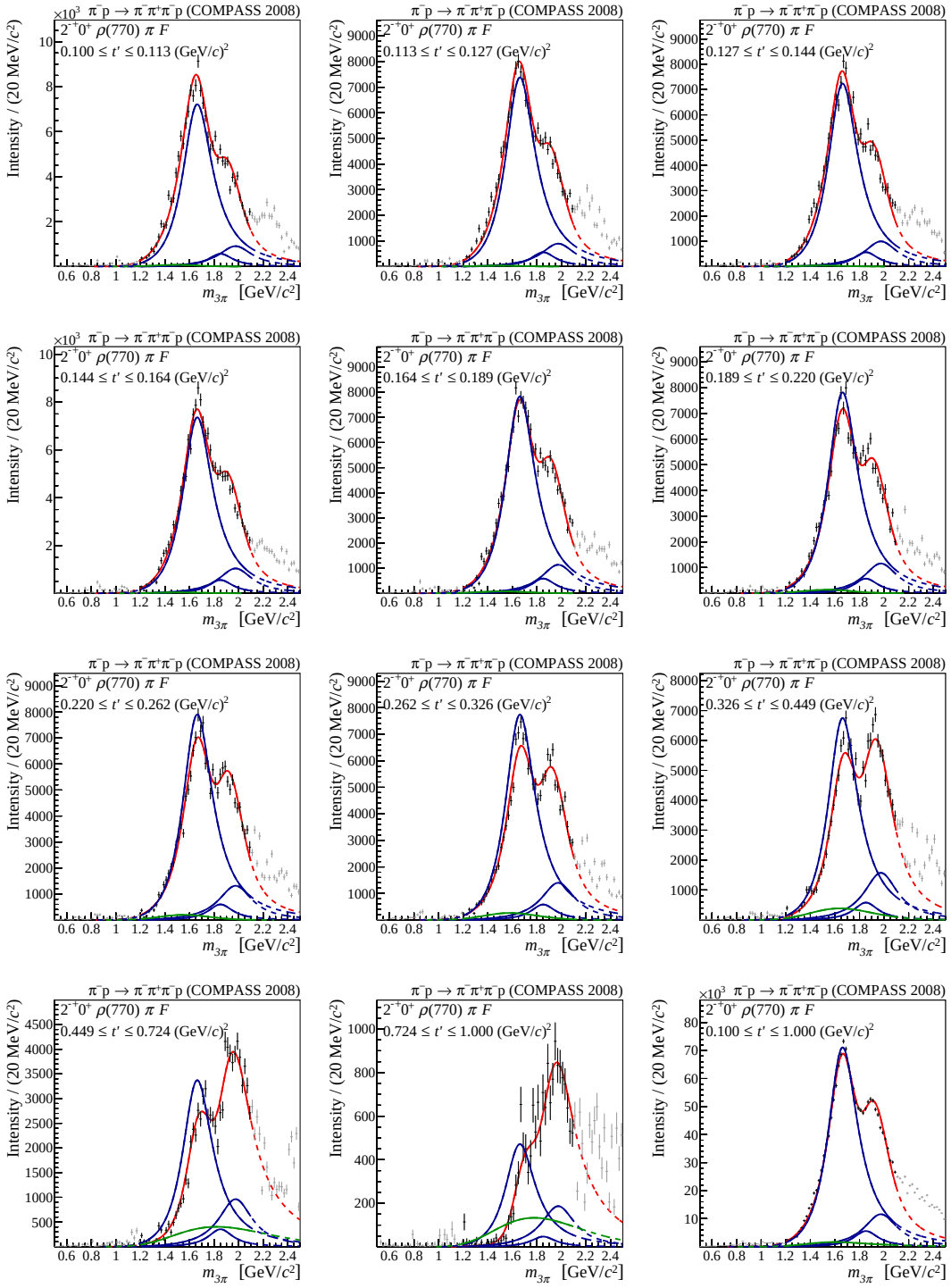

Figure F.77: Intensity spectra in the different t' bins of the $2^{-+}0^+\rho(770)\pi F$ wave.

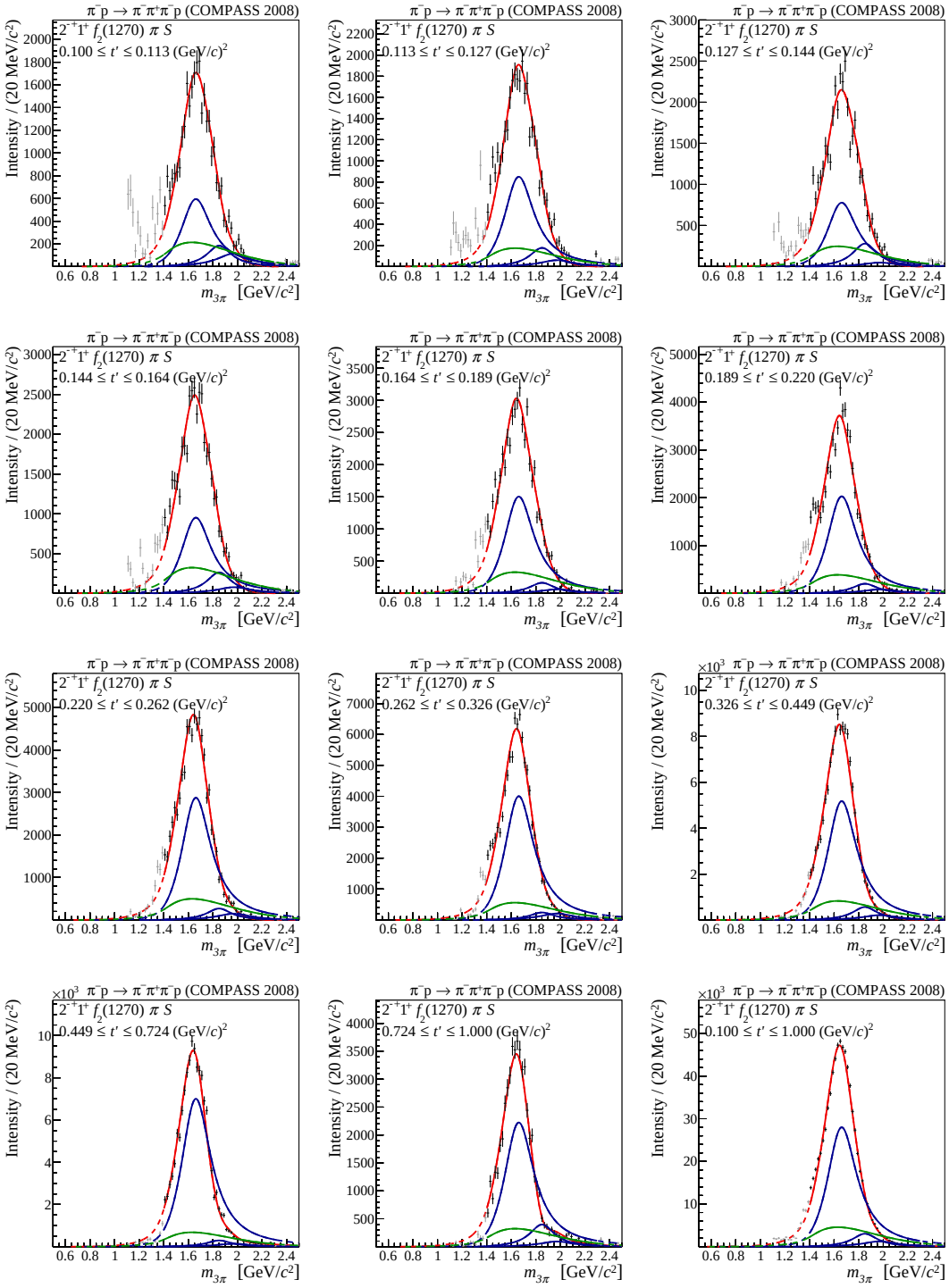

Figure F.78: Intensity spectra in the different t' bins of the $2^{-+}1^+ f_2(1270)\pi S$ wave.

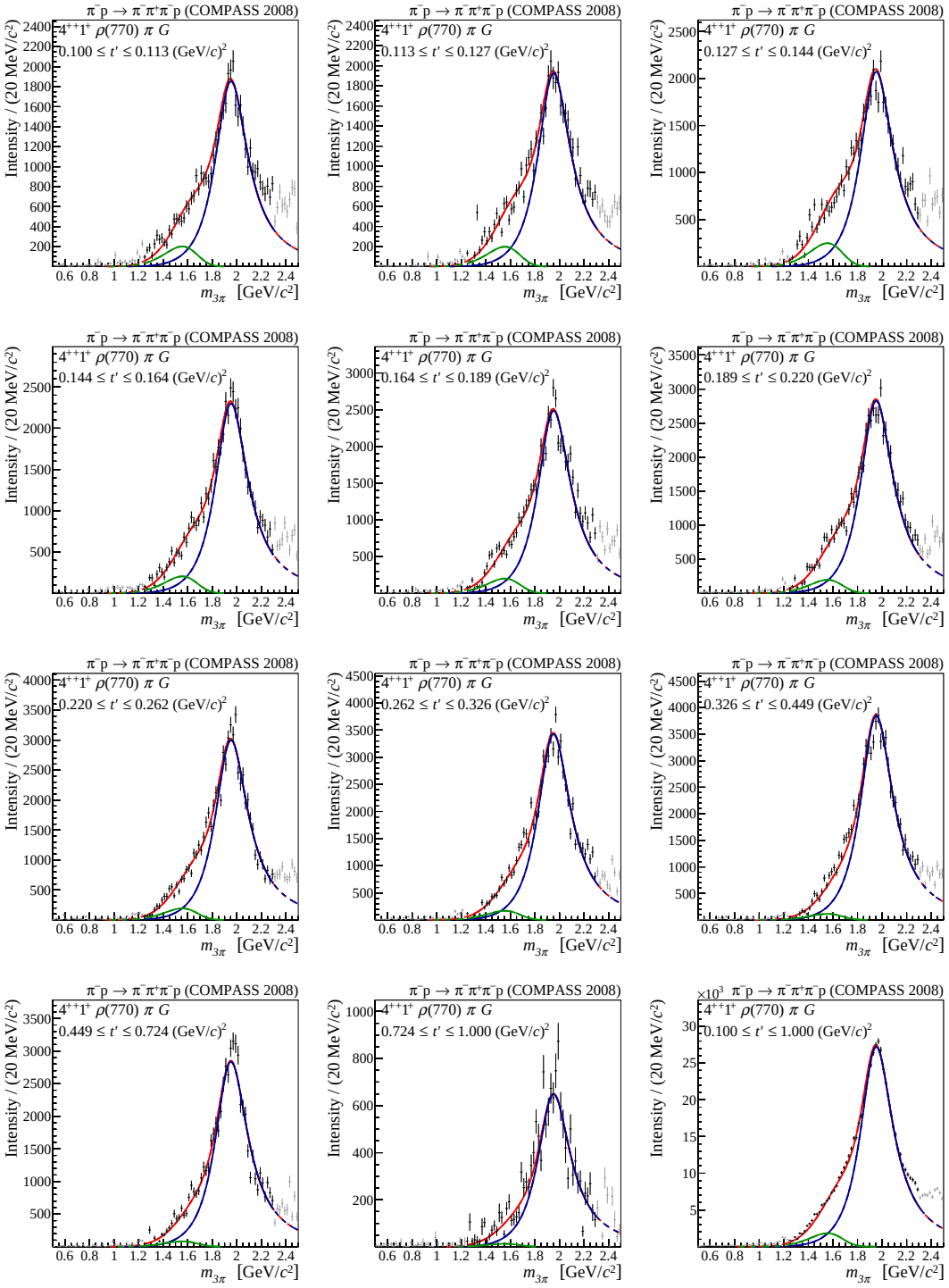

Figure F.79: Intensity spectra in the different t' bins of the $4^{++}1^+\rho(770)\pi G$ wave.

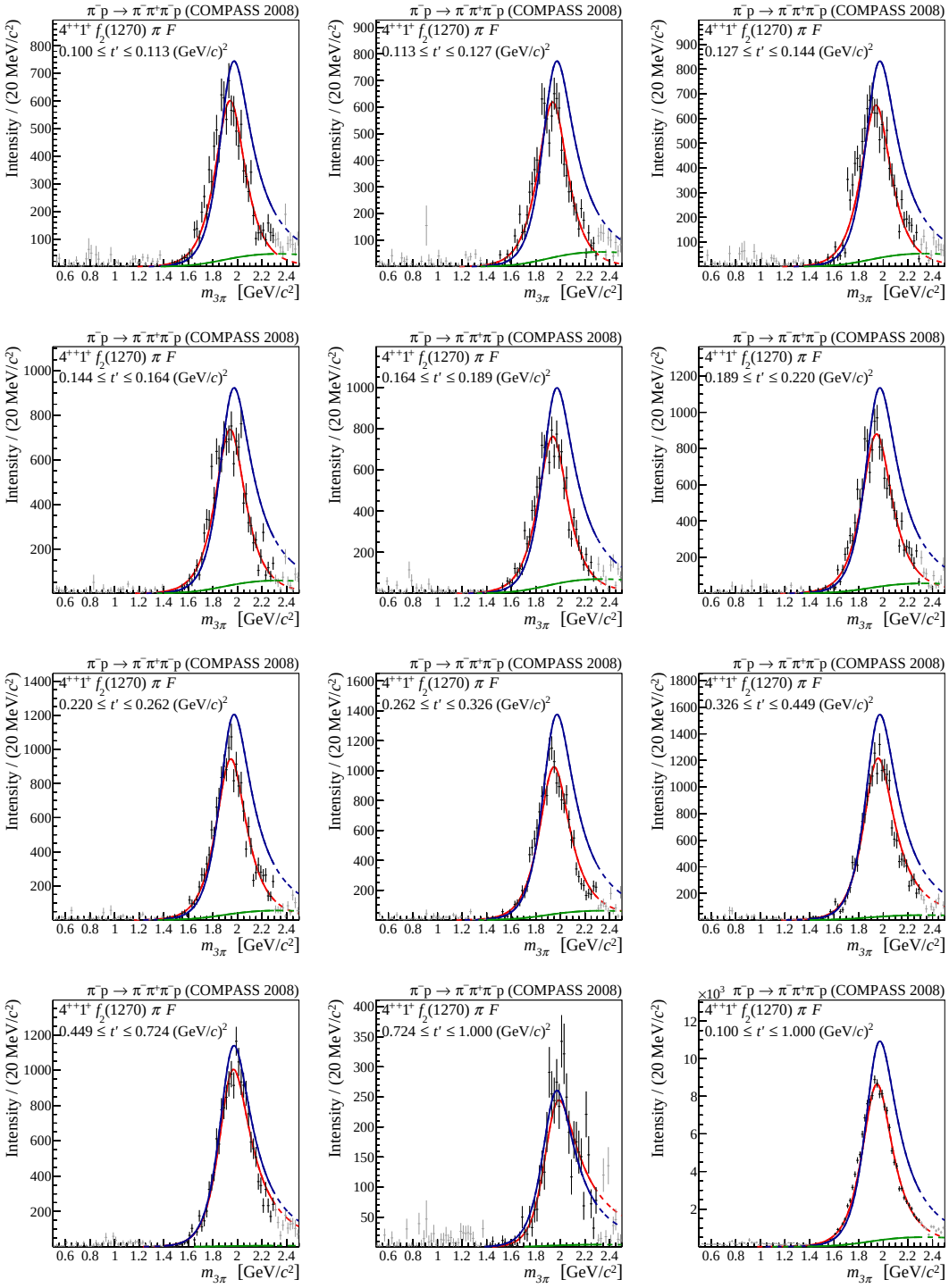

Figure F.80: Intensity spectra in the different t' bins of the $4^{++}1^+ f_2(1270)\pi F$ wave.

APPENDIX G

t' Dependence of the Model Components

On the following pages, all t' dependencies of the various model components are collected. The top plot in figures (a) shows the extracted t' dependency of the intensities (black bars) and their statistical error (gray boxes). The red bars are a single-exponential fit on the t' spectra. The plot on the bottom of figures (a) is the production phase as a function of t', extracted for the corresponding component. The production phase is measured relative to the $a_1(1260)$ component in the $1^{++}\,0^+\,\rho(770)\,\pi\,S$ wave. In figures (b) the Main results and the corresponding fit (red bars/line) are overlaid with the extracted t' intensity spectra from the various systematic studies (top) and their production phase (bottom). Figures (c) compares the obtained slope parameters (horizontal axis) of the single-exponential fit from the different studies (vertical axis). The different colors encode the difference in χ^2 between the t' fit in the corresponding study and the Main fit. The dashed lines in figures (c) represent the estimated for the systematic uncertainties. The same scheme is used in figures (d) but now the maximal observed production-phase motion over the full analyzed t' range is shown for each study.

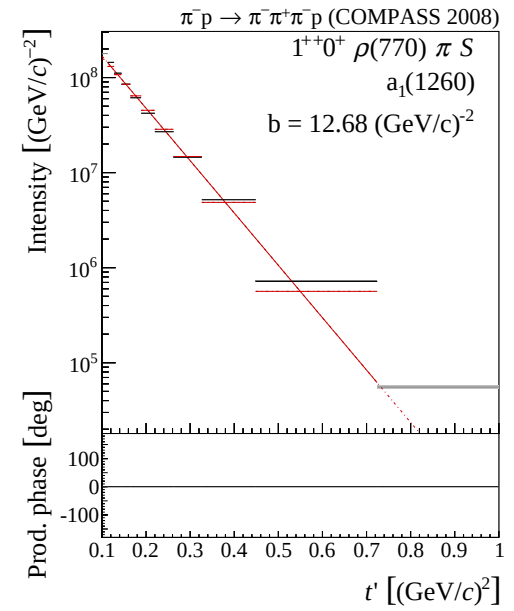

(a) t' dependence of the Main fit

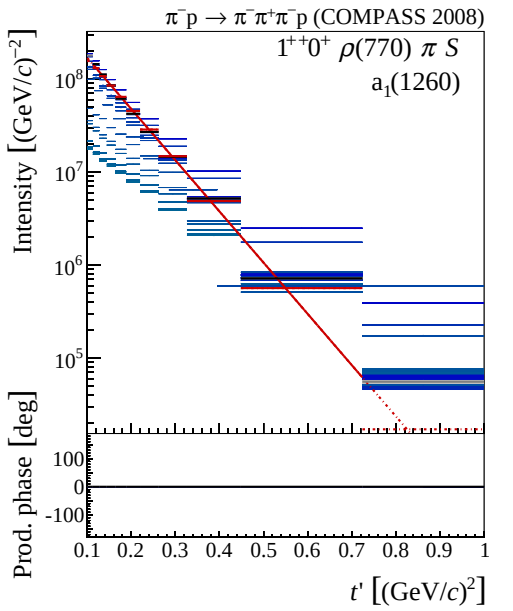

(b) t' dependence in all systematic studies

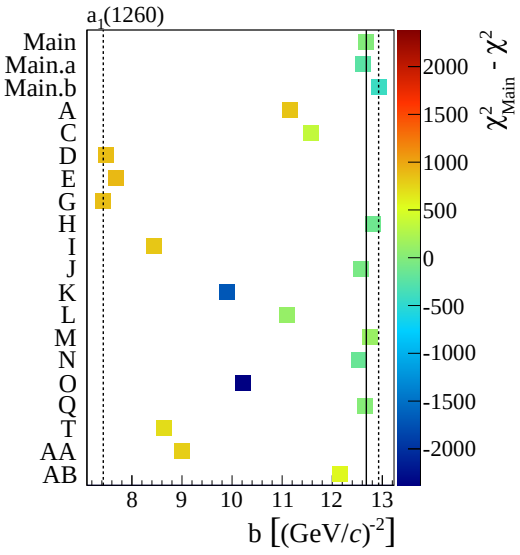

(c) Systematics of the t' slope parameter

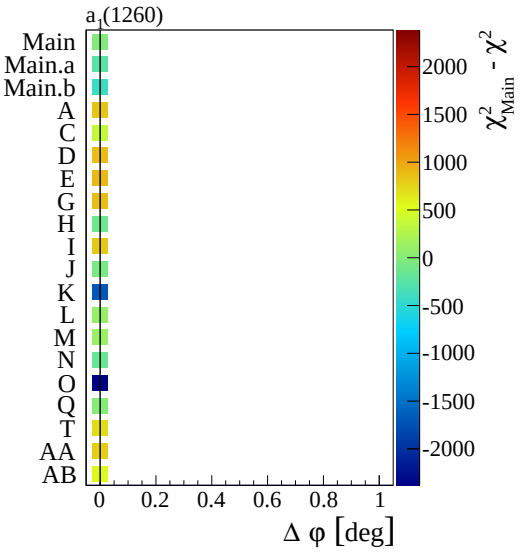

(d) Systematics of the maximal phase motion

Figure G.1: t' dependence and systematic studies for $a_1(1260)$ in $1^{++}0^+\rho(770)\pi S$.

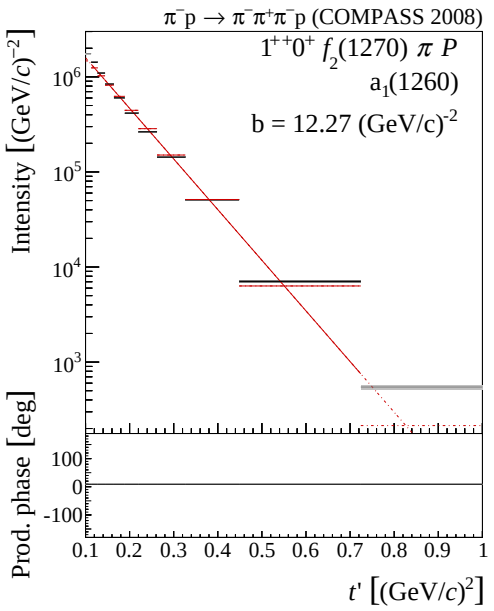

(a) t' dependence of the Main fit

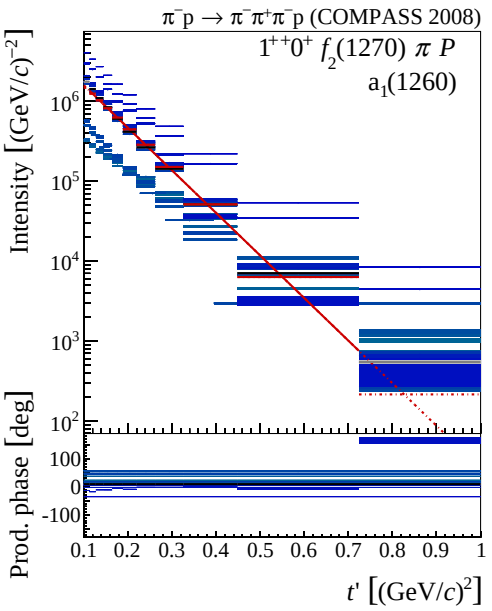

(b) t' dependence in all systematic studies

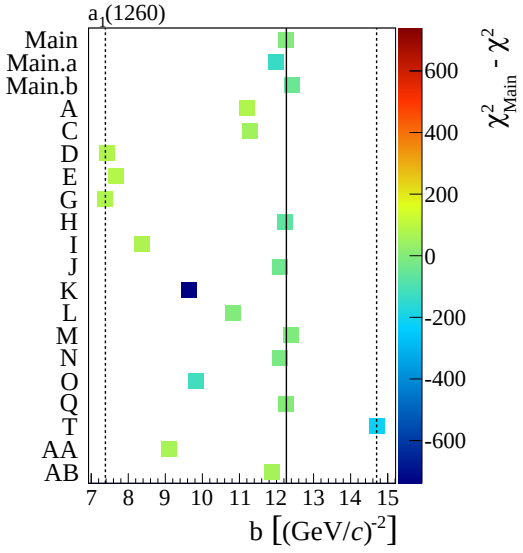

(c) Systematics of the t' slope parameter

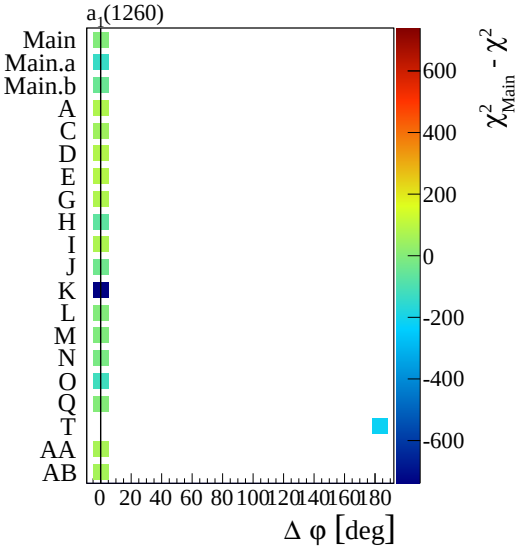

(d) Systematics of the maximal phase motion

Figure G.2: t' dependence and systematic studies for $a_1(1260)$ in $1^{++}0^+ f_2(1270)\pi P$.

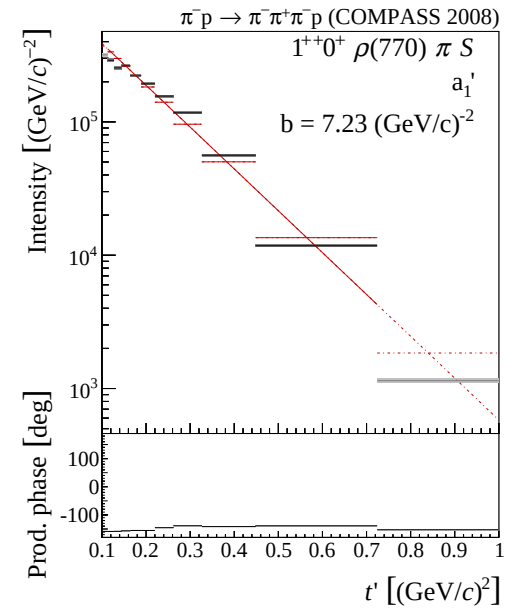

(a) t' dependence of the Main fit

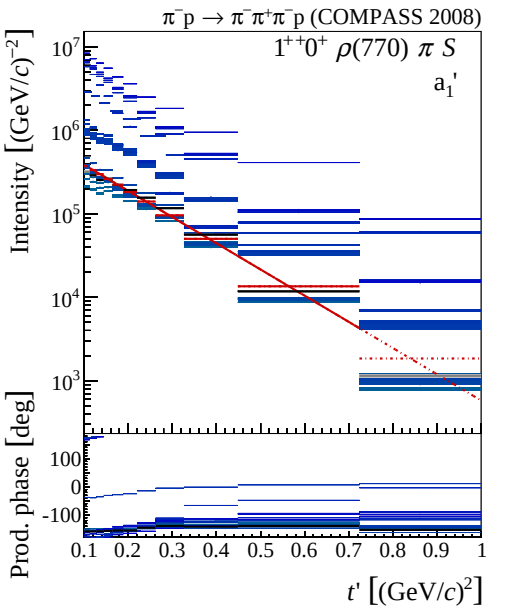

(b) t' dependence in all systematic studies

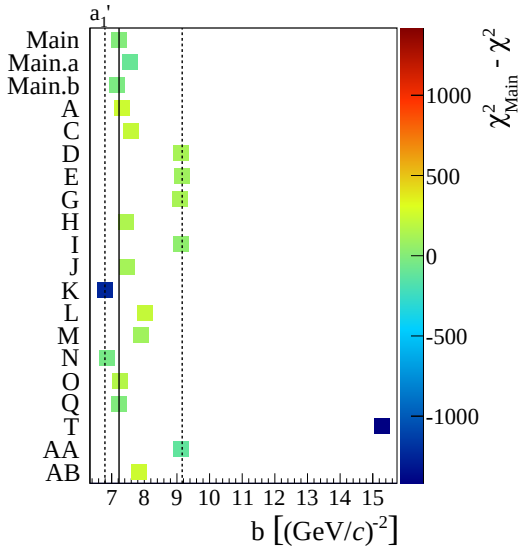

(c) Systematics of the t' slope parameter

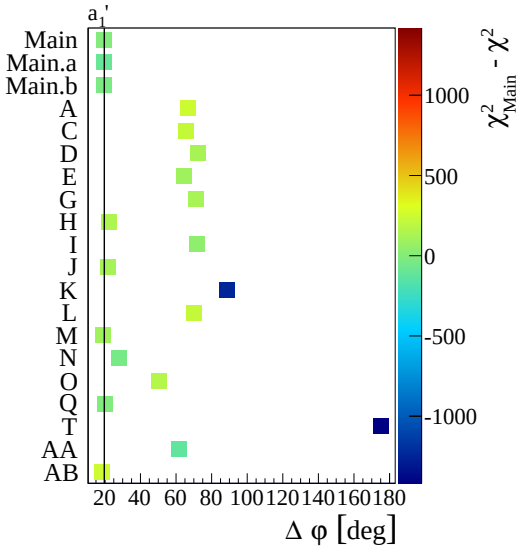

(d) Systematics of the maximal phase motion

Figure G.3: t' dependence and systematic studies for a_1' in $1^{++}0^+\rho(770)\pi S$.

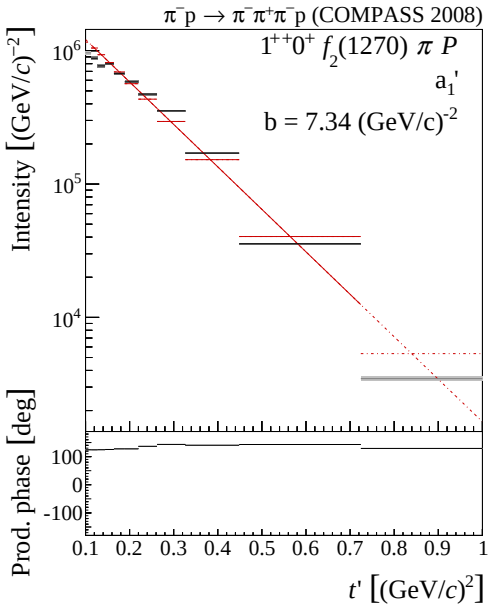

(a) t' dependence of the Main fit

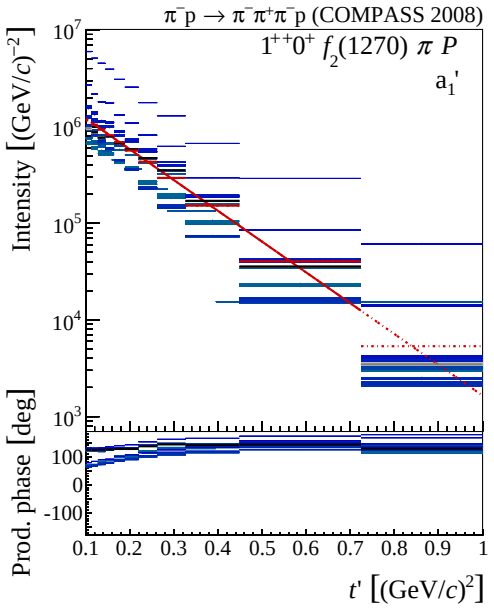

(b) t' dependence in all systematic studies

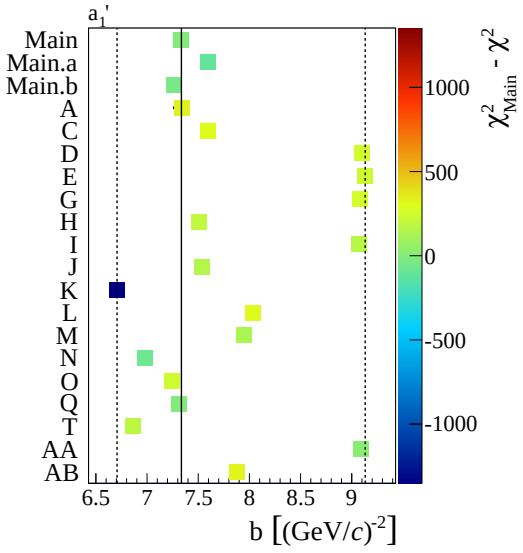

(c) Systematics of the t' slope parameter

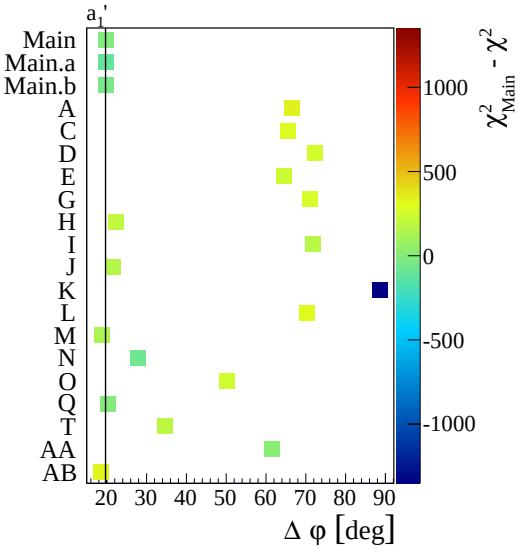

(d) Systematics of the maximal phase motion

Figure G.4: t' dependence and systematic studies for a_1' in $1^{++}0^+ f_2(1270)\pi P$.

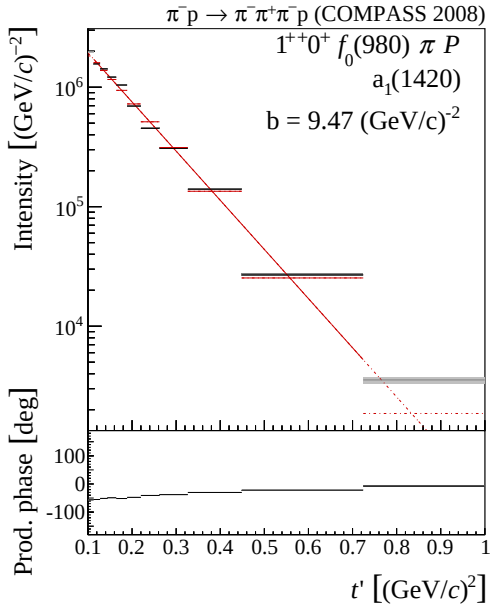

(a) t' dependence of the Main fit

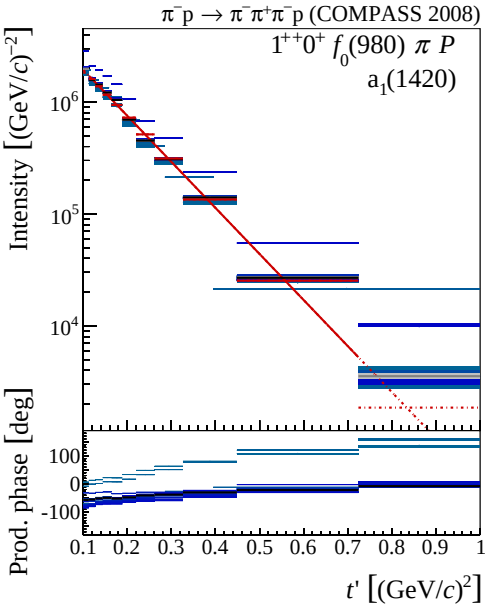

(b) t' dependence in all systematic studies

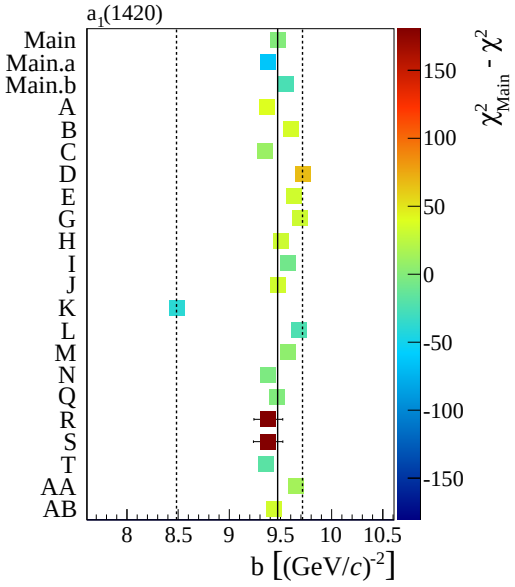

(c) Systematics of the t' slope parameter

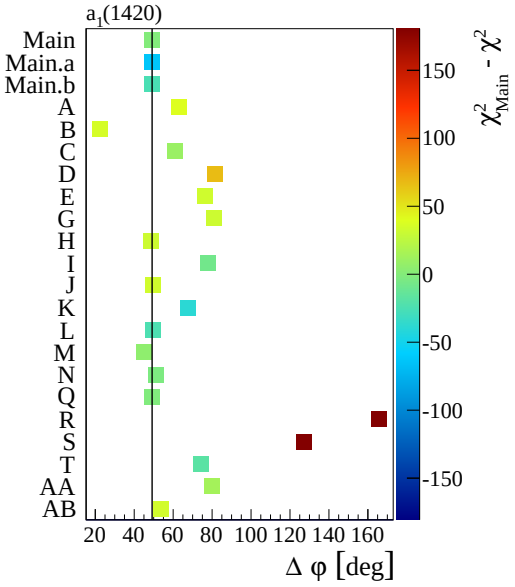

(d) Systematics of the maximal phase motion

Figure G.5: t' dependence and systematic studies for $a_1(1420)$ in $1^{++}0^+ f_0(980)\pi P$.

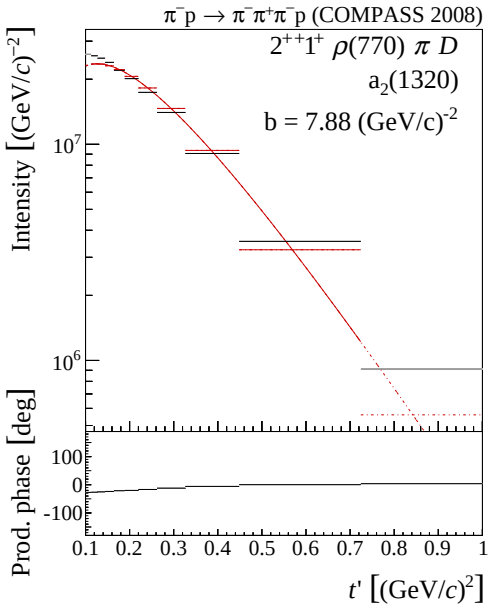

(a) t' dependence of the Main fit

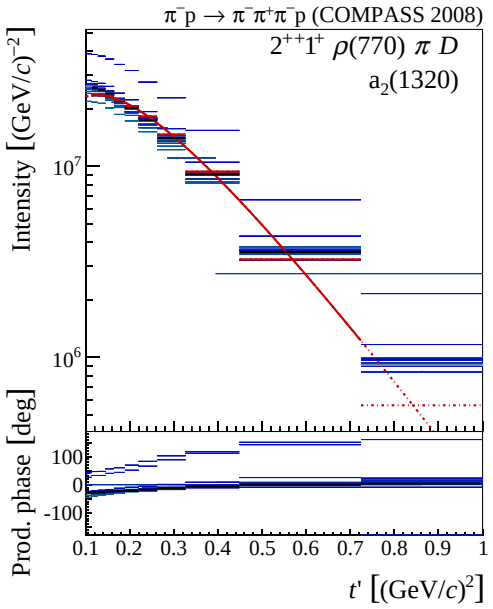

(b) t' dependence in all systematic studies

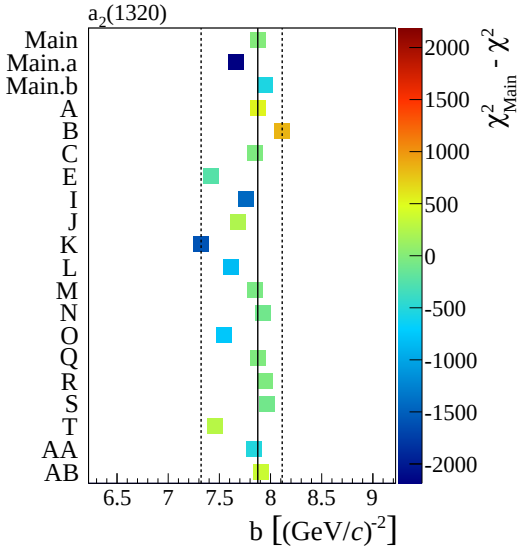

(c) Systematics of the t' slope parameter

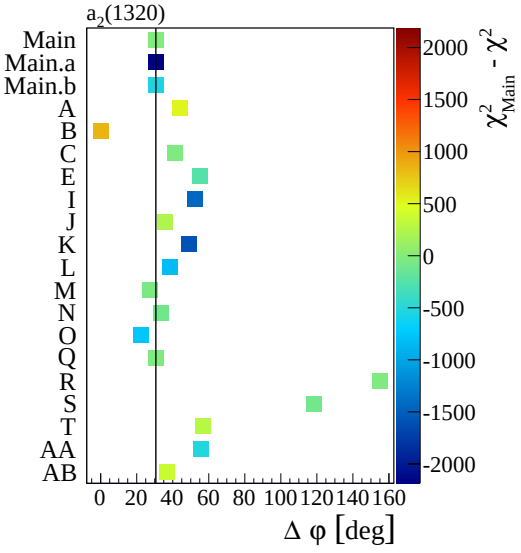

(d) Systematics of the maximal phase motion

Figure G.6: t' dependence and systematic studies for $a_2(1320)$ in $2^{++}1^+\rho(770)\pi D$.

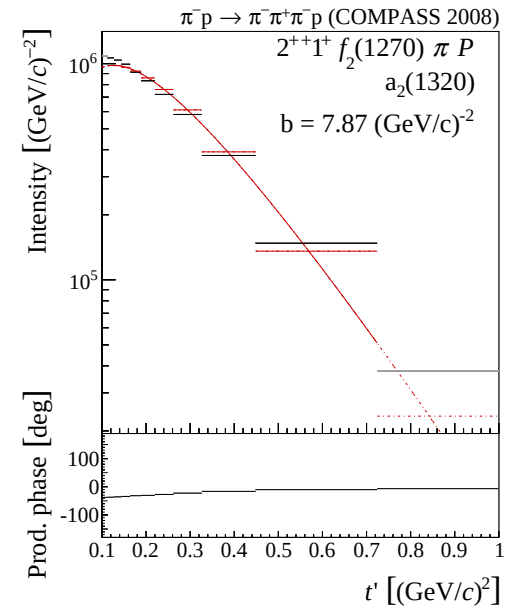

(a) t' dependence of the Main fit

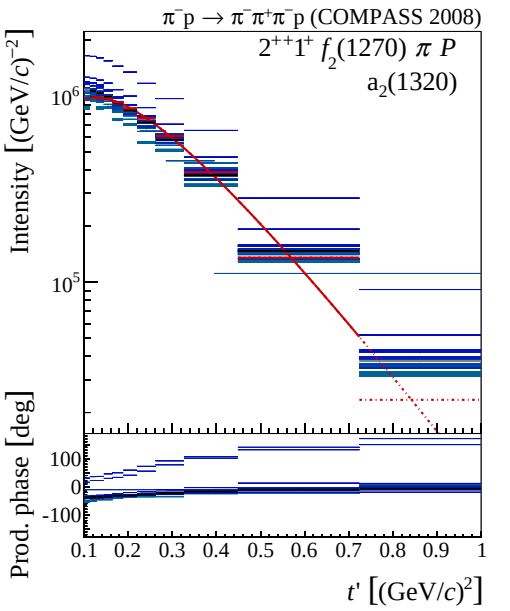

(b) t' dependence in all systematic studies

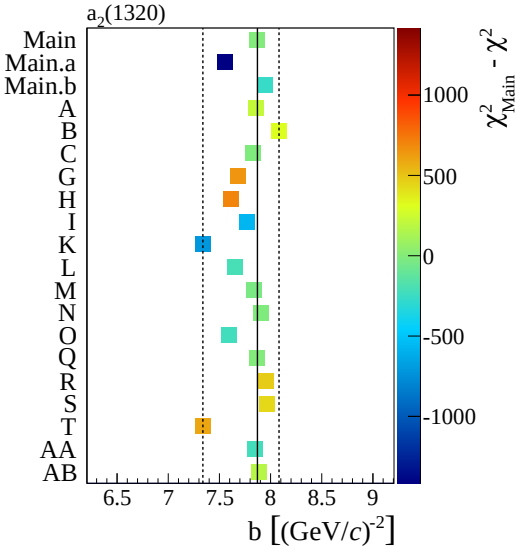

(c) Systematics of the t' slope parameter

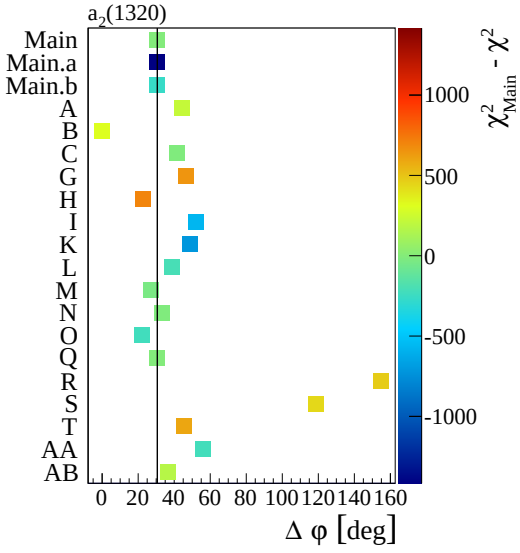

(d) Systematics of the maximal phase motion

Figure G.7: t' dependence and systematic studies for $a_2(1320)$ in $2^{++}1^+ f_2(1270)\pi P$.

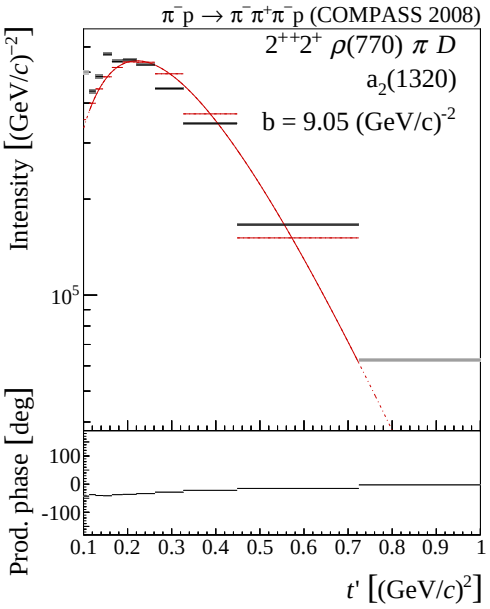

(a) t' dependence of the Main fit

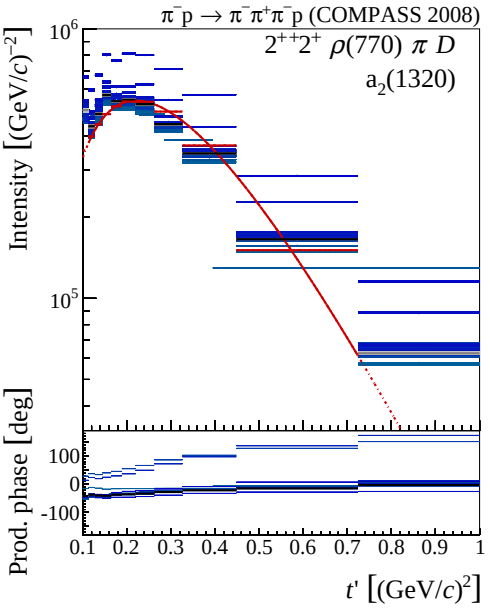

(b) t' dependence in all systematic studies

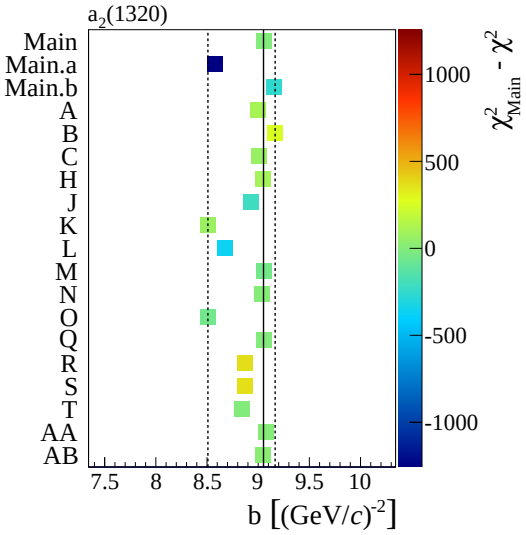

(c) Systematics of the t' slope parameter

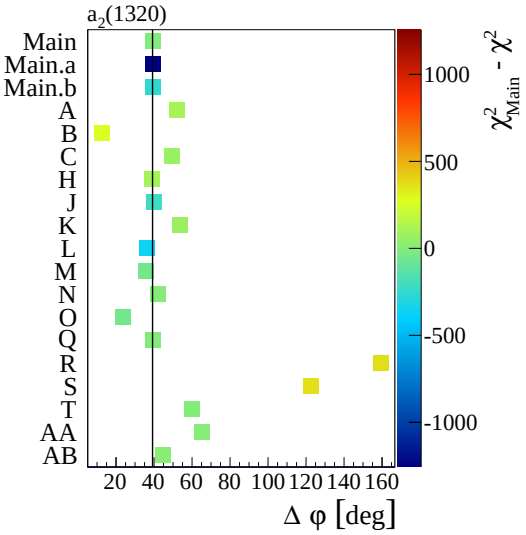

(d) Systematics of the maximal phase motion

Figure G.8: t' dependence and systematic studies for $a_2(1320)$ in $2^{++}2^{+}\rho(770)\pi D$.

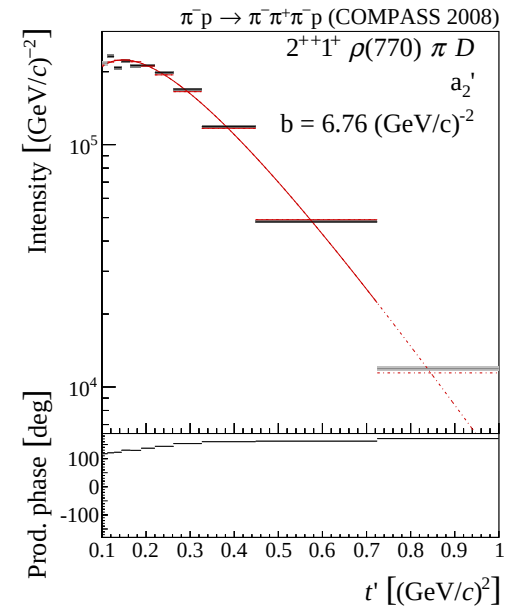

(a) t' dependence of the Main fit

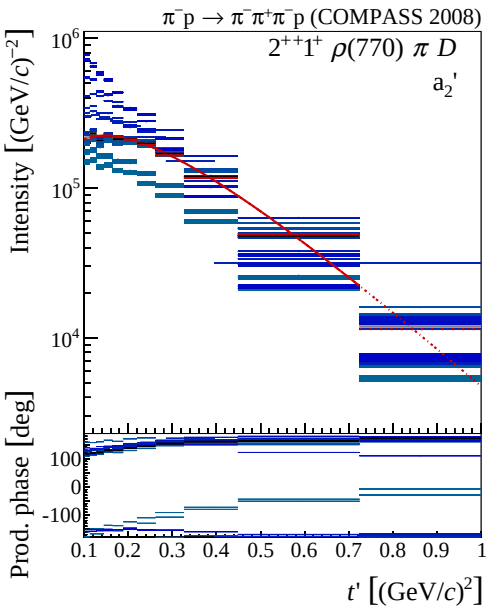

(b) t' dependence in all systematic studies

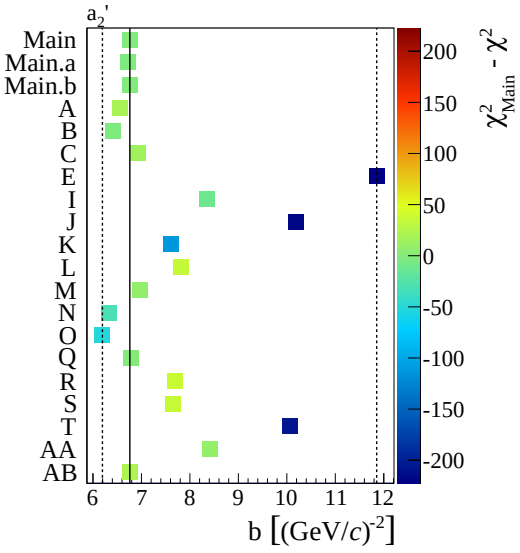

(c) Systematics of the t' slope parameter

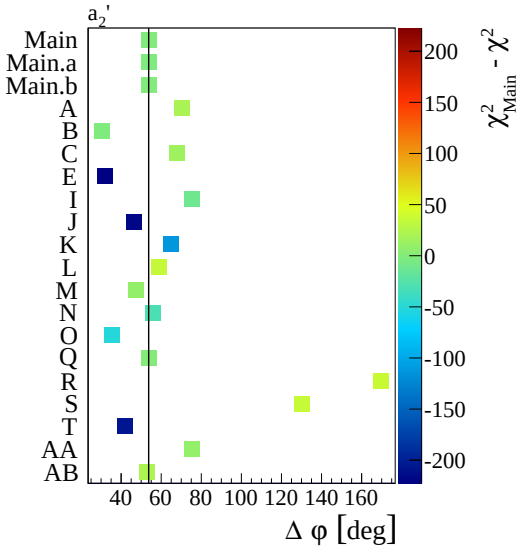

(d) Systematics of the maximal phase motion

Figure G.9: t' dependence and systematic studies for a_2' in $2^{++}1^{+}\rho(770)\pi D$.

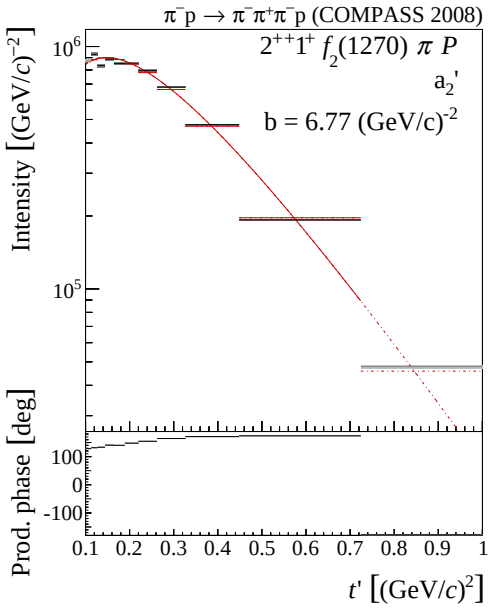

(a) t' dependence of the Main fit

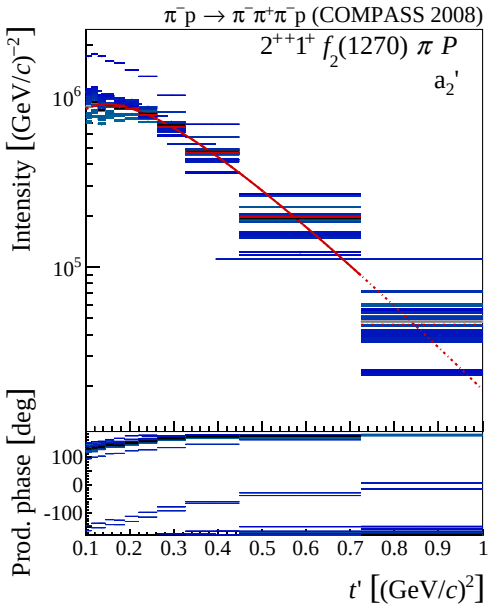

(b) t' dependence in all systematic studies

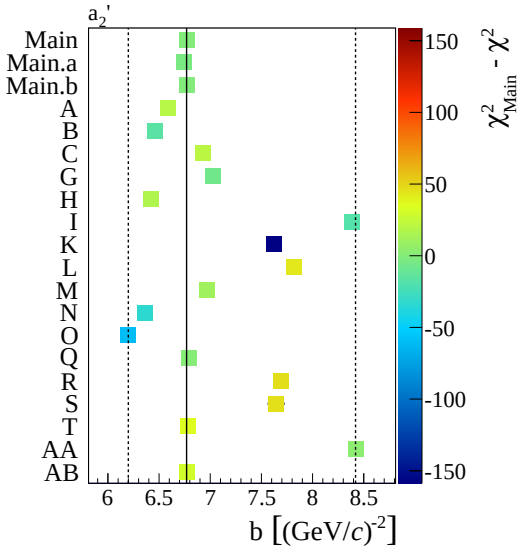

(c) Systematics of the t' slope parameter

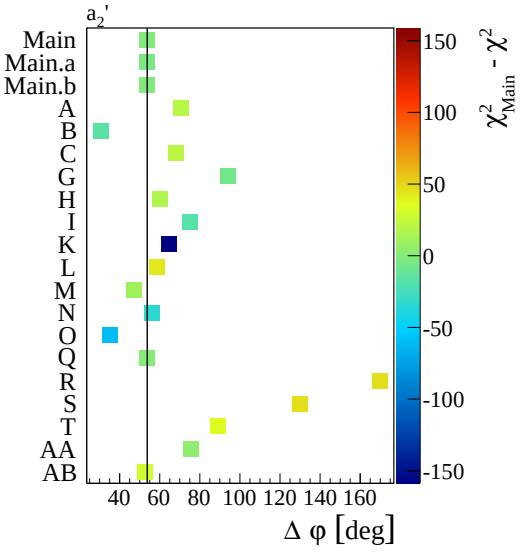

(d) Systematics of the maximal phase motion

Figure G.10: t' dependence and systematic studies for a_2' in $2^{++}1^+ f_2(1270)\pi P$.

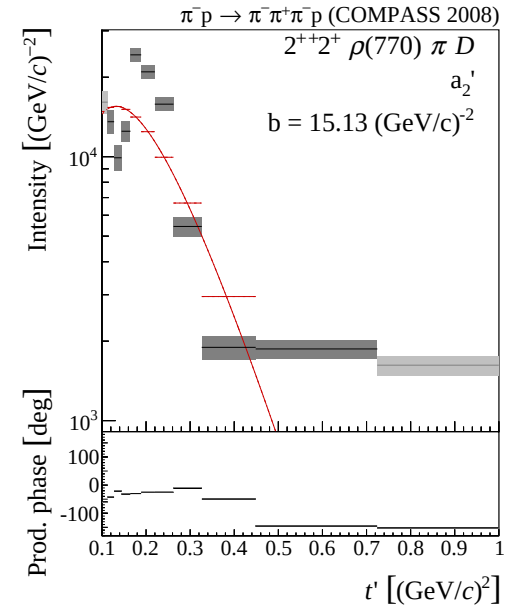

(a) t' dependence of the Main fit

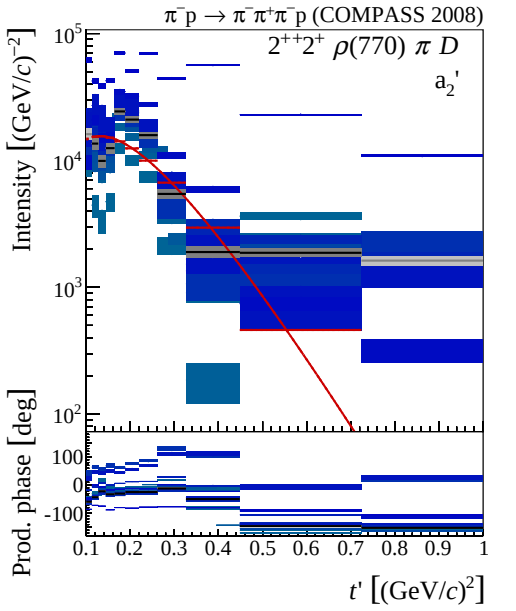

(b) t' dependence in all systematic studies

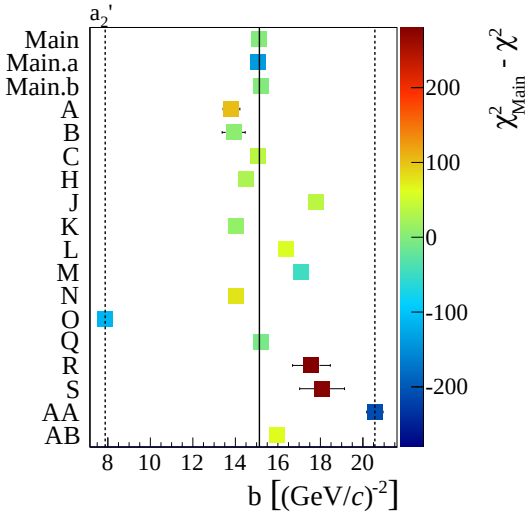

(c) Systematics of the t' slope parameter

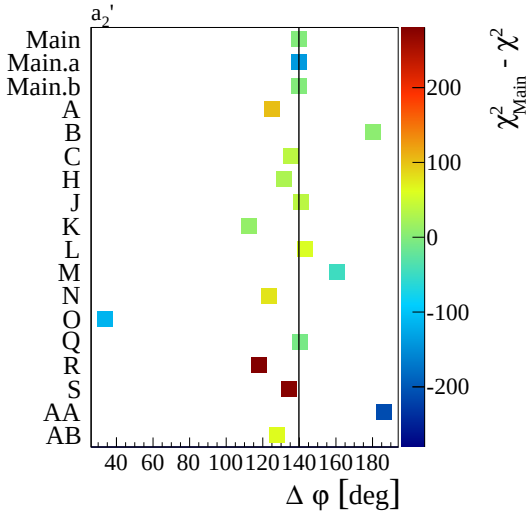

(d) Systematics of the maximal phase motion

Figure G.11: t' dependence and systematic studies for a_2' in $2^{++}2^{+}\rho(770)\pi D$.

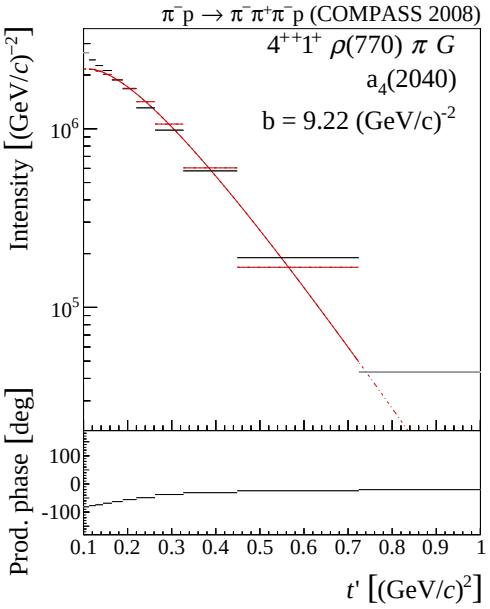

(a) t' dependence of the Main fit

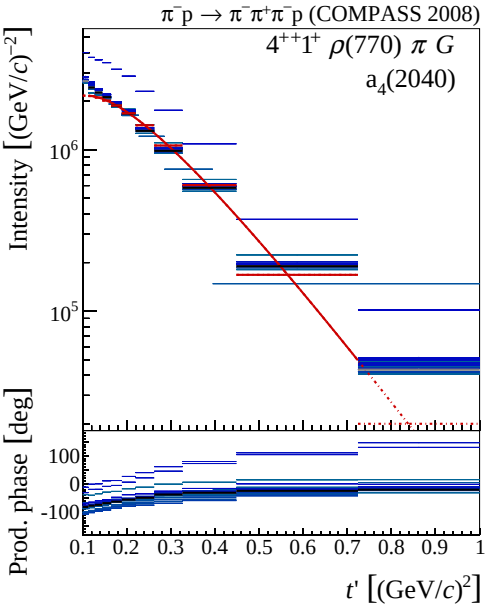

(b) t' dependence in all systematic studies

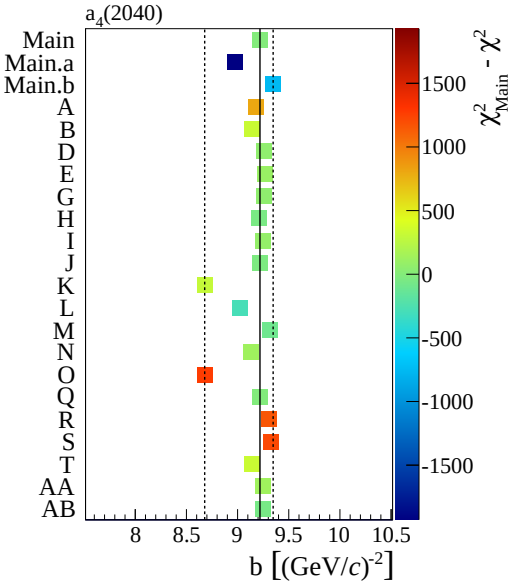

(c) Systematics of the t' slope parameter

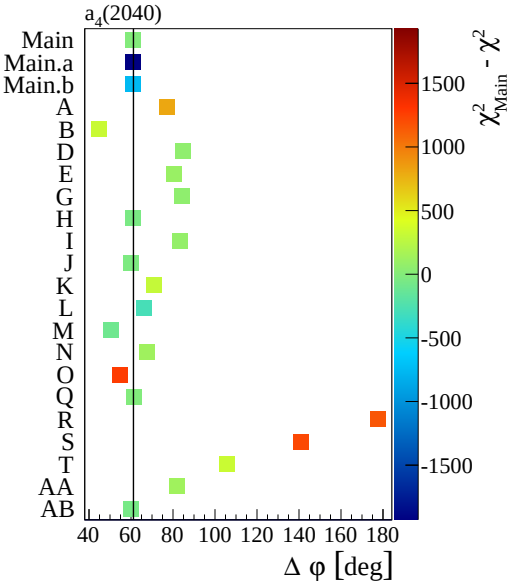

(d) Systematics of the maximal phase motion

Figure G.12: t' dependence and systematic studies for $a_4(2040)$ in $4^{++}1^{+}\rho(770)\pi G$.

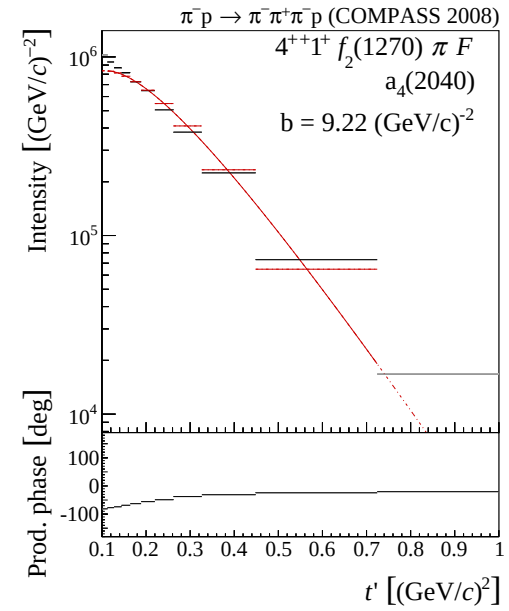

(a) t' dependence of the Main fit

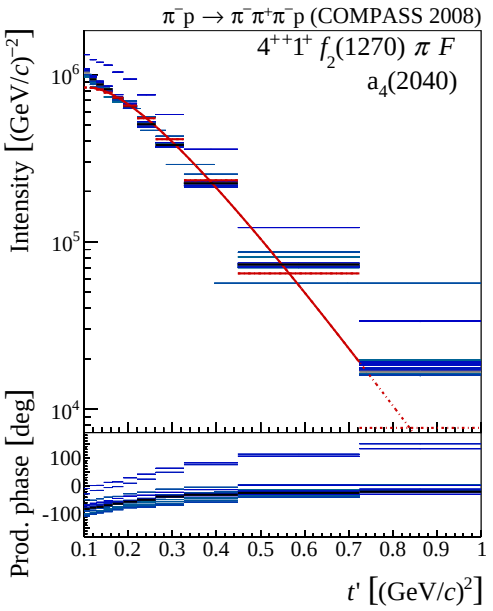

(b) t' dependence in all systematic studies

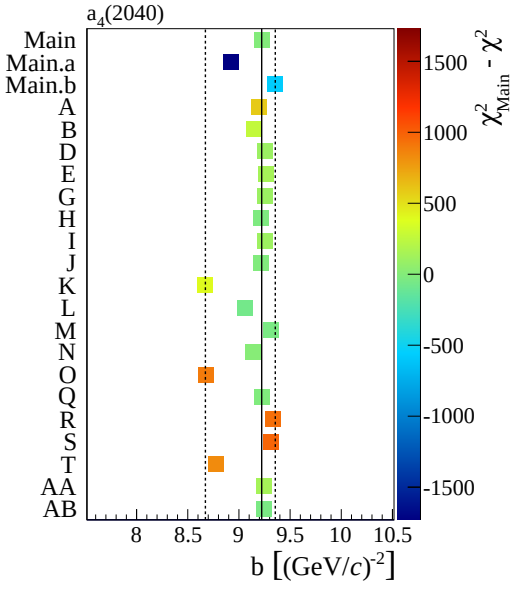

(c) Systematics of the t' slope parameter

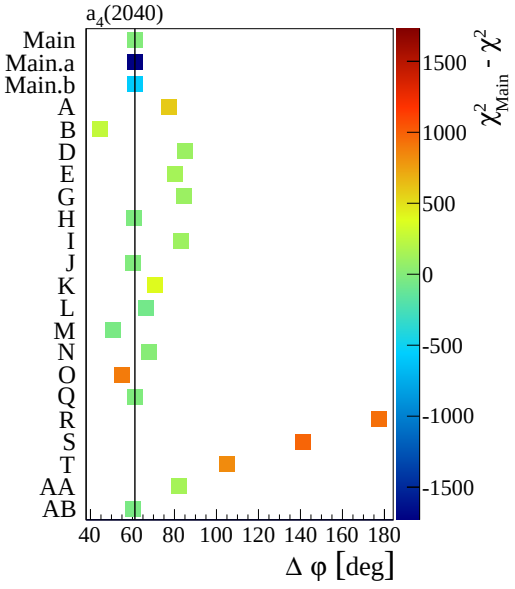

(d) Systematics of the maximal phase motion

Figure G.13: t' dependence and systematic studies for $a_4(2040)$ in $4^{++}1^{+}\,f_2(1270)\pi F$.

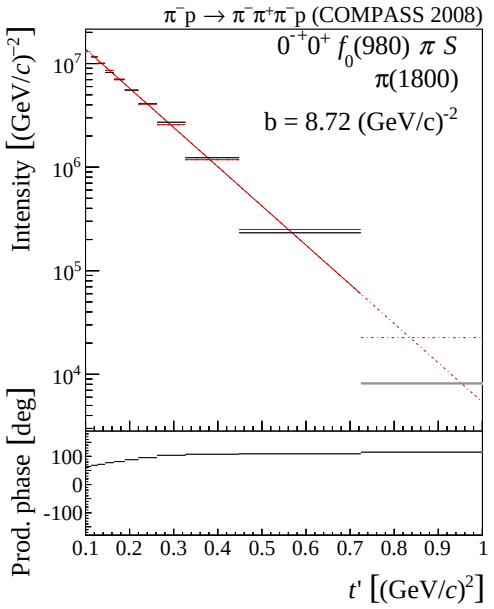

(a) t' dependence of the Main fit

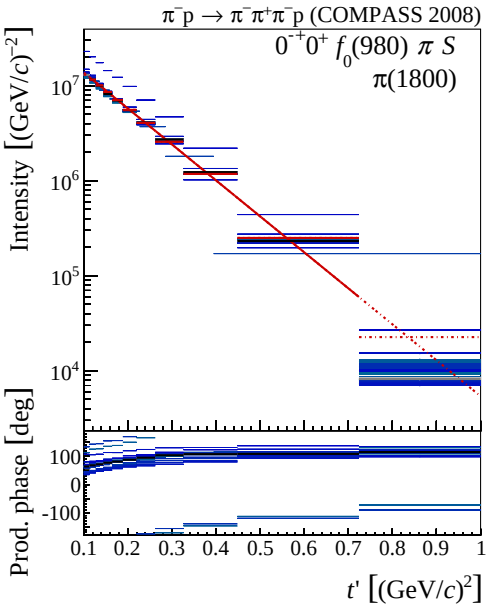

(b) t' dependence in all systematic studies

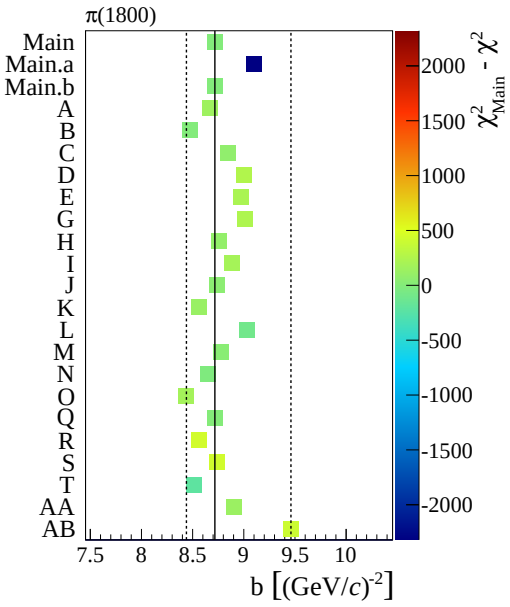

(c) Systematics of the t' slope parameter

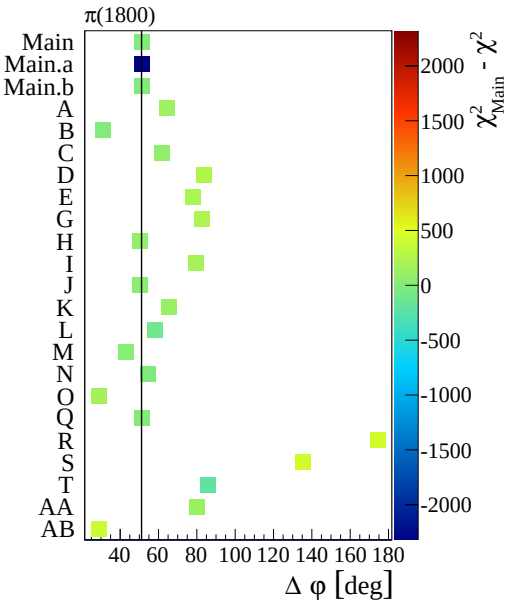

(d) Systematics of the maximal phase motion

Figure G.14: t' dependence and systematic studies for $\pi(1800)$ in $0^{-+}0^{+}f_0(980)\pi S$.

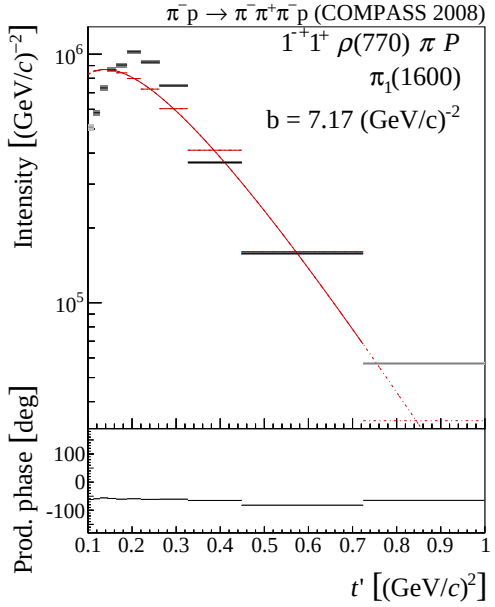

(a) t' dependence of the Main fit

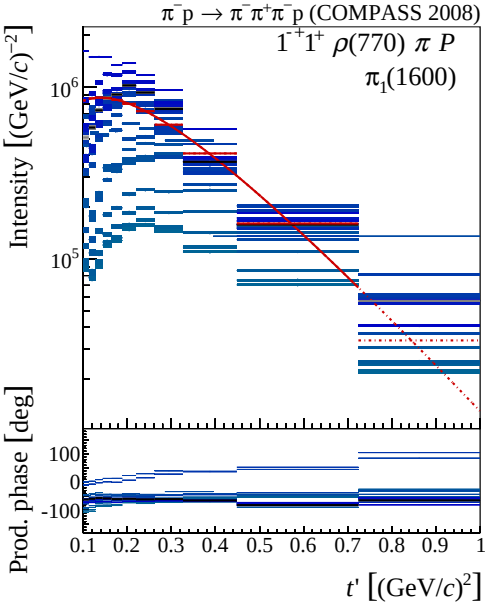

(b) t' dependence in all systematic studies

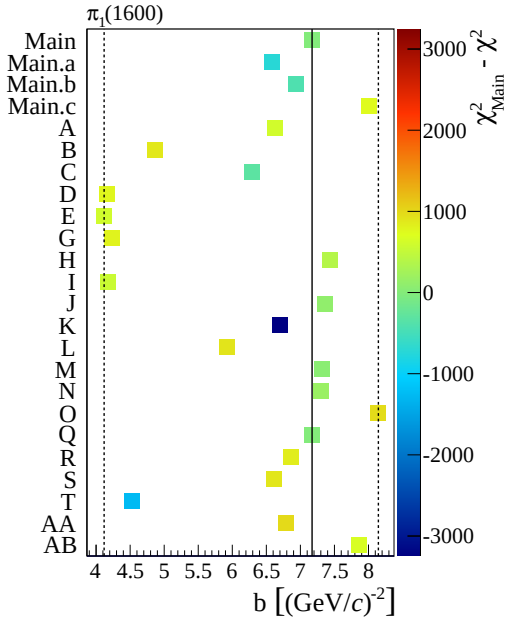

(c) Systematics of the t' slope parameter

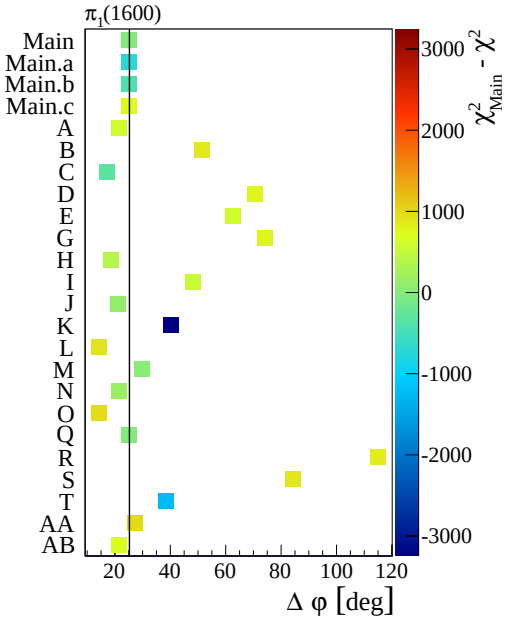

(d) Systematics of the maximal phase motion

Figure G.15: t' dependence and systematic studies for $\pi_1(1600)$ in $1^{-+}1^+\rho(770)\pi P$.

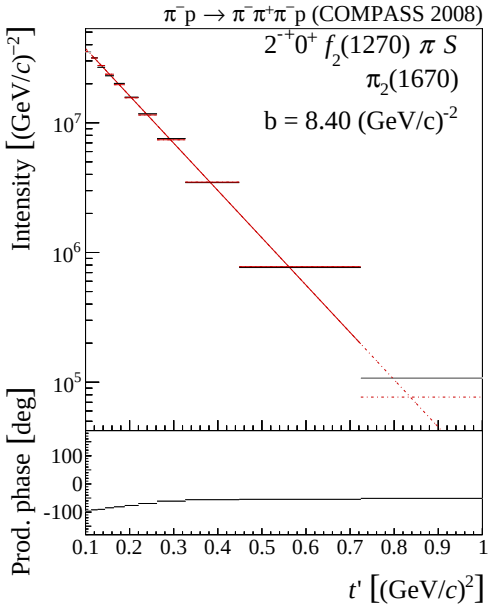

(a) t' dependence of the Main fit

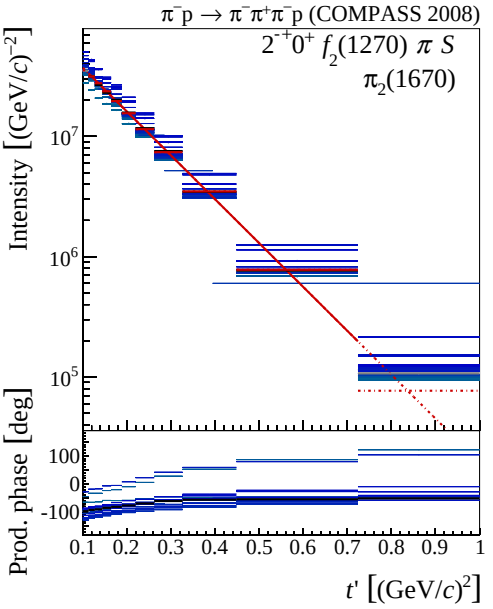

(b) t' dependence in all systematic studies

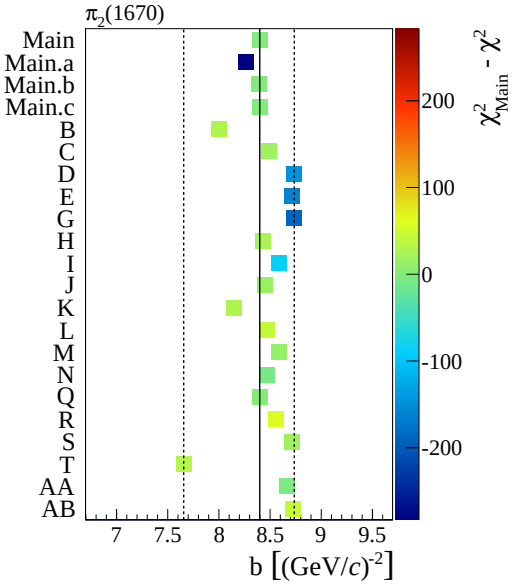

(c) Systematics of the t' slope parameter

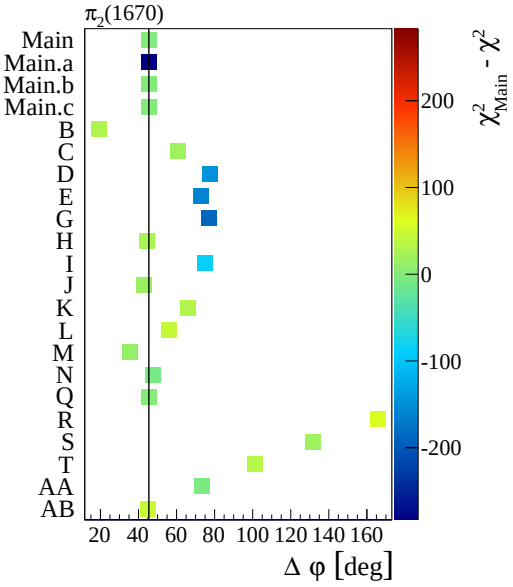

(d) Systematics of the maximal phase motion

Figure G.16: t' dependence and systematic studies for $\pi_2(1670)$ in $2^{-+}0^+ f_2(1270)\pi S$.

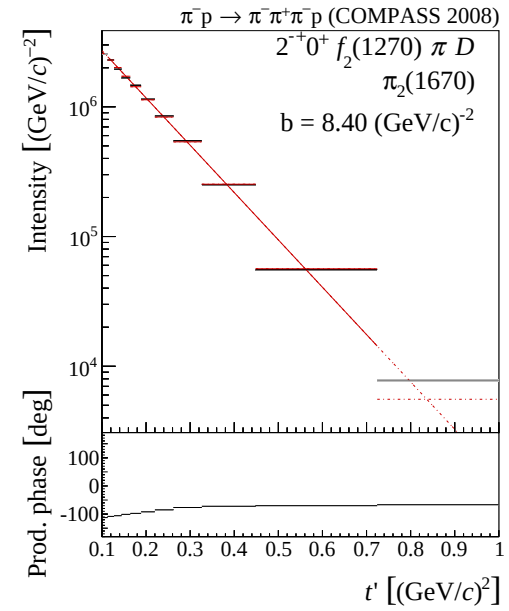

(a) t' dependence of the Main fit

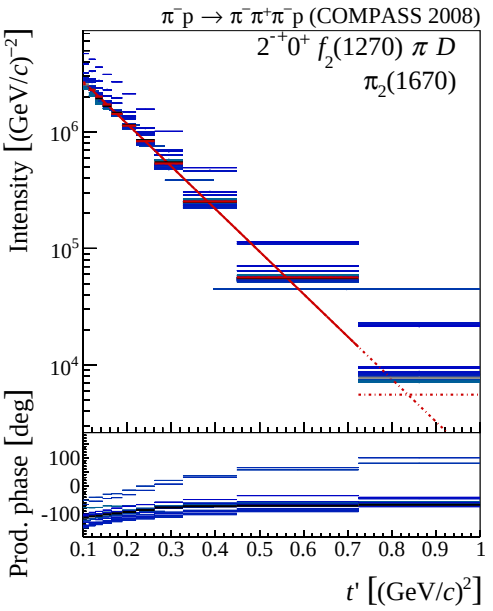

(b) t' dependence in all systematic studies

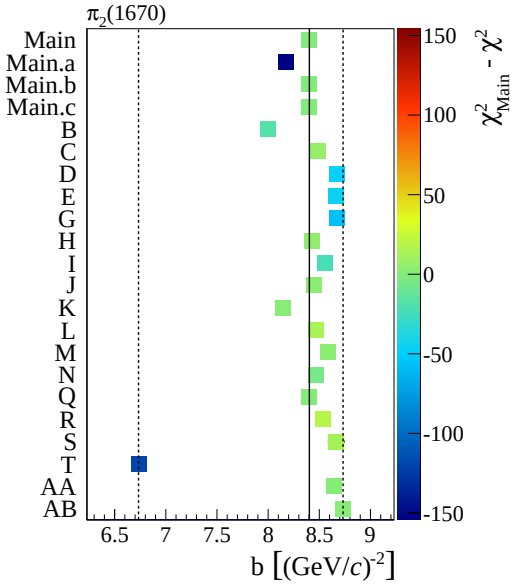

(c) Systematics of the t' slope parameter

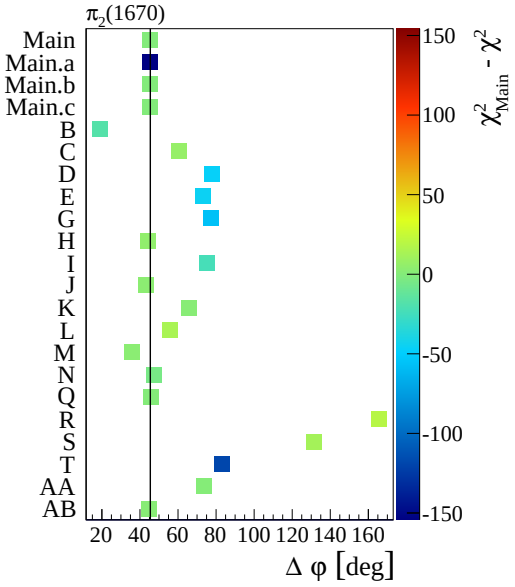

(d) Systematics of the maximal phase motion

Figure G.17: t' dependence and systematic studies for $\pi_2(1670)$ in $2^{-+}0^+ f_2(1270)\pi D$.

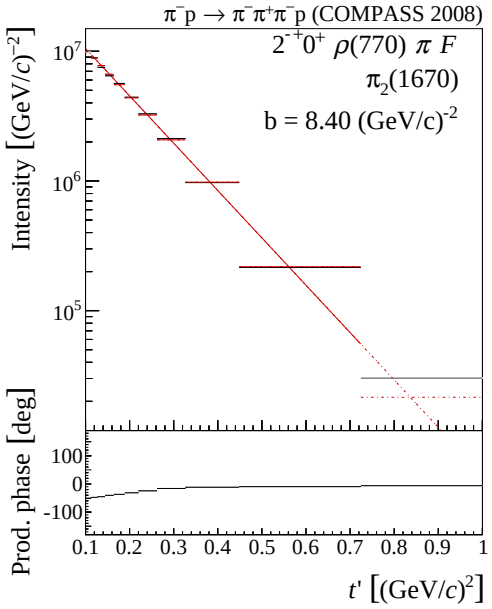

(a) t' dependence of the Main fit

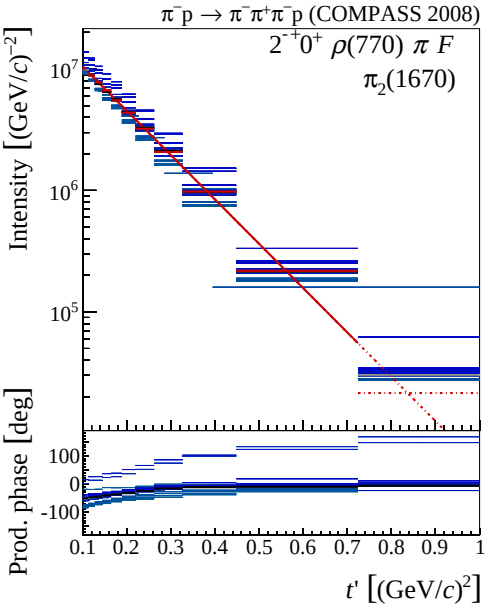

(b) t' dependence in all systematic studies

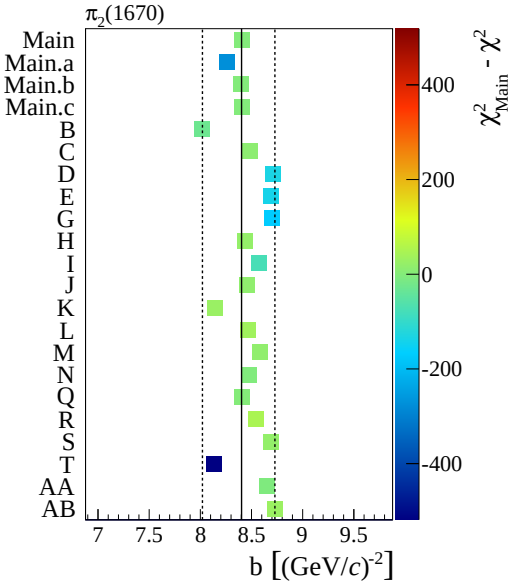

(c) Systematics of the t' slope parameter

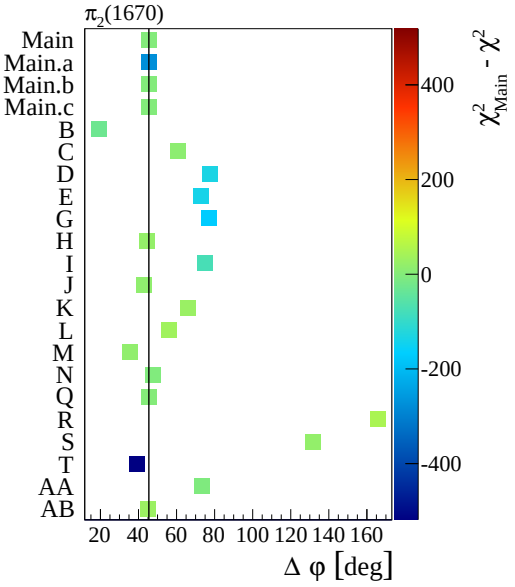

(d) Systematics of the maximal phase motion

Figure G.18: t' dependence and systematic studies for $\pi_2(1670)$ in $2^{-+}0^+\rho(770)\pi F$.

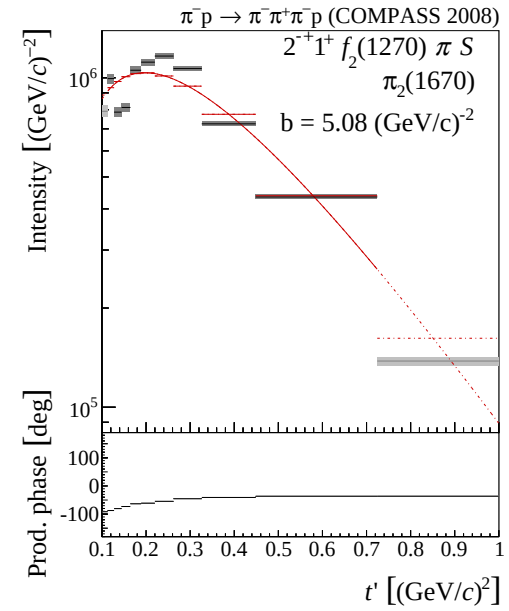

(a) t' dependence of the Main fit

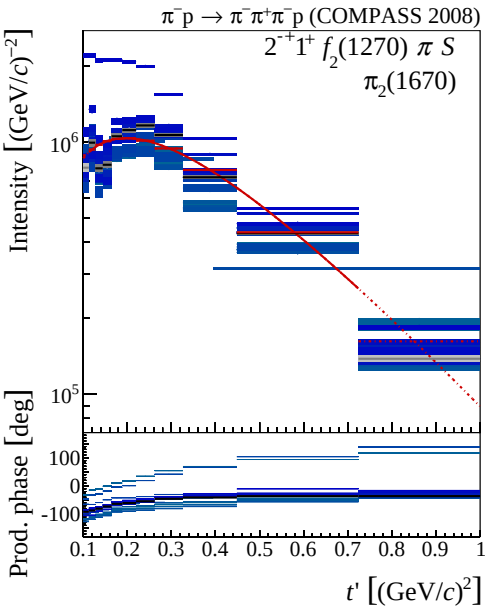

(b) t' dependence in all systematic studies

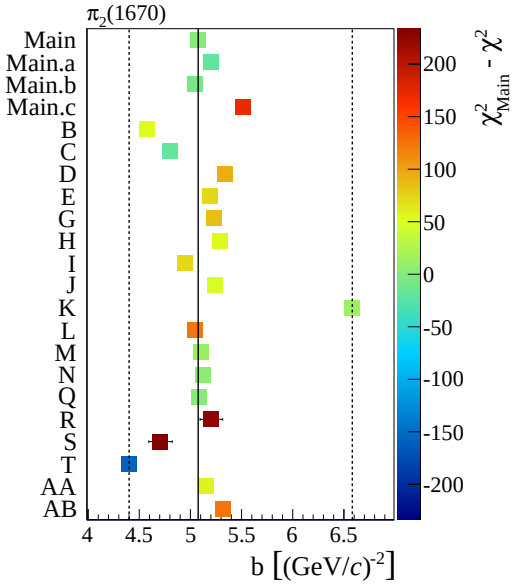

(c) Systematics of the t' slope parameter

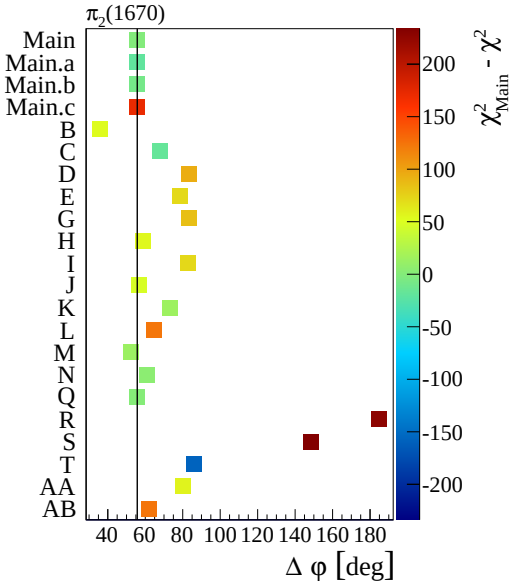

(d) Systematics of the maximal phase motion

Figure G.19: t' dependence and systematic studies for $\pi_2(1670)$ in $2^{-+}1^+ f_2(1270)\pi S$.

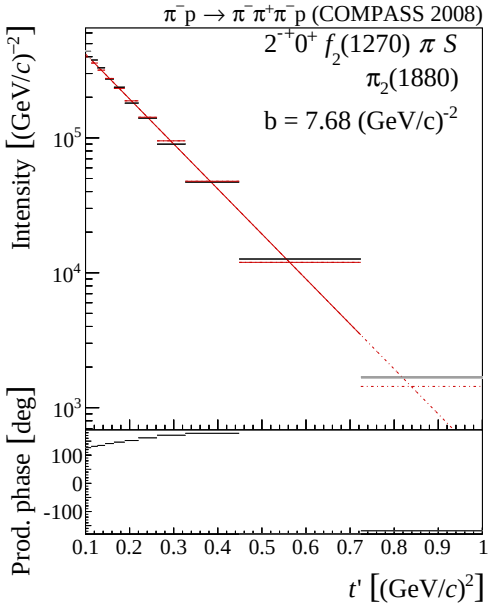

(a) t' dependence of the Main fit

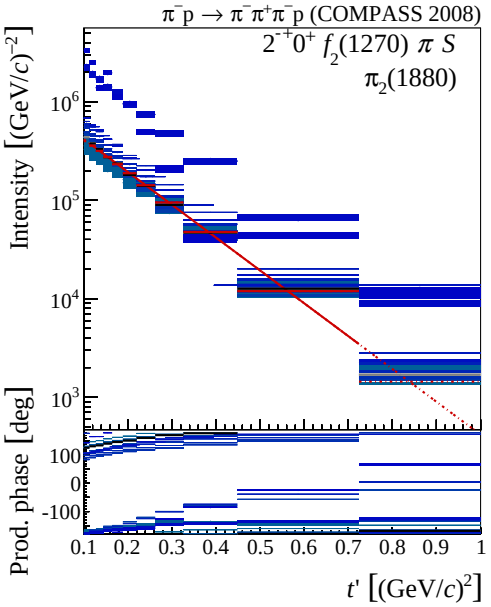

(b) t' dependence in all systematic studies

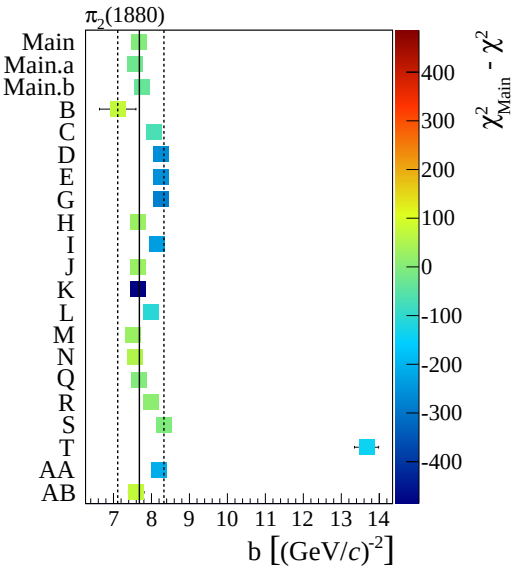

(c) Systematics of the t' slope parameter

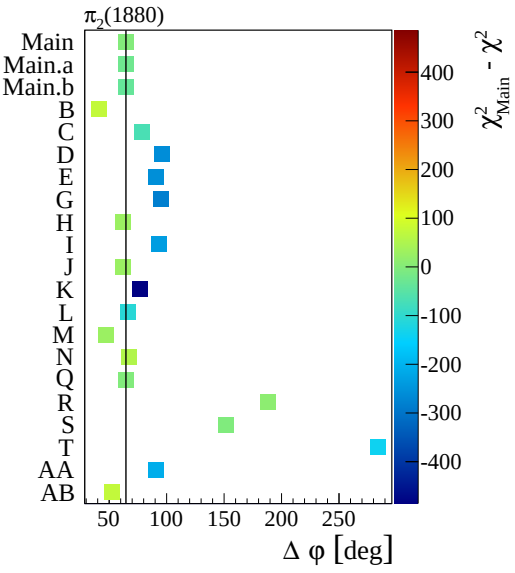

(d) Systematics of the maximal phase motion

Figure G.20: t' dependence and systematic studies for $\pi_2(1880)$ in $2^{-+}0^+ f_2(1270)\pi S$.

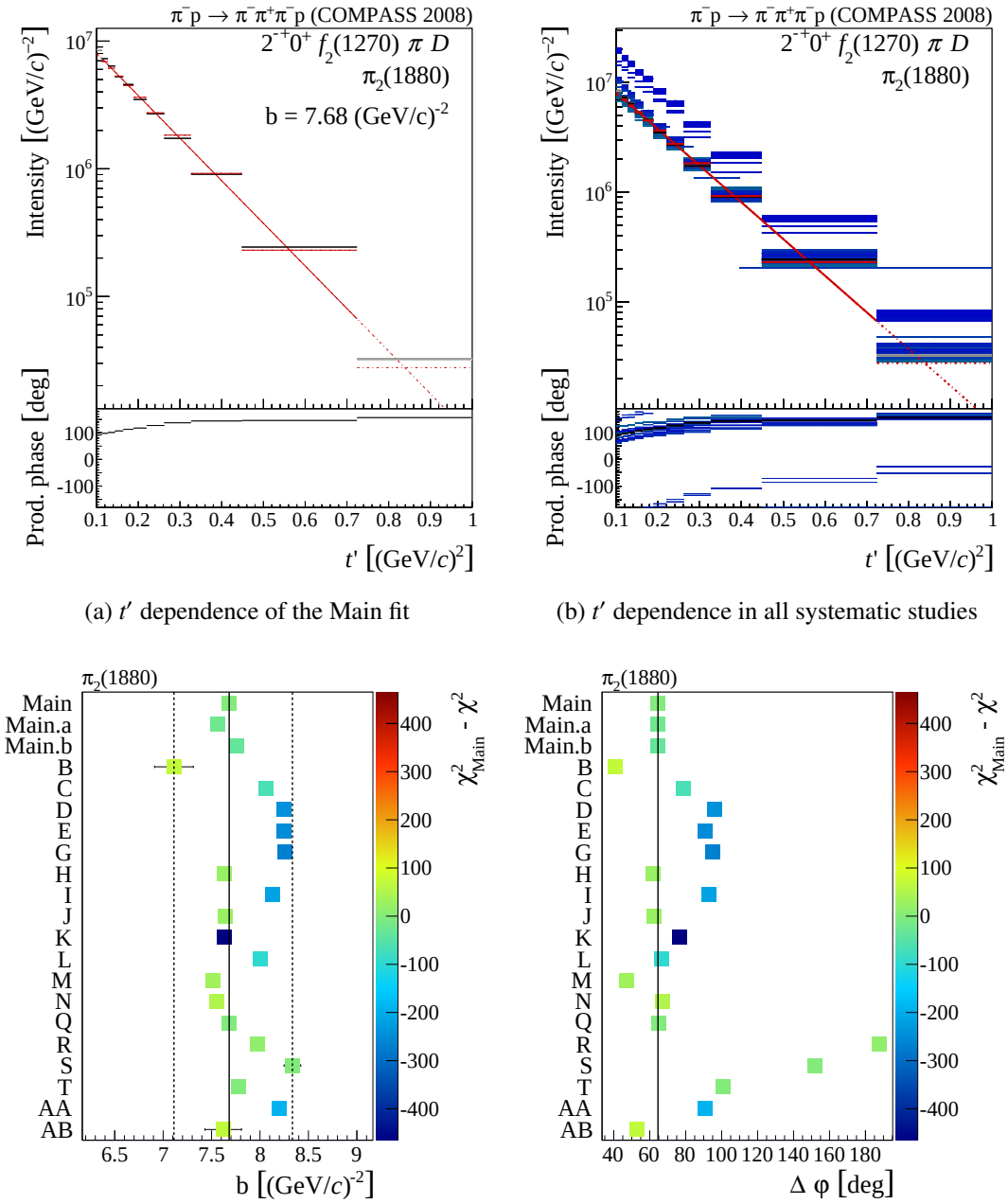

(a) t' dependence of the Main fit

(b) t' dependence in all systematic studies

(c) Systematics of the t' slope parameter

(d) Systematics of the maximal phase motion

Figure G.21: t' dependence and systematic studies for $\pi_2(1880)$ in $2^{-+}0^+ f_2(1270)\pi D$.

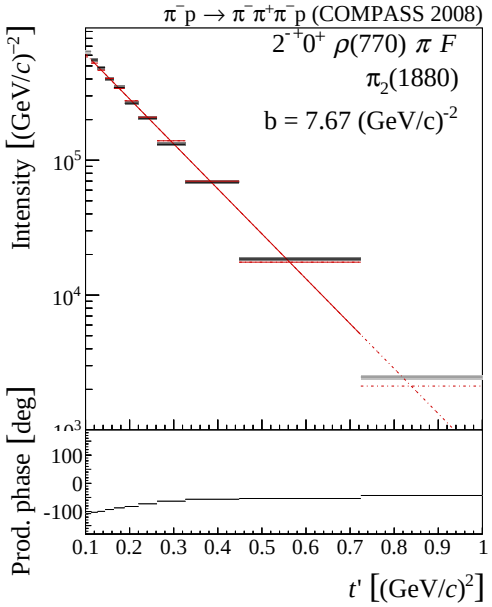

(a) t' dependence of the Main fit

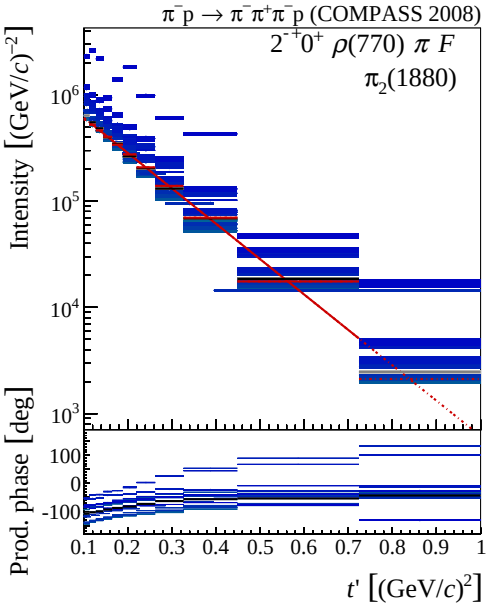

(b) t' dependence in all systematic studies

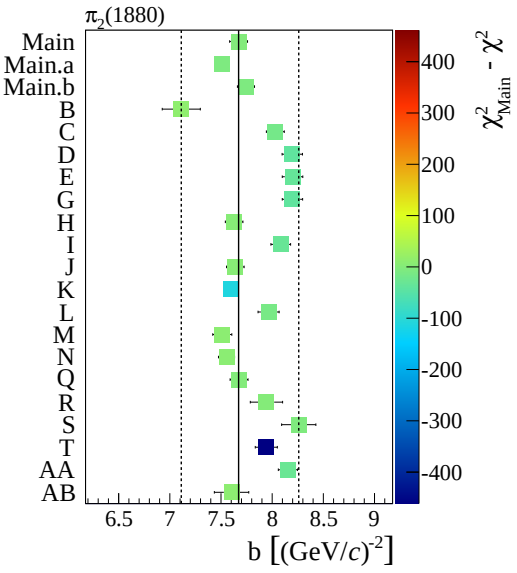

(c) Systematics of the t' slope parameter

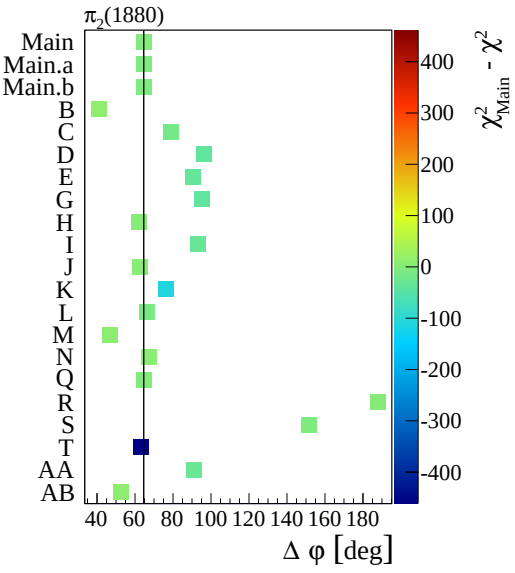

(d) Systematics of the maximal phase motion

Figure G.22: t' dependence and systematic studies for $\pi_2(1880)$ in $2^{-+}0^+\rho(770)\pi F$.

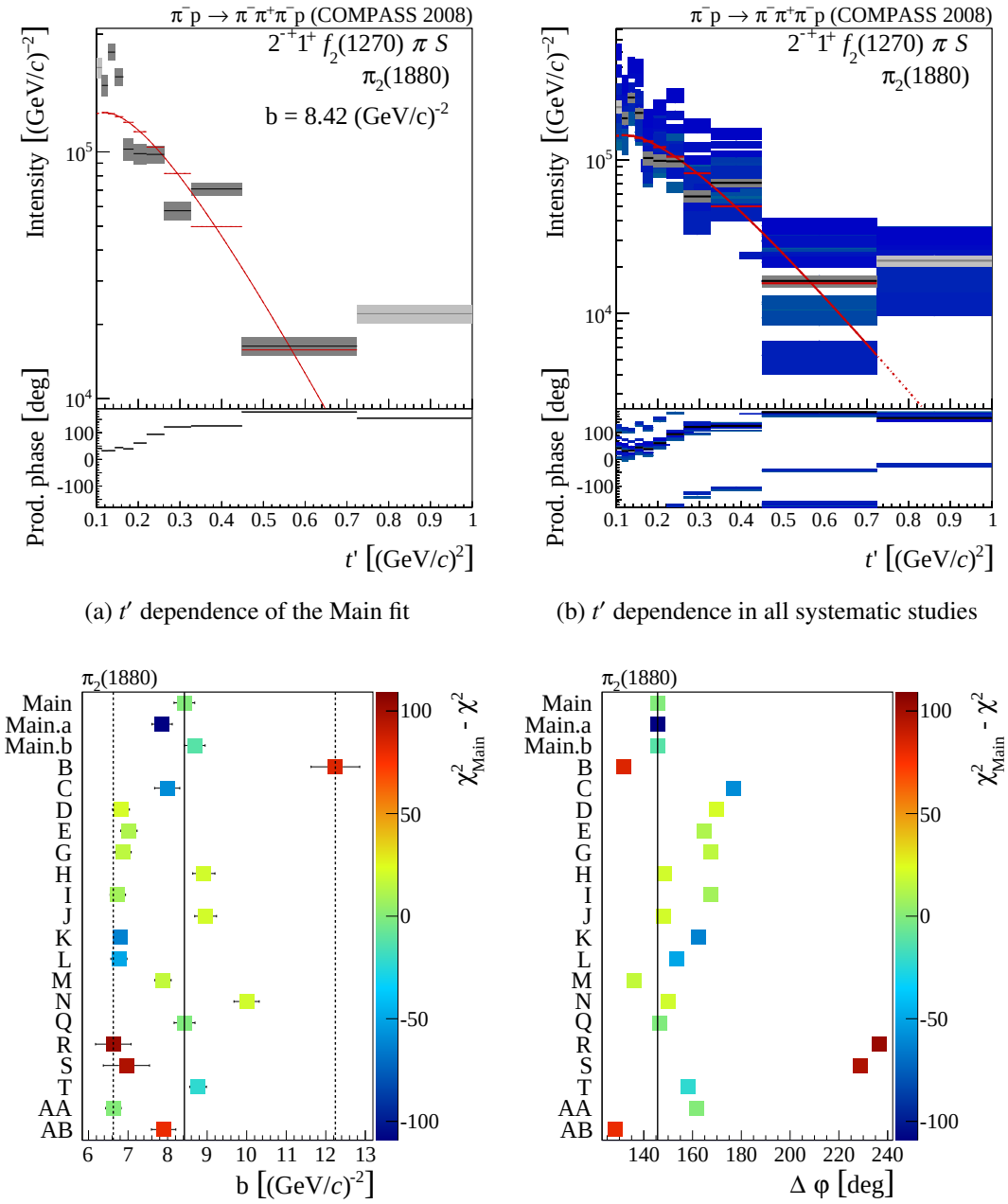

(a) t' dependence of the Main fit

(b) t' dependence in all systematic studies

(c) Systematics of the t' slope parameter

(d) Systematics of the maximal phase motion

Figure G.23: t' dependence and systematic studies for $\pi_2(1880)$ in $2^{-+}1^+ f_2(1270)\pi S$.

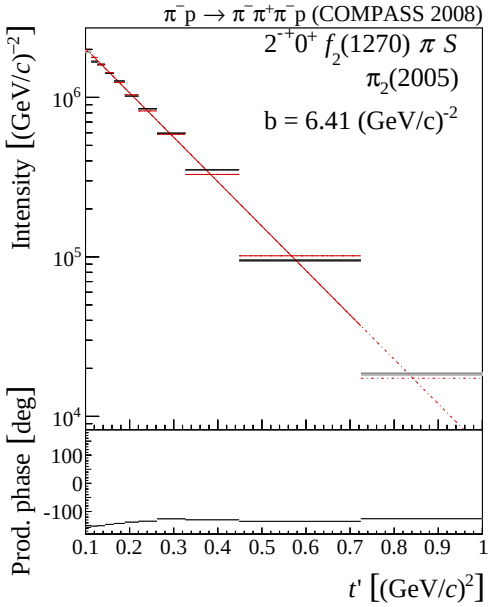

(a) t' dependence of the Main fit

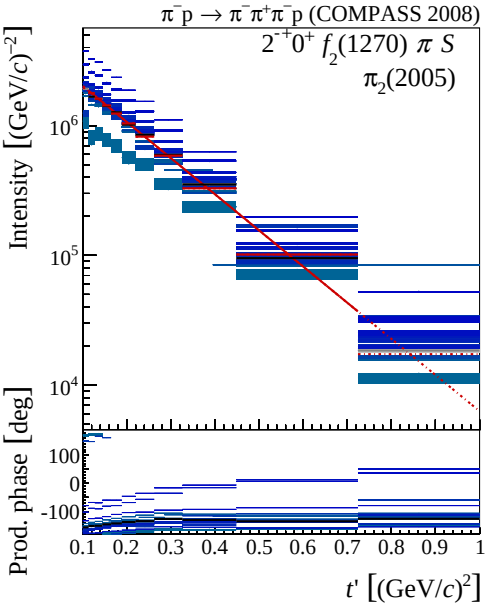

(b) t' dependence in all systematic studies

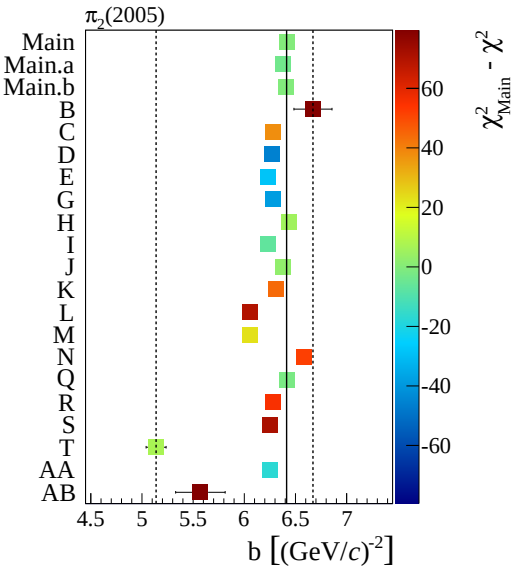

(c) Systematics of the t' slope parameter

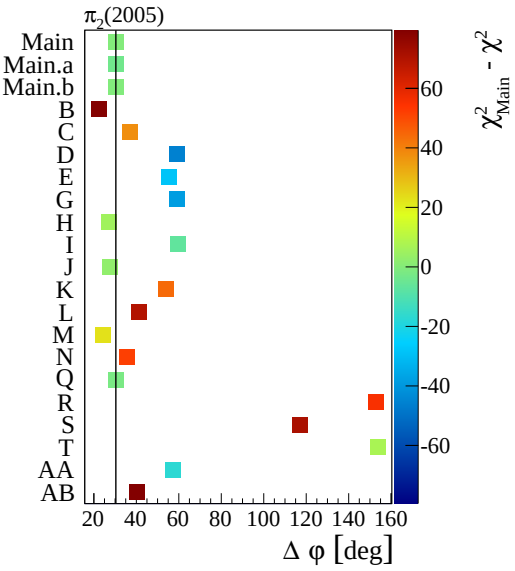

(d) Systematics of the maximal phase motion

Figure G.24: t' dependence and systematic studies for $\pi_2'(2005)$ in $2^{-+}0^+ f_2(1270)\pi S$.

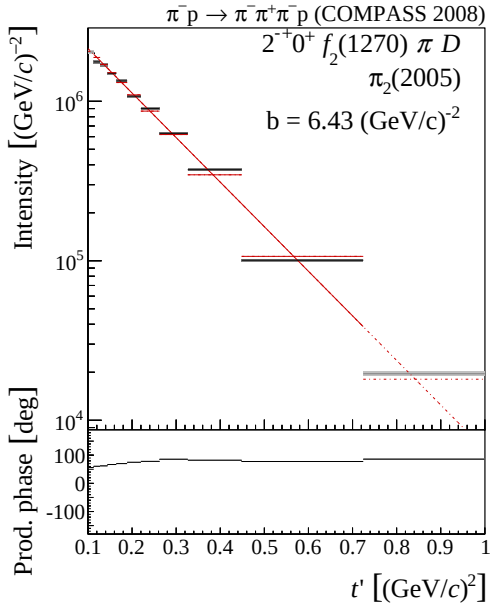

(a) t' dependence of the Main fit

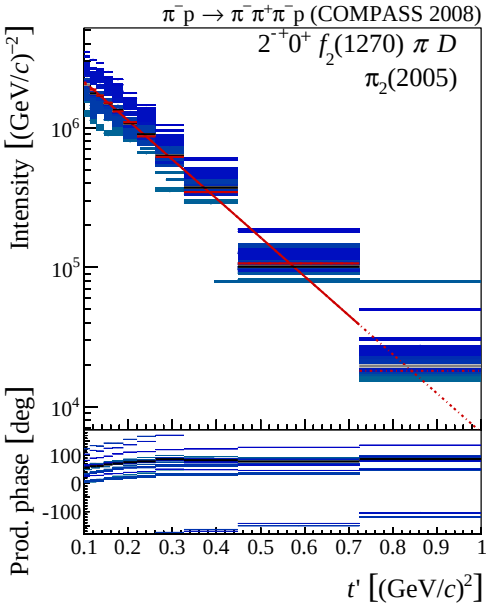

(b) t' dependence in all systematic studies

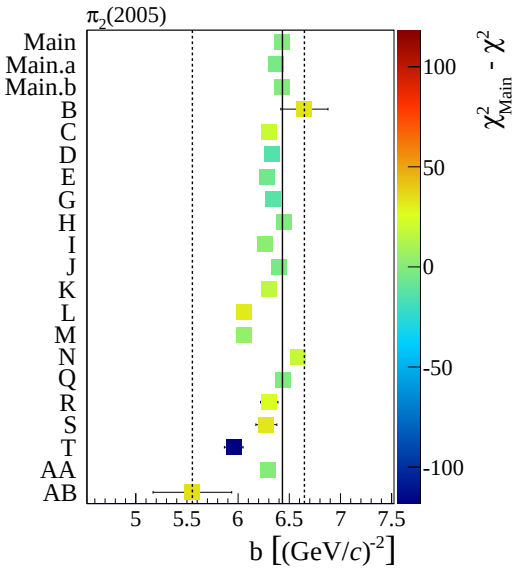

(c) Systematics of the t' slope parameter

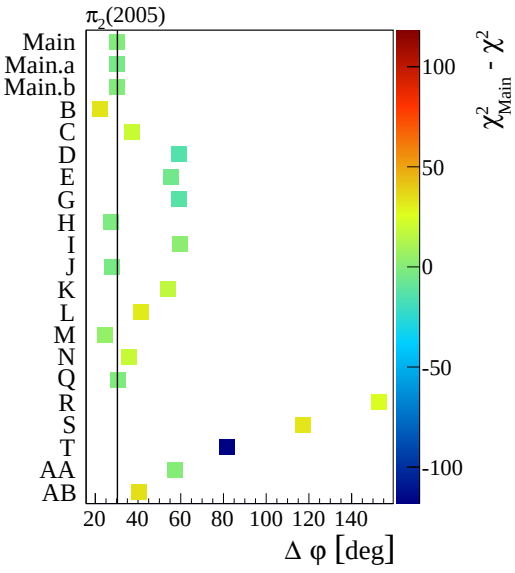

(d) Systematics of the maximal phase motion

Figure G.25: t' dependence and systematic studies for $\pi_2'(2005)$ in $2^{-+}0^+ f_2(1270)\pi D$.

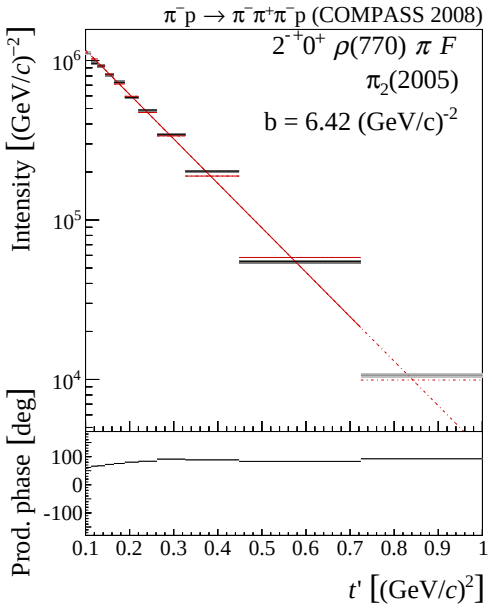

(a) t' dependence of the Main fit

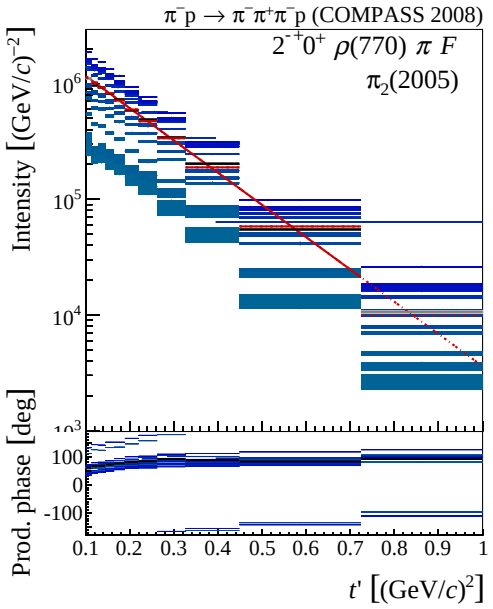

(b) t' dependence in all systematic studies

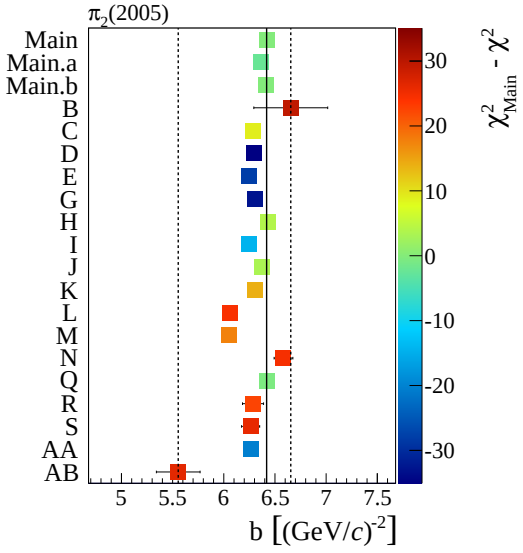

(c) Systematics of the t' slope parameter

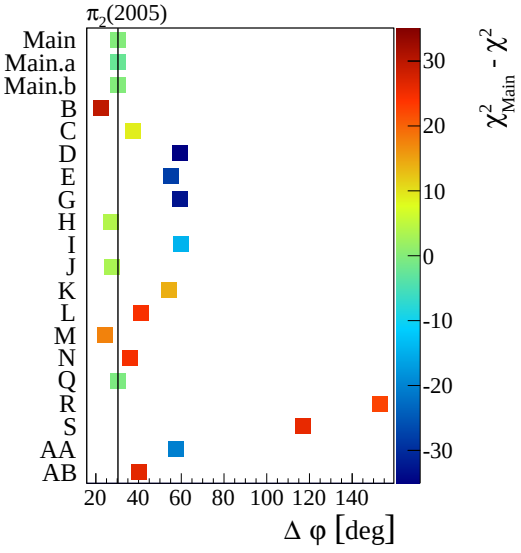

(d) Systematics of the maximal phase motion

Figure G.26: t' dependence and systematic studies for $\pi_2'(2005)$ in $2^{-+}0^+\rho(770)\pi F$.

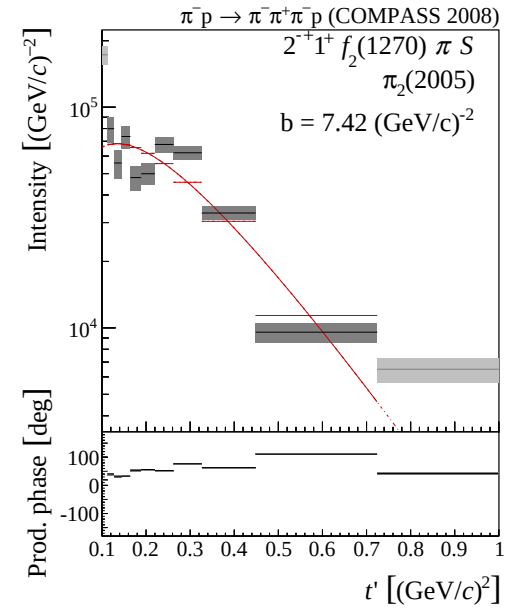

(a) t' dependence of the Main fit

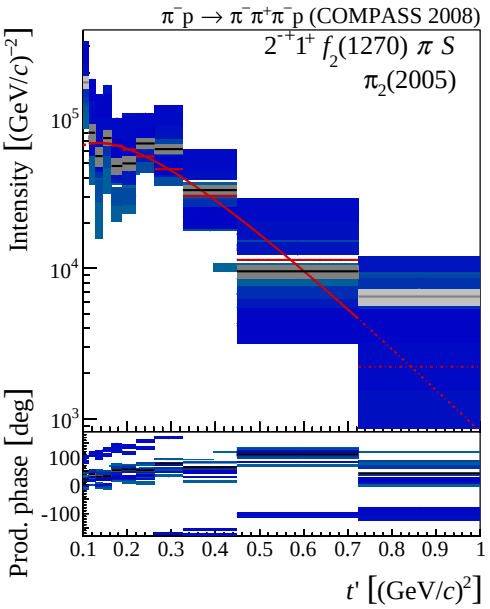

(b) t' dependence in all systematic studies

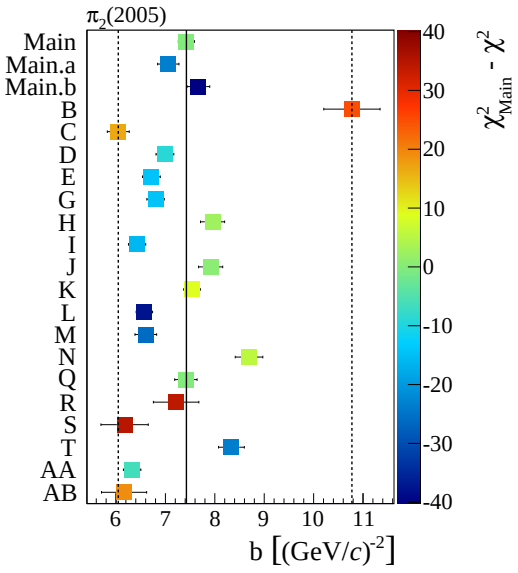

(c) Systematics of the t' slope parameter

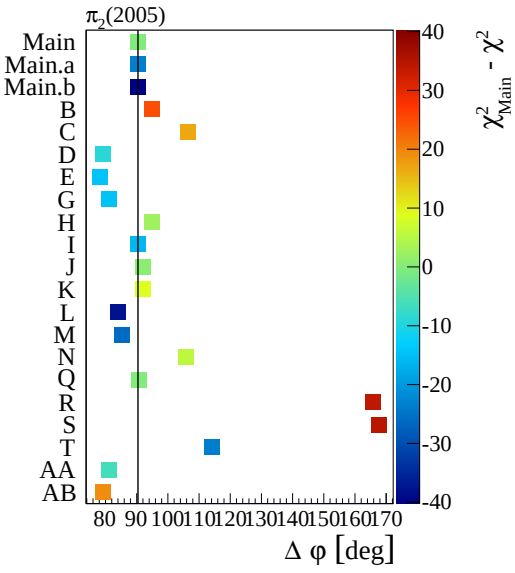

(d) Systematics of the maximal phase motion

Figure G.27: t' dependence and systematic studies for $\pi_2'(2005)$ in $2^{-+}1^+ f_2(1270)\pi S$.

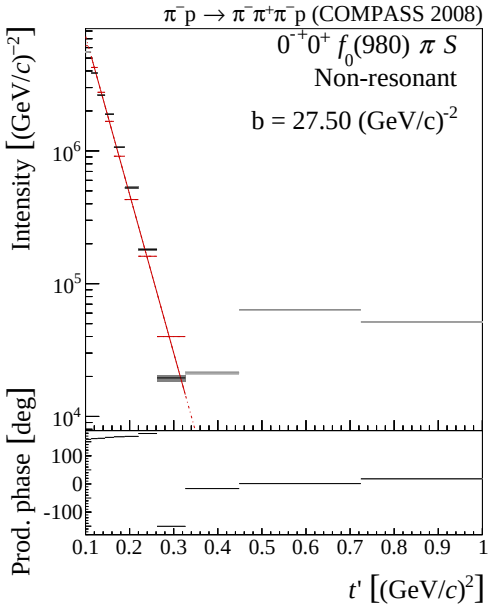

(a) t' dependence of the Main fit

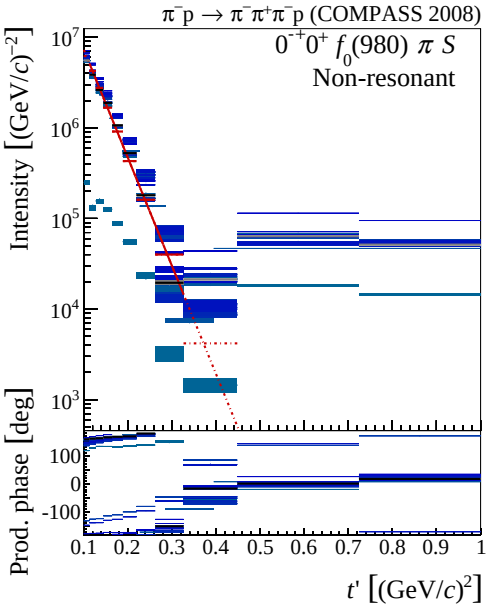

(b) t' dependence in all systematic studies

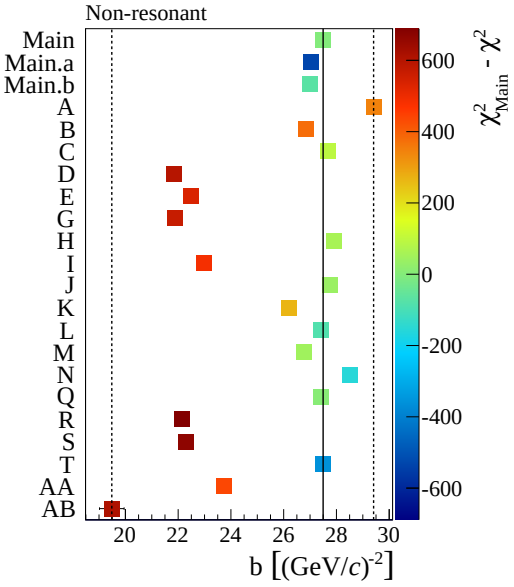

(c) Systematics of the t' slope parameter

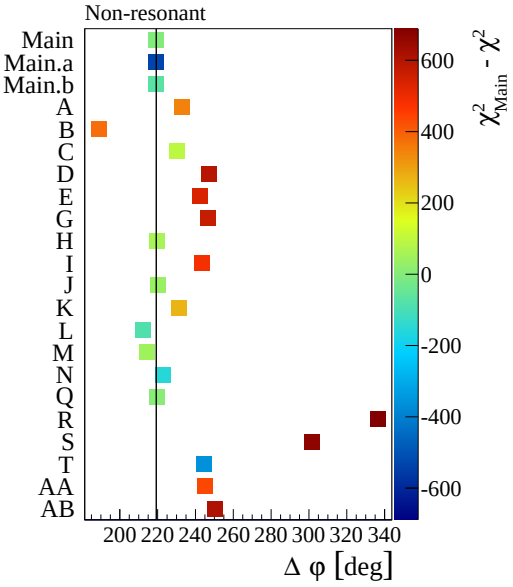

(d) Systematics of the maximal phase motion

Figure G.28: t' dependence and systematic studies for Non-Resonant in $0^{-+}0^{+}f_0(980)\pi S$.

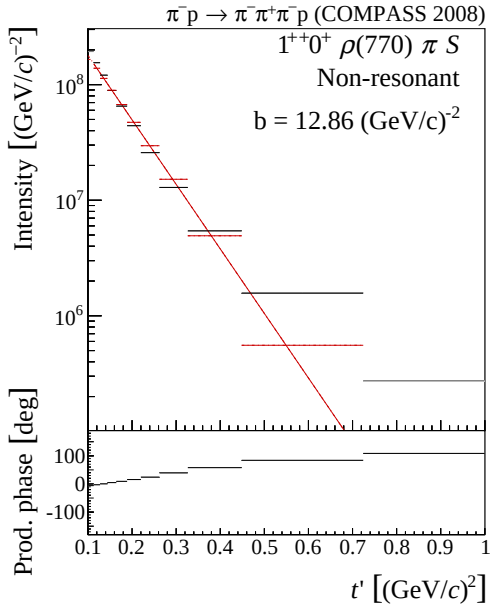

(a) t' dependence of the Main fit

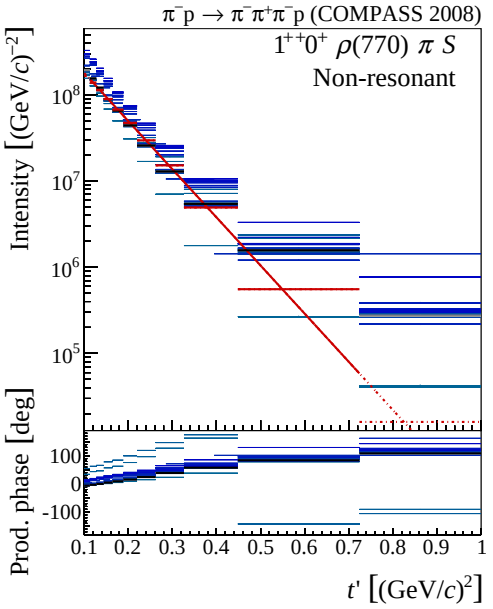

(b) t' dependence in all systematic studies

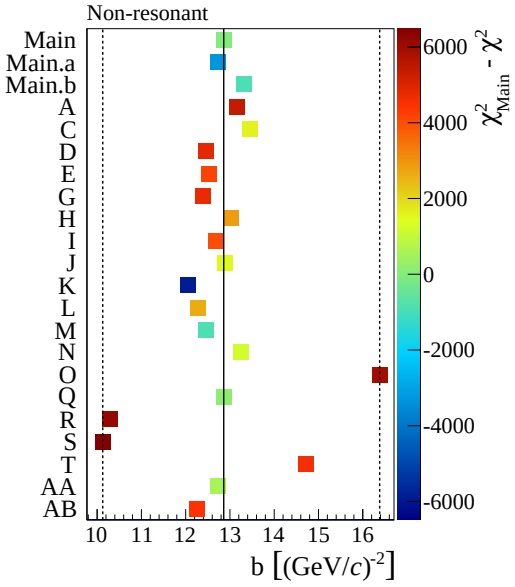

(c) Systematics of the t' slope parameter

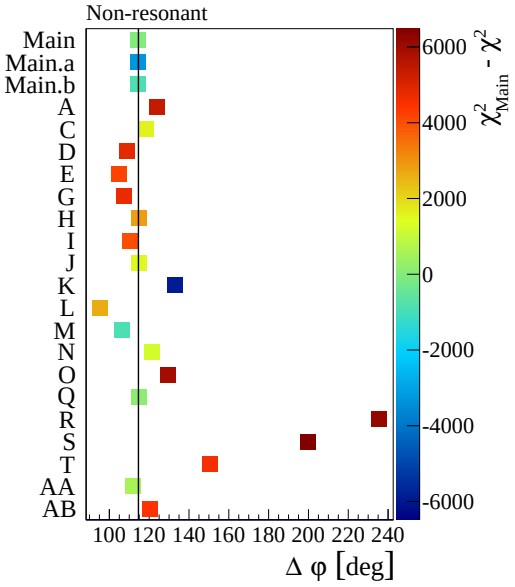

(d) Systematics of the maximal phase motion

Figure G.29: t' dependence and systematic studies for Non-Resonant in $1^{++}0^{+}\rho(770)\pi S$.

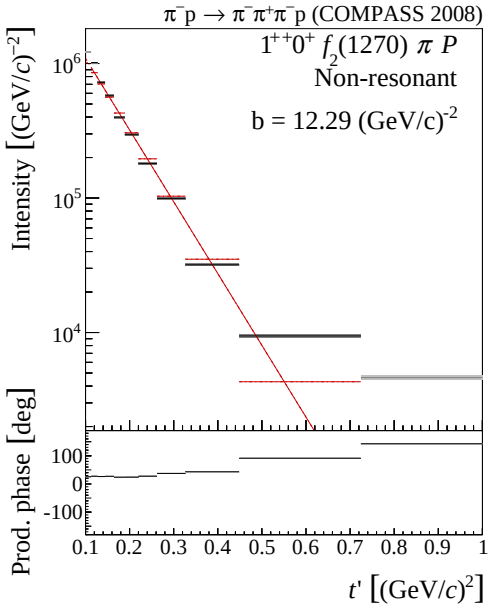

(a) t' dependence of the Main fit

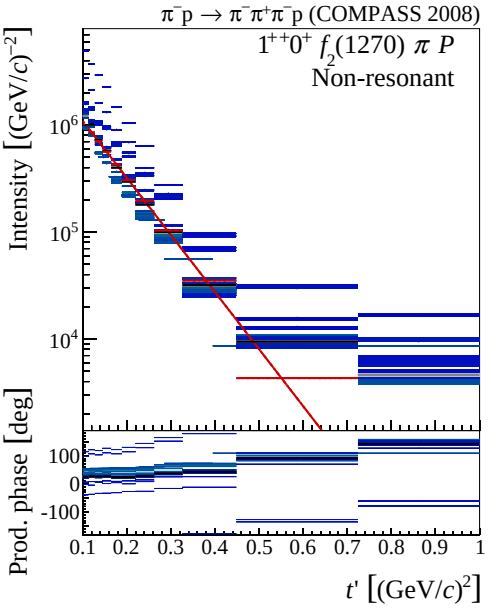

(b) t' dependence in all systematic studies

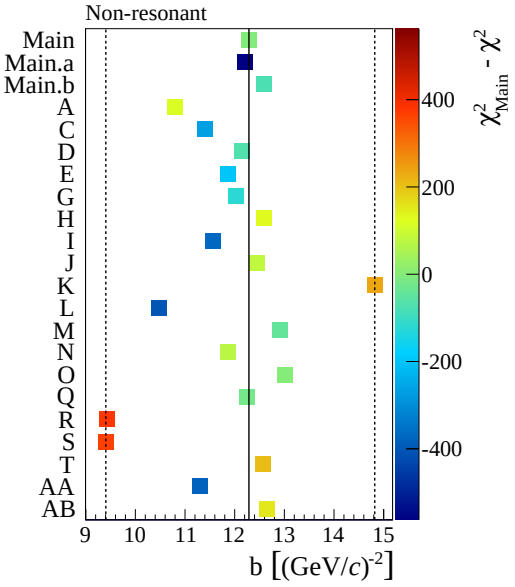

(c) Systematics of the t' slope parameter

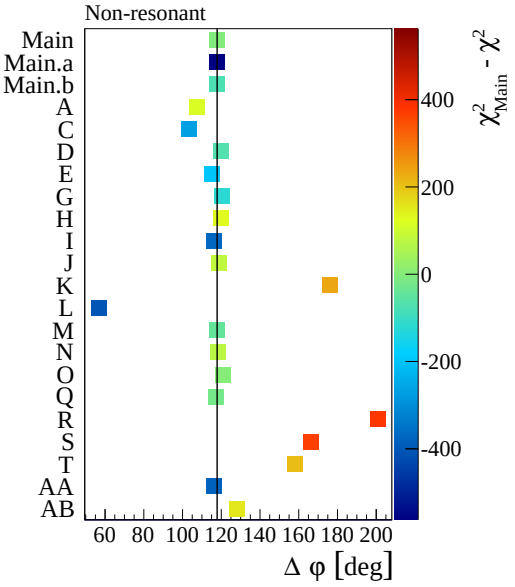

(d) Systematics of the maximal phase motion

Figure G.30: t' dependence and systematic studies for Non-Resonant in $1^{++}0^{+}f_2(1270)\pi P$.

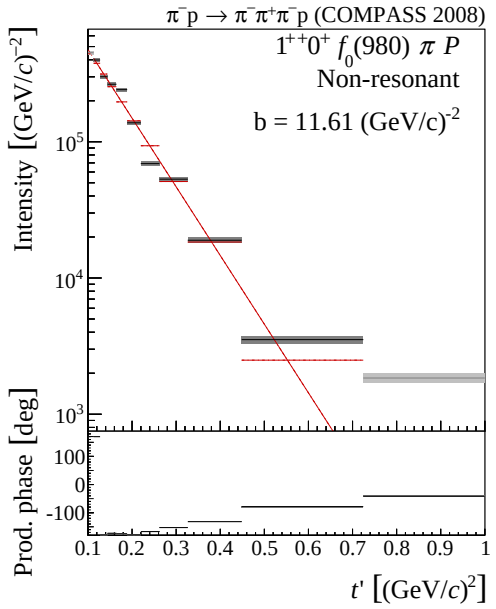

(a) t' dependence of the Main fit

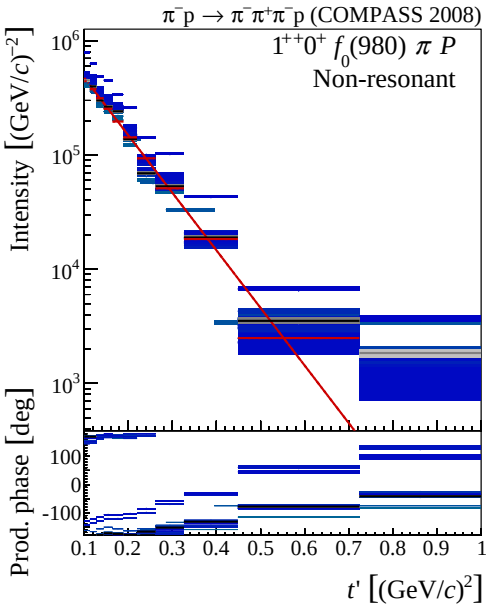

(b) t' dependence in all systematic studies

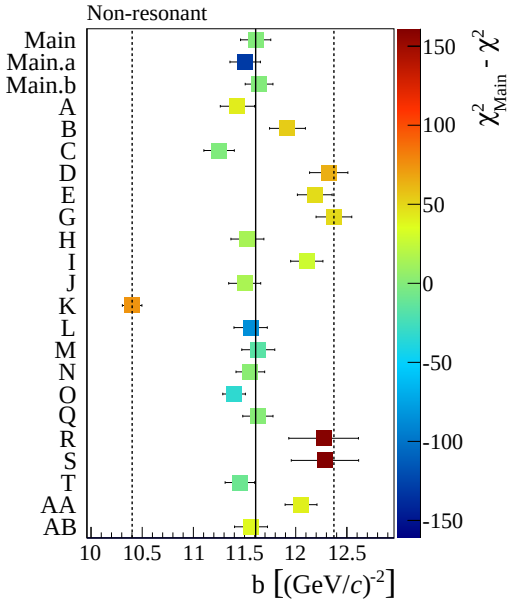

(c) Systematics of the t' slope parameter

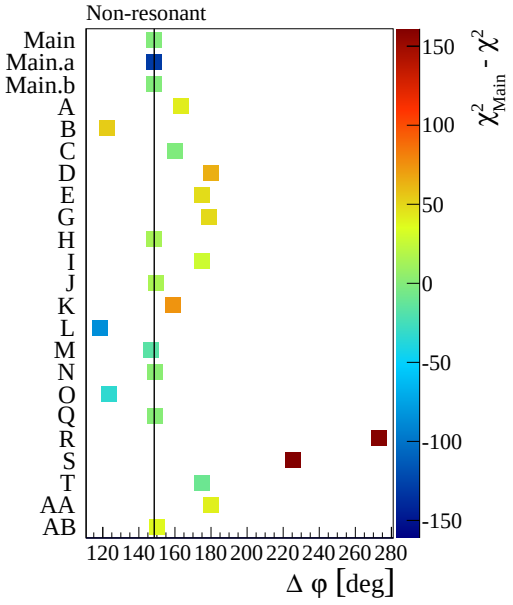

(d) Systematics of the maximal phase motion

Figure G.31: t' dependence and systematic studies for Non-Resonant in $1^{++}0^{+}f_0(980)\pi P$.

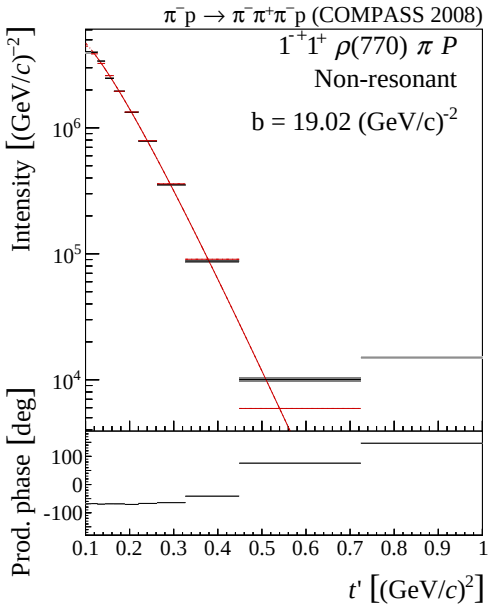

(a) t' dependence of the Main fit

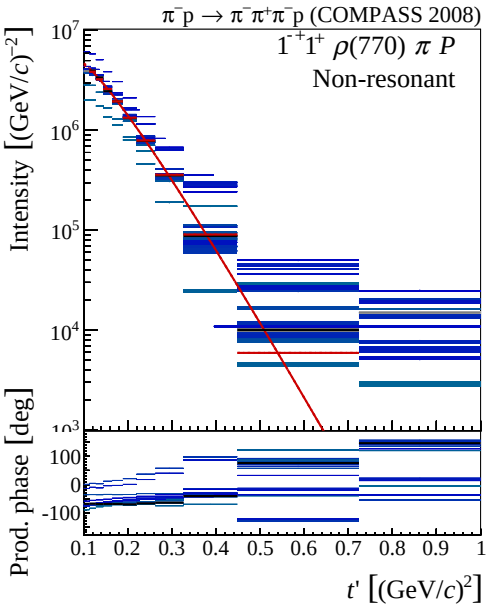

(b) t' dependence in all systematic studies

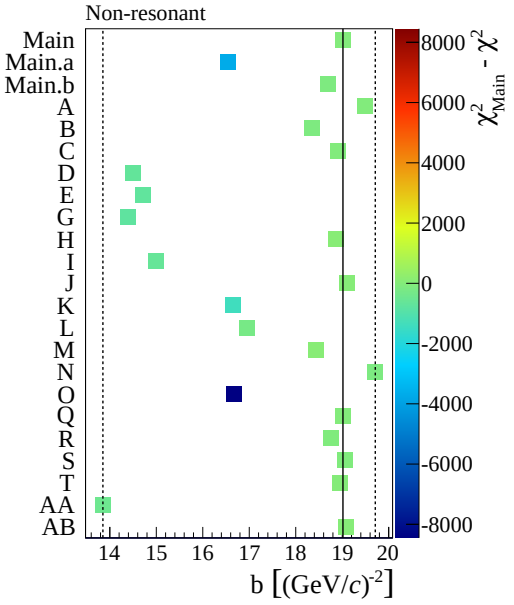

(c) Systematics of the t' slope parameter

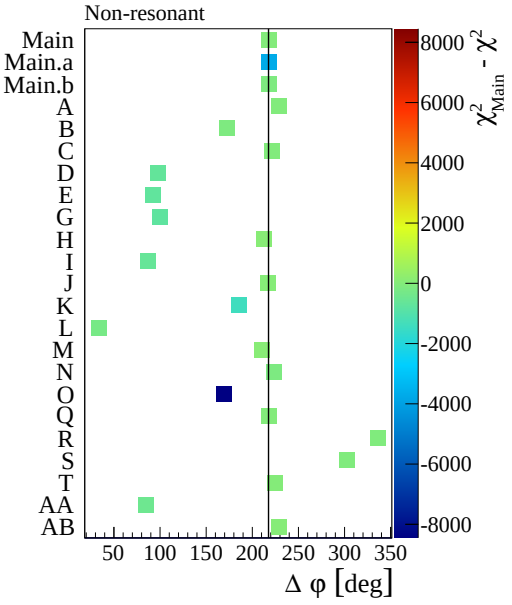

(d) Systematics of the maximal phase motion

Figure G.32: t' dependence and systematic studies for Non-Resonant in $1^{-+}1^{+}\rho(770)\pi P$.

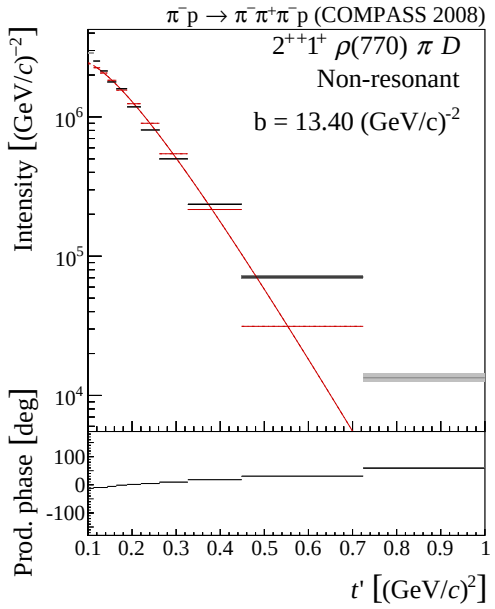

(a) t' dependence of the Main fit

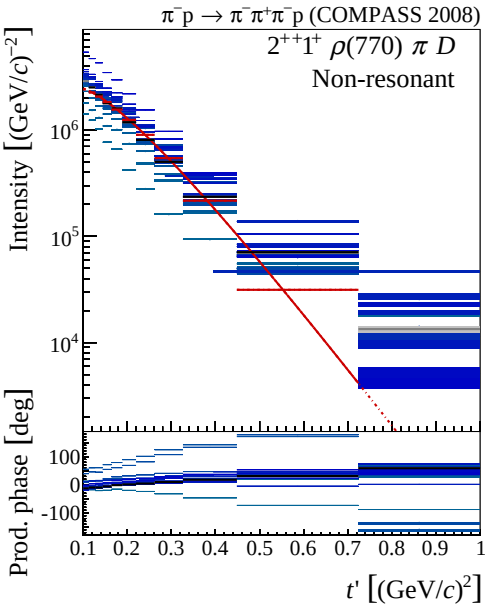

(b) t' dependence in all systematic studies

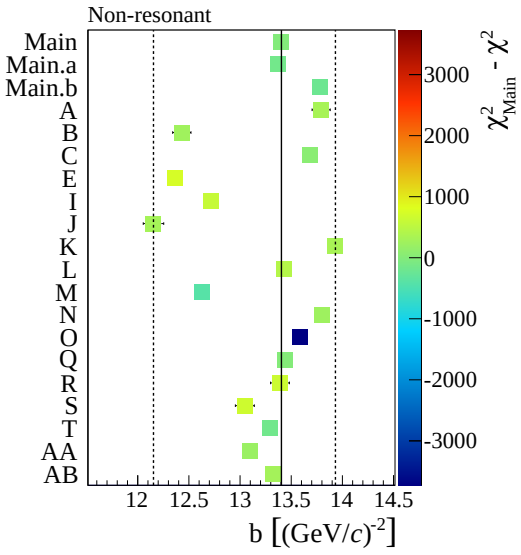

(c) Systematics of the t' slope parameter

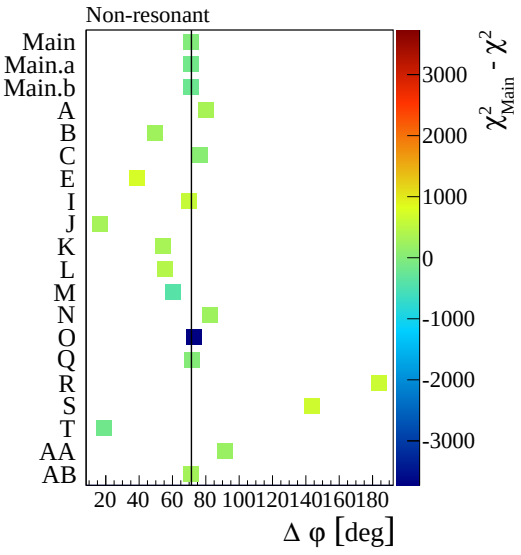

(d) Systematics of the maximal phase motion

Figure G.33: t' dependence and systematic studies for Non-Resonant in $2^{++}1^{+}\rho(770)\pi D$.

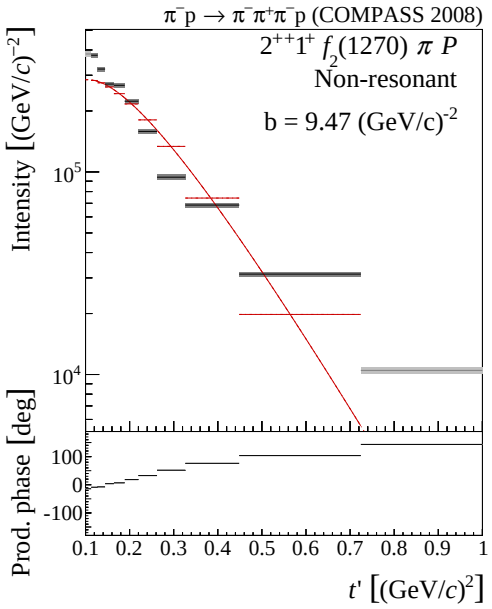

(a) t' dependence of the Main fit

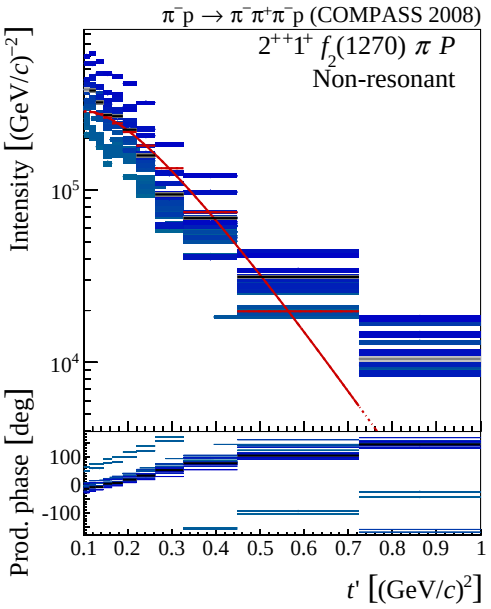

(b) t' dependence in all systematic studies

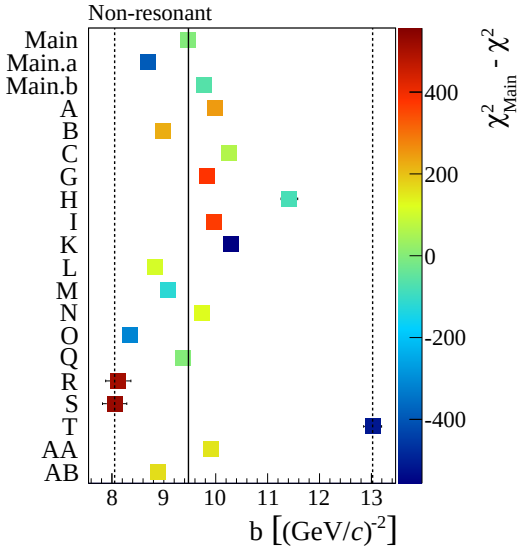

(c) Systematics of the t' slope parameter

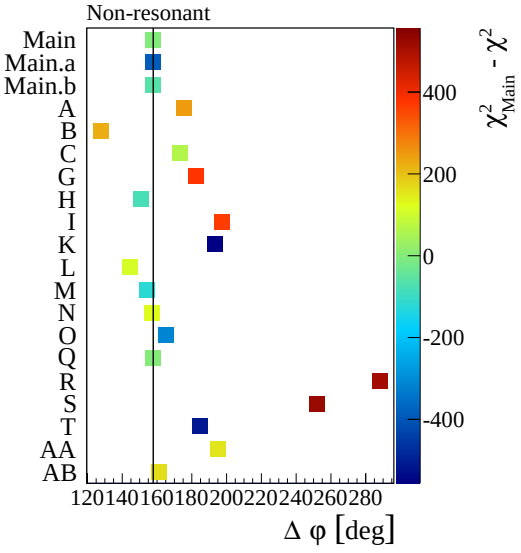

(d) Systematics of the maximal phase motion

Figure G.34: t' dependence and systematic studies for Non-Resonant in $2^{++}1^{+}f_2(1270)\pi P$.

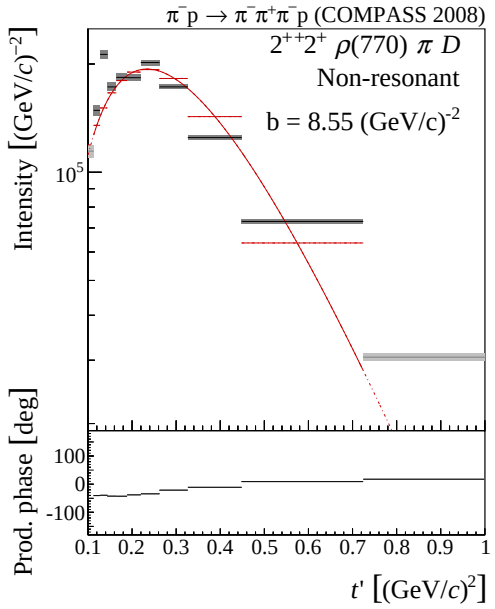

(a) t' dependence of the Main fit

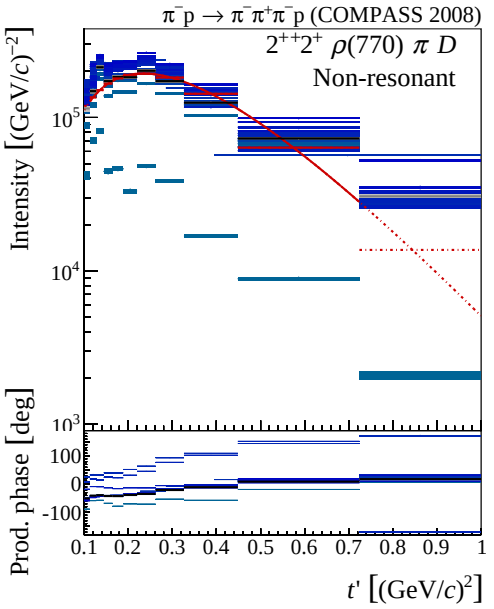

(b) t' dependence in all systematic studies

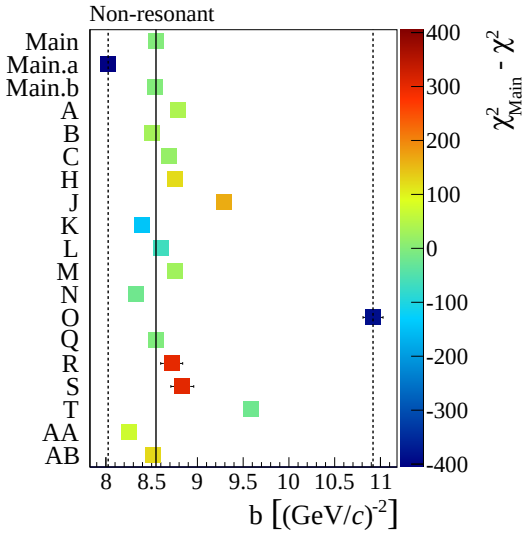

(c) Systematics of the t' slope parameter

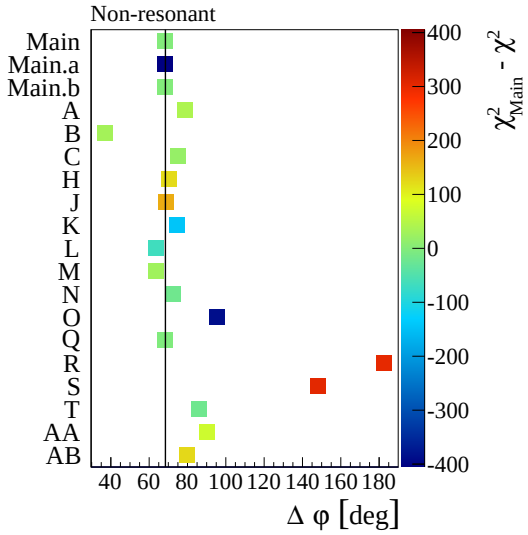

(d) Systematics of the maximal phase motion

Figure G.35: t' dependence and systematic studies for Non-Resonant in $2^{++}2^+\rho(770)\pi D$.

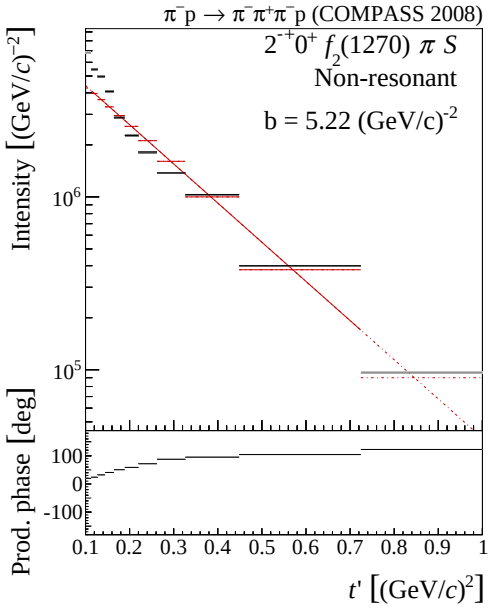

(a) t' dependence of the Main fit

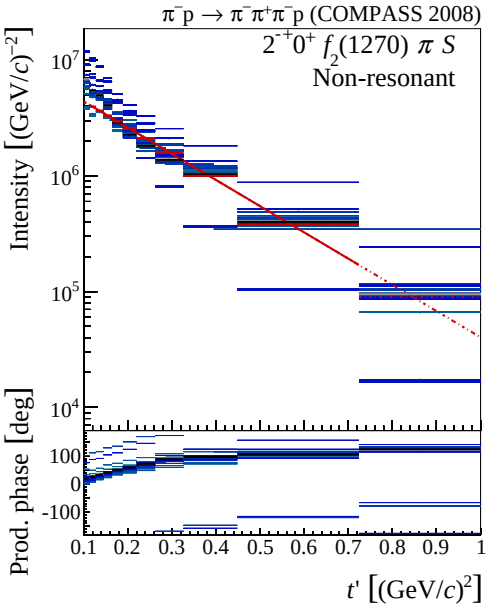

(b) t' dependence in all systematic studies

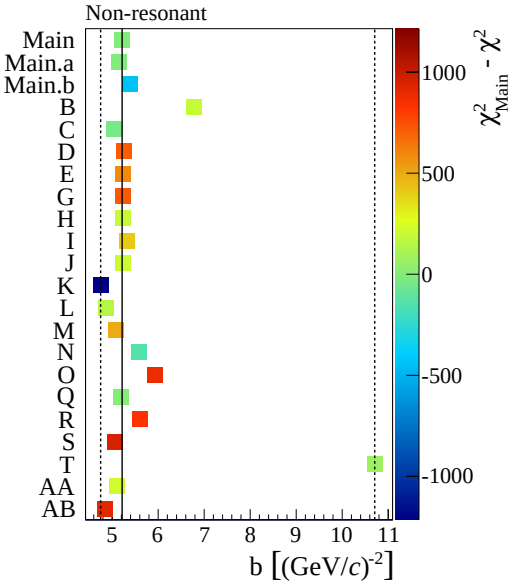

(c) Systematics of the t' slope parameter

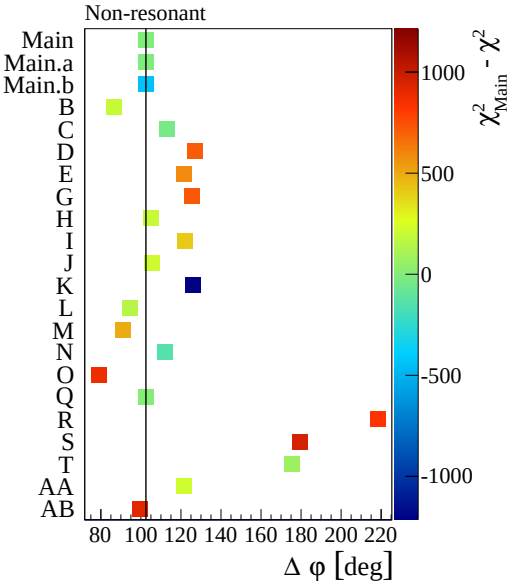

(d) Systematics of the maximal phase motion

Figure G.36: t' dependence and systematic studies for Non-Resonant in $2^{-+}0^{+}f_2(1270)\pi S$.

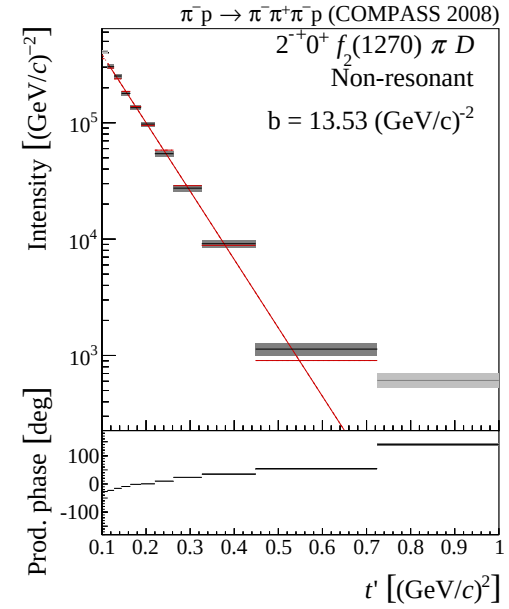

(a) t' dependence of the Main fit

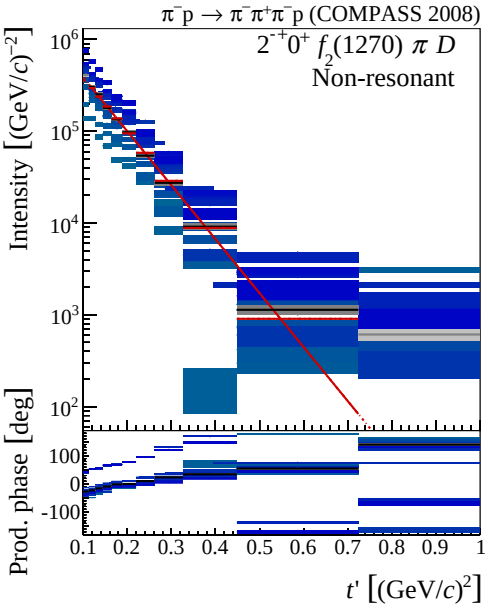

(b) t' dependence in all systematic studies

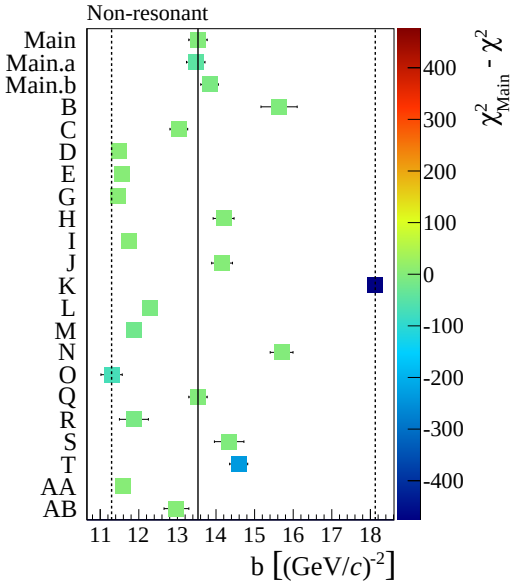

(c) Systematics of the t' slope parameter

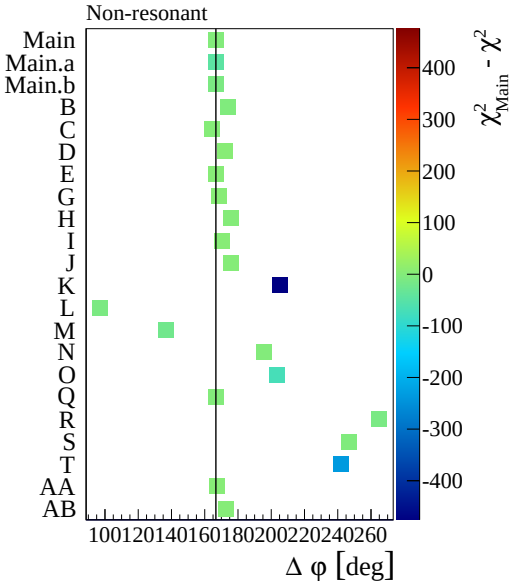

(d) Systematics of the maximal phase motion

Figure G.37: t' dependence and systematic studies for Non-Resonant in $2^{-+}0^{+}f_2(1270)\pi D$.

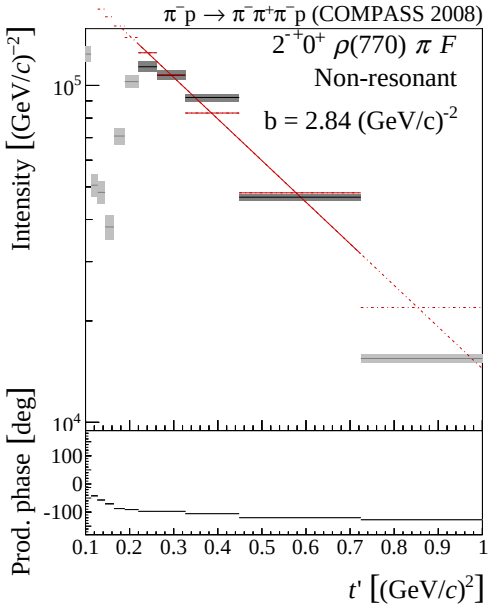

(a) t' dependence of the Main fit

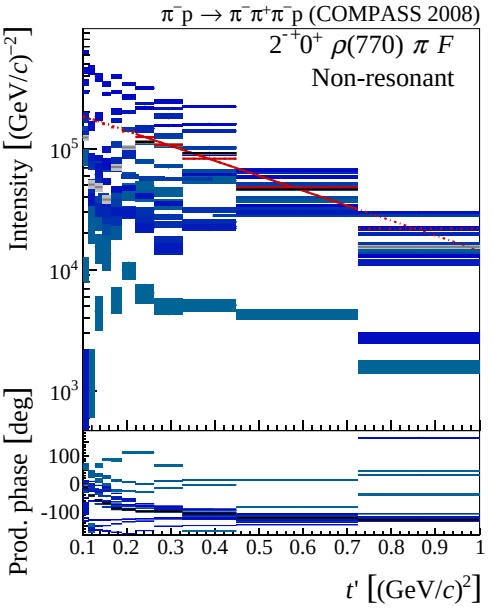

(b) t' dependence in all systematic studies

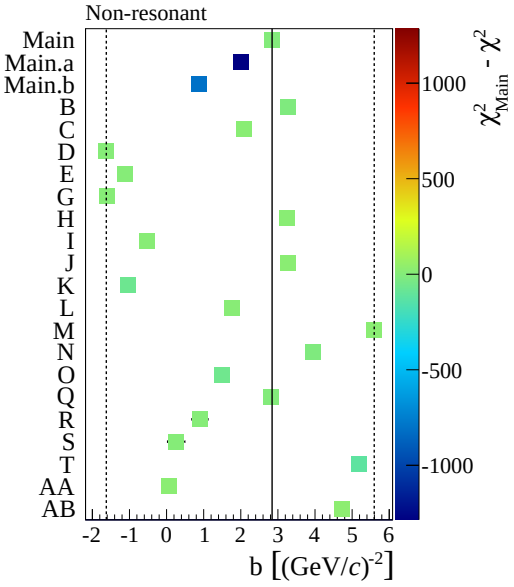

(c) Systematics of the t' slope parameter

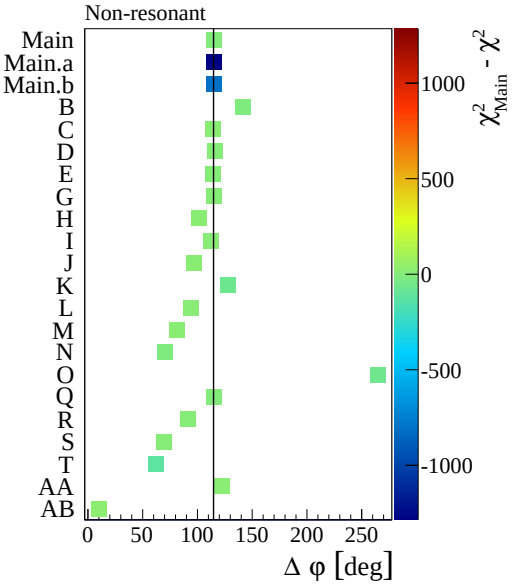

(d) Systematics of the maximal phase motion

Figure G.38: t' dependence and systematic studies for Non-Resonant in $2^{-+}0^{+}\rho(770)\pi F$.

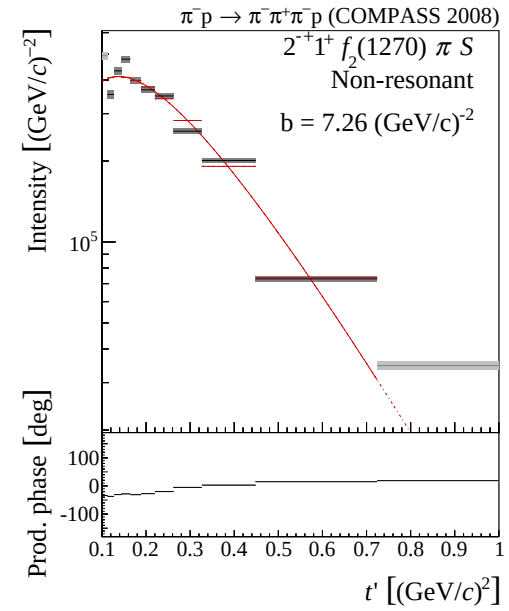

(a) t' dependence of the Main fit

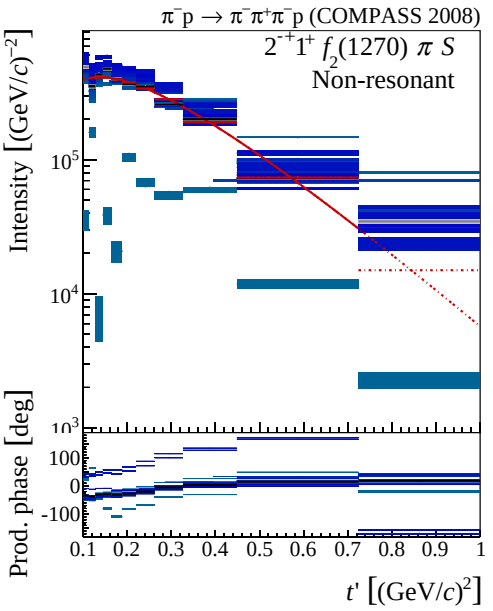

(b) t' dependence in all systematic studies

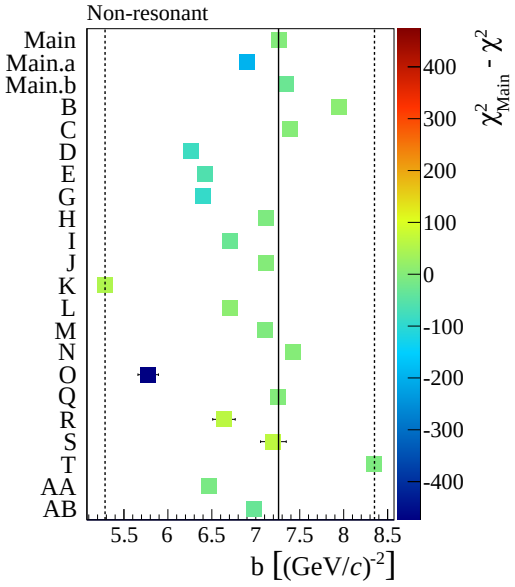

(c) Systematics of the t' slope parameter

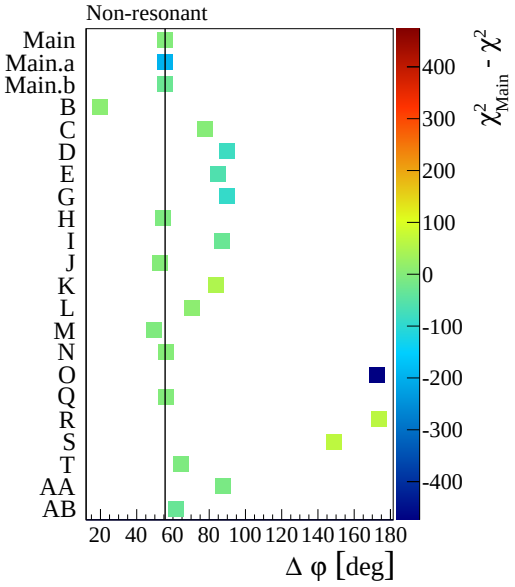

(d) Systematics of the maximal phase motion

Figure G.39: t' dependence and systematic studies for Non-Resonant in $2^{-+}1^{+}f_2(1270)\pi S$.

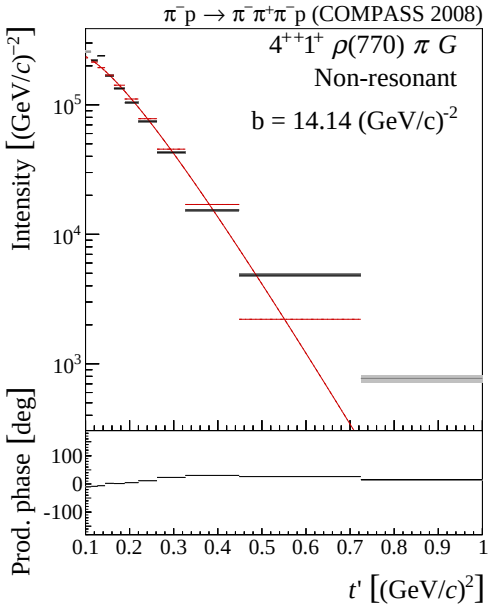

(a) t' dependence of the Main fit

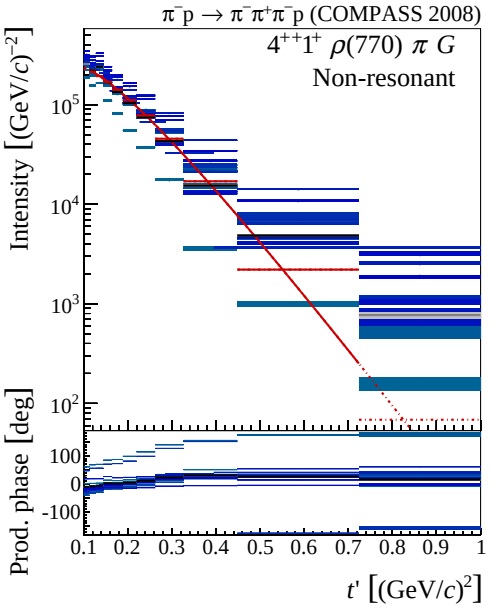

(b) t' dependence in all systematic studies

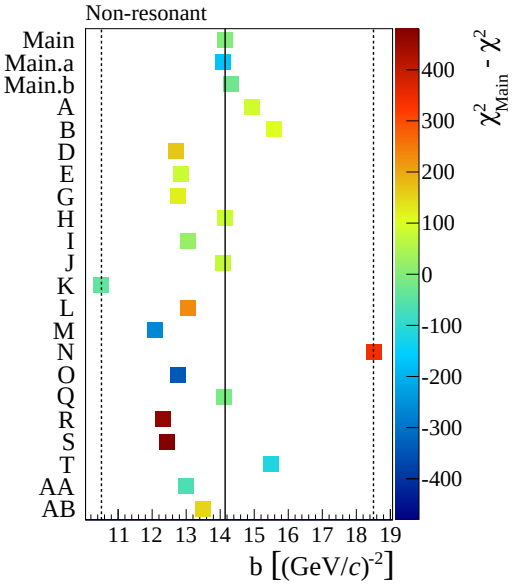

(c) Systematics of the t' slope parameter

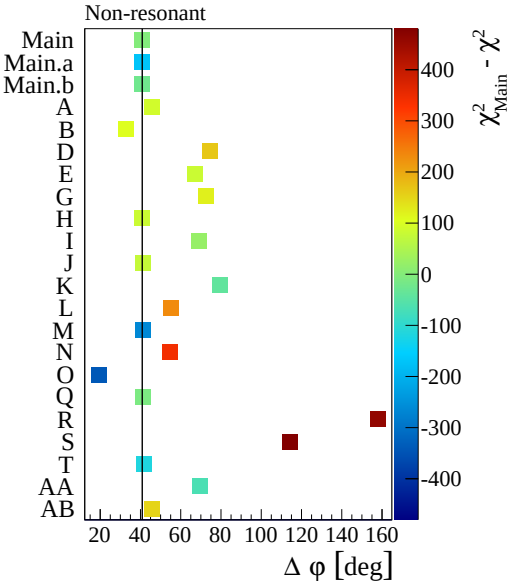

(d) Systematics of the maximal phase motion

Figure G.40: t' dependence and systematic studies for Non-Resonant in $4^{++}1^{+}\rho(770)\pi G$.

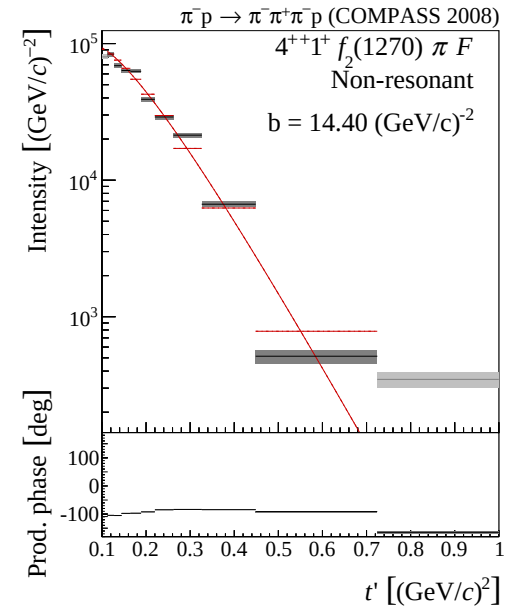

(a) t' dependence of the Main fit

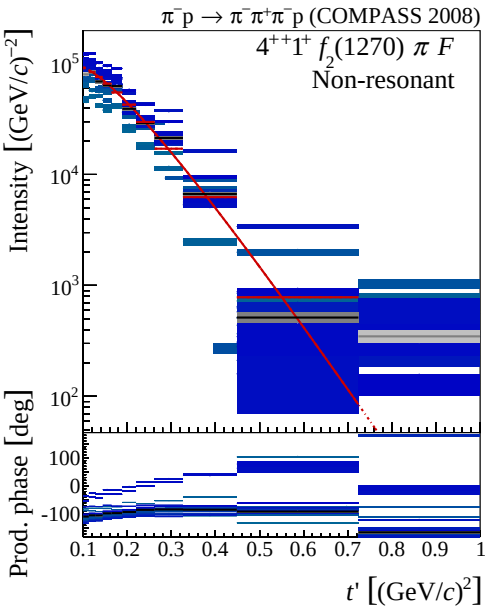

(b) t' dependence in all systematic studies

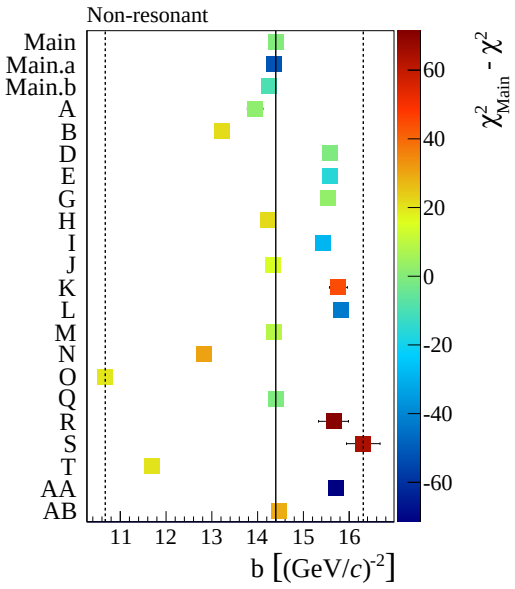

(c) Systematics of the t' slope parameter

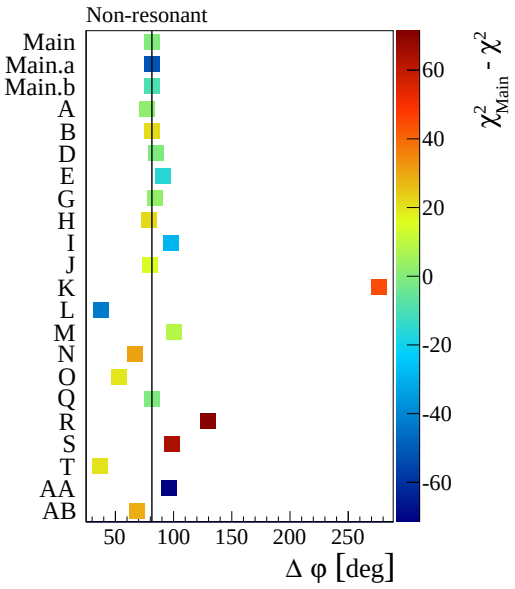

(d) Systematics of the maximal phase motion

Figure G.41: t' dependence and systematic studies for Non-Resonant in $4^{++}1^{+}f_2(1270)\pi F$.

Bibliography

[1] F. Haas, "Two-Dimensional Partial-Wave Analysis of Exclusive 190 GeV $\pi^- p$ Scattering into the $\pi^-\pi^-\pi^+$ Final State at COMPASS (CERN)," PhD thesis: Munich, Tech. U., 2014. (Cited on pages 2, 4, 5, 12, 19, 23, 74, 95, 117, 267)

[2] C. Adolph et al.,
"Resonance Production and $\pi\pi$ S-wave in $\pi^- + p \to \pi^-\pi^-\pi^+ + p_{recoil}$ at 190 GeV/c,"
(2015) 74, arXiv: 1509.00992. (Cited on pages 3, 6, 13, 15, 16, 18–21, 23, 24, 120)

[3] J. J. Dudek et al., "Toward the excited isoscalar meson spectrum from lattice QCD,"
Physical Review D **88**.9 (2013) 094505, ISSN: 1550-7998. (Cited on page 3)

[4] M. Battaglieri et al.,
"Analysis Tools for Next-Generation Hadron Spectroscopy Experiments," (2014) 1–28,
arXiv: 1412.6393. (Cited on pages 3, 5)

[5] C. M. G. LATTES et al., "Processes Involving Charged Mesons,"
Nature **159**.4047 (1947) 694–697, ISSN: 0028-0836. (Cited on page 3)

[6] K. A. Olive et al., "Review of Particle Physics," Chin. Phys. **C38** (2014) 90001.
(Cited on pages 3, 4, 14, 15, 29, 57, 86, 87, 89, 113, 127)

[7] R. T. Deck, "Kinematical interpretation of the first pi - rho resonance,"
Phys. Rev. Lett. **13** (1964) 169–173. (Cited on pages 4, 7)

[8] J. L. Basdevant and E. L. Berger,
"Unitary coupled-channel analysis of diffractive production of the a_1 resonance,"
Physical Review D **16**.3 (1977) 657–678, ISSN: 0556-2821. (Cited on page 4)

[9] D. Amelin et al.,
"Study of resonance production in diffractive reaction $\pi^- A \to \pi^+\pi^-\pi^- A$,"
Physics Letters B **356**.4 (1995) 595–600, ISSN: 03702693. (Cited on page 4)

[10] M. Lu et al., "Exotic Meson Decay to $\omega\,\pi^0\,\pi^-$,"
Physical Review Letters **94**.3 (2005) 032002, ISSN: 0031-9007. (Cited on pages 4, 14, 87–89)

[11] A. Zaitsev et al., "Study of exotic resonances in diffractive reactions,"
Nuclear Physics A **675**.1-2 (2000) 155–160, ISSN: 03759474. (Cited on pages 4, 14, 61)

[12] S. U. Chung et al., "Exotic and $q\overline{q}$ resonances in the $\pi^+\pi^-\pi^-$ system produced in $\pi^- p$ collisions at 18 GeV/c," Phys. Rev. D **65**.7 (2002) 72001. (Cited on pages 4, 5, 14)

[13] A. R. Dzierba et al., "Partial wave analysis of the $\pi^-\pi^-\pi^+$ and $\pi^-\pi^0\pi^0$ systems and the search for a $J^{PC} = 1^{-+}$ meson," Physical Review D **73**.7 (2006) 072001, ISSN: 1550-7998, arXiv: 0510068 [hep-ex]. (Cited on page 4)

[14] S. Schmeing, "Resonance Extraction in Diffractive 3 π Production using 190 GeV/c π^- at the COMPASS experiment (CERN)," MA thesis: Munich, Tech. U., 2014.
(Cited on pages 5, 28–30, 33, 34, 36, 267)

[15] I. A. Kachaev et al., "Study of reaction $\pi^- A \to \pi^+\pi^-\pi^- A$ at VES setup,"
AIP Conf. Proc. **619** (2002) 577–581, arXiv: hep-ex/0111067 [hep-ex].
(Cited on pages 5, 14)

[16] C. Daum et al.,
"A2 meson production at high energies in the reaction $\pi^- p \to \pi^-\pi^-\pi^+ p$,"
Physics Letters B **89**.2 (1980) 276–280, ISSN: 03702693. (Cited on page 5)

[17] M. G. Alekseev et al., "Observation of a $J^{PC} = 1^{-+}$ Exotic Resonance in Diffractive Dissociation of 190 GeV/c π^- into $\pi^-\pi^-\pi^+$,"
Physical Review Letters **104**.24 (2010) 241803, ISSN: 0031-9007,
arXiv: 0910.5842 [hep-ex]. (Cited on pages 5, 86)

[18] S. Donnachie et al., *Pomeron Physics and QCD (Cambridge Monographs on Particle Physics, Nuclear Physics and Cosmology)*, Cambridge University Press, 2005,
ISBN: 0521675707. (Cited on page 6)

[19] L. L. Foldy and R. F. Peierls, "Isotopic Spin of Exchanged Systems,"
Phys. Rev. **130**.4 (1963) 1585–1589. (Cited on page 6)

[20] P. Abbon et al., "The COMPASS setup for physics with hadron beams,"
Nuclear Instruments and Methods in Physics Research Section A: Accelerators, Spectrometers, Detectors and Associated Equipment **779** (2015) 69–115, ISSN: 01689002.
(Cited on pages 9–11)

[21] A. Austregesilo, "Central Production of Two-Pseudoscalar Meson Systems at the COMPASS Experiment at CERN," PhD thesis: CERN, 2014. (Cited on page 9)

[22] C. Adolph et al., "Measurement of the Charged-Pion Polarizability," Physical Review Letters **114**.6 (2015) 062002, ISSN: 0031-9007. (Cited on page 9)

[23] M. Alekseev et al., "Gluon polarisation in the nucleon and longitudinal double spin asymmetries from open charm muoproduction," Physics Letters, Section B: Nuclear, Elementary Particle and High-Energy Physics **676**.1-3 (2009) 31–38, ISSN: 03702693. (Cited on page 9)

[24] F. Von Hippel and C. Quigg, "Centrifugal-barrier effects in resonance partial decay widths, shapes, and production amplitudes," Phys. Rev. **D5** (1972) 624–638. (Cited on pages 21, 126)

[25] K. A. Bicker, "Model Selection for and Partial-Wave Analysis of a Five-Pion Final A State at the COMPASS Experiment at CERN," PhD thesis in preperation: TU München, 2015. (Cited on pages 22, 27)

[26] M. L. Perl, *High energy hadron physics*, 1974, ISBN: 0-471-68049-4. (Cited on pages 26, 95)

[27] M. BOWLER, "The A1 revisited," Physics Letters B **182**.3-4 (1986) 400–404. (Cited on pages 28, 125)

[28] F. James, "MINUIT Function Minimization and Error Analysis: Reference Manual Version 94.1," (1994). (Cited on page 32)

[29] D. Ryabchikov, *private communication*, 2015. (Cited on pages 33, 79, 126, 127, 130)

[30] B. Grube, *private communication*, 2015. (Cited on pages 61, 267)

[31] M. R. Pennington, *private communication*, 2015. (Cited on pages 63, 115)

[32] S. Uhl, "Performance optimization of PixelGEM tracking system and precission spectroscopy at COMPASS.," PhD thesis in preperation: TU München, 2015. (Cited on pages 71, 114, 116)

[33] C. Daum et al., "Diffractive production of 3π states at 63 and 94 GeV," Nuclear Physics B **182**.3 (1981) 269–336, ISSN: 05503213. (Cited on pages 74, 95)

[34] B. Hyams et al., "$\pi\pi$ Phase-shift analysis from 600 to 1900 MeV," Nuclear Physics B **64** (1973) 134–162, ISSN: 05503213. (Cited on page 74)

[35] F. Krinner, *private communication*, 2015. (Cited on page 79)

[36] P. C. Mahalanobis, "On the generalised distance in statistics," *Proceedings National Institute of Science, India*, vol. 2, 1, 1936 49–55. (Cited on page 80)

[37] O. Drotleff, "Model Selection for Partial-Wave Analysis of $\pi^- + p \to \pi^-\pi^+\pi^- + p$ at the COMPASS Experiment at CERN," Diploma thesis in preperation: TU München, 2015. (Cited on page 82)

[38] C. Adolph et al.,
"Odd and even partial waves of $\eta\pi^-$ and $\eta'\pi^-$ in $\pi - p \to \eta' \pi^- p$ at 191GeV/c,"
Physics Letters B **740** (2015) 303–311, ISSN: 03702693. (Cited on page 86)

[39] D. V. Amelin et al., "Investigation of the reaction $\pi^- + A \to \omega\pi^-\pi^0 + A$,"
Phys. Atom. Nucl. **62** (1999) 445–453. (Cited on pages 86–88)

[40] C. Baltay, C. V. Cautis, and M. Kalelkar, "Diffractive and Nondiffractive A1, A3, and A4 Production in $\pi^+ p$ Interactions at 15 GeV/c,"
Physical Review Letters **39**.10 (1977) 591–594, ISSN: 0031-9007. (Cited on page 87)

[41] A. Anisovich et al.,
"Partial wave analysis of $\bar{p}p$ annihilation channels in flight with I=1,C=+1,"
Physics Letters B **517**.3-4 (2001) 261–272, ISSN: 03702693. (Cited on page 88)

[42] J. Kuhn et al., "Exotic meson production in the $f_1(1285)\pi^-$ system observed in the reaction $\pi^- p \to \eta\pi^+\pi^-\pi^- p$ at 18 GeV/c," Physics Letters B **595**.1-4 (2004) 109–117, ISSN: 03702693. (Cited on page 88)

[43] M. Mikhasenko, B. Ketzer, and A. Sarantsev, "Nature of the $a_1(1420)$,"
Phys. Rev. D **91**.9 (2015) 94015. (Cited on pages 108, 114)

[44] Ỹ. Khokhlov et al.,
"Partial wave analyses of the $\pi^-\pi^0\pi^0$ and $\pi^-\pi^0$ systems with VES setup,"
PoS **Hadron2013** (2013) 88. (Cited on page 114)

[45] C. Adolph et al., "Observation of a New Narrow Axial-Vector Meson $a_1(1420)$,"
Phys. Rev. Lett. **115**.8 (2015) 82001. (Cited on page 114)

[46] J. Weinstein and N. Isgur, "$K\overline{K}$ molecules," Phys. Rev. D **41**.7 (1990) 2236–2257. (Cited on page 114)

[47] M. Alford and R. L. Jaffe, "Insight into the Scalar Mesons from a Lattice Calculation,"
(2000) 16, ISSN: 05503213, arXiv: 0001023 [hep-lat]. (Cited on page 114)

[48] Z.-G. Wang, "Light axial-vector tetraquark state candidate: $a_1(1420)$," (2014) 5,
arXiv: 1401.1134. (Cited on page 114)

[49] H.-X. Chen et al., "$a_1(1420)$ resonance as a tetraquark state and its isospin partner,"
Phys. Rev. D **91**.9 (2015) 94022. (Cited on page 114)

[50] J.-L. Basdevant and E. L. Berger, "Peak Locations and Relative Phase of Different Decay Modes of the a_1 Axial Vector Resonance in Diffractive Production," Phys. Rev. Lett. **114**.19 (2015) 192001. (Cited on page 114)

[51] F. Krinner, *Review of diffraction in COMPASS*, Bad Honnef, 2015. (Cited on page 115)

[52] A. Szczepaniak, *private communication*, 2015. (Cited on page 115)

[53] V. Anisovich and A. Sarantsev, "K-matrix analysis of the ($IJ^{PC} = 00^{++}$)-wave in the mass region below 1900 MeV," The European Physical Journal A - Hadrons and Nuclei **16**.2 (2003) 229–258, ISSN: 1434-6001. (Cited on page 115)

[54] The GlueX Collaboration et al., "A study of meson and baryon decays to strange final states with GlueX in Hall D (A proposal to the 39th Jefferson Lab Program Advisory Committee)," (2012) 20, arXiv: 1210.4508. (Cited on page 116)

[55] N. A. Törnqvist, "UNDERSTANDING THE SCALAR MESON $q\bar{q}$ NONET," Zeitschrift für Physik C Particles and Fields **68**.4 (1995) 35, ISSN: 0170-9739, arXiv: 9504372 [hep-ph]. (Cited on page 126)

[56] A. Kaidalov and K. Ter-martirosyan, "The pomeron-particle total cross section and diffractive production of showers at very high energies," Nuclear Physics B **75**.3 (1974) 471–482, ISSN: 05503213. (Cited on page 127)

[57] M. R. Atayan et al., "A study of double pomeron exchange in $\pi^+ p$ and $K + p$ interactions at 250 GeV/c," Zeitschrift für Physik C Particles and Fields **50**.3 (1991) 353–360, ISSN: 0170-9739. (Cited on page 127)

List of Figures

List of Tables

Own Contributions

The main goal of this thesis was the improvement of the resonance-model fit and the estimation of the systematic uncertainties of the extracted resonance parameters. The data used for the analysis were collected by the COMPASS collaboration. The event selection and partial-wave decomposition, as described in chapters 2 and 3, were performed by F. Haas [1]. These partial-wave decomposed data are the basis for my analysis. The fitting scheme and solution cuts, described in section 4.3, were developed by S. Schmeing [14].

The starting point of this thesis was the 13-wave resonance model developed by S. Schmeing. To investigate a possible resonance content in the spin-exotic $1^{-+}\,1^{+}\,\rho(770)\,\pi\,P$ wave, I replaced the $1^{++}\,0^{+}\,f_0(980)\,\pi\,P$ wave, which contains the $a_1(1420)$ resonance, in the original wave set by this spin-exotic wave. During the first half of the thesis, I extended and repeated the in [14] performed systematic studies with the new wave set. For example, to investigate influences of the non-resonant parameterization, the spin-parity decomposition of Monte Carlo events, which were generated according to a model for Deck-like processes, was used as non-resonant parameterization (see section 6.1.5). This required the implementation of this parameterization in the fitting software and also a major restructuring of the python wrapper, which was developed in [14]. In total, I performed more than 200 systematic studies. The result of each of these studies contains a large amount of information from the different partial waves and components in the resonance model. To be able to perform this large amount of studies, I extended the python wrapper to easily compare the results of the studies and to make the user interface simple and robust.

During these systematic studies it turned out, that the $1^{++}\,0^{+}\,\rho(770)\,\pi\,D$ wave, which was originally included instead of the $1^{++}\,0^{+}\,f_2(1270)\,\pi\,P$ wave, introduces very large systematic uncertainties and unphysical solutions. To overcome this problem, I replaced this wave by the $1^{++}\,0^{+}\,f_2(1270)\,\pi\,P$ wave. The parameterization of the non-resonant components, used in [14], includes the two-body break-up momentum in the $X^{-} \to \xi\,\pi^{-}$ decay, which is not defined below the $\xi\,\pi^{-}$ threshold. To be able to fit the $1^{++}\,0^{+}\,f_2(1270)\,\pi\,P$ down to the $f_2(1270)\pi^{-}$ threshold at approximately $1.4\,\mathrm{GeV}/c^2$, the original non-resonant parameterization was refined, such that it is smoothly continued into the mass region below the two-body threshold, by considering the finite with of the isobar ξ (see appendix D) [30]. Furthermore, I added the third π_2 resonance to the resonance model, in order to describe all features of the 2^{-+} waves. Additionally, to determine the systematic uncertainties of the $a_1(1420)$ using this improved resonance model, I added the

$1^{++}\,0^{+}\;f_0(980)\,\pi\,P$ wave to the wave set. With this improved resonance model I could extract the resonance parameters and, by repeating the essential systematic studies, I could also determine their systematic uncertainties, as presented in chapters 5 to 7.

In parallel to these efforts, an alternative approach to parameterize the transition amplitudes in the so-called K-matrix formalism (see section 8.2) was proposed by Adam Szczepaniak and Michael Pennington. I implemented a simple K-matrix parameterization and performed first fits which gave promising results.

Acknowledgments

First of all, I want to thank Prof. Stephan Paul, not only for giving me the possibility to work on such a fascinating topic, but also for his ideas and suggestions. Furthermore, I like to thank him for the opportunity to become acquainted with the hadron-physics community. It was an enriching experience for me over the last year.

My sincerest thanks go to Boris Grube. He guided me through the jungle of partial-wave analysis and had always time to answer my various questions with his impressive knowledge about hadron physics. Without his advise and purposive attitude, I would have got lost in all the fascinating details of the analysis. Furthermore, I want to thank him for proofreading this thesis. I learned a lot from him. Thanks Boris.

Many thanks go to Dmitri Ryabchikov for our fruitful discussions about my results and about the implementation of the fit . He supported me when I implemented new features in the software. Forthermore, I like to thank all my E18 and COMPASS colleagues who had an open ear for my questions, especially Fabian Krinner, Karl Bicker and Sebastian Uhl. For a pleasant atmosphere in our office, I want to thank Christian Dreisbach, Andreas Hönle, Johannes Rauch and Arseniy Tsipenyuk. I want to thank Robert Glas for proofreading this thesis.

I like to thank the COMPASS collaboration for the opportunity to work with such a great data set. My special thanks go to Florian Haas, who performed the event selection and partial-wave decomposition, and Stephan Schmeing, who developed the resonance-model fit method. It was an honor to continue their work.

Also thanks go to the DFG Cluster of Excellence “Origin and Structure of the Universe”. A large fraction of the systematic studies were performed on their computing facilities (C2PAP).

Ich möchte herzlich meinen Eltern danke sagen. Nicht nur für eure Unterstützung während der Masterarbeit, sondern ganz besonders dafür, dass ihr mich immer ermutigt habt meinen eigenen Weg zu gehen.

Last but non least I thank Veronika Blache. Your are one of the most important reasons for my achievements during the last six years. Without your love and support this would not have been possible.

$$\frac{1}{x^2} \rightarrow +\infty^{+\infty}$$